X-ray spectral variability of Seyfert galaxies

Andrew Lobban

Doctor of Philosophy

Keele University

June 2013

Abstract

Active galactic nuclei are among the most persistently energetic objects in the known Universe. A large subset are observed to exhibit significant X-ray spectral variability on both short (ks) and long ($\gtrsim$ day) timescales. However, the source of the variability is unknown. Both intrinsic and reprocessing mechanisms such as relativistically-blurred reflection and partially-covering absorption have been invoked to account for it. Since no two sources appear to behave in exactly the same way, it could be that a combination of processes are at work.

In-depth analyses are performed on recent *Suzaku*, *Chandra* and *XMM-Newton* observations of two Seyfert galaxies (NGC 7213 and NGC 4051) which are found to lie at opposite ends of the observable parameter space. Their broad-band continuum and emission-line properties are studied in detail and the nature of their long-term spectral variability is assessed. NGC 7213 is a very low-accretion-rate source and shows no evidence either for a wind or for reprocessing by a standard accretion disc. It is found to be slowly variable with the long-term variations simply accounted for by changes in the normalisation of the intrinsic power-law continuum. Conversely, NGC 4051 (a much higher-accretion-rate source) displays extreme variability with the spectral shape hardening when the observed flux is low. It is suggested that this can be accounted for by changes in the covering-fraction of a Compton-thick clumpy accretion-disc wind.

By considering notable examples from the literature along with recent evidence for high columns of outflowing gas in the line-of-sight towards higher-accretion-rate type-1 Seyfert galaxies, this work is placed into context. It is suggested that reprocessing by absorbing material, possibly arising from accretion-disc winds in higher-accretion-rate sources, may play a pivotal role in modifying the observed X-ray spectra of type-1 active galaxies; a result which may have strong implications for unified schemes.

Acknowledgements

I first and foremost wish to express my sincere gratitude to my supervisor, Dr James Reeves, who has offered fantastic support and guidance throughout the course of my Ph.D. and to whom I am indebted. Without his enthusiasm, honesty and good ideas, this thesis would not have been possible. On a scientific note, I also wish to thank my collaborators for their valuable input and encouragement; most notably, this includes Jane Turner, Lance Miller, Valentina Braito, Delphine Porquet, Alex Markowitz, Mike Crenshaw and Steve Kraemer.

I would like to thank those who taught me physics at undergraduate level for the inspiring three years prior to my Ph.D. Primarily, this includes Nye Evans, Rob Jeffries, Arumugam Mahendrasingam, Pierre Maxted and Jacco van Loon. My thanks extends to the rest of the astrophysics department at Keele University for providing me with such a friendly, enjoyable and inspiring environment in which to work. I would like to thank Barry Smalley for all his technical assistance and, most notably, I wish to express my gratitude towards David Anderson and Alexis Smith for the spontaneous sanity-rescuing outings and many fond memories that I will take away with me from these two great friendships.

I could also not have survived without the fantastic companionship of my fantastic friends (both old and new) away from the office who have always been there to provide well-needed distractions. This includes Philip Symons, Aaron Pointon, Becky Flynn, Ed Daniels, Matt Smith, Darren McDonald, Jennifer Evans, Chris Khosa, Jason Gofford, Adam Patrick, Stephen Pitchfork, Rebecca Harrison, Mark Jackson and Ian Edwards (R.I.P.) plus the great friends that I made in Paris in the summer of 2009. I also wish to give a very special mention to Chris Greenaway for the many hilarious escapades (often at my expense) on the south coast and to Emily Sage for the wonderful company and stress-relief on the squash court.

Finally, I wish to express my thanks to my close family for all their love and support and for putting up with me during the difficult times; in particular, my parents, Amanda and Peter, and my sister, Katie. Apologies for anyone that I may have neglected to mention here by name - this is almost certainly down to accident, not design!

The last three-and-a-half years of my life may have provided some of the most mentally exhausting and stressful times ... but they were also the best times. Thank you.

Some of the research reported in this thesis was the result of collaboration with a group of investigators. The primary role of these collaborators (who appear as co-authors on the lead author's two published manuscripts) was to assist with scientific interpretation and discussion and to participate in review of the final published manuscripts. An exception to this appears in Sections 5.2.1, 5.3.1 and 5.3.3.3 where the author of the thesis instead engaged in scientific discussion and interpretation but was not primarily responsible for the research. Consequently, the corresponding text references the work conducted and published by these collaborators to reflect this. Otherwise, all other research including all data reduction, analysis and spectral modelling was conducted by the author of the thesis.

Contents

List of Figures

List of Tables

1 Introduction to Active Galactic Nuclei

1.1 Overview

Galaxies are huge gravitationally-bound systems consisting of typically 10^{11} stars, stellar remnants, dark matter and an interstellar medium of gas and dust. Normal galaxies are found to differ in their geometries yet can generally be classified as one of three different morphological types: spiral, elliptical and irregular, each with masses ranging from 10^6 to 10^{12} solar masses ($M_\odot$). Their sizes can be of the order of up to hundreds of kpc in diameter with the formation of the earliest galaxies thought to have taken place when the universe was young ($<10^9$ years after the Big Bang) in the majority of cases. In fact, some of the earliest quasars have now been discovered at redshifts of $z > 6$ (i.e. from the Sloan Digital Sky Survey (SDSS) and the Canada-France High-z Quasar Survey (CFHQS); Fan et al. 2001; Bertoldi et al. 2003; Walter et al. 2003; Willott et al. 2007) including one quasar recently discovered at a redshift of $z = 7.09$ (Mortlock et al. 2011), corresponding to a time when the universe was just ∼5% of its current age. There are believed to be over 10^{11} galaxies in the observable universe alone.

The majority of the electromagnetic radiation from these galaxies comes from the combined output of the nuclear reactions in stars. However, it was discovered that a certain subset of galaxies display unusual characteristics within their cores (Seyfert 1943). Approximately 10% of all galaxies are found to have intrinsically bright point-like nuclei with luminosities ranging from 10^7 to 10^{15} solar luminosities ($L_\odot$; or $L \sim 10^{40-48}\,\mathrm{erg\,s^{-1}}$), often outshining the rest of the galaxy by a factor of 100 or more. Instead of just radiating strongly across a narrow wavelength band, these objects also differ from normal galaxies in the sense that they radiate across the entire electromagnetic spectrum (with emission-line spectra covering wide ranges in ionisation; Peterson 1997) showing an excess at X-ray and infrared wavelengths by several orders of magnitude or more.

This radiation output is, in some cases, highly variable with significant changes in the brightness at certain wavelengths (particularly X-rays) potentially occurring on timescales as

short as just a few hours (Lawrence et al. 1985; McHardy & Czerny 1987). From light-crossing arguments, these fluctuations place strict limits on the maximum size of the radiation-emitting region as an object cannot brighten quicker than the time it takes for the light to travel from one side of the emitting region to the other (even if all parts of the object were to brighten simultaneously, one would still see a "lag"). From these calculations it can be shown that the nuclei of these galaxies are each constrained within a small volume perhaps with diameters on the order of light-days or less. Furthermore, the study of orbital motions of stars around the nucleus (e.g. Gillessen et al. 2009) suggests that a large, compact mass of up to around $10^{10}\,\mathrm{M}_{\odot}$ must be present at the centre resulting in the remarkable conclusion that huge luminosities ($\sim$100 times greater than that of the host galaxy) are being generated by a mass on the scale of billions of solar masses in a region with a diameter on a similar scale as that of the Solar System. The centres of these "active galaxies" are termed "active galactic nuclei" (AGN) and are believed to be the most highly luminous continuously emitting objects in the observable universe.

1.1.1 Accretion Process

The current theory suggests that the active nucleus is powered by the accretion of matter onto a supermassive black hole (SMBH; Rees 1984) of mass generally in the region of 10^6 to $10^9\,\mathrm{M}_{\odot}$. Essentially, a black hole will form when a mass, M, collapses to within a sphere of radius, r_{S}, where:

$$r_{\mathrm{S}} = \frac{2GM}{c^2}. \tag{1.1}$$

This is known as the Schwarzschild radius and is the radius of the sphere surrounding the central collapsed mass at which point the gravitational field strength is so strong that the (classical) escape velocity equals the speed of light, c. The sphere is known as the "event horizon" and it defines a region of spacetime in which no light or information can escape. As such, the black hole may grow by absorbing additional matter which has crossed the event horizon. Supermassive black holes in AGN have Schwarzschild radii of typically just a few

AU ($1\,\mathrm{AU} \approx 1.5 \times 10^{13}\,\mathrm{cm}$).[1]

Assuming that the accreting material is made of completely ionised hydrogen and that it accretes isotropically, the inward force acting on the gas must be equal to or in excess of the outward radiation force (due to Thomson scattering) for the system to remain intact. This leads to a derivation of the "Eddington limit" (L_{Edd}; also known as the "Eddington luminosity"), which can be thought of as the maximum luminosity of a source of a given mass that is powered by spherical accretion. It is given by:

$$L_{\mathrm{Edd}} = \frac{4\pi G c m_{\mathrm{p}}}{\sigma_{\mathrm{T}}} M \approx 1.26 \times 10^{38} (M/M_{\odot}), \tag{1.2}$$

and has units $\mathrm{erg\,s^{-1}}$, where M is the mass of the central object in g and σ_{T} is the Thomson scattering cross-section (which is given by $\sigma_{\mathrm{T}} = (8\pi/3)(e^2/4\pi\epsilon_0 m_{\mathrm{e}} c^2)^2 = 6.65 \times 10^{-25}\,\mathrm{cm}^2$). The derivation of the Eddington limit can also be used to determine a minimum mass for a source of luminosity, L. This is known as the "Eddington mass" and is given by:

$$M_{\mathrm{Edd}} = 8 \times 10^5 L_{44} M_{\odot}, \tag{1.3}$$

where L_{44} is the bolometric luminosity (L_{bol}) of the central source in units $10^{44}\,\mathrm{erg\,s^{-1}}$.

Assuming that the majority of the thermal emission arises from the innermost regions of the disc (i.e. within $5\,r_{\mathrm{S}}$) and ignoring relativistic effects, the energy available from a particle of mass m falling from distance is given by:

$$U = \frac{GMm}{5\,r_{\mathrm{S}}} = \frac{GMm}{10GM/c^2} = 0.1mc^2. \tag{1.4}$$

This suggests that a mass could potentially radiate ∼10% of its rest energy before finally spiraling into the black hole. This efficiency value of $\eta \sim 0.1$ (actually $\eta \sim 0.06$ for a Schwarzschild and $\eta \sim 0.35$ for a Kerr black hole; Thorne 1974), where η relates to the mass-energy equivalence by:

$$L = \eta \dot{M} c^2 \tag{1.5}$$

[1]Note that such distances may also be expressed as gravitational radii, where $1\,r_{\mathrm{g}}$ is half of $1\,r_{\mathrm{S}}$ (i.e. $r_{\mathrm{g}} = GM/c^2$).

(where $\dot{M} = dM/dt$ is the mass accretion rate), is far greater than the approximate value of $\eta \sim 0.007$ associated with nuclear fusion of hydrogen in stars and within an order of magnitude of the annihilation energy, mc^2, making accretion onto black holes the most efficient continuous mass-energy conversion process (aside from matter-antimatter annihilation) known.

Since the luminosity of the source (where $L = dE/dt$) can be described by equation 1.5, it can be seen that for $\eta = 0.1$, even a highly-luminous source (e.g. $L \approx 10^{46}\,\mathrm{erg\,s^{-1}}$) can be fueled and sustained by an accretion rate of just $\dot{M} \approx 2\,\mathrm{M_\odot\,yr^{-1}}$. It is then also possible to establish the "Eddington accretion rate", $\dot{M}_{\mathrm{Edd}}$:

$$\dot{M}_{\mathrm{Edd}} = \frac{L_{\mathrm{Edd}}}{\eta c^2}, \tag{1.6}$$

which can be thought of as the required mass accretion rate in order to sustain the Eddington luminosity of the source for a given mass of the central object. This equates to $\dot{M}_{\mathrm{Edd}} \approx 2.2 M_8\,\mathrm{M_\odot\,yr^{-1}}$. Note that this 'maximum' critical accretion rate can be exceeded, however, for accretion models that are not spherically symmetric. One such scenario would be if the matter accretes equatorially in a disc (see below) but the emergent radiation is emitted perpendicularly to the plane of the disc. Indeed, a spherical accretion process is unlikely to be a true representation of the source since a spherically symmetrical inflow of matter (i.e. where all properties of the accretion flow are determined by the distance, r, from the central mass) would require the material to have zero net angular momentum. This scenario is highly unlikely and so the accretion flow is more likely to form a disc, like in the case of interacting binary stars.

The gravitational field of the black hole is indeed thought to accelerate clouds of gas and dust towards it causing them to fall into orbit and eventually align into a disc. The huge observed luminosities are then generated as the accreting matter loses gravitational potential energy which is converted into kinetic and radiative energy via viscous dissipation. As the orbits are Keplerian, the inner regions orbit faster than those in more distant radial zones. A resultant viscous drag arises through this differential rotation of the disc and this viscosity causes particles to orbit slower than their required Keplerian orbital velocity for

their particular radial location from the central mass. Therefore, the particles fall into lower orbits losing angular momentum (which is transferred outwards)[2] and gravitational potential energy in the process. This results in a gradual infall of material and forms an "accretion disc" around the black hole. From the virial theorem, half of the released gravitational potential energy is radiated as heat (i.e. thermalised) and half goes towards increasing the kinetic energy of the particles allowing them to form stable orbits at smaller radii. As gravitational potential energy is released at the rate $GM\dot{M}/r$, the rate at which the disc radiates (under the assumption that the energy is dissipated locally and the medium is optically-thick) is given by:

$$L = \frac{GM\dot{M}}{2r} = 2\pi r^2 \sigma_{\rm SB} T(r)^4, \tag{1.7}$$

where $\sigma_{\rm SB}T^4$ is the energy radiated per unit area (i.e. from the Stefan-Boltzmann law), πr^2 is the area of the disc and the additional factor of 2 accounts for the fact that the disc has two sides. Rearranging to solve for the temperature yields:

$$T(r) = \left(\frac{GM\dot{M}}{4\pi\sigma_{\rm SB} r^3} \right)^{1/4}. \tag{1.8}$$

A more complex but correct derivation where the energy is dissipated through work done by viscous torques yields an extra factor of 3 and, expressing this in terms of $r_{\rm S}$ (i.e. Peterson 1997) yields:

$$T(r) \approx \left[\frac{3GM\dot{M}}{8\pi\sigma_{\rm SB} r_{\rm S}^3} \right]^{1/4} \left(\frac{r}{r_{\rm S}} \right)^{-3/4}, \tag{1.9}$$

which is appropriate for the regime where $r \gg r_{\rm S}$. Then, combining this with equation 1.1 allows it to be written as:

$$T(r) \approx \left[\frac{3c^6}{64\pi\sigma_{\rm SB} G^2} \right]^{1/4} \dot{M}^{1/4} M^{-1/2} \left(\frac{r}{r_{\rm S}} \right)^{-3/4}. \tag{1.10}$$

[2]Given that $|L|/m = rv = \sqrt{GMr}$, it can be shown that for a particle to fall from a radial location of tens of kpc from the black hole to within a few $r_{\rm g}$, its angular momentum must decrease by a factor on the order of $\sim 10^5$.

Finally, this can be written in terms of the Eddington accretion rate (equation 1.6) and for masses appropriate for AGN yielding a final expression for the radial dependency of the disc temperature:

$$T(r) \approx 6.3 \times 10^5 (\dot{M}/\dot{M_{\rm Edd}})^{1/4} M_8^{-1/4} \left(\frac{r}{r_{\rm S}}\right)^{-3/4} {\rm K}, \tag{1.11}$$

which is appropriate for standard, geometrically-thin, optically-thick accretion discs. Since the temperature gradient scales as $r^{-3/4}$, the disc can be thought of as a series of annuli, each emitting a blackbody spectrum characteristic of its temperature which cools at further radii. It can also be seen that at a given radius, the temperature will increase with accretion rate (with respect to the Eddington rate) but will decrease with increasing mass.

If matter falls within $\sim 3\, r_{\rm S}$ of the event horizon of a stationary black hole, it is expected to fall rapidly into the black hole and so the accretion disc is expected to extend inwards no closer than this. This is known as the innermost stable circular orbit (ISCO). However, in the case of a rotating (Kerr) black hole with angular momentum $J = aM$, the ISCO will decrease. Eventually, the last stable orbit reduces to $\sim 1.24\, r_{\rm g}$ for a maximal Kerr black hole when $a = 0.998$.

Interestingly, the earliest known quasars (see Section 1.2.1.3) can be traced back to a time when the universe was $\lesssim 10^9$ years old which suggests that SMBHs can be formed relatively quickly (e.g. Willott et al. 2007; Mortlock et al. 2011). Either a very high accretion rate was responsible for the quick growth or there was a large mass to begin with (Rees 1984). Since the material in the inner regions also requires a mechanism to lose angular momentum and so form the inner accretion disc, galaxy mergers could play an important role. It is perhaps conceivable that they result in a strong star-burst stage which could not only form the central SMBH but also provide a source of accretion fuel (Shlosman, Begelman & Frank 1990).

It should be noted that alternative scenarios to the black hole paradigm do exist such as the nuclear starburst model of Terlevich et al. (1992) in which the radiated energy originates from a cluster of young stars in the nucleus of the galaxy with various observed features such as optical / ultraviolet (UV) variability and broad emission lines attributed to various

supernovae. However, the model has difficulty explaining both the existence of radio-loud AGN and rapid X-ray variability (e.g. McHardy et al. 2004) with light-crossing arguments suggesting that the emission must originate from a region of diameter $< 10^{-3}$ pc. The star cluster would also have to be unusually compact since the nuclei of active galaxies remain unresolved even at the highest attainable spatial resolution.

Instead, strong evidence has been found for the existence of high mass, compact objects at the centres of galaxies through dynamical studies of gas (Ford et al. 1994), reverberation mapping (a technique whereby reflected light is used to map out the structure surrounding an emitting region) of broad-line regions (e.g. Korista et al. 1995; Peterson et al. 2004) and from studying the proper motion of stars at the centre of our own galaxy, the Milky Way (Gillessen et al. 2009).

1.1.2 Standard Model

The standard model of an AGN is shown in Figure 1.1 and, in its simplest form, consists of the following fundamental components:

1.1.2.1 The Central Engine

The so-called "central engine" consists of a supermassive black hole surrounded by an accretion disc. Viscous drag causes the disc to heat up and become a strong source of thermal emission with the innermost particle temperatures in excess of 10^5 K. The thermal emission in AGN is expected to be relatively prominent at UV wavelengths with the peak temperature scaling as $M^{-1/4}$ (see equation 1.11). This suggests that, for a given accretion rate, the peak temperature of the accretion disc will be higher for smaller black holes which may explain why Galactic black hole candidates (GBHCs) emit strongly in the X-ray band (indeed the thermal emission from a stellar-mass black hole with $M_{\rm BH} \approx 1\,{\rm M}_\odot$ would be expected to peak at a couple of keV). As the material falls inwards it must lose angular momentum which, in order to conserve the total angular momentum of the disc, must be transported outwards perhaps via turbulence-enhanced viscosity or magnetorotational instabilities (Balbus & Hawley 1991). The accretion disc is also thought to be linked to a hot corona (existing on compact

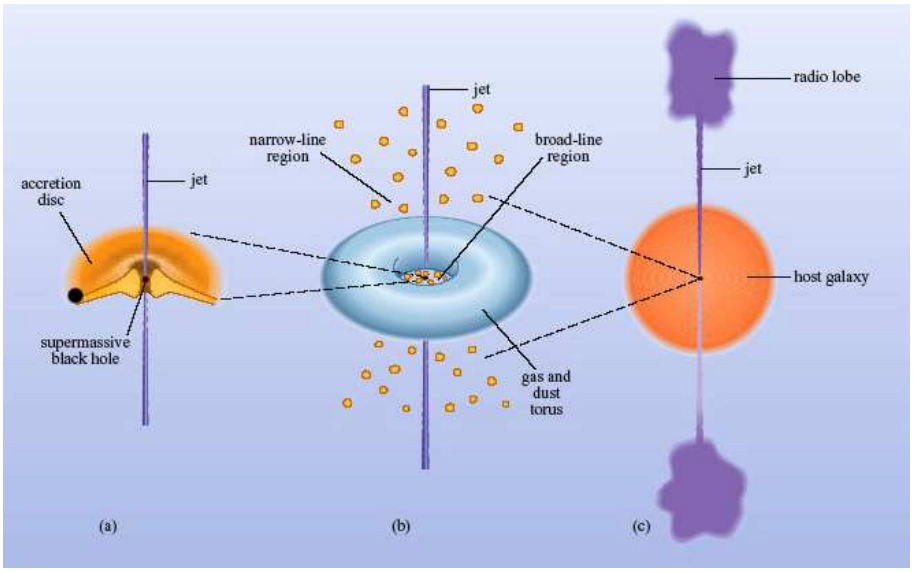

Figure 1.1: The standard model of an AGN on three different scales: *(a)* the central engine showing the supermassive black hole surrounded by the accretion disc; *(b)* the broad- and narrow-line regions and the molecular torus surrounding the central engine, and *(c)* the entire nucleus (in the radio-loud case). Figure taken from http://openlearn.open.ac.uk/.

size-scales of tens of $r_{\rm g}$) of relativistic electrons (Haardt & Maraschi 1991) which may be responsible for producing the primary X-ray continuum via inverse-Compton scattering of optical and UV seed photons from the disc. Precisely how the disc and corona are coupled, however, is not well understood, although it may be related to magnetic dissipation. Alternatively, photon-photon collisions may produce electron-positron pairs which then populate the corona (Fabian 1994).

The basic accretion-disc structure is primarily dependent upon the accretion rate of the source (Chen et al. 1995). The simplest case is that of the standard, geometrically thin (i.e. the height is small compared to the diameter) but optically-thick accretion disc which occurs when the accretion rate is fairly high, i.e. $\dot{M}/\dot{M_{\rm Edd}} \lesssim 1$ (see Figure 1.2). In this structure, the rate at which heat is vertically radiated away far exceeds the rate at which it is advected inwards, resulting in a high level of efficiency ($\eta \approx 0.1$) and thus producing a composite

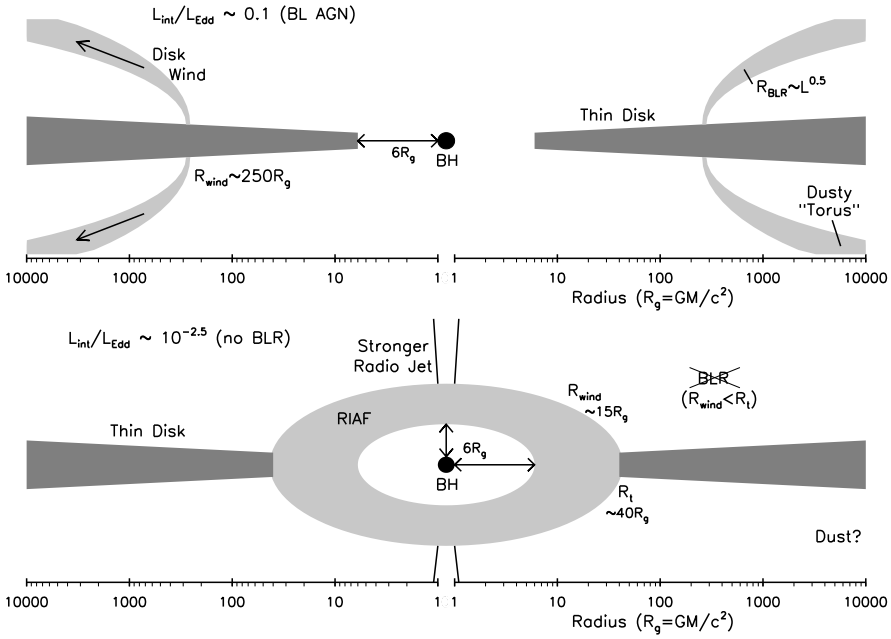

Figure 1.2: Schematic diagram showing how the accretion disc changes with the accretion rate of the source, resulting in the inner disc being replaced with a radiatively inefficient accretion flow when the accretion rate falls below some critical value. The x-axis show the radial distance from the black hole in units $r_{\rm g}$ although the y-axis is qualitative only. Figure taken from Trump et al. (2011).

spectrum of optically-thick thermal emission over the radial temperature-range present. A simple "α-disc" model (where the α parameter describes the viscosity) was proposed by Shakura & Sunyaev (1973) which assumes that the disc is optically-thick, geometrically-thin and is in local thermal equilibrium. This is a low-energy scenario with a disc temperature on the order of $\sim 10^{4-6}$ K and sub-sonic turbulence (lower than the rotation velocity of the disc) allowing the disc to re-adjust with a slow inward drift of accreting material.

For alternative accretion rates, various types of accretion flows have been proposed. For low-accretion-rate sources (sub-Eddington; $\dot{M} \ll \dot{M}_{\rm Edd}$), different types of radiatively-inefficient accretion flows (RIAFs) have been suggested (see Figure 1.2). ADAFs (advection-dominated accretion flows; Narayan & Yi 1995), for example, are hot, geometrically-thick (due to gas pressure), optically-thin flows where a two-temperature plasma forms consisting

of electrons ($T_\mathrm{e} \sim 10^9\,\mathrm{K}$) and an ion torus where the protons are hot ($T_\mathrm{ion} \sim 10^{12}\,\mathrm{K}$). This occurs when the material has low density so that the protons and electrons do not interact enough to have their temperatures equilibrated which allows the electrons to radiate and so cool more rapidly than the protons. ADAFs require a low accretion rate to form from a geometrically-thin cool disc because this allows evaporation into the hot flow to dominate in the inner regions of the disc (Liu et al. 1999; Różańska & Czerny 2000). Other proposed accretion flows for low accretion rates include convection-dominated accretion flows (CDAFs; Narayan, Igumenshchev & Abramowicz 2000) and advection-dominated inflows-outflows (ADIOs; Blandford & Begelman 1999).

In the case of high-accretion-rate sources (super-Eddington; $\dot{M} \gg \dot{M}_\mathrm{Edd}$), radiation may be trapped by inflowing material causing the disc to vertically expand into a toroidal or "Polish doughnut" shape (Paczyński & Wiita 1980). Such geometries are radiatively inefficient and energy is advected inwards quicker than the disc can cool with an emitted spectrum closely resembling a single-temperature blackbody on the order of $10^4\,\mathrm{K}$.

1.1.2.2 The Broad-Line Region (BLR)

The broad- and narrow-line regions which surround the central engine are responsible for the vast majority of optical and UV emission lines as they absorb incident UV and X-ray radiation (Osterbrock 1989; Peterson 1997) and so emit characteristic lines of the gases present. The BLR is situated close to the central engine ($r < 0.1\,\mathrm{pc}$ and gravitationally bound to the SMBH) consisting of hot, dense ($n_\mathrm{e} \sim 10^{9-10}\,\mathrm{cm}^{-3}$), fast-moving clouds covering a wide range in ionisation and travelling at velocities on the order of several thousand $\mathrm{km\,s}^{-1}$. This results in the emission of such lines as Lyα, Hα, Hβ, He I, He II, O VI, Mg II, C IV and many lines from Fe II with broad line widths due to Doppler broadening. The line intensities suggest that the temperature of the gas is on the order of $\sim 10^4\,\mathrm{K}$ (e.g. Netzer 1990). This would imply a thermal velocity of around $10\,\mathrm{km\,s}^{-1}$ and so the observed widths of the lines are instead most likely produced by bulk motion of the clouds although whether the gas is infalling, outflowing or in orbital motion remains unclear (Czerny & Hryniewicz 2011). The BLR has a low mass on the order of $\sim 10\,\mathrm{M}_\odot$, covering about 10–50% of the sky as seen from the

central source (Peterson 1997). Although BLRs are not observed in all AGN, it is believed that they are always present in higher-accretion-rate sources but in some cases are obscured by the molecular torus (see Section 1.1.2.4). BLRs may not, however, be always present in low-accretion-rate sources. This may be explained by the model of Elitzur & Ho (2009) which proposes that the BLR is formed by regions of a clumpy wind arising from the accretion disc. If the mass accretion rate falls too low, the mass outflow rate of the clumpy wind also falls (from considerations of mass conservation) and so the BLR cannot be sustained.

1.1.2.3 The Narrow-Line Region (NLR)

In contrast to the BLR, the NLR-clouds are positioned much further away ($1\,\mathrm{pc} < r \lesssim 1\,\mathrm{kpc}$ from the nucleus) with temperatures of a few $10^4\,\mathrm{K}$ and line widths $< 1\,000\,\mathrm{km\,s^{-1}}$ (Peterson 1997). The low orbital velocities result in narrow permitted lines (e.g. from H I, He I, He II) and the presence of strong forbidden lines (such as [O II], [O III], [C III]) suggests that these clouds are of very low density ($n_\mathrm{e} \sim 10^{3-6}\,\mathrm{cm^{-3}}$) since such transitions have not been collisionally suppressed. The NLR clouds are thought to be photoionised by the continuum emission from the central source (Ferland & Netzer 1983) although it has been hypothesised that this could also occur via shock excitation from high-velocity radio jets (Dopita & Sutherland 1995). The total mass of the NLR is thought to be on the order of $10^6\,\mathrm{M_\odot}$ (Peterson 1997) and the large size of this region ($r \geq 100\,\mathrm{pc}$) with light-crossing times on the order of $\sim$100 yr means that variability of the narrow lines is not expected to be observed. As the NLR is thought to reside outside of the torus, it should never be completely obscured and so is expected to be observed in all AGN. Finally, since the symmetry of the NLR is generally found to lie along the polar axes, its bi-conical structure suggests that the ionising continuum is emitted anisotropically and so is perhaps collimated by an extended obscuring torus (see below; Pogge 1989).

1.1.2.4 The Molecular Torus

The central engine is thought to be obscured by a dusty, molecular torus comprising high-density clouds of gas which, when heated up enough by the central engine, will radiate energy

at the same rate that it receives it. Incoming gas from kpc scales (within the host galaxy) is thought to feed the torus (Shlosman, Begelman & Frank 1990; Wilson & Tsvetanov 1994) with the gas / clouds in the inner regions of the torus losing sufficient angular momentum through frictional collisions to the extent that they form the outer regions of the accretion disc (Krolik & Begelman 1988). The torus may well lie in the same plane as the accretion disc, possibly obscuring the central engine when viewed edge-on (e.g. Antonucci & Miller 1985; Urry & Padovani 1995). The torus cannot, however, exceed a temperature of $\sim$2 000 K (to avoid sublimation; Barvainis 1987). This places a rough estimate of the radius of the inner regions to be a few pc from the central source (Jaffe et al. 2004) but the outer regions may extend out to a radius of a few hundred pc with an equivalent hydrogen column density of up to $\sim 10^{25}\,\mathrm{cm}^{-2}$. The large column densities make the torus optically-thick to photons at optical, UV and soft X-ray wavelengths and so this feature is thought to be responsible for the strong infrared emission observed in most AGN due to the thermalisation / re-radiation of UV and X-ray emission from the central engine. Only hard X-ray photons may realistically penetrate the torus except where $N_{\mathrm{H}} \gtrsim 10^{25}\,\mathrm{cm}^{-2}$ when the torus becomes completely Compton-thick to hard X-rays.

1.1.2.5 Relativistic Jets

At the centres of some AGN, extremely powerful, collimated jets of plasma are observed to emerge, perpendicular to the plane of the disc. They are capable of transferring energy and momentum over large distances of up to several hundred thousand light-years before they interact with the inter-galactic medium (Marscher 2009). Jets are observed to be diverse ranging from sub-relativistic and weak (e.g. in Seyfert galaxies) to highly luminous, collimated jets travelling at relativistic speeds, such as in the case of blazars (Urry & Padovani 1995). They radiate strongly from the radio band (dominated by synchrotron emission) through to high-energy γ-rays (by the synchrotron-self-Compton (SSC) process and/or external inverse-Comptonisation) and are the mechanism by which the core supplies energy to the giant radio lobes observed in some radio-loud AGN. The kinetic power of the jets is often a significant fraction of the bolometric luminosity of the source (Marscher 2009). The radio

properties are, however, sensitive to orientation. If the orientation of the jet is along the line-of-sight then it may be relativistically Doppler beamed and so appear to have increased brightness (e.g. in the case of blazars). When, however, the jet is viewed perpendicularly to the line-of-sight, the giant radio lobes are instead observed (e.g. Fanaroff-Riley galaxies; Fanaroff & Riley 1974). Jets may be launched by magneto-hydrodynamic processes when twisting magnetic fields in the accretion disc collimate the outflow along the rotational axis (e.g. Meier, Koide & Uchida 2001; McKinney 2006) and it is thought that the power of the jets could be related to the spin of the black hole perhaps due to the acceleration of charged particles through electromagnetic interactions via dragging and tightening of magnetic field lines in the innermost regions (Blandford & Znajek 1977). However, the formation and composition of the jets are still largely a matter of debate in the literature.

1.2 Classes of AGN

AGN can be broadly classified into two groups based on radio emission: radio-quiet and radio-loud, with few intermediates. To distinguish between them, a definition of radio-loudness ($R_{\rm L}$) is used (Wilkes & Elvis 1987):

$$R_{\rm L} = \log_{10} \frac{F_{5\,\rm GHz}}{F_{\rm B}}, \tag{1.12}$$

where $F_{5\,\rm GHz}$ is the radio flux at 5 GHz and $F_{\rm B}$ is the B-band ($\sim$4 400 Å) flux. Typically, a value of $R_{\rm L} \leq 1$ signifies a radio-quiet object and, conversely, a value of $R_{\rm L} \geq 1$ signifies a radio-loud object. The radio emission can differ by a factor of $\sim$1 000 between radio-loud and radio-quiet objects. Both radio-quiet and radio-loud AGN are divided into further sub-classes, some of which are summarised below.

1.2.1 Radio-Quiet AGN

Radio-quiet AGN form the majority of active galaxies, outnumbering radio-loud AGN by a factor of 20 or more. The main sub-classes of radio-quiet AGN are described below.

1.2.1.1 Seyfert Galaxies

Seyfert galaxies are lower-luminosity AGN with bright, point-like nuclei but with clearly detectable host galaxies. They are identified spectroscopically by the presence of strong, highly-ionised emission lines and morphologically tend to occur in spiral galaxies. The observed emission lines include common transitions such as the Balmer series of lines from hydrogen (e.g. Hα, Hβ) along with narrow lines such as those from [O III]; the formation of which requires very hot gas. Seyfert galaxies can be split into two main subgroups: types 1 and 2, which differ in terms of their emission. Type-1 Seyfert galaxies show two sets of emission lines: 'narrow' forbidden lines with widths corresponding to velocities of several hundred $\mathrm{km\,s^{-1}}$ (but still broader than typical non-AGN emission lines), characteristic of ionised gas with a low density ($n_\mathrm{e} \approx 10^{3-6}\,\mathrm{cm^{-3}}$) and much broader lines (e.g. H I, He I, He II, Fe II) with widths corresponding to velocities up to $\sim 10^4\,\mathrm{km\,s^{-1}}$. The observed 'broad' lines only occur from permitted transitions and so the absence of broad forbidden lines suggests that non-electric-dipole transitions are collisionally suppressed. This means that the gas responsible must have a high density ($n_\mathrm{e} \gtrsim 10^9\,\mathrm{cm^{-3}}$). Type-2 Seyfert galaxies, however, differ in the sense that the 'broad' lines are not observed and so only the 'narrow' lines are present, as shown in Figure 1.3. The continuum level is also much weaker in type-2 Seyfert galaxies primarily due to absorption at X-ray wavelengths (or dust extinction in the optical band) to the extent that it is often difficult to distinguish it from the stellar continuum of the host galaxy. Seyfert galaxies may also be further sub-divided using the notation of Osterbrock (1981) into the categories of Seyfert 1.5, 1.8 and 1.9. These are defined by the relative strength of the broad lines with respect to the narrow lines in the optical spectra (i.e. a Seyfert 1.9 will have weaker broad components relative to the narrow components than a Seyfert 1.5 or 1.8). However, as a note of caution, this sub-classification scheme is sensitive to the variability of the source and it is possible for a type-1 Seyfert galaxy to be mis-classified as a type-2 Seyfert galaxy in the event that the source is observed during a period of lower flux (e.g. Penston & Perez 1984).

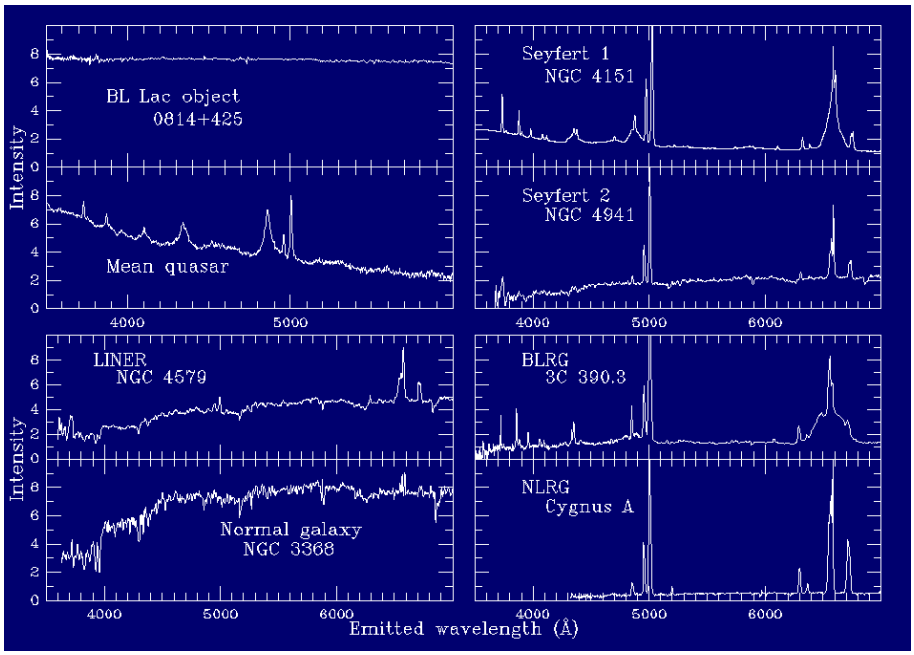

Figure 1.3: Optical spectra of AGN of various classifications highlighting the differences in the emission characteristics. Figure taken from http://www.astr.ua.edu/keel/agn/spectra.html.

1.2.1.2 Narrow-Line Seyfert Galaxies

One other notable sub-class of Seyfert galaxies was identified by Osterbrock & Pogge (1985): these are the "narrow-line type-1 Seyfert galaxies" (NLS1s). These have all the properties of type-1 Seyfert galaxies but, while their Hα lines remain broad, their Hβ lines are narrow and they display strong optical Fe II lines. A Seyfert galaxy is quantitatively defined as a NLS1 if the full-width at half-maximum (FWHM) of the Hβ line is $< 2\,000\,\mathrm{km\,s^{-1}}$ (Osterbrock & Pogge 1987) and if the [O III] / Hβ emission ratio is <3 (Goodrich 1989). However, it should be stressed that there is a continuous distribution of optical line widths in type-1 Seyferts. NLS1s are generally radio-quiet and have strong soft X-ray excesses (e.g. Laor et al. 1994). They are also found to have lower black-hole masses than other Seyferts, on the order of $\sim 10^6\,\mathrm{M_\odot}$, but with comparable bolometric luminosities. This suggests that NLS1s are accreting at a higher rate. They are also observed to exhibit rapid, high-amplitude X-ray

variability (e.g. Vaughan et al. 1999; Vaughan et al. 2011), such as in the case of NGC 4051 where the soft X-ray emission can be found to vary by a factor of 2–3 on a timescale of a few hundred seconds (Singh 1999), along with large-amplitude variability on much longer timescales (e.g. Guainazzi et al. 1998; McHardy et al. 2004).

1.2.1.3 Other Radio-Quiet AGN

Quasars, or quasi-stellar objects (QSOs) form the most luminous sub-class of AGN and are the more distant (with redshifts as high as $z \sim 7$; Mortlock et al. 2011), highly-luminous cousins of Seyfert galaxies. Their spectra are very similar to those of Seyfert galaxies but differ in the fact that stellar absorption features are much weaker and the narrow lines are relatively weaker when compared to the broad lines than in the case of Seyfert galaxies. They can be highly variable and can have bolometric luminosities as high as $\sim 10^{46-47}\,\mathrm{erg\,s^{-1}}$. Although the majority of QSOs are radio-quiet objects it should also be noted that around 5–10% are in fact strong radio sources powered by relativistic jets (radio-loud quasars) travelling perpendicular to the plane of the disc. Interestingly, QSOs are found to have been far more common in the early universe and show where the most massive black holes were growing rapidly via accretion. It should be noted that Seyfert galaxies and quasars form a continuous sequence in luminosity and that the most highly-luminous Seyfert galaxies are impossible to distinguish from quasars.

Another class of radio-quiet AGN are low-ionisation nuclear-emission-line region galaxies (LINERs), which were identified by Heckman (1980). They are low-luminosity objects which spectroscopically resemble type-2 Seyfert galaxies except that the low-ionisation emission lines (e.g. O I, N II) are relatively stronger. They are distinguished from normal AGN on the basis of their [O III] / Hβ, [N II] / Hα and [Si II] / Hα flux ratios. Many LINERs appear to be low-luminosity Seyfert galaxies (perhaps with ADAFs) although similar spectra could also be produced via cooling flows, starburst-driven winds and in shock-heated gas (Heckman, Armus & Miley 1987; Filippenko et al. 1992).

1.2.2 Radio-Loud AGN

Approximately 2% of all AGN are radio-loud (see equation 1.12) and are typically surrounded by two giant, extended radio lobes situated somewhat symmetrically on either side of the galactic centre and up to distances on the order of Mpc away. Such lobes are probably fed by relativistic jets, the likes of which are absent in radio-quiet AGN. These are termed radio galaxies and are generally associated with giant elliptical galaxies. The extended radio structures can be divided based on their luminosity according to the criteria of Fanaroff & Riley (1974). The weaker radio sources which are brighter in the centre are known as FR-I galaxies whereas FR-II sources are limb-brightened, often displaying enhanced emission at the edge of the radio structures. Furthermore, the optical spectra of radio galaxies differ in the same sort of way as radio-quiet AGN in the sense that there exists "broad-line radio galaxies" (BLRGs) and "narrow-line radio galaxies" (NLRGs) which can perhaps be thought of as analogous to type-1 and type-2 Seyfert galaxies, respectively. Radio-loud quasars do also exist which behave much in the same way as radio-quiet quasars with strong X-ray emission plus broad and narrow emission lines but with the additional emission from a jet.

Although all AGN show continuum variability throughout the electromagnetic spectrum, a small subset of AGN show much larger variability on short timescales at optical wavelengths although they typically display weak optical emission lines. They also tend to be highly optically polarised (up to a few per cent), a feature which is also variable both in magnitude and angle. These are known as "optically-violent variables" (OVVs; e.g. 3C 279, Sahayanathan & Godambe 2012; 3C 273, Dai et al. 2009). Similar sources known as "BL Lacertae objects" (BL Lacs) also exist which share the same variability properties as OVVs but differ due to the absence of emission and absorption features (neither broad nor narrow) in their spectra. OVVs and BL Lacs are often collectively referred to as "blazars" and are all strong radio sources which are thought to have a strong, beamed component, such as a jet, close to the line-of-sight. There is no direct radio-quiet equivalent of blazars, however, since there is no strong jet in the radio-quiet case. A comparison of various optical spectra is shown in Figure 1.3.

It still remains unclear as to why such a radio-loud / radio-quiet dichotomy exists

although it seems that it may be a consequence of a fundamental property of the source. Indeed, the solution may lie with the angular momentum of the black hole where the rapidly rotating regions around Kerr black holes could form a jet through magnetic induction (e.g. Meier, Koide & Uchida 2001). Since the radio-loudness distribution is bi-modal, it could be related to the formation of the active nucleus with rapidly-rotating black holes perhaps arising from mergers during a collision between two host galaxies. This is supported by the fact that radio-loud AGN only occur in elliptical galaxies whereas radio-quiet AGN are also prominent in spirals (e.g. Antonucci 1993; Urry & Padovani 1995).

1.2.3 Unification Scheme

The standard model of an AGN consists of an accreting supermassive black hole surrounded by broad- and narrow-line regions and a molecular torus of gas and dust. A unification scheme exists in which it states that all AGN are essentially the same type of object yet the classification of the source depends upon the conditions under which it is observed. The favoured unified model works on the basis of orientation (Antonucci 1993; Singh, Shastri & Risaliti 2011). This is illustrated in Figure 1.4. For example, in terms of radio-quiet AGN, the model states that type-1 and type-2 Seyfert galaxies differ only according to the angle at which they are viewed. In the case of a type-1 Seyfert, the AGN is viewed at an acute angle to the pole of where the jet would be and consequently the X-ray and UV emission from the central engine can be directly observed along with the emission from the BLR. Conversely, with a type-2 Seyfert, the observer has no direct view of the active nucleus. This is because the AGN is viewed through the plane of an obscuring structure (most likely the torus) at angles up to 90° to the polar axis and so the X-ray emission and broad optical emission lines will be blocked from view resulting in the spectrum of a type-2 AGN. This is supported by observational evidence such as the permitted BLR lines being directly seen in the spectra of type-1 AGN whereas they can only be observed in scattered, polarised light in the spectra of type-2 AGN (Antonucci & Miller 1985). The large X-ray column densities seen obscuring the central source in type-2 AGN (Risaliti, Maiolino & Salvati 1999) are also less apparent in observations of type-1 AGN, consistent with the role of the torus obscuring the line-of-sight.

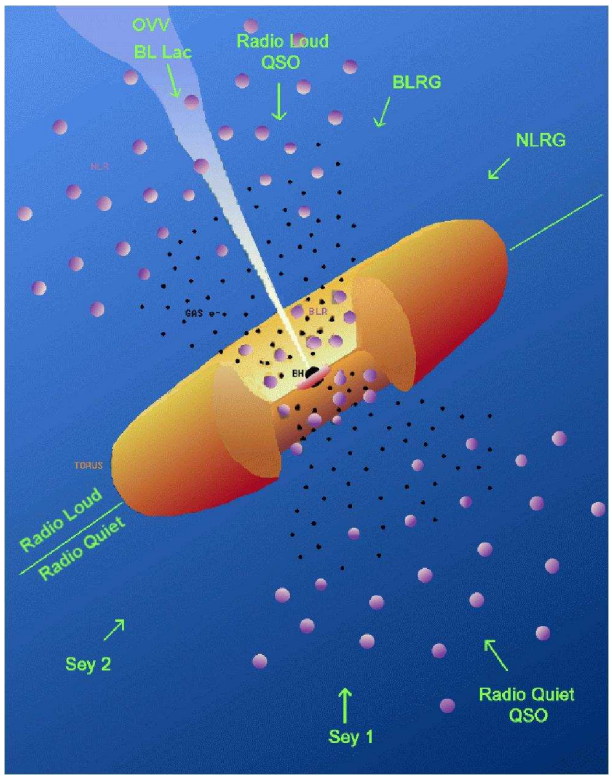

Figure 1.4: Schematic interpretation of the orientation-based unification scheme for AGN. See Section 1.2.3 for details. Figure taken from Urry & Padovani (1995).

Furthermore, since number density studies of type-1 and type-2 Seyfert galaxies suggest that type-2 Seyfert galaxies are more common (Schmitt et al. 2001), this could suggest that the torus is a large structure where the viewing angle to the central engine is small - perhaps around $\sim 30°$. Naturally, however, most AGN will be observed somewhere between the two extremes. At higher luminosities, radio-quiet quasars become analogous to type-1 Seyferts with type-2 quasars assumed to be the analogy of type-2 Seyferts (Reyes et al. 2008).

Attempts have also been made to unify radio-loud galaxies where relativistic jets are prominent (see Urry & Padovani 1995). In this scenario, when the AGN is viewed at acute angles to the jet (or even directly down the jet), a highly-variable blazar is observed. Conversely, when viewing at an angle perpendicular to the jet (through the torus), the obscuration

of the central engine leads to the observation of an NLRG where the extended radio lobes are viewed on the plane of the sky. In between these two extremes (i.e. within the opening angle of the torus but not directly down the jet), a core-dominated radio-loud quasar will be observed at angles closer to the jet (with significant Doppler boosting but lacking the strong variability of a blazar) and lobe-dominated quasars and BLRGs will be observed at angles further away from the jet (again, see Figure 1.4).

Ultimately, it seems that the properties of many varied AGN can be simply described according to their luminosity, radio-loudness (i.e. the presence of a jet) and orientation with a good degree of success.

1.3 Spectral Energy Distribution (SED)

AGN show a broad range of emission over most of the electromagnetic spectrum. Contrary to normal galaxies where the observed SED is the sum of the thermal emission from stars, the broad-band flux density (from radio to γ-rays) in AGN can be approximated as a power law (i.e. $F_\nu \propto \nu^{-\alpha}$, with energy / spectral index, $\alpha \sim 1$)[3]. Figure 1.5 shows a schematic representation of typical AGN SEDs. The somewhat flat νF_ν spectrum implies that roughly the same amount of energy is emitted per frequency decade suggesting that the emission is largely non-thermal. However, the wide range of emission suggests that several physical components are responsible resulting from both primary and secondary (reprocessed) radiation.

1.3.1 Multi-Wavelength Emission

The fundamental processes at work to produce the observed continuum emission at different wavelengths are summarised below:

- *Radio*: The majority of radio emission (typically at frequencies $< 10^{12}$ Hz) in AGN is dominated by synchrotron radiation which is a non-thermal process. Synchrotron

[3]An equivalent parameterisation of AGN spectra is given by $N(E) \propto E^{-\Gamma}$ and has units photons $\mathrm{cm}^{-2}\,\mathrm{s}^{-1}\,\mathrm{keV}^{-1}$, where E is the energy and Γ is the photon index. The photon index is related to the spectral index by $\Gamma = \alpha + 1$.

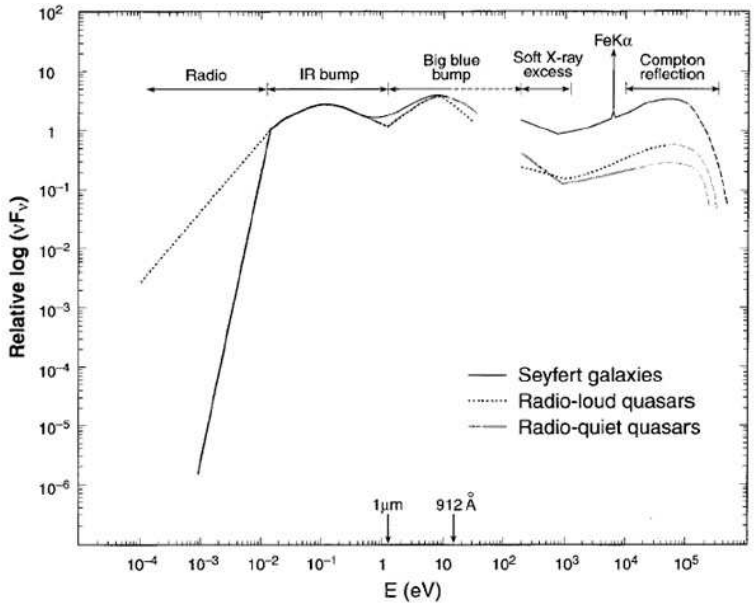

Figure 1.5: A schematic representation of the typical observed SEDs of Seyfert galaxies and radio-quiet and radio-loud quasars. Note the difference in radio flux between the radio-quiet and radio-loud cases. Figure taken from http://ned.ipac.caltech.edu/level5/Sept04/Koratkar/.

emission occurs when relativistic electrons are accelerated in a magnetic field which then lose energy, spiral inwards and thus radiate.[4] The overall emission usually has a flat power-law shape (i.e. $\alpha < 0.5$) but with a cut-off at low frequencies due to synchrotron self-absorption (with the most absorbed sources being the most compact). In the case of radio-loud AGN, the radio emission typically consists of two components: a flat component arising from the inner regions of the jet and a steeper component (i.e. $\alpha \geq 0.5$) originating from the extended radio lobes. Steep-spectrum sources are then those which are lobe-dominated and emit synchrotron radiation isotropically whereas flat-spectrum sources are those in which the jet is close to the line-of-sight (e.g. 3C 273; Pearson et al. 1981). In some cases, such as

[4]For synchrotron radiation, a power-law form often holds where the electrons are distributed as $N(E) \propto E^{-s}$. The frequency-dependent photon flux is then given by $I_\nu \propto \nu^\alpha$, where $\alpha = (1-s)/2$.

blazars, a geometric effect of relativistic bulk motion of material in the jet close to the line-of-sight results in the observation of superluminal motion (Blandford, McKee & Rees 1977). Note that since no powerful jets are produced in radio-quiet AGN, however, the radio emission can be weaker by a factor of $\sim$1 000. The point in the spectrum of radio-quiet AGN below which the SED decreases rapidly is known as the "submillimetre break".

- *Infrared*: The infrared continuum (from 1 mm to 750 nm) in AGN typically may consist of two components. The first arises from an extension of the synchrotron emission observed in the radio band and is apparent in radio-loud AGN such as blazars. The second component has a thermal origin and is important in both radio-loud and radio-quiet AGN. It manifests itself in a feature known as the "infrared bump" which is found at wavelengths $> 1\,\mu$m and is thought to result from reprocessing of the central continuum by warm dust (e.g. Barvainis 1990) at temperatures below the sublimation temperature (i.e. $T \lesssim 2\,000$ K). Interestingly, variability studies show that the infrared emission lags behind the optical / UV emission, which is thought to originate close to the central engine, by several months or longer (e.g. Sitko et al. 1993). Light-crossing arguments then typically place the infrared source on pc-scales from the central engine; i.e. outside of the dust sublimation radius. Therefore, it is likely that the origin of the infrared component arises from the re-radiation of the optical / UV continuum by the distant molecular torus.

- *Optical / UV*: The optical portion of the electromagnetic spectrum is from 390–750 nm with UV radiation occurring in the wavelength range 10–400 nm (or from 3–124 eV in energy). A large proportion of the bolometric luminosity of AGN is often emitted in the optical and UV wavelength bands. The dominant feature in the spectrum arises from thermal emission from material with temperatures in the region of 10^{4-6} K. This is known as the "big blue bump" (BBB) and peaks in the UV band but can extend into the X-ray regime (up to energies of 1–2 keV). It is likely that the BBB arises from the accretion disc with the thermal radiation in the optical band arising from more distant disc radii than the UV (i.e. as $T(r) \propto r^{-3/4}$;

see equation 1.11). Variability studies also show that the optical and UV continua vary in phase with the variations increasing in amplitude from the optical to the UV. However, the picture is far from clear since the temperature of a typical AGN accretion disc should be too low to extend into the X-ray bandpass and it is difficult to produce physical models consistent with the broad wavelength range of the BBB. The problem is compounded by the fact that the majority of the BBB emission in the extreme ultraviolet (EUV; 10–124 eV) part of the spectrum is unobservable due to absorption by neutral hydrogen in the Milky Way.

- *γ-rays*: γ-rays generally have energies $\gtrsim 500$ keV which can typically extend up to MeV and GeV energies in astrophysical sources. Numerous AGN have been detected at high energies (e.g. with the Large Area Telescope (LAT) on-board *Fermi*; Abdo et al. 2010b), many of which are blazars, suggesting that the γ-ray emission is mainly Doppler-boosted in a relativistic jet close to the line-of-sight (Abdo et al. 2010a). γ-ray emission has also been observed from quasars where the emission is found to be highly variable but very high energy with some quasars detected at energies on the order of TeV (e.g. Mrk 501, Aharonian et al. 1997; PMN J0948+0022, Abdo et al. 2009a; Foschini et al. 2011). Recent detections have also been made with the *Fermi* LAT (Abdo et al. 2009b) including the first NLS1s (see Foschini 2011). The high-energy component is much weaker in Seyfert galaxies, typically rolling over at $\sim$100-200 keV (e.g. Malizia et al. 2003; Dadina 2008 from *BeppoSAX* observations) and is perhaps a smooth continuation of the X-ray continuum (i.e. produced by inverse-Compton scattering of optical / UV disc photons).

This thesis focuses primarily on the X-ray emission from Seyfert galaxies. The fundamental observed components in typical X-ray spectra are discussed below.

1.3.2 X-Ray Emission

X-rays are high-frequency photons with energies roughly ranging from 1 keV to upwards of 100 keV (lower- and higher-energy X-ray photons are often termed ‘soft’ and ‘hard’ respec-

tively). As AGN are highly energetic sources (especially within the inner regions of the accretion disc), X-rays provide an excellent probe into the very centre of the active nucleus. This is because they are thought to originate close to the black hole (within a few $r_{\rm g}$), as evidenced by variability calculations which show that the central source is very compact (certainly $<$1 pc) and the fact that these objects are unresolvable by even the most powerful optical and radio telescopes. Indeed, AGN are observed to be copious X-ray emitters with the X-ray radiation contributing roughly 10% of the bolometric luminosity.

Since the inner accretion disc itself strongly emits optically-thick thermal radiation peaking in the UV / EUV (i.e. with temperatures typically of $kT \sim$ 10–20 eV), the X-rays themselves are thought to be produced via multiple inverse-Compton scattering of soft disc photons by relativistic thermal electrons in a hot, optically-thin corona ($kT \sim$ few hundred keV), enveloping the accretion disc (Haardt & Maraschi 1991; Haardt & Maraschi 1993). This thermal Comptonisation can naturally give rise to an X-ray power-law spectrum although it should be noted that in radio-loud AGN the role of the jet could be important in X-ray production if it is beamed close to the line-of-sight via synchrotron or inverse-Compton mechanisms. Very little X-ray emission below 10 keV is observed in type-2 Seyfert galaxies due to the large line-of-sight column densities ($N_{\rm H} \sim 10^{23-25}\,{\rm cm}^{-2}$; Risaliti, Maiolino & Salvati 1999), most likely due to the obscuring torus. However, in the case of type-1 Seyferts (which are primarily the focus of this work), the observed X-ray power law may be significantly modified by secondary reprocessing effects (see Figure 1.6).

1.3.2.1 Compton Reflection and Iron Fluorescence

Since the primary X-ray continuum is produced via inverse-Compton scattering of disc photons in a corona of hot electrons (i.e. thermal Comptonisation), this X-ray emission may then itself irradiate the cold accretion disc resulting in what is termed as a "Compton-reflection component" via Compton down-scattering in the X-ray spectrum. In the simplest case, the disc is modelled as a plane-parallel semi-infinite slab of relatively cold gas (Lightman & White 1988; George & Fabian 1991). The disc can also be modelled as a photo-ionised slab (Ross, Fabian & Young 1999) or an accretion disc in hydrostatic equilibrium (Nayakshin, Kazanas

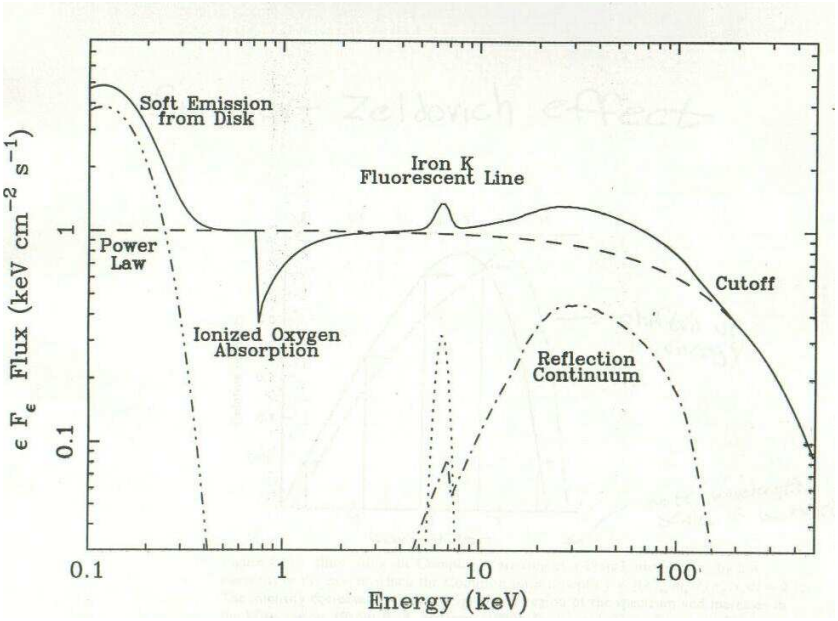

Figure 1.6: A typical average X-ray spectrum of a type-1 Seyfert galaxy showing the primary continuum emission modified by secondary reprocessing effects such as Compton reflection and warm absorption. See the text for details. Figure taken from http://www2.astro.psu.edu/ niel/.

& Kallman 2000).

When illuminated by a hard X-ray power-law continuum, each photon can undergo one of numerous various interactions. Most importantly, the photon may be Compton-(down-)scattered out of the slab by free electrons or photoelectrically absorbed by an atom (see below). Harder photons (tens of keV) are rarely absorbed and so tend to Compton-back-scatter out of the slab at lower energies. Softer photons, however, are absorbed far more readily due to the enhanced photoelectric cross-section at lower energies and this can give rise to a broad hump-like shape superimposed on the primary power-law continuum at energies $> 10\,\mathrm{keV}$, peaking at $\sim$30 keV. At higher energies this Compton-reflection component rolls over both due to the exponential cut-off in the illuminating spectrum and the decrease in the Compton cross-section. The strength of the Compton-reflection component is measured by the reflection ratio, R, which is the equal to the solid angle (Ω) subtended by an optically-thick

medium (e.g. the accretion disc) from the primary X-ray source divided by 2π sr (Magdziarz & Zdziarski 1995). In the case of a standard geometrically-thin accretion disc for a given inclination angle, the expected solid angle subtended from the source would approximate to 2π sr and so R would be $\sim$1.

The softer photons which have been absorbed may then result in the ejection of an Auger electron or Kα line emission from the most abundant metals. Fluorescent Kα emission occurs when a K-shell ($n = 1$) electron is ejected from the ion following the absorption of an X-ray photon. An L-shell electron ($n = 2$) may then drop into the K-shell, emitting a photon of some signature energy depending on the element and the ionisation state. The Kα line is actually a doublet consisting of two separate components (for Fe: Kα_1 = 6.404 keV; Kα_2 = 6.391 keV, with a branching ratio of 2:1) however these are unresolvable with current instruments. Due to the high abundance and high fluorescence yield (Bambynek et al. 1972), the Kα line due to near-neutral iron (Fe I-XVII) at $\sim$6.4 keV is by far the strongest transition in the X-ray spectrum. This line is intrinsically narrow and so the observed profile is shaped by Doppler broadening and relativistic effects (e.g. gravitational redshift and Doppler boosting). This may result in Fe Kα lines which are broadened to a FWHM of at least a few thousand km s^{-1} and so are termed "broad iron lines" (Fabian et al. 2000) or "double-horned disc lines" (Laor 1991). For cosmic abundances, the optical depth of the disc surface for bound-free Fe absorption is close to the Thomson depth[5]. Therefore, when a surface is irradiated by X-rays, the Fe-line emission takes place at depths similar to the Thomson depth (<1% of a typical accretion-disc thickness). Consequently, iron line fluorescence is an ideal probe of the accretion-disc surface as it is a function of the elemental abundances of the reflecting material, the geometry of the accretion disc itself and the ionisation state of the surface layers.

1.3.2.2 Soft X-Ray Excess

A common feature in the X-ray spectra of AGN is an excess of emission at energies $\lesssim$ 2 keV when a power-law model is extrapolated downwards from higher energies (Turner & Pounds

[5]The Thomson depth is defined as $\tau_{\rm T} = N_{\rm H}\sigma_{\rm T}$, where $N_{\rm H}$ is the column density in units cm^2 and $\sigma_{\rm T}$ is the Thomson cross-section, where $\sigma_{\rm T} = 6.65 \times 10^{-25}$ cm^{-2}.

1989). Such a "soft excess" is particularly common in NLS1s (Boller, Brandt & Fink 1996). This has often been interpreted in terms of the hard / Wien tail of the BBB which is thought to peak in the EUV. However, the measured temperatures are typically too hot (i.e. $kT \sim 0.1$–$0.2\,\mathrm{keV}$) for this feature to have an accretion-disc origin and are largely constant irrespective of black hole mass (Czerny et al. 2003; Gierliński & Done 2004). The presence of atomic features in the soft X-ray band (as revealed by grating observations) has suggested that strong atomic features such as O VII and O VIII lines and the Fe M-shell unresolved transition array (UTA)[6] could significantly affect the shape of the soft excess (Gierliński & Done 2004). However, one particular problem with this interpretation is that soft excesses are often smooth and many predicted features seem to be absent.

Other interpretations that have been put forward include thermal emission from hot, diffuse plasmas (Smith et al. 2001; Starling et al. 2005), absorption in high-velocity ionised gas (Schurch & Done 2006), photoionisation of circumnuclear gas by the primary emission from the AGN (Guainazzi & Bianchi 2007) and circumnuclear gas heated by shocks induced by high-velocity outflows (Pounds, Page & Reeves 2007). Furthermore, relativistically blurred, ionised reflection models have also been invoked to explain the smooth nature of the soft excess (e.g. Crummy et al. 2006) although absorption-based models fit the data equally well without the requirement for any relativistic blurring (e.g. Mrk 766, Turner et al. 2007; MCG–6-30-15, Miller, Turner & Reeves 2008). Interestingly, Middleton, Done & Gierliński (2007) find that absorption-based models for the soft excess provide a better description of the data than reflection models in the case of stellar-mass black holes. Finally, recent models by Done et al. (2012) suggest that a colour-temperature-corrected thermal disc spectrum modified by inverse-Compton scattering (which takes place in the disc itself) may actually be observable in the soft X-ray band in low-black-hole-mass, high-accretion-rate sources. Here, the colour-temperature-correction arises from the fact that each radius of the disc only emits as a true blackbody if the disc is optically-thick to absorption at all energies. However, as free-free absorption drops as a function of energy, higher-energy photons from each successive radius are unlikely to thermalise. This forms a modified blackbody whose effective temperature is

[6]The UTA is a blend of various unresolved inner-shell (mainly $2p$–$3d$) absorption lines from Fe M-shell ions.

higher than it would be for complete thermalisation. Such a model could maybe then explain some of the strong components of soft excess observed in the spectra of NLS1s with low $M_{\rm BH}$ and high $\dot{M}/\dot{M}_{\rm Edd}$.

1.3.2.3 Warm Absorbers and Outflows

Recent systematic X-ray studies of AGN with *ASCA* (*Advanced Satellite for Cosmology and Astrophysics*), *Chandra*, *XMM-Newton* (*X-ray Multi-Mirror Mission - Newton*) and *Suzaku* have established that at least half of all active galaxies host photo-ionised "warm" absorbers (e.g. Reynolds & Fabian 1995; Blustin et al. 2005; McKernan, Yaqoob & Reynolds 2007) and that they may in fact be ubiquitous in AGN, becoming observable only in certain lines-of-sight (Krongold et al. ; although one other interpretation is that ∼50% of AGN do not have warm absorbers). When observed at high spectral resolution (such as with the transmission gratings on-board *Chandra* or the reflection gratings on-board *XMM-Newton*), these absorbers are known to produce numerous narrow absorption features ranging from various elements such as O, Si, Ne, C, N, S, Mg and Fe (e.g. Kaspi et al. 2002; Crenshaw, Kraemer & George 2003; McKernan, Yaqoob & Reynolds 2007). The associated lines are often blueshifted, thus implying outflowing winds (ranging in velocity from several hundred to several thousand $\mathrm{km\,s^{-1}}$; Blustin et al. 2005) and arise from a wide range of column densities, $N_{\rm H}$ (units $\mathrm{cm^{-2}}$) and levels of ionisation. The absorbing gas is typically characterised by its ionisation parameter, ξ, which is defined as:

$$\xi = \frac{L_{\rm ion}}{nR^2}, \tag{1.13}$$

and has units $\mathrm{erg\,cm\,s^{-1}}$ where $L_{\rm ion}$ is the ionising luminosity from 1 to 1 000 Rydberg, n is the gas density in $\mathrm{cm^{-3}}$ and R is the radius of the absorbing / emitting material from the central source of X-rays.

Through the study of blueshifted absorption lines of K-shell Fe, recent observations of higher-luminosity AGN have also suggested the presence of highly-ionised ("hot") absorbers originating in high-velocity disc winds ($v_{\rm out} \sim 0.1c$) with around a dozen cases to date (e.g. PG 1211+143, Pounds et al. 2003a; PDS 456, Reeves, O'Brien & Ward 2003) although there

are a set of lower-luminosity sources that still exhibit deep absorption lines at Fe K but require high column densities and have outflow velocities on the order of a few thousand $\mathrm{km\,s^{-1}}$ (e.g. Mrk 766, Miller et al. 2007; NGC 3516, Turner et al. 2005; NGC 1365, Risaliti et al. 2005; NGC 3783, Reeves et al. 2004). Recently, Tombesi et al. (2010) found evidence for blueshifted Fe absorption features in 17 objects within their sample of 42 radio-quiet AGN observed with *XMM-Newton*, detecting 22 absorption lines at rest-frame energies >7.1 keV. This implies that high-velocity outflows may be a common feature in radio-quiet AGN. Such ultra-fast outflows indicate that the gas must be located very close to the nucleus of the AGN and so deep studies of these objects are vital in order to establish a greater understanding of the outflow kinematics and locations relative to the central continuum source which in turn can help to ultimately unravel the inner structure of AGN.

One possible interpretation regarding accretion-disc outflows is that they are perhaps produced as a result of radiation pressure a few r_{g} from the event horizon (Proga, Stone & Kallman 2000). The high luminosities of these systems are the result of radiatively efficient accretion onto a supermassive black hole and such outflows could be a consequence of near-Eddington accretion (King & Pounds 2003), driven by Thomson scattering or bound-bound / bound-free opacity in the higher- and lower-ionised cases respectively. An alternative interpretation of many outflows is that they could be magnetohydrodynamically- (MHD) driven as has been suggested for such objects as GRO J1655-40 (Miller et al. 2008) and NGC 4151 (Kraemer et al. 2005; Crenshaw & Kraemer 2007). The derived outflow rates can in some cases be comparable to the mass accretion rate (several solar masses per year) of the AGN and so in terms of kinetic power, the outflow can be a significant proportion of the bolometric luminosity. As a result, outflows are considered to be an important phenomenon in AGN and are believed to play a key role in feedback processes between the black hole and the host galaxy (King 2003; King 2010), ultimately leading to the observed M–σ relation for galaxies (Ferrarese & Merritt 2000; Gebhardt et al. 2000).

1.3.2.4 Atomic Processes

The primary physical / atomic processes thought to be responsible for the different components of X-ray emission observed in Seyfert galaxies are briefly summarised below:

- *Blackbody radiation*: The concept of a blackbody is described by an object which perfectly emits / absorbs radiation and is in thermal equilibrium with its surroundings. The spectral form is described by the Planck function:

$$I_\nu(T) = \frac{2h\nu^3}{c^2(e^{h\nu/kT} - 1)}, \tag{1.14}$$

  where $I_\nu(T)$ is the intensity of the emitted radiation per unit frequency interval at a frequency ν, h is Planck's constant, c is the speed of light in a vacuum, k is the Boltzmann constant and T is the temperature of the body in units K. Despite being a theoretical concept, blackbody radiation can be approximately applied to astrophysical scenarios where thermal radiation is emitted from an optically-thick body (e.g. AGN accretion discs).

- *Compton scattering*: Compton scattering is a high-energy phenomenon in which inelastic scattering of X-ray and γ-ray photons in matter results in a decrease in energy (with Thomson scattering being the elastic equivalent). Part of the energy is transferred to the scattering electron which recoils while the remaining energy is contained in the form of a photon which is re-emitted in a different direction to the one it originally had. The shift in energy (or wavelength) arises as a result of a single photon imparting momentum to a single electron; a quantity which is conserved in the process. Compton scattering is described by the relation:

$$\lambda' - \lambda = \Delta\lambda = \frac{h}{m_\mathrm{e}c}(1 - \cos\theta), \tag{1.15}$$

  where λ is the wavelength of the initial photon, λ' is the wavelength after scattering, h is Planck's constant, m_e is the rest mass of an electron, c is the speed of light in a vacuum and θ is the scattering angle.

Inverse-Compton scattering (or Comptonisation) can also occur and this is a very important phenomenon in high-energy astrophysics. In this case, lower-energy photons may be scattered to higher energies by hot, relativistic electrons. In the limit of $E \ll m_{\rm e}c^2$ (where E is the energy of the incoming photon and $m_{\rm e}$ is the mass of an electron), the Thomson cross-section, $\sigma_{\rm T}$, may be applied. However, at higher energies (i.e. X-rays and γ-rays), quantum electrodynamics yields a cross-section determined by Klein-Nishina effects. For energies $E \gg m_{\rm e}c^2$, the cross-section is approximately:

$$\sigma_{\rm KN} \simeq \frac{3}{8\epsilon}\sigma_{\rm T}\left(\ln 2\epsilon + \frac{1}{2}\right), \tag{1.16}$$

where $\epsilon = E/m_{\rm e}c^2$ (e.g. Beckmann & Shrader 2012). This has the effect of reducing the Compton-scattering cross-section at higher energies; an effect which becomes important above a few keV.

Inverse-Compton scattering is thought to be responsible for the production of the X-ray power-law component observed around accreting black holes as thermal optical / UV photons from the accretion disc are Compton-upscattered to higher energies by relativistic electrons in the surrounding corona (Rybicki & Lightman 1979; Pozdnyakov, Sobol & Syunyaev 1983).

- *Photoelectric absorption*: Photoelectric absorption occurs when a photon of a particular energy is absorbed by an electron in an atom. The transition that occurs is either bound-free (i.e. the electron absorbs a photon of greater energy than its binding energy and escapes, thus the atom becomes ionised) or bound-bound (i.e. the electron becomes excited but remains bound to the atom). The probability of a photon interacting with an atom is represented by the photoelectric cross-section, $\sigma(E)$, which is a function of energy (Morrison & McCammon 1983; Verner et al. 1996). The cross-section is greatest at the energy where the electron just escapes from the atom and this increased opacity has the effect of producing an absorption edge in the spectrum. The cross-section is also dependent upon the ionisation state

of the material; more highly-ionised material will usually increase the energy of the absorption edge which makes the absorber appear more transparent since the absorption cross-section has been effectively reduced. The effect that absorption has on the spectrum is related by:

$$F_0(E) = F_\mathrm{I}(E) \cdot e^{-N_\mathrm{H}\sigma(E)}, \tag{1.17}$$

where $F_0(E)$ is the reprocessed spectrum, $F_\mathrm{I}(E)$ is the input spectrum and N_H is the hydrogen column density of the absorber. Bound-free and bound-bound transitions from atoms such as O, Ne, Si and Fe contribute primarily towards absorption in the X-ray spectra of AGN where warm-absorber features are often observed in the soft X-ray band as absorbing material is photoionised by the central continuum (see Section 1.3.2.3).

- *Atomic line emission*: When photons incident on absorbing material excite bound electrons to higher energy levels, fluorescent line emission may be observed which occurs when electrons de-excite via the emission of a photon. In the X-ray spectra of AGN, the strongest atomic emission feature is the ubiquitous Fe Kα fluorescence line at $\sim$6.4 keV (Nandra & Pounds 1994) although other features are often prominent in the 6–8 keV energy band such as transitions from Fe Kβ, Ni Kα, Fe XXV (forbidden and resonance) and Fe XXVI. At lower energies, emission lines from O K-shell and Fe L-shell transitions are also often detected. The observed line energy depends upon the ionisation state of the material, and the relative strengths of the observed transitions to the level of the continuum emission is an important diagnostic which allows properties such as the density and temperature of the gas to be inferred.

1.4 Motivation: X-Ray Spectral Variability in Seyfert Galaxies

One particular problem in the field of AGN is that of the origin of the observed X-ray spectral variability. Through studies with *Suzaku*, *XMM-Newton* and *Chandra*, numerous

type-1 AGN are observed to exhibit significant broad-band variability on both short ($\lesssim$ ks) and long (tens of ks to days / months) timescales, although the exact nature of the variability remains relatively unknown. One commonly observed trend is for a systematic hardening of the observed mean X-ray spectrum as the source flux drops, as shown in Figure 1.7. However, it is unclear as to whether the mechanism behind these spectral changes can also explain the rapid variability often observed within observations themselves. Understanding the physical mechanism behind such variability is important as it should be directly linked to the physical processes at work in the central engines of AGN. Isolating the nature of the variability will help us to understand scaling relations between supermassive black holes and stellar-mass black holes (in Galactic black-hole X-ray binary systems), the relationship between the variability in the X-ray band and in other wavebands and how the nuclear properties of the source may affect the larger-scale properties within the host galaxy. Furthermore, it may provide an important diagnostic for probing and placing constraints upon the location and kinematics of circumnuclear material. No two AGN are observed to be exactly the same, however, and this perhaps suggests that different processes could be at work in different sources forming a rather complex picture.

A variety of different models have been proposed to isolate the physical processes responsible for variability. These range from intrinsic mechanisms (Section 1.4.1) to models dominated by reprocessing of the primary continuum by circumnuclear material (Section 1.4.2), motivated by the discovery of strong pronounced spectral curvature from 2–8 keV (e.g. Nandra et al. 2007; Miller et al. 2008) in many Seyfert galaxies.

1.4.1 Intrinsic Continuum Changes

In some Seyfert galaxies, the spectral variability in the X-ray band does not appear to be linked to features generated by circumnuclear reprocessing material (see Section 1.4.2). Instead, intrinsic continuum variations may be the driving factor. One such mechanism has involved the intrinsic power law pivoting about some high energy. In terms of a standard two-phase disc-corona model whereby the hot corona is illuminated by low-energy seed photons from the disc to produce the X-ray continuum via inverse-Compton scattering (which,

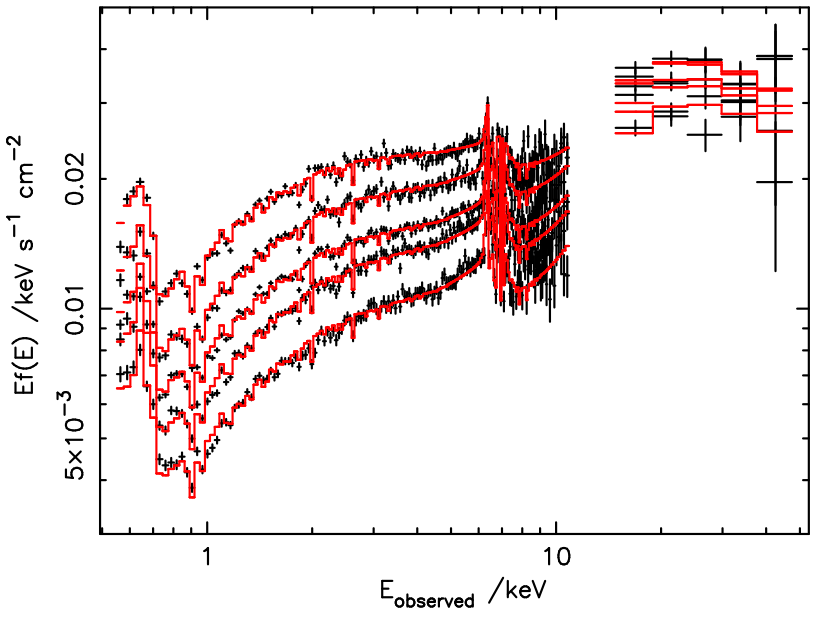

Figure 1.7: Simultaneous fits of a complex absorption model to the broad-band *Suzaku* intensity-sliced spectra of MCG–6-30-15 taken from Miller, Turner & Reeves (2008). Note how the X-ray spectrum is harder when the source flux is lower.

in turn, feeds back by heating the disc), spectral pivoting could conceivably occur if there are significant changes in the luminosity of the seed photons from the disc. For example, an increase in the luminosity of the seed photons may result in Compton-cooling of the corona to the extent at which significantly fewer seed photons are up-scattered to higher energies, thus producing a softer spectrum while the observed continuum flux is higher (Zdziarski et al. 2002; Taylor, Uttley & McHardy 2003; alternatively, magnetic flaring could play a role; see Pounds et al. 2003b).

Another popular model is based on inward propagating fluctuations within the accretion flow itself (Lyubarskii 1997; Kotov, Churazov & Gilfanov 2001). In this model, random mass-accretion-rate fluctuations in the outer disc propagate inwards exciting the outer regions of the corona of hot electrons. This is responsible for producing softer X-rays. These low-frequency variations propagating inwards then modulate higher-frequency modes generated at smaller

radii which may then excite the inner, harder-X-ray-emitting region of the corona. This may then produce the hard X-ray delay often observed at low frequencies (i.e. harder X-rays lagging behind softer X-rays). In addition, the central X-ray emission which illuminates the optically-thick disc will respond to variations in the X-ray luminosity with a short time delay set by the light-travel time between the emission sites. This can produce the short delay seen in the reflected light at higher frequencies. Examples of AGN where the timing properties have been found to be qualitatively consistent with propagating-fluctuation models include NGC 3783 (Markowitz 2005) and Mrk 766 (Markowitz et al. 2007).

Such inward-propagation models often successfully reproduce many of the more rapid observed variations within single observations particularly in lower-accretion-rate sources where the intrinsic emission can perhaps be more directly viewed. One such example could be NGC 5548 which is a low-accretion-rate source displaying relatively simple variability (see Figure 1.8). Brenneman et al. (2012) modelled the variability with simple changes in the flux of the intrinsic power law. The variations in this source have also been accounted for by spectral pivoting of the intrinsic power law ($\Delta\Gamma \sim 0.2$; Nicastro et al. 2000) and thermal instabilities in the accretion disc (Uttley et al. 2003) and so it may be the case that there is less reprocessing material in the inner regions than in higher-accretion-rate sources and so the simpler nature of the variability may arise from intrinsic processes as opposed to reprocessing of the primary emission (Section 1.4.2).

However, in other sources, higher-amplitude, longer-timescale variations are also often superimposed on the intrinsic source flickering and simple continuum variations may not be the only process at work since they would fail to account for the strong spectral curvature observed $<6\,\mathrm{keV}$.

1.4.2 Reprocessing Origins for Spectral Variability

Motivated by the discovery that many local Seyfert galaxies show a systematic hardening of the observed spectrum as the source flux lowers (e.g. Papadakis et al. 2002; Vaughan & Fabian 2004; Miller et al. 2007; Turner et al. 2008), alternative hypotheses have been put forward. Since many variations occur on timescales shorter than typical observation lengths,

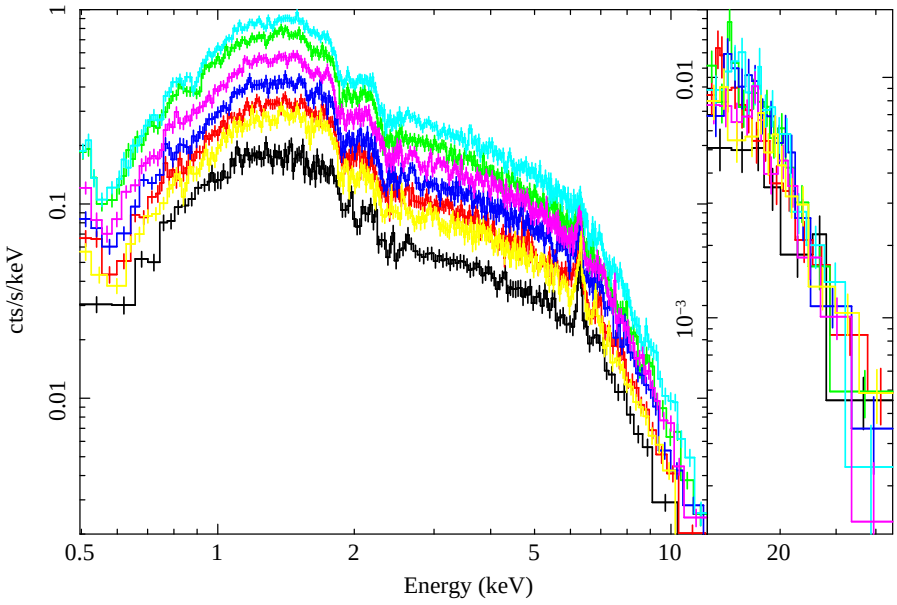

Figure 1.8: Seven *Suzaku* (XIS and HXD PIN) observations of NGC 5548 separated by weekly timescales. The continuum flux varies by a factor of ∼2 between observations. Figure taken from Brenneman et al. (2012).

model-fitting to mean spectra alone risks missing key information. Instead, performing time-resolved spectroscopy and principal components analysis (PCA; a more versatile method of analysing primary source variations; see Vaughan & Fabian 2004 and Miller et al. 2007) can allow attempts to be made to deconvolve and isolate the principal modes of variation. An example of this is shown in Figure 1.9 in the case of Mrk 766. In many cases, this has shown that the spectral variations can largely be described by a two-component model in which significant changes in a variable soft component are superimposed on a quasi-constant hard component. Then, when the source flux drops, the soft component effectively disappears from view leaving behind a reflection-dominated component of hard spectral index. However, the cause of these variations is unknown. In many variable AGN, the existence of strong spectral curvature from 2–8 keV has also been well established (e.g. Nandra et al. 2007; Miller et al. 2008) which has led to the development of models based on reprocessing of the continuum

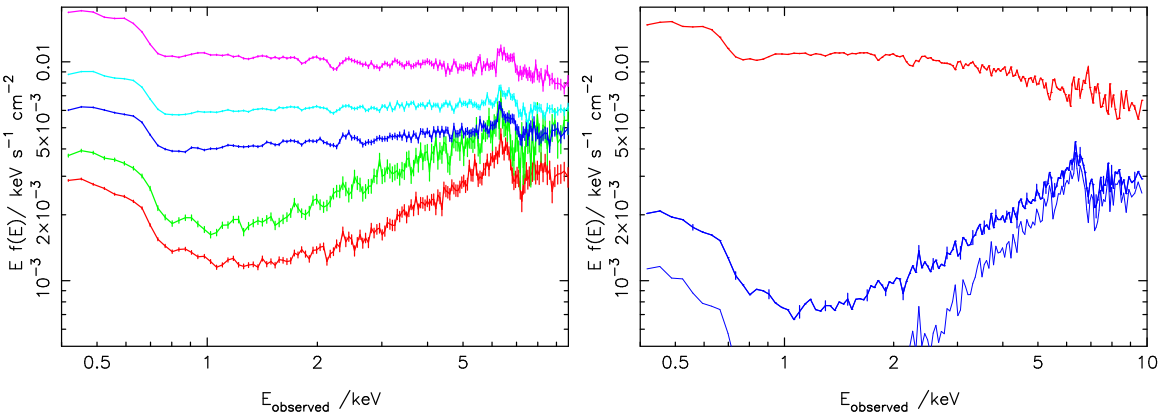

Figure 1.9: Left panel: *XMM-Newton* intensity-sliced EPIC-pn spectra of Mrk 766 from 0.4–10 keV unfolded against a power law of photon index $\Gamma = 2$. Note how the spectral shape hardens as the source flux drops. Right panel: The primary PCA spectra of Mrk 766 from the same *XMM-Newton* dataset. The red line shows the principal varying component (eigenvector one) whereas the blue set of spectra show the possible range of the invariant zero-point spectrum with a much harder shape. Figures taken from Turner & Miller (2009).

emission by circumnuclear material close to the black hole. Models for explaining the X-ray spectral variability in terms of reprocessing generally fall into two groups: those dominated by reflection and those dominated by absorption, although it has often proven difficult to distinguish between them. These are summarised below.

1.4.2.1 Reflection-Dominated Models

Reflection-dominated models have been proposed since the strong curvature from 2–8 keV has often been dubbed the "red wing" of broad, relativistic Fe K emission (e.g. Wilms et al. 2001; Vaughan & Fabian 2004; Miniutti et al. 2007; Nandra et al. 2007), appearing as an excess above the continuum and becoming particularly prominent when the source flux is low. This component has been widely interpreted as being gravitationally-redshifted Fe Kα emission originating just a few $r_{\rm g}$ from the black hole. In some cases, the implied redshift is so large that the emission would need to originate from within the ISCO of a Schwarzschild black hole and so this has led to claims of the detection of black hole spin in some AGN

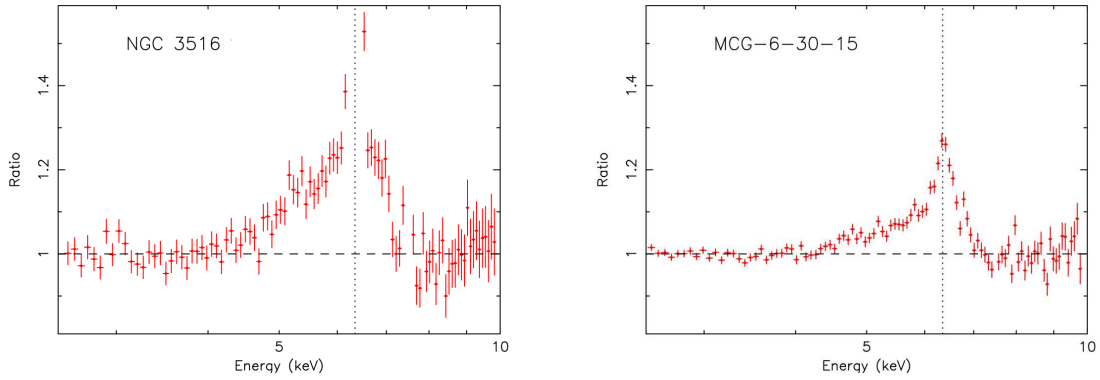

Figure 1.10: Data/model ratios of *XMM-Newton* spectra of NGC 3516 and MCG–6-30-15 derived from 2–10 keV while excluding the 4.5–7.5 keV region and fitting with a simple power-law modified by Galactic absorption. Figures taken from Nandra et al. (2007).

(Wilms et al. 2001). One notable example is the case of MCG–6-30-15 (e.g. Miniutti et al. 2007, but also see Miller, Turner & Reeves 2009 and Patrick et al. 2011a) which is shown in Figure 1.10 alongside a second example: NGC 3516.

Often, to account for the strong curvature in the 2–8 keV band, blurred reflection models have been used whereby standard reflection spectra (Ross & Fabian 2005) are convolved with the emission effects that one might expect to see from the regions of a rotating accretion disc very close to the black hole. Such approaches have been motivated by the expectation that the signatures of material within a few tens of $r_{\rm g}$ from a black hole in an AGN might be realistically measured with current instrumentation. Indeed, if the production of the X-ray continuum takes place on a compact scale within a few $r_{\rm g}$ of the event horizon, then for common disc geometries, significant reflection may be expected to occur within $\sim$20 $r_{\rm g}$ of the black hole; a region where general relativistic effects are thought to be prominent (assuming that the accretion disc extends this close to the black hole).

A recent study by Nandra et al. (2007) based on available *XMM-Newton* data concluded that the emission from a significant number of local AGN is best-fitted with blurred reflection models. However, it should be noted that the absorption models that were considered in this

study were not permitted to have the covering fraction as a free parameter (i.e. they were fully-covering; see Section 1.4.2.2) and the ability to account for long-term spectral variability of the models was not tested. Turner & Miller (2009) point out that when the absorbers are allowed to partially cover the source, acceptable fits can also be obtained to time-averaged spectra (e.g. Mrk 766, Miller et al. 2007; Turner et al. 2007).

When accounting for spectral variability, the biggest problem for reflection-dominated models has been the lack of any significant or simple correlation between the observed strengths of the continuum and reflection components (e.g. MCG–6-30-15; Miniutti et al. 2003; Miller, Turner & Reeves 2008) in that that the observed red wing remains remarkably constant in flux despite large apparent changes in the flux of the intrinsic continuum emission, contrary to what one might expect if the line is produced very close to the continuum source (Turner & Miller 2010). This led to the development of a "light-bending" model which accounts for the apparent constancy of the red wing of the Fe Kα emission lines which otherwise may be expected to vary in phase with the continuum. In this model, the observed effects are driven by the height of a compact continuum source above the accretion disc (e.g. Fabian & Vaughan 2003; Miniutti et al. 2003; Miniutti & Fabian 2004). Since light follows geodesics near the black hole, general relativistic effects become more pronounced when the continuum source is closer to the disc. The continuum flux received by a distant observer then drops and the photons arrive either at the surface of the disc or they cross the event horizon. In the case where more photons strike the surface of the disc, this can have the effect of increasing the relative strength of the observed reflection component compared to the intrinsic component, explaining the hard spectral shape.

Such a blurred reflection model was used to account for MCG–6-30-15 whereby the primary continuum source was required to be located within 3–4 $r_{\rm g}$ of the black hole and varying in height (i.e. above the disc) from $\sim$3–8 $r_{\rm g}$ (e.g. Miniutti et al. 2003; Miniutti & Fabian 2004). Brenneman & Reynolds (2006) also modelled *XMM-Newton* data (exposure time $\sim$ 350 ks) from 2001 with a blurred reflection model which they argue requires a rapidly spinning black hole, consistent with maximal spin. Alternatively, see Patrick et al. (2011a) where a full broad-band *Suzaku* analysis taking into account the warm absorber at energies $<$3 keV ruled out maximal spin and instead reported an intermediate value. Other AGN

modelled in this way include NGC 4051 (Ponti et al. 2006), 1H0707–495 (Zoghbi et al. 2010) and NGC 3783 (Brenneman et al. 2011).

However, explaining these phenomena by invoking changes in the height of the primary continuum source above the disc has been described by opponents as *ad hoc*. Further potential issues revolve around the extreme model parameters often required such as the high values of emissivity (implying that the majority of the emission is extremely centrally concentrated) required in such sources as 1H0707–495 (Zoghbi et al. 2010) and NGC 3783 (Brenneman et al. 2011). Significantly super-solar abundances of Fe are also required to explain many spectra fitted this way; something for which no independent evidence currently exists (e.g. a factor > 9 overabundance of Fe would be required in the NLS1, 1H 0707–495; Zoghbi et al. 2010, but also see Miller et al. 2010a and Miller & Turner 2011).

Furthermore, in the cases where the observed 2–10 keV flux drops significantly, high apparent values for the reflection-strength (obtained from simultaneous data >10 keV; i.e. with *Suzaku*) are required to model the hard spectra and thus the relative magnitude of the reflection component has become an interesting topic of debate. Indeed, if (blurred) reflection alone is to account for this, it would indicate that solid angles $> 2\pi$ sr would be required for the optically-thick medium subtending the primary continuum. The observed strength of the reflection spectrum is critically dependent upon the surface illumination pattern along with the observer's viewing angle although some favourable inner geometry of the disc (e.g. a deep funnel) could play a significant role. It could also be possible that the continuum / reflection ratio may not be directly measurable if some of the primary illuminating continuum is hidden from view so that only Thomson-scattered radiation is observed. In this case, the reflecting medium may then see the rest of the illuminating continuum that is not visible to the observer thus modifying the shape of the observed spectrum to appear more reflection-dominated.

Finally, reflection-dominated models also rely on the X-ray continuum production taking place on very compact scales. An extended corona would not produce disc-reflection spectra that were in any way weighted towards smaller radii which may then not produce such significant blurring. However, AGN are often observed to display significant variability on much shorter timescales too. Based on light-crossing arguments, the rapidity of this variability suggests that the X-ray emitter must be very compact (e.g. Rees 1977), perhaps even

on the order of just a few ks across (in terms of the light-crossing time). So there is evidence to suggest that the primary X-ray illumination of the disc is very centrally concentrated and so it is plausible that significant reflection could take place within $\sim 20\, r_{\rm g}$ of the black hole.

1.4.2.2 Absorption-Dominated Models

Alternatively, absorption-dominated models have been proposed by some authors. The motivation behind such models has arisen from the discovery of multiple components of complex absorption varying in ionisation, column density and kinematics from high-resolution UV observations of Seyfert galaxies (Crenshaw, Kraemer & George 2003). Since the highest-ionisation lines in high-accretion-rate sources are suggestive of an origin in a disc wind (Gaskell 1982; Murray & Chiang 1998), this, coupled with the fact that winds have been theoretically predicted to be driven off accretion discs (King & Pounds 2003, possibly extending close to the black hole; Proga, Stone & Kallman 2000), has motivated the search for such absorption signatures via X-ray spectroscopy. The application of photoionisation models alongside direct detection of absorption lines (e.g. with grating data) through such X-ray observations has confirmed that absorbing gas exists with higher ionisation states and column densities than those observed in the UV band (e.g. Blustin et al. 2005; McKernan, Yaqoob & Reynolds 2007) and may be linked to large-scale outflows.

In absorption-dominated scenarios, the changes in the spectral shape of variable sources can be accounted for by allowing the line-of-sight covering fraction of a "partial-covering" absorber to vary (e.g. Miller, Turner & Reeves 2009). When the covering fraction is high, a large proportion of the continuum photons are absorbed and scattered out of the line-of-sight, hence reducing the observed flux at lower energies and producing the observed hard spectral shape, while there is no overall change when integrated over all solid angles. In this case, the "red wing" of the Fe Kα emission line is simply an artifact of the variations of the partial-coverer and the constancy in flux of the associated narrow component of emission can then be accounted for if it arises in more distant material (e.g. the torus). In many cases, the absorption models require covering fractions $\lesssim 1$ with the variability accounted for by allowing for changes in the covering fraction of tens of per cent (e.g. Reeves et al. 2002;

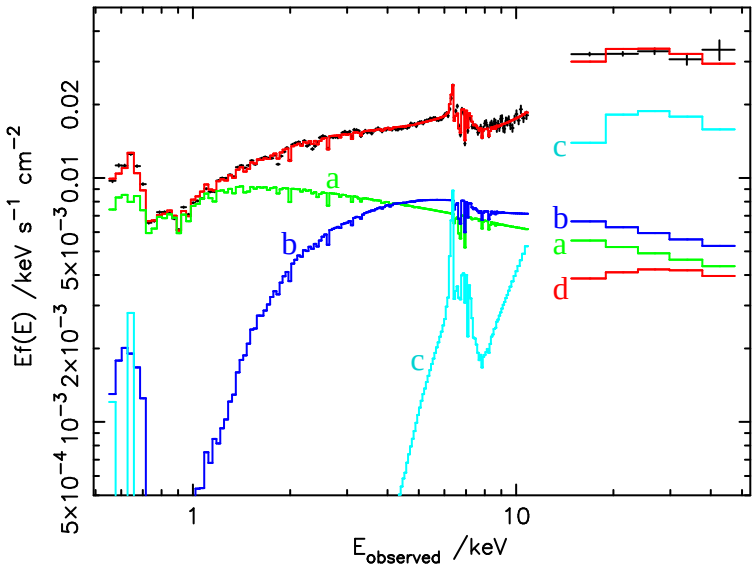

Figure 1.11: Spectral model of Miller, Turner & Reeves (2008) fitted to the mean broad-band *Suzaku* spectrum of MCG–6-30-15. Component (a) is the primary power-law continuum (absorbed by three warm-absorber zones), (b) is the partially-covered power law, (c) is a low-ionisation distant reflection component and (d) is a component of cosmic X-ray background (CXB) emission. Figure taken from Miller, Turner & Reeves (2008).

Turner et al. 2007). This scenario is consistent with the simple two-component models borne out of PCA whereby the variability is driven primarily by changes in a soft power-law-like component (of constant slope) superimposed on a quasi-constant hard component (e.g. Mrk 766, Miller et al. 2007; NGC 4051, Miller et al. 2010b). Temporal changes in the ionisation structure and/or the opacity of the warm absorber (e.g. Krongold et al. 2005) have also been considered to explain the spectral variability of some sources but it is often found that the most extreme variations require changes in the line-of-sight covering fraction.

One such AGN to be modelled in this way is MCG–6-30-15 (see Figure 1.11). Contrary to the reflection-dominated models of Miniutti et al. (2003), Miller, Turner & Reeves (2008) developed an absorption-dominated model based upon the detection of a wealth of discrete absorption features in the *Chandra* grating data (also see Miller, Turner & Reeves 2009).

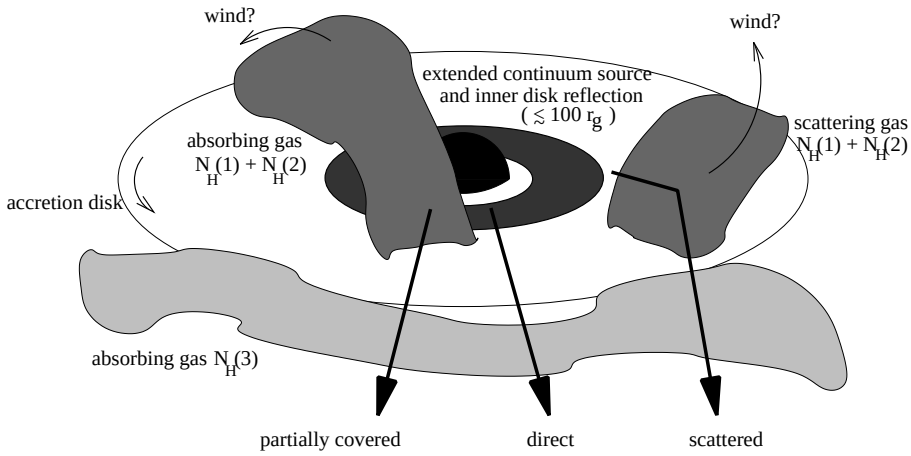

Figure 1.12: A schematic representation of the inner regions of the Mrk 766 models described in (and taken from) Turner et al. (2007). Here, direct, partially-covered and scattered emission components (all of which are absorbed by more distant Compton-thin gas) may all fall into the observer's sightline. Note that a distant reflector is also present in the models but omitted here for clarity.

They account for the variability by allowing for changes in the line-of-sight covering fraction of a single warm-absorber zone which they argue most likely originates in a clumpy disc wind. Such a scenario is supported by the observation of an eclipse-like event in the lightcurve (McKernan & Yaqoob 1998) which can be interpreted as an occultation by the wind.

In the case of partial covering, common arguments against it have been based upon probability since for an absorber to partially cover the source, it should have some structure on a similar size scale to the source that it is obscuring. If the absorber is made up of discrete clouds then these clouds should be expected to be of comparable size to the source (e.g. BLR-sized clouds). Then, if the absorbing clouds are distant from the source, it is implied that it is not only somewhat coincidental that the clouds have passed into the line-of-sight but also that there must be a large distribution of clouds across this region if there is to be a significant chance of one falling across the observer's sightline. However, it could be that the clouds exist at radial locations close to the source and the timescales of variations in some sources may suggest that this is plausible (e.g. NGC 1365; Risaliti et al. 2009, NGC 3516; Turner et al. 2008).

Alternatively, partial-covering could be a more likely scenario if the X-ray absorber were to exist as part of a clumpy disc wind as opposed to being in the form of discrete clouds. Figure 1.12 shows a schematic representation of such a disc-wind scenario based on models developed for Mrk 766 (Turner et al. 2007). Clumpy absorbers comprising wide ranges of scale sizes are predicted in the disc-wind models of Proga, Ostriker & Kurosawa (2008) and, as mentioned above, such winds have been theoretically predicted to be driven off accretion discs (King & Pounds 2003). If this scenario is correct, it would help to counter the argument about probability since an equatorial disc wind would have a preferred plane and hence the observed spectral variations due to varying covering fractions would simply depend upon the observer's viewing angle to the disc.

Turner & Miller (2009) point out that when fitting partial-covering models to X-ray spectra, they are often indistinguishable from models whereby a fully covered, absorbed continuum source is observed plus a significant 'Thomson-scattered' component that has been energy-independently scattered into the line-of-sight. In some cases, such models may provide alternative explanations for the spectra of some type-1 AGN but with high scattering fractions.

1.4.2.3 Additional Variability and Evidence for Compton-Thick Gas in Type-1 AGN

The spectral behaviour in type-1 Seyfert galaxies is often complicated further by the observation of additional modes of spectral variations within a given flux level. For example, observed spectral changes during a period of very low flux in MCG–6-30-15 were interpreted by Reynolds et al. (2004) as arising from correlated variations between the disc features and the continuum. The authors suggested that the lack of such behaviour at higher flux levels was due to line saturation events. Complex behaviour during the phases of lowest flux have also been interpreted in terms of patchy ionisation of the accretion disc (Reynolds & Wilms 2000) or, in the case of light-bending models, the continuum source becoming located very close to the spin axis of the black hole (Miniutti & Fabian 2004). Alternatively, complex spectral behaviour within extended periods of low flux may also be interpreted in terms of

absorption models as either changes in the opacity or ionisation level / structure of the gas or as systematic evolution of the relative sizes of the source and the absorber (Miller et al. 2008).

In some sources, additional components of variability have also been required when the observed flux was high. One example is NGC 3516 (Turner et al. 2008) where an unusually hard spectrum was accompanied by a strong dip in the lightcurve. Contrary to sources such as MCG–6-30-15, harder spectral states are observed during some epochs of high X-ray flux suggesting that a simple two-component model or spectral pivoting cannot account for the observed variations, thus posing problems for both partial-covering and light-bending models (see Figure 1.13). Turner et al. (2011) suggest that the additional mode of variation may be explained by passages of Compton-thick clouds across the line-of-sight and may be a consequence of an uncommon source orientation whereby our line-of-sight perhaps intercepts the edge of some strongly-absorbing structure, thus collimating the nuclear emission and leading to the bi-conical structure observed for the optical NLR. Overall, the spectral variability in NGC 3516 could be largely driven by the line-of-sight covering fraction of an absorber of column density $N_{\rm H} \sim 10^{23}\,{\rm cm}^{-2}$ varying from $\sim$40% up to >96%, while appearing unusually independent of the intrinsic continuum flux. However, the origin of the hard excess is a matter of debate since this has been modelled by Markowitz et al. (2008) as a strong reflector but also by Turner et al. (2011) as a Compton-thick ($N_{\rm H} > 10^{24}\,{\rm cm}^{-2}$) partial-coverer. Such a scenario would provide a natural extension to the standard absorption-dominated model. A similar drop in flux was observed in MCG–6-30-15 (McKernan & Yaqoob 1998) and may provide additional evidence for significant amounts of absorbing material lying in our sightline.

Further evidence for Compton-thick columns of gas in the sightline of type-1 AGN has also come from *Suzaku* observations of PDS 456 (Reeves et al. 2009) and 1H 0419-577 (Turner et al. 2009). Extrapolating model fits from 0.5–10 keV to higher energies (i.e. $E > 10\,{\rm keV}$) reveals a significant hard excess of counts in both cases, which are difficult to model with blurred reflection but can be accounted for with a layer of Compton-thick gas covering as much as $\sim$90% of the continuum. The implication is that the continuum source at energies >10 keV is relatively unaffected by the absorbing gas, hence explaining its relative lack of variability

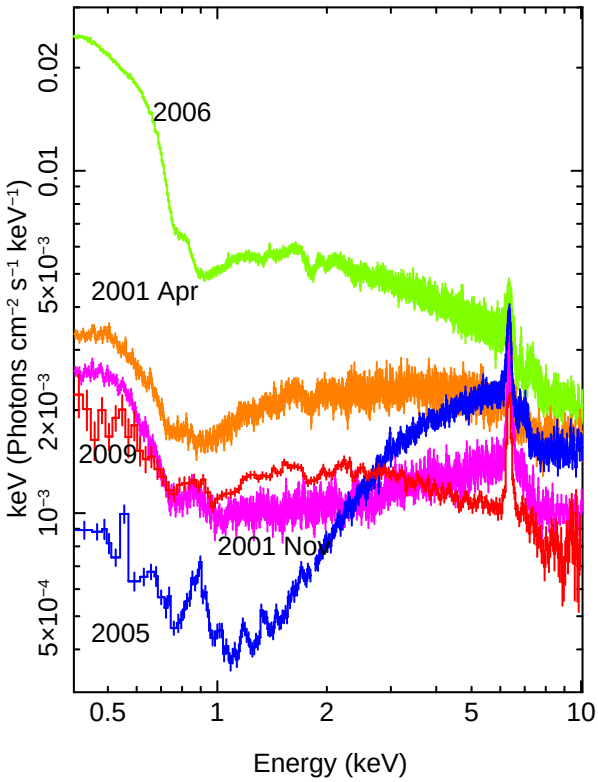

Figure 1.13: X-ray spectra of NGC 3516 from *XMM-Newton* (2001 and 2006) and *Suzaku* (2005 and 2009) showing the significant variability exhibited by this source. Note how the *Suzaku* spectrum from 2005 is much harder despite having a much higher flux above 2 keV than spectra acquired in 2001 and 2009. Figure taken from Turner et al. (2008).

when compared to the 2–10 keV flux. Indeed, even for column densities up to $\sim 10^{25}$ cm^{-2}, transmitted radiation is still visible >10 keV (Matt, Pompilio & La Franca 1999). Other notable objects with significant hard excesses (i.e. significantly exceeding those expected from reflection off a thin disc subtending 2π sr to the illuminating continuum) include MCG–6-30-15 (Ballantyne, Vaughan & Fabian 2003; Miniutti et al. 2007), Mrk 335 (Larsson et al. 2008) and NGC 4051 (see Chapters 4 and 5). Interestingly, the cases of 1H 0419-577 and PDS 456 in particular suggest that Compton-thick gas may lie in the line-of-sight to the nucleus of even type-1 AGN (a hypothesis further supported by new *Swift* BAT results; see Section 6.1.1) with a likely origin within the BLR (Turner et al. 2009). If this is the case,

it may have implications for true X-ray luminosity estimations of these local sources, which have perhaps been underestimated (Tatum et al. 2012).

So the observed X-ray spectral variability of Seyfert galaxies forms a highly complex picture, most likely involving a non-trivial combination of various physical processes. Questions over the exact location of reprocessing material in AGN remain unanswered although the rapidity of the short-term variations in many sources suggests that the bulk of the material is close to the black hole (e.g. Turner et al. 2008; Risaliti et al. 2009). It is also perhaps likely that both reflection and absorption are natural phenomena arising in high-accretion-rate sources. However, the dominant process and the direct mechanism behind it is still strongly debated and it is unknown whether the spectral shapes observed during periods of very low flux are disc-reflection-dominated, heavily absorbed or just intrinsically low. Nevertheless, great progress has been made over recent years and further detailed analyses of long-look observations may provide our best opportunity for such models to become disentangled. This is important if we are to fully comprehend the physical processes at work in the X-ray regime and so understand the accretion process through which AGN are powered.

1.4.3 Thesis Outline

In this thesis, recent X-ray observations of two X-ray-bright Seyfert galaxies are analysed in detail and best-fitting models are derived. These sources are NGC 7213 and NGC 4051. NGC 7213 is a nearby low-luminosity Seyfert galaxy. It is a low-accretion-rate source that is more slowly variable (Bell et al. 2011; Emmanoulopoulos et al. 2012) and historically displays little evidence for any strong reflection components (Bianchi et al. 2008). NGC 4051, however, is a much higher-accretion-rate source with a black hole of much smaller mass. It is found to be extremely variable both on short and long timescales (Guainazzi et al. 1998; McHardy et al. 2004), often falling into extended periods of low flux (Terashima et al. 2009). As such, these two sources offer contrasting views of the Seyfert 1 phenomena and lie at opposing ends of parameter space in the context of X-ray variability. The results of these studies are discussed in the context of the long-term X-ray spectral variability that they display.

To summarise: Chapter 2 details the methodology, instrumentation, statistical issues

and data reduction techniques used in the subsequent analysis. In Chapter 3, recent *Suzaku* and *XMM-Newton* observations of NGC 7213 are analysed. The time-averaged spectrum is modelled in a physical way and the long-term variations are discussed. Chapters 4 and 5 present the analysis of a deep contemporaneous study at the opposite end of the observable parameter space of the rapidly variable NLS1 NGC 4051 with *Suzaku* and *Chandra*. In particular, the *Suzaku* data from 2008 are modelled simultaneously with those obtained in 2005 in order to assess the nature of the observed spectral variability. Finally, in Chapter 6, the results obtained in Chapters 3–5 are placed into context, the validity of models to describe the long-term X-ray spectral variability of type-1 Seyfert galaxies as a whole is summarised and potential future prospects are outlined.

2 X-Ray Astronomy: Overview, Data Reduction and Spectral Analysis

2.1 Space-Based X-Ray Astronomy

Cosmic X-rays are completely absorbed by the Earth's atmosphere. This means that ground-based X-ray astronomy is not a possibility and so observatories must be launched above the atmosphere and into space where they are able to observe the full range of the X-ray spectrum. Since X-rays are high energy photons, they do not reflect or refract well with ordinary mirrors or lenses. As a result, materials that are non-transparent to X-rays must be used in order to detect them. If the correct materials and angles are chosen, "grazing-angle incidence" mirrors can be used to try and focus X-rays from a wider area of the sky via total external reflection. X-rays that are incident perpendicular to a given material are usually absorbed instead of being reflected, thus ruling out the use of ordinary mirrors such as those used for optical astronomy. To reflect an X-ray photon, dense materials such as gold (e.g. as used on-board the *Suzaku*, *XMM-Newton* and *Swift* satellites) and iridium (e.g. the *Chandra* satellite) are commonly used. To form an X-ray image over a finite field of view (FOV), the basic principle requires that a concave parabolic mirror followed by a convex hyperboloid is in the optical path of the incoming X-ray photons (Wolter 1952a; Wolter 1952b; Figure 2.1). Focusing X-rays not only allows sharper images to be formed and sources with small angular separation to be resolved but it also helps to allow for the observation of fainter sources.

The X-ray background is also an important consideration. X-rays can hit the telescope from all angles, originating from the satellite's own power sources, high-energy solar photons reflected off the Earth's atmosphere and high-energy particles from the Sun which can react with the detector and be mistaken for X-rays. Therefore, X-ray telescopes often have non-focusing collimators which restrict the field of view of the instrument. This is done with dense materials which reduce the spatial cross-section of the incident stream of radiation and serve to increase one's confidence that the detected photons originate from within the field of view of the telescope and not from the side or behind.

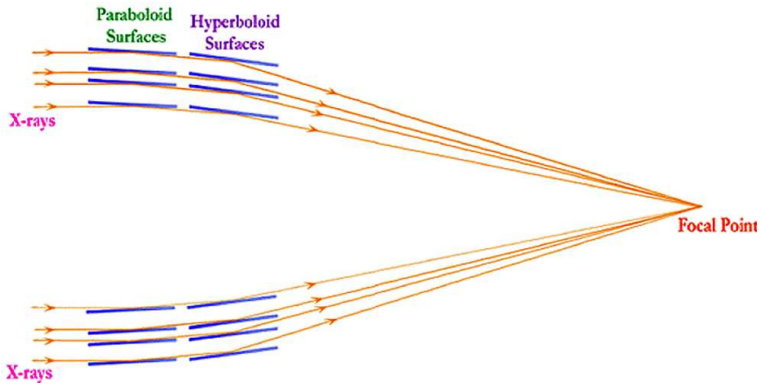

Figure 2.1: A plot showing a standard Wolter-I mirror configuration for focusing X-rays. Figure taken from http://opticalengineering.spiedigitallibrary.org.

Once the telescope has collected radiation from an astronomical source, the photons must be delivered to a detector, the purpose of which is to determine the energy (or wavelength) and flux of the photons in addition to the direction from which they came and the time at which they arrived with as great a degree of accuracy as possible. As opposed to optical detectors which usually rely on many optical photons hitting the detector at once in order to generate a strong signal, X-ray detectors generally detect individual photons.

In order to detect the photons, the detector must be specifically made of materials that will interact with X-rays in a desirable way. This is because the X-ray photon must be stopped inside the detector. If the detector is transparent to X-rays, the photon will travel straight through with no measurable trace and if it interacts with the detector but still makes it all the way through (albeit having lost some of its energy), this will produce a false measurement. Therefore, the 'housing' of the detector should be as transparent as possible whereas the measurement device should be made of something dense that will completely absorb X-ray photons. This can range from silicon chips to dense gases that the X-rays will only get halfway through before giving up all of their energy and thereby producing some form of measurable signal.

To date, X-ray detectors generally produce a signal in one of three ways. One of these

occurs when an incoming X-ray interacts with the atoms in the detector and either ionises them or causes photo-electrons to be emitted which then produce an electric current. From the strength of the measured electric charge, it is then possible to determine the energy of the incoming photon. Such a technique is used in devices such as charge-coupled devices (CCDs; semiconductors), microchannel plates and proportional counters. A second form of signal involves the amount of light produced when X-rays interact with atoms and are absorbed, causing photons to be emitted via the photo-electric effect. This method is used by detectors such as scintillators and phosphors. Finally, the amount of heat produced in the material when an incident X-ray photon is absorbed can also be measured. This technique is used in calorimeters.

Above the Earth's atmosphere, the sky is X-ray rich and there are photons hitting the telescope from all angles. In addition to the ambient background, any other Galactic or extragalactic astronomical sources within the field of view of the instrument may contribute to the background noise. In fact, it is sometimes the case that the overall X-ray background is of a comparable amplitude to that of the target source itself. As a result, one would also want the detector to be capable of either filtering out the background radiation instantly or providing the observer with accurate information regarding the direction and energy of the incident photons so that source and background radiation can be easily distinguished. Therefore, since different detectors have their individual strengths and weaknesses, different detectors are chosen for different applications. A summary of the specific key detector types used for this research is given in Section 2.1.1.

2.1.1 Modern X-Ray Detectors

The most frequently used detectors in modern X-ray astronomy include the following:

- *CCDs*: A CCD is a solid-state detector consisting of an array of linked capacitors. Photons interact with a semiconductor substrate, usually made of silicon, and will be photoelectrically absorbed with a probability that is constant per unit length. Unlike optical CCDs which detect photons that impact on the surface, X-ray CCDs work by measuring photons that penetrate into the middle of the chip. The attenuation

length depends upon the energy of the incident photon and the active region of a typical X-ray CCD provides the best sensitivity to photons with energies ranging from a few hundred eV to ∼10 keV. Photons with energies below a few hundred eV will either become absorbed at the surface and either incompletely detected or not detected at all whereas photons with energies $\gtrsim 10$ keV will most likely pass right through the active region without interacting. When a photon does penetrate into the middle of the CCD, the photoelectric absorption generates electron-hole pairs and liberates electrons, the number of which linearly increases with the energy of the incident photon. The charge cloud may then diffuse and recombine or, if an electric field is applied, it may drift under its influence. The charge cloud must then be collected and stored and a measurement of the charge provides an accurate estimate of the energy of the original X-ray photon.

Regular clocked readouts of the CCD provide decent timing measurements although one disadvantage is that CCDs are typically small and so do not have large collecting areas. So while the energy measurements are very accurate (limited only by the Fano factor; Fano 1947), CCDs don't always provide as many measurements as larger detectors such as proportional counters. Therefore, it is often advantageous to combine a CCD detector with telescope mirrors to focus more X-rays onto them. X-ray CCDs may also be 'front-illuminated' or 'back-illuminated' (e.g. such as on-board *Suzaku*; see Section 2.2.1). A front-illuminated CCD detects X-ray photons that pass through a gate structure contained on one surface of the CCD which is used to transfer charge packets to the readout gate. The additional photoelectric absorption at the gate structure reduces the quantum detection efficiency[1] (QDE) of the CCD at low energies. Conversely, a back-illuminated CCD receives photons from the opposite side and so retains a higher quantum detection efficiency at low energies. However, such CCDs tend to have thinner depletion layers resulting in a lower efficiency in the higher-energy band.

[1]The quantum efficiency is defined as the probability of a photon being detected as an event having struck the detector.

CCDs are currently widely used in X-ray astronomy and form part of the focal-plane instrumentation of many major missions. Examples include the Advanced CCD Imaging Spectrometer (ACIS; Garmire et al. 2003) on-board *Chandra*, the European Photon Imaging Camera (EPIC; Turner et al. 2001; Strüder et al. 2001) and the Reflection Grating Spectrometer (RGS; den Herder et al. 2001) both on-board *XMM-Newton* and the X-Ray Imaging Spectrometer (XIS; Koyama et al. 2007) on-board *Suzaku*. A CCD was also previously flown on-board *ASCA* (Solid-state Imaging Spectrometer; SIS; Tanaka, Inoue & Holt 1994).

- *Scintillators*: Scintillators have become useful detection devices at higher energies (e.g. $>50\,\mathrm{keV}$) since detectors such as proportional counters were impractical because they had to provide a large enough column density of gas in order to stop an incident X-ray photon. This required them to be built either very deep or to withstand very high pressures. Instead, a scintillator works by using a crystal which will emit optical photons when absorbing X-rays, which are then collected by photomultiplier tubes. If one combines two different crystals (one surrounding the other), one can be used for X-ray detection while the other is used to reject background events. If an interaction occurs in the surrounding crystal, this implies that the X-ray photon has arrived from the side or the back of the detector and so must be due to the background. Instead, if an X-ray photon is absorbed by the central crystal, it must have entered from the front of the detector and so should be due to the source. Note that highly energetic particles such as cosmic rays may interact with both crystals. Since the scintillation (i.e. optical emission) will have different decay times in each crystal, it is then possible to separate the source events from the background events. NaI(Tl) and CsI(Na) crystals were used for the High-Energy X-ray Timing Experiment (HEXTE) on-board the *Rossi X-Ray Timing Explorer* (*RXTE*; Rothschild et al. 1998) and the Phoswich Detector System (PDS) on-board *BeppoSAX* (Frontera et al. 1997) to detect source and background events respectively. Similarly, the Hard X-ray Detector (HXD) on-board *Suzaku* carries a scintillator in the form of the Gadolinium Silicate (GSO) instrument which uses Gd_2SiO_5 crystals for the X-ray detection and

$Bi_4Ge_3O_{12}$ crystals for background rejection (Takahashi et al. 2007).

- *CZT*: Cadmium zinc telluride (CdZnTe; CZT) is a compound which can be used to form high-energy detectors since the high atomic numbers of Cd and Te result in high sensitivity for X-rays and gamma-rays. It works as a semiconductor in a similar way to a CCD whereby incident X-rays create electron-hole pairs, requiring an energy of 1–2 eV to create such a pair. This results in a better energy resolution than offered by scintillator detectors down to just a few per cent in the 10–100 keV energy range. A CZT detector is used in the Burst Alert Telescope (BAT) on-board *Swift* (Barthelmy et al. 2005) and is the primary instrument on-board the recently-launched *Nuclear Spectroscopic Telescope Array* (*NuSTAR*; Rana et al. 2009).

- *Microcalorimeters*: A microcalorimeter is a thermal device which works by measuring the change in temperature of a material when it absorbs an X-ray photon. It generally consists of a thermal mass to absorb the X-ray(s) and convert the energy to heat, a thermometer to measure the temperature rise and a thermal link to a heat sink to allow the energy to escape in order to cool the thermal mass. The temperature change can be measured to great precision allowing an energy resolution of just a few eV to be achieved at 6 keV, which is very useful for studies in the Fe K band. Furthermore, microcalorimeters overcome the low efficiency problem associated with diffraction gratings which largely limits their use to bright sources only. Since the change in temperature must be measured on the order of a few millikelvin, the detector must be cooled down to the millikelvin range. This requires a complex cryogenic system. A microcalorimeter (X-Ray Spectrometer; XRS; Kelley et al. 2007) was installed on *Suzaku* but the liquid-helium cryogen vented into space before any astronomical observations could be made. The next attempt to fly a microcalorimeter on-board a satellite will be with *Astro-H*, due for launch in 2014.

2.2 X-Ray Satellites

This section will provide a brief overview of the major X-ray satellites that have been made use of during this research. A comparison of the main instruments used in this thesis is given in Table 2.1.

2.2.1 Suzaku

Suzaku was launched in July 2005 and is, in collaboration with the USA, Japan's fifth X-ray satellite (Mitsuda et al. 2007) and the direct successor to *ASCA* (the *Advanced Satellite for Cosmology and Astrophysics*). It is a joint mission developed by the Institute of Space and Astronautical Science (ISAS) and the National Aeronautics and Space Administration's Goddard Space Flight Center (NASA / GSFC). *Suzaku* is in a near-circular low-Earth orbit with an apogee of 568 km, an inclination angle of 31.9° to the equator and an orbital period of ∼96 minutes.

Suzaku consists of a functioning X-Ray Imaging Spectrometer (XIS; Koyama et al. 2007) and a Hard X-Ray Detector (HXD; Takahashi et al. 2007), both of which function simultaneously resulting in high X-ray sensitivity and a broad bandpass from 0.2–600 keV (Figure 2.2). The satellite was launched with four functional XIS cameras each with a silicon CCD operating in a photon-counting mode; three front-illuminated (FI; 0.4–12 keV) and one back-illuminated (BI; 0.2–12 keV), each in the focal plane of a dedicated X-ray telescope, all of which feature an X-ray mirror with an angular resolution of $\sim 2'$. The XIS has a large field of view ($17.8' \times 17.8'$) with an energy resolution of ∼130 eV (FWHM) at 6 keV. The front-illuminated detectors have a smaller effective area than the back-illuminated detector at low energies ($\lesssim 1.5$ keV) but this becomes larger at higher energies (∼8 keV; see Figure 2.3). The background level of the front-illuminated detectors is also lower at higher energies. Furthermore, the quantum detection efficiency of the front-illuminated detectors is more limited at low energies than the back-illuminated detector but this effect is reversed at higher energies. In November 2006, a charge leak was discovered in one of the front-illuminated detectors

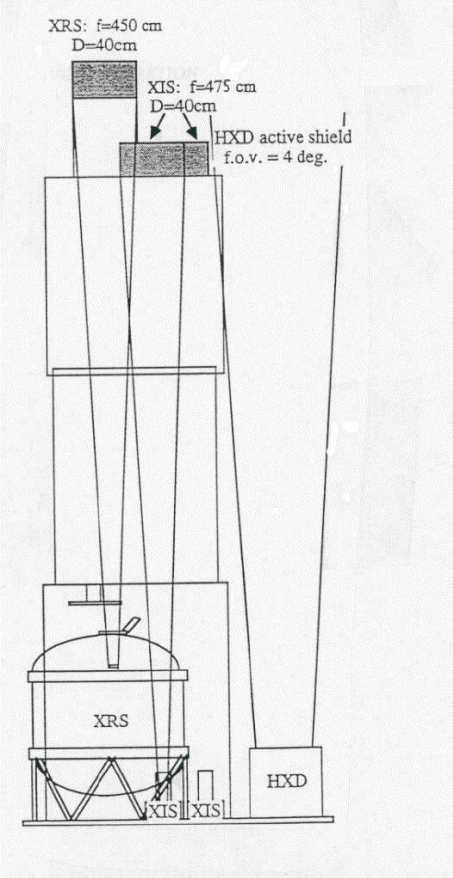

Figure 2.2: Schematic showing the XIS and HXD instruments on-board *Suzaku*. Figure taken from http://www.heasarc.nasa.gov.

(XIS 2) most likely due to a micro-meteoroid impact[2]. As a result, this rendered XIS 2 unable to produce useful astronomical data and so *Suzaku* has operated with just three XIS detectors ever since.

The HXD is a non-imaging instrument but extends the bandpass of *Suzaku* to 600 keV. It consists of two sensors: 2 mm thick Positive Intrinsic Negative (PIN) silicon diodes (10–70 keV) and gadolinium silicate (GSO) crystal scintillators (40–600 keV). The effective areas

[2]http://www.astro.isas.ac.jp/suzaku/doc/suzakumemo/suzakumemo-2007-08.pdf

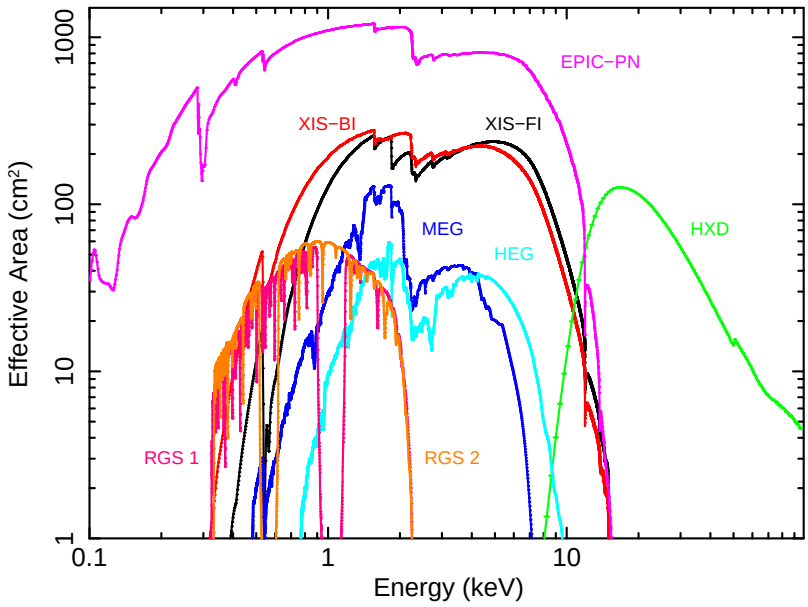

Figure 2.3: The relative instrumental efficiency as a function of energy for the primary detectors on-board *Suzaku*, *Chandra* and *XMM-Newton*. The *Suzaku* individual FI (of which there are two operating currently) and BI XIS detectors are shown in black and red respectively with the HXD shown in green. The MEG and HEG of which *Chandra*'s HETG is comprised (in the optical path of the ACIS) are shown in navy blue and cyan respectively and the two RGS gratings and the EPIC-pn on-board *XMM-Newton* are shown in pink, orange and magenta respectively. Note that the FI XIS CCD effective area curve plotted here is for a single FI CCD and so will be a factor of 2 higher for most observations (or a factor of 3 higher for observations pre-dating November 2006).

of the two detectors peak at $\sim$160 cm^2 at 20 keV and $\sim$260 cm^2 at 100 keV respectively. The HXD has a large field of view ($4.5^\circ \times 4.5^\circ$ for the GSO above 100 keV; $35' \times 35'$ for the PIN below 70 keV) and an energy resolution of $\sim$4.0 keV (FWHM). Although the HXD is designed to observe faint X-ray sources, it can also tolerate very bright sources up to an order of magnitude brighter than the Crab Nebula. The line-of-sight axes with the highest effective area differ by $\sim 3.5'$ between the XIS and HXD. As a result, either pointing axis may be chosen depending on the observation resulting in an approximately 10% increase in effective area for the corresponding detector.

Suzaku excels for studies of soft X-ray sources of low luminosity, observations simul-

taneously above and below 10 keV (i.e. X-ray reflection components) and rapid variability studies (down to a 10 ms timescale) due to decent timing resolution. However, for studies requiring high spatial and spectral resolution, satellites such as *Chandra* or *XMM-Newton* which offer arcsecond spatial resolution (energy resolution, $E/\Delta E \sim 1\,000$) would be more appropriate.

2.2.2 Chandra

The *Chandra* X-ray observatory (Weisskopf et al. 2000) was launched in July 1999 and is still operating today. At the time of launch, it was sensitive to X-ray sources up to 100 times fainter than all previous X-ray missions due to the high angular resolution of its mirrors and is currently sensitive to sources up to 10 times fainter than *XMM-Newton*. It was placed into a highly elliptical orbit to avoid spending time in the radiation belts around the Earth and so offers up to 48 hours (∼173 ks) of uninterrupted observing time. Its mirrors have a focal length of 10 m and are capable of focusing from 80–95% of the incident photon energy into a circle of $1''$. It also has an angular resolution of $0.5''$ but has a lower collecting area than *XMM-Newton*.

Chandra has two focal-plane instruments although only one may be used at any given time. These are the Advanced CCD Imaging Spectrometer (ACIS; Garmire et al. 2003) and the High Resolution Camera (HRC; Murray et al. 2000). The ACIS consists of the ACIS-S (an array of 6 CCDs used for spectroscopy) and the ACIS-I (an array of 4 CCDs used for imaging) and has an operating bandpass of 0.2–10 keV whereas the HRC has two microchannel plate components and is sensitive over the 0.1–10 keV energy range offering timing resolution of $\Delta t = 16\,\mu$s. The detectors are kept at a very low operating temperature (∼150 K) to reduce thermal noise and the incidence of pixel defects. The cameras may be operated independently, however, high-resolution spectroscopy can be obtained if one of two transmission gratings is swung into the optical path between the focusing mirrors and the detectors. These are the High Energy Transmission Grating Spectrometer (HETGS; sensitive from 0.4–10 keV; see Figure 2.4; Canizares et al. 2005) and the Low Energy Transmission Grating Spectrometer (LETGS; sensitive from 0.2–10 keV with the ACIS-S and with a FWHM reso-

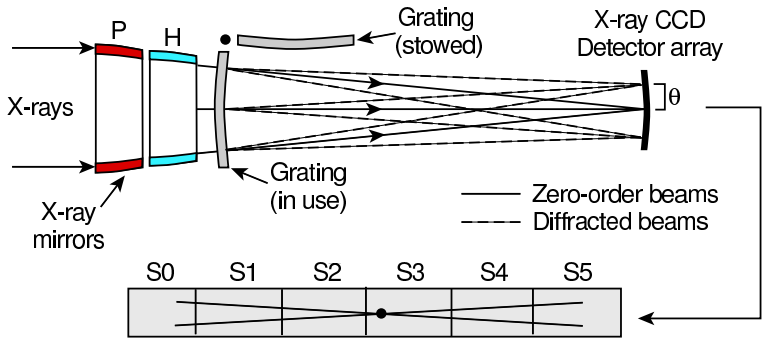

Figure 2.4: Schematic showing the HETG in the focal plane of the ACIS-S on-board *Chandra*. Figure taken from Canizares et al. (2005).

lution $\Delta\lambda \sim 0.05$ Å; Brinkman et al. 2000). The HETG consists of both the Medium Energy Grating (MEG) and the High Energy Grating (HEG). Diffraction gratings are components with periodic structures that split and diffract light, and thus X-rays will undergo diffraction according to their wavelength. The energy of the diffracted photons are then measured by their displacement from the zero-order image and the flux at a given energy is determined by summing the counts in rectangular regions of width equal to the energy resolution in the dispersion direction and height equal to the spatial resolution in the cross-dispersion direction. The resolution of each grating is approximately constant in wavelength with FWHM of $\Delta\lambda \sim 0.023$ Å and $\Delta\lambda \sim 0.012$ Å for the MEG and HEG respectively. Since these are sensitive over the 0.4–5 keV and 0.4–10 keV energy ranges respectively, this corresponds to $E/\Delta E$ ranging from 100 - 1 300 for each grating (e.g. for the HEG, $\lambda/\Delta\lambda \sim 1\,000$ at 1 keV). The effective areas (combined ± 1 orders) of the MEG and the HEG are shown in Figure 2.3.

Chandra excels for X-ray imaging studies and observations with very high spectral and spatial resolution. However, it cannot provide any measurement of hard X-rays and so *Suzaku* would be more appropriate for studies where photons both above and below ∼10 keV are of interest.

2.2.3 XMM-Newton

XMM-Newton (*X-ray Multi-Mirror Mission - Newton*; Jansen et al. 2001) was launched by the European Space Agency (ESA) in December 1999 and was designed to perform high quality X-ray spectroscopy. It was placed in an elliptical orbit at an angle of 40° and with an orbital period of ∼48 hours. The satellite consists of three different mirror systems with a combined collecting area of 4 300 cm^2, each of which has its own detector(s). One system contains the European Photon Imaging Camera (EPIC-pn; Strüder et al. 2001) and the other two have the Reflection Grating Spectrometers (den Herder et al. 2001) behind them although it is possible to focus the X-rays onto the two EPIC MOS (metal-oxide semiconductor; Turner et al. 2001) cameras. The difference between the EPIC-pn and the EPIC MOS cameras is that they use different technologies to collect and store charge clouds and the fundamental difference between the reflection gratings used on-board *XMM-Newton* and the transmission gratings used on-board *Chandra* is that with reflection gratings the diffracted (i.e filtered) beam is on the same side of the grating as the incident beam whereas with transmission gratings the incident and diffracted beams are on different sides of the grating. *XMM-Newton* also has a co-aligned UV-optical telescope (OM; Mason et al. 2001) with a diameter of 12" which is capable of acquiring images.

The RGS on-board *XMM-Newton* deflects about half of the incident X-ray light and is sensitive at energies $\lesssim$ 2.5 keV down to ∼0.3 keV with an effective area which peaks at about 150 cm^2 (at ∼0.83 keV; see Figure 2.3) and high resolving power ($E/\Delta E$ =150–800). The remaining undeflected light passes straight through to be detected by the EPIC MOS camera(s) in the focal plane. The EPIC-pn and EPIC MOS cameras are cooled to ∼180 K and ∼140 K respectively to increase sensitivity (and to keep pixel defects to a minimum) and are active in the 0.2–12 keV energy range. They operate in a photon-counting mode although different read-out strategies can be used in the case of bright sources to improve timing capabilities and reduce pileup. These modes range from "full-frame mode" (FOV = 376 × 384 pixels) to "large window" (FOV = 198 × 384 pixels) and "small window" (FOV = 63 × 64 pixels) modes plus additional timing modes.

Although *XMM-Newton* has a lower spatial resolution than *Chandra*, the satellite has a

Mission	Instrument	Peak Effective Area (cm^2)	Resolving Power ($E/\Delta E$)	Bandpass (keV)
Suzaku	XIS (FI)	400	46 @ 6 keV	0.4–12
	XIS (BI)	400	46 @ 6 keV	0.2–12
	HXD PIN	160	4 @ 17 keV	10–70
Chandra	MEG/ACIS-S	145	540 @ 1 keV	0.4–5
	HEG/ACIS-S	67	1 000 @ 1 keV	0.8–10
XMM-Newton	EPIC-pn	1 300	46 @ 6 keV	0.2–12
	RGS	120	750 @ 1 keV	0.35–2.5
BeppoSAX	LECS	60	31 @ 1 keV	0.1–4
	MECS	150	12.5 @ 6 keV	1.3–10
	PDS	600	7 @ 60 keV	15–300
Swift	BAT	1 400	18 @ 60 keV	14–195

Table 2.1: Comparison of X-ray instruments of primary interest in this thesis.

larger collecting area, a higher effective area in the Fe K band and a slightly superior spectral resolution than the ACIS. However, it is not sensitive to hard X-ray emission at energies $\gtrsim 10$ keV.

2.2.4 Other Satellites

Data from the following satellites have been used alongside data from the three major satellites described above:

- *Swift*: The *Swift* Gamma-Ray Burst Mission was launched in November 2004 and is managed by the NASA GSFC. It is a multi-wavelength observatory, operating in the gamma-ray, X-ray, UV and optical wavebands, and was primarily designed to study gamma-ray bursts and their afterglows. It has an orbital height of 600 km and an orbital period of ∼90 minutes. In the X-ray band, *Swift* has an on-board X-Ray Telescope (XRT; Burrows et al. 2000) which is sensitive from 0.2–10 keV and uses 12 nested mirrors to focus X-rays onto a single MOS CCD. At higher energies, *Swift* also has the Burst Alert Telescope (BAT; Barthelmy et al. 2005) which continuously scans

the sky with its two-steradian FOV watching for gamma-ray bursts and pointing at specific targets. The BAT uses CZT detector tiles and is sensitive from 14–195 keV with an on-axis effective area of $\sim$1 400 cm^2 at 60 keV. It is gradually building up the most sensitive survey of the sky in this hard X-ray band which, to date, has resulted in an online catalog of 1 092 sources based on the first 58 months of the mission sensitive down to the *Suzaku* XRT resolution; a flux of 1.48×10^{-11} erg cm^{-2} s^{-1} in the 14–195 keV energy range over 90% of the sky (Baumgartner et al. 2010).

- *BeppoSAX*: *BeppoSAX* was an Italian-Dutch satellite (Boella et al. 1997a) which was launched into orbit in April 1996 at a height of 600 km and with an orbital period of 96 minutes. It was capable of simultaneously observing over a large energy range from 0.1–300 keV. Five science instruments were flown on-board *BeppoSAX*: the Low and Medium Energy Concentrator Spectrometers (LECS and MECS respectively; Parmar et al. 1997; Boella et al. 1997b) which utilised gas scintillation proportional counters operating from 0.1–4 and 1.3–10 keV respectively; the High Pressure Gas Scintillation Proportional Counter (HPGSPC; Manzo et al. 1997) which was sensitive to photons with energies up to 120 keV; the Phoswich Detector System (PDS; Frontera et al. 1997), which used a crystal scintillator to detect photons up to 300 keV in energy and had a low background rate (due to the low inclination of the spacecraft orbit) but modest spectral resolution, and the Wide Field Camera (WFC; Jager et al. 1997), which consisted of two cameras operating from 2–30 keV, each with a large FOV of $40^\circ \times 40^\circ$. Scientific observations were made for 8 years until April 2002. *BeppoSAX* re-entered the Earth's atmosphere in April 2003[3].

2.3 Data Reduction

Whereas instruments designed to operate at longer wavelengths measure integrated fluxes, X-ray detectors work by collecting individual photons. This is because X-ray photons have

[3]http://www.asdc.asi.it/bepposax/reentry/

relatively high energies which makes them easier to detect and they often have relatively low fluxes making them easier to count. When an observation has been concluded, the raw data are stored in an event file which is usually in FITS (Flexible Image Transport System) format. The event file usually stores the list of detected events, each of which has various attributes (arrival time, position on the detector, etc). Since the raw data are unsuitable for scientific analysis, they must be screened according to various criteria. This can involve the following considerations (and more):

- *Event grade*: In the case of CCDs, when the charge of a pixel exceeds a given threshold, this is defined as an "event". The charges in the surrounding 3×3 or 5×5 pixel region are also recorded and, according to the morphology of this pattern, each event is assigned a "grade" (or a "pattern" in the case of *XMM-Newton*). The grade is determined by which of these surrounding pixels have an induced charge above a given value and this varies according to the type of event. For example, in the case of the *Chandra* ACIS grade system, a grade 0 event is also known as a single-pixel event and occurs when only the charge of one pixel exceeds the given threshold. This type of event has the best energy resolution. A grade 255 event, however, occurs when the charges in all nine pixels in the 3×3 grid surrounding the central pixel exceed the given threshold. Such events are often filtered out of the data as they almost certainly correspond to a particle impact as opposed to an X-ray photon.

- *Pileup*: Pileup may occur when two or more photons hit the same or adjacent CCD pixels within a single frame. They cannot be distinguished and, as a result, may look like a single event with a higher energy and possibly a more complex pixel pattern. The event may then either be rejected due to its grade or the two photons will appear as a single event with a combined energy. In the case of bright sources where pileup may be an issue, the resultant spectrum might appear to have a reduced flux at lower energies and an increased flux at higher energies as lower energy photons either are rejected or have their energies combined. The effect of pileup can be reduced by planning an observation accordingly; e.g. by using a smaller window (section) of the CCD and requesting a faster read-out time. Alternatively, the spectroscopic

effects can be minimised by modelling the effects during the spectral analysis (Davis 2001) or choosing events only from the wings of the point response during the data reduction procedure. Pile-up will be more severe in cases where the point-spread function (PSF) is small, such as with the *Chandra* ACIS instrument ($\sim 0.5''$).

- *Cut-off rigidity*: This is a measure of how the Earth's magnetosphere shields the spacecraft from high-energy particles. Therefore, charged particles can only be detected by an instrument if their rigidity (i.e. momentum per unit charge) exceeds that of the specified cut-off.

- *South-Atlantic Anomaly*: The South-Atlantic Anomaly (SAA) is a region of the Earth's atmosphere above the South Atlantic where the Earth's inner Van Allen radiation belt comes closest to the Earth's surface. This region has an intense flux of energetic particles which are capable of damaging certain instruments. Such instruments are often turned off during the spacecraft's passage through the SAA. Furthermore, the particle bombardment may generate short-lived radioactive particles which may also become detected as they decay. Therefore, it may be important to also consider rejecting data acquired within a given time frame since the last passage through the SAA. The SAA primarily affects satellites in low-Earth orbits and so is relevant to the XIS and HXD detectors on-board *Suzaku* and the BAT instrument on-board *Swift*.

- *Pointing direction angles*: Various considerations should be made regarding data acquired during times when the spacecraft had a particular pointing direction. For example, the angle between the pointing direction and the Earth's limb should be considered since the Earth's extended atmosphere is capable of absorbing low-energy X-rays. The angle between the pointing direction and the Earth's day-night terminator (or "twilight zone") should also be considered since X-rays from the area of the Earth which is sunlit may be visible due to scattering and fluorescence of solar emission in the atmosphere. Furthermore, the angle between the pointing direction and the Sun is also important because solar X-rays may scatter into the detector at

small angles.

- *Hot spots and flickering pixels*: Detectors may suffer from electronic hotspots which produce apparent signals at times when there are no detected events. Events from these regions can sometimes be excluded on-board the spacecraft or filtered out during the data processing. However, CCDs may suffer from the sporadic problem of flickering pixels; a problem which is sensitive to the running temperature of the instrument. Often, missions have pixel sizes that are much smaller than the instrument's point response (e.g. the XIS + XRT on-board *Suzaku*) and so hot / flickering pixels can be identified by comparing their brightness to that of surrounding pixels. Alternatively, in some cases such as *Chandra*, the instruments operate at a cold enough temperature for this to not be a problem.

Events of interest may then be selected according to various criteria. For example, events may be filtered according to region (if the instrument offers spatial resolution; e.g. the XIS on-board *Suzaku*), time interval, intensity (i.e. by extracting events when the source or background count rate surpassed a specified threshold) and spectral channel (e.g. if a specific energy band is of scientific interest or to filter out less efficient channels at the extreme ends of the bandpass so as to improve signal-to-noise).

Such subsidiary products are then extracted from the events file. When using non-dispersive spectrometers, such as CCDs, charge is accumulated for each X-ray that is detected. This is known as the pulse-height amplitude (PHA). For CCDs, the total event charge is stored in a vector which sums all the charges in the 3×3 or 5×5 surrounding pixels above the given threshold value when calculating the grade. The relationship between the PHA and the energy of a photon may not be linear as it is sensitive to time and detector position. When this variability is corrected, it is stored as a PI (PHA invariant) file. Converting this to energy is then the job of the response matrix, as described in Section 2.4.

For dispersive spectrometers, such as diffraction gratings, the wavelength is determined from the distance in the dispersion direction between the zeroth-order (the un-dispersed position of the source) and the position of the photon. The potential overlap between different diffraction orders may then be accounted for by the detector's own energy resolution (such as

that provided by *Chandra*'s ACIS). The dispersion distance and PI may then be plotted two-dimensionally where each order of the grating lies along a different curve allowing different orders and the background to be separated.

The spectrum will then be generated from the PI column and the background will generally be extracted from a same-sized region but from an area on the chip away from the source and usually away from any calibration edges. Finally, the spectrum should be binned so as to increase signal-to-noise and perhaps to allow for Gaussian errors to be approximated (see Section 2.4.1.1).

2.4 Spectral Fitting and Statistics

Instruments such as the XIS on-board *Suzaku* and the EPIC-pn on-board *XMM-Newton* acquire data via non-dispersive spectrometers. However, what is obtained is actually photon counts per instrument channel (i.e. voltage / pulse height) as opposed to the actual spectrum. The relationship between the source and the observed counts can be described by:

$$C(I) = T \int f(E) R(I, E) dE, \tag{2.1}$$

where $C(I)$ is the observed count rate in channel I, T is the duration of the observation in seconds, $f(E)$ is the source flux in units photons $\mathrm{cm}^{-2}\,\mathrm{s}^{-1}\,\mathrm{keV}^{-1}$ (this may also include the background emission) and $R(I, E)$ is instrumental response function. The detector response is often split up into two components: a unitless matrix (the response matrix file; RMF) and a vector (the ancillary response file; ARF) with units of cm^2. The RMF gives the probability that a photon of given energy will end up as a count in a particular spectral bin. This arises because real detectors always have some degree of spread in their response and so there is always some chance of a photon of energy E ending up as a count in channel $I - 1$, I or $I + 1$ and so on. The ARF uses the energy-dependent effective area curve to specify the quantum efficiency of the telescope-detector system as an energy-dependent function (it is in fact the product of the quantum efficiency and the effective area of the telescope as a function of energy). Therefore, the observed count spectrum arises from the convolution of

the actual source (plus background) spectrum with the overall response of the detector. Such an equation resists any easy solution to obtain the source spectrum and so a forward-fitting procedure must be undertaken.

Firstly, a possible model spectrum is specified based on the physics of the source. This could be as simple as a power law or something more complicated built up of several components that one might expect to be present. The spectrum is then convolved with the total response of the detector (as in equation 2.1) and compared to the observed counts spectrum. The goodness-of-fit of this model is determined by some statistical measure. Then, the parameters of the original model are varied and the fit statistic is re-calculated. This iterative process is repeated until the best value of the fit statistic is obtained. If this value is unacceptable, then the model may be rejected or modified and even if the fit statistic is acceptable, the final best-fitting parameters of the model should be considered to determine whether the model is physically appropriate.

Many spectroscopic models are available for X-ray analysis and can be combined in various ways. Some emission models are simply additive in nature, such as power laws and blackbody spectra, and some are multiplicative (e.g. absorption) and adjust the model by energy-dependent factors. Components can also be convolved, perhaps to create a smoothing effect with some function, such as velocity broadening, or to relativistically blur a component such as ionised Compton reflection from the inner regions of the accretion disc.

One potential issue to be aware of with a forward-fitting approach is that of local minima. Since the fit statistic is quantified by the difference between the specified model and the observed data, most fitting methods change the model parameters at each iterative step by using information local to the current parameters (for example, by calculating the derivatives of the statistic with respect to the parameters at their current values) and then moving 'downhill'. However, depending on where the fit process was started, it is possible that the fit may get trapped in a local minimum instead of finding the global minimum. This problem can be amplified by more complicated models where parameters are highly correlated. It is therefore important to undertake the fitting process at different starting points and to thoroughly examine all information when estimating confidence regions as this can provide clues if the fit is stuck in a local minimum.

2.4.1 Statistics

When analysing X-ray observations, statistics are an essential part of evaluating and interpreting the data. When performing a parameterised, forward-fitting approach, the goal is to find and evaluate a model that best describes the data and this involves parameter estimation, calculating confidence limits to determine how well the data are constrained and testing various hypotheses to quantitatively determine how well the model describes the data.

2.4.1.1 Probability Distributions & Fit Statistics

In X-ray astronomy, the two most widely used probability distributions are the Gaussian and Poisson distributions, which describe the fraction of a certain type of event happening given a large number of identical trials. Supposing that the X-ray data are independent and drawn from one of these probability distributions, a model described by various parameters can be used to calculate a predicted count rate, M_i, for each data point. Then, the function that describes the probability that the ith data point has a value X_i given a predicted value of M_i from the defined model is known as the likelihood function. The focus of such analysis is to find the model parameters that maximise this probability (i.e. find the maximum-likelihood function). In the case of Gaussian and Poisson statistics, the likelihood functions are given by the χ^2 and C statistics respectively.

Gaussian Distribution and the χ^2 Statistic

Some detectors generate data that varies with a Gaussian form with an independent standard deviation. The Gaussian (or normal) distribution is described by:

$$N(n;\nu,\sigma) = \frac{1}{\sigma\sqrt{2\pi}}\exp\left[\frac{-(n-\nu)^2}{2\sigma^2}\right], \tag{2.2}$$

where N is the probability of n events occurring given a mean, ν and a variance, σ^2. If ν is the count rate, then N would describe the probability of receiving n photons in an exposure time, t. The Gaussian distribution is appropriate if the number of counts per bin is large enough; usually around $n \sim 25$ (the Poisson distribution is well approximated by the

Gaussian distribution at high count rates). Therefore, for Gaussian statistics to be applied, one should take care to bin the data such that no bin has $n \lesssim 25$. The most common fit statistic applied to Gaussian data is given by:

$$S^2 = \sum_i^N \frac{(X_i - M_i)^2}{\sigma_i^2} \tag{2.3}$$

and is commonly referred to as χ^2. In equation 2.3, σ_i is the error for channel i and is usually estimated by $\sqrt{X_i}$. One major advantage of this statistic is that it provides a useful "goodness-of-fit" test (see Section 2.4.1.4). However, it should be noted that it should not be used with Poisson data since this can lead to biased results (see below).

Poisson Distribution and the C Statistic

Another common probability distribution in X-ray astronomy is the Poisson distribution which is more appropriate when n is small. This distribution is driven by counting statistics and is applicable in cases where the only source of noise is due to the number of events arriving at the detector. The Poisson distribution is given by:

$$P(n;\nu) = \frac{e^{-\nu}\nu^n}{n!}, \tag{2.4}$$

where $P(n;\nu)$ is the probability of n events give a mean, ν. The most commonly used maximum-likelihood function for Poisson statistics is the C statistic (Cash 1979):

$$C = 2\sum_i^N (M_i - X_i \ln M_i). \tag{2.5}$$

It is important to use the C statistic when dealing with weak sources with low count rates or high-resolution (grating) spectra with many resolution channels. This is because during the statistic calculation, many bins may have very few or even zero counts. In the case of the χ^2 fit statistic, the presence of σ_i^2 in the denominator (where σ_i^2 is estimated by X_i) leads to bins with $X_i < M_i$ becoming weighted more heavily than bins with $X_i > M_i$. This can result in the model being driven lower than the data but with an anomalously low fit statistic. Such biases can be greatly reduced by using the most appropriate fit statistic.

It should be noted, however, that since the magnitude of the C statistic is dependent upon the number of bins considered and the values of the data themselves, one disadvantage is that no simple goodness-of-fit measure can be computed. One solution to this problem would be to perform Monte Carlo simulations.

Alternatively, and in practice, the maximum-likelihood statistic used here within XSPEC (see Section 2.5) is given by:

$$C = 2\sum_{i}^{N}(M_i - X_i + X_i(\ln X_i - \ln(M_i)). \tag{2.6}$$

This statistic asymptotically approaches S^2 (equation 2.3) in the limit of large counts[4]. However, this statistic cannot be used in all cases since it only works on spectra which have not been background-subtracted.

2.4.1.2 Assessing the Reality of Model Components

When performing a spectral fitting procedure, of key importance is to quantitatively assess the reality of individual model components in order to justify their inclusion or requirement in the overall model. This is done using a chosen fit statistic appropriate for the distribution of the data being considered (e.g. χ^2) and is particularly important when considering components such as additive emission lines which may interact with one another when the fitting algorithm is run. As a result, the overall significance of a component is judged with respect to a fit that includes all other possible components. This is done by removing the component from the full model containing all other components, re-fitting and assessing the change in χ^2. The confidence level of the requirement for this component is then determined by the change in χ^2 while considering the number of parameters of interest.

2.4.1.3 Confidence Bounds

As well as measuring the best-fitting parameters of a given model, it is also important to determine how well the parameters are constrained. This level of constraint can depend on

[4]https://heasarc.gsfc.nasa.gov/xanadu/xspec/manual/XSappendixStatistics.html

various factors including the quality of the data and the degree of degeneracy between model parameters. The most popular method is to calculate a confidence bound which, for example, may state that there is a 90% probability that the true value of a parameter lies between x and y. What this actually means it that if the observation was to be made n times then the best-fitting value would lie between x and y 90% of the time. This is generally done by varying the parameter value of interest to find the point at which the fit statistic differs from the best-fitting value by a critical amount. This critical value, $\Delta\chi^2$, depends upon the confidence level that one requires and the number of parameters of interest being varied. For example, to determine the 90% confidence region for a single parameter, this would have a critical value of $\Delta\chi^2 = 2.71$ (Avni 1976). The same approximation also asymptotically holds for the C statistic (Cash 1979). It should be noted that Markov Chain Monte Carlo (MCMC) simulations are also widely used for determining confidence regions (e.g. Wilks, Richardson & Spiegelhalter 1996; van Dyk et al. 2001).

2.4.1.4 Hypothesis Testing & the Goodness-of-Fit Test

It is not sufficient to just measure the best-fitting parameters of a given model since there may be other models which fit the data just as well or even better. Hypothesis testing is used to help resolve this. Two hypotheses are put forward: the first one is the *null hypothesis*, H_0, which is initially accepted; the second is the *alternative hypothesis*, H_1, which is the hypothesis that one attempts to prove. Two types of error can result from a hypothesis test: a false positive occurs when the null hypothesis is rejected when it is really true (a type-I error); a false negative occurs when the null hypothesis is accepted when it is really false (a type-II error). Since it is not possible to simultaneously minimise both types of error, the most common approach is to limit the probability of a type-I error occurring to below a given level of significance, α. One can then determine the probability with which H_0 can correctly be rejected. Once a significance level has been chosen (e.g. 5%), a chosen test statistic can be calculated for the observed data which, in turn, allows the probability of such a test statistic value being observed (i.e. the p-value) to be inferred. Then, if $p < \alpha$, H_0 can be rejected.

The χ^2 goodness-of-fit test is the most common test statistic applied in X-ray astronomy

and is used to quantitatively assess the degree of confidence that one can have that the observed data could be produced by the best-fitting model. This is given by:

$$\chi^2 = \sum_i^N \frac{(X_i - M_i)^2}{M_i} \tag{2.7}$$

and was first determined by Pearson (1900). By comparing the model to the observed data, the test statistic can be trivially calculated and the p-value can be inferred using the χ^2 distribution. A simple method of estimating the goodness-of-fit is to calculate the so-called "reduced χ^2" value, which is given by $\chi^2/d.o.f.$, where $d.o.f.$ is the number of degrees of freedom (i.e. the number of data bins − the number of free parameters). As a general rule, $\chi^2/d.o.f.$ should be approximately 1. If the reduced χ^2 value is much greater than 1 then the model is not a good fit to the data. Conversely, if the value is much less than 1 then this suggests that the errors have been over-estimated. Within XSPEC (see Section 2.5), the null hypothesis probability is also calculated which takes into account the χ^2 value and the number of degrees of freedom and calculates the probability of the observed data being drawn from the given model assuming that the specified model is correct. Of course, even if the model passes the goodness-of-fit test, it does not mean that it is the only acceptable model. Often, other models will be found to be equally as acceptable and it is in these cases where it becomes a matter of scientific judgement.

It should be noted that no such simple goodness-of-fit test applies to data that follow the Poisson distribution. While the maximum-likelihood approach mentioned in Section 2.4.1.1 approximates to χ^2 when the count rate is high, a better approach would be to simulate the data many times based upon the model and its best-fitting parameters and then determine the percentage of observations for which the fit statistic is less than that for the observed data. If the majority of simulations return a fit statistic that is less than the observed value then one may assume that the model is incorrect.

2.5 Software

Data reduction for major missions such as *Suzaku*, *XMM-Newton* and *Chandra* can largely be performed by various mission-dependent and mission-independent software packages and tools. The *HEA*SOFT[5] package (also known as FTOOLS, provided by the HEASARC[6]; NASA's High Energy Astrophysics and Science Archive Research Center), is a collection of programs and scripts for calibration and data analysis as written by various instrument teams and contains the complete set of mission-dependent tools for satellites such as *Suzaku* and *Swift* plus a suite of mission-independent programs for use with all X-ray satellites. So it can also be useful for analysing data from *Chandra* and *XMM-Newton*. However, the standard software packages for use with these two satellites are CIAO[7] (Chandra Interactive Analysis of Observations; Fruscione et al. 2006) and the SAS[8] (Scientific Analysis System) respectively. These software suites contain all the relevant mission-dependent tools and are supported by extensive online documentation. In the case of *Suzaku*, most data screening is performed within XSELECT, a program within HEASOFT used for data analysis purposes. It allows data from the raw event files to be extracted into images, spectra and lightcurves ready for analysis by the input of simple shell commands. Filters can also be applied to select data according to user-defined times, energy bands or fluxes.

Regarding spectral analysis, a number of programs exist which are capable of applying theoretical models to X-ray spectra, performing complex fitting algorithms, calculating appropriate statistical tests and accounting for low count rates and the response of satellite instruments. The most widely used of these programs is XSPEC[9] (Arnaud 1996), also from the HEASARC. XSPEC is a flexible, command-driven X-ray spectral fitting package designed for use with any spectrometer and contains an extensive library of theoretical models to apply to X-ray data with the added capability of allowing users to easily incorporate additional local models.

[5]http://heasarc.gsfc.nasa.gov/docs/software/lheasoft
[6]http://heasarc.gsfc.nasa.gov
[7]http://cxc.harvard.edu/ciao
[8]http://xmm.esac.esa.int/external/xmm_user_support/documentation/sas-usg/USG
[9]http://xspec.gsfc.nasa.gov

When processing data and creating response files, it is also always important to ensure that the most up-to-date calibration files are used. This is because the calibration data may vary in time due to instrumental changes and improvements in the understanding of how the instruments work. Usually, the variations are subtle and not significant enough to affect spectral results. However, any time-dependent changes in the calibration (such as variations in the effective area or the energy redistribution) are corrected for by using time-dependent response matrices generated with the calibration data relevant to the epoch of a particular observation. So, for instance, multiple spectra of the same AGN acquired at different times can be compared since the response matrices used allow for any changes or discrepancies in the calibration of the instrument(s) / telescope.

The HEASARC's calibration database (CALDB)[10] consists of a file structure with a directory for each mission and can be set up locally or accessed remotely. This can be used for all X-ray missions except for *XMM-Newton* which instead uses a database entitled The Current Calibration File (CCF)[11]. The calibration databases store all the vital calibration data that are required during standard data reduction techniques including all information about the detectors which is important when creating instrumental response files in order to proceed with spectral analysis for a given observation.

2.5.1 XSPEC Models

This section briefly describes some of the spectral fitting models made use of in this thesis (see Figures 2.5 and 2.6 for example plots):

- DISKLINE: This is an additive emission-line component arising from a relativistic accretion disc around a Schwarzschild black hole (Fabian et al. 1989). The model primarily takes into account transverse Doppler shifts and gravitational redshift. The shape of the line is dependent upon the centroid energy, $E_{\rm c}$, in units of keV, the inner ($r_{\rm in}$) and outer ($r_{\rm out}$) radii of the emission annulus in units of GM/c^2 (i.e. $r_{\rm g}$), the

[10] http://heasarc.gsfc.nasa.gov/docs/heasarc/caldb
[11] http://xmm.vilspa.esa.es/external/xmm_sw_cal/calib

inclination angle to the observer's sightline (from a face-on view of the disc) in units of degrees, the power-law dependence of emissivity, q, which scales as r^{-q} and the normalisation in units of photons $\mathrm{cm}^{-2}\,\mathrm{s}^{-1}$. The inner radius cannot be set smaller than $6\,r_{\mathrm{g}}$, the smallest radius of the ISCO in the Schwarzschild metric. To describe the effects in a Kerr geometry (i.e. surrounding a rotating black hole), the LAOR model should instead be used (Laor 1991).

- PEXRAV: The reflected continuum spectrum from an exponentially-cut-off power-law spectrum incident on a semi-infinite slab of neutral material (Magdziarz & Zdziarski 1995). The observed spectrum contains the Compton-scattered component and Fe K absorption edge and is a function of the incident power-law index, Γ, the cut-off energy of the power law, E_{cut}, in units of keV, the inclination angle to the observer's sightline in units of degrees, the redshift of the source, z, the normalisation (photon flux at 1 keV in units of photons $\mathrm{cm}^{-2}\,\mathrm{s}^{-1}\,\mathrm{keV}^{-1}$) and the reflection scaling factor, R, where $R = 0$ implies that there is no reflected component and $R = 1$ would correspond to reflection from neutral material subtending 2π sr to the source. H and He atoms are assumed to be fully ionised and the abundances of elements heavier than He are variable relative to the solar values of whichever set of abundances has been defined within XSPEC.

- REFLIONX: An additive component consisting of the reflected spectrum from ionised material calculated from 1 eV to 1 MeV (Ross & Fabian 2005). It consists of the emergent spectrum when a power law irradiates a photo-ionised, optically-thick slab of gas. The model assumes a high-energy exponential cut-off, $E_{\mathrm{cut}} = 300$ keV, and uses the abundances of Anders & Ebihara (1982). The advantage of the REFLIONX model is that it self-consistently models both the reflected continuum and line emission for the following astrophysically abundant ions (plus additional fully-ionised species): C III-VI, N III-VII, O III-VIII, Ne III-X, Mg III-XII, Si IV-XIV, S IV-XVI and Fe VI-XXVI. The model parameters are the photon index, Γ, of the illuminating power law, the ionisation parameter, ξ, of the reflecting material in units of erg cm s^{-1}, the redshift, z, the abundance of Fe relative to the solar value and the normalisation of the

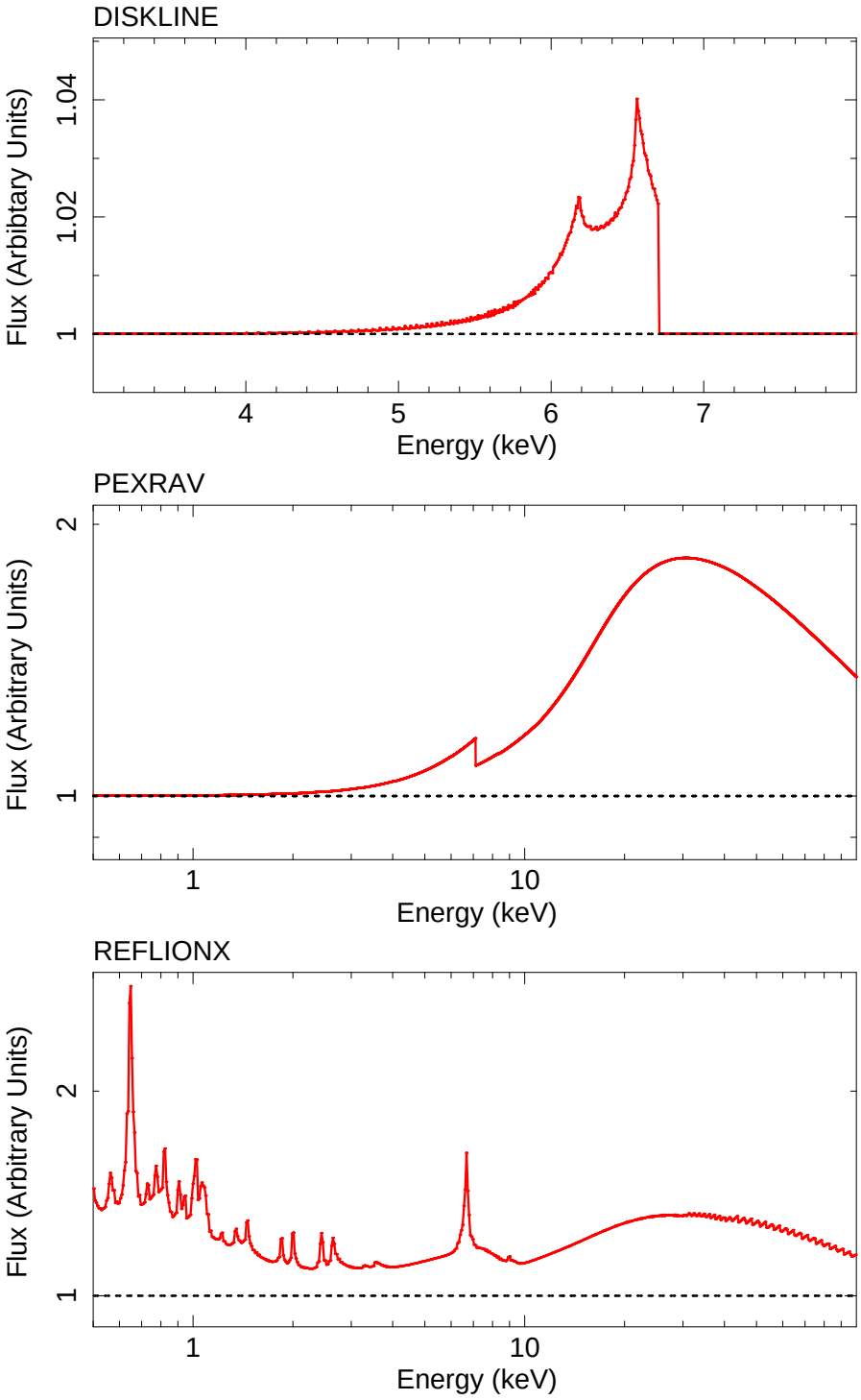

Figure 2.5: Examples of spectral models relevant to this work. All models are additional components to a flat power law (black) of photon index $\Gamma = 2$. The shape of the additional model component is shown in red. Upper panel: The DISKLINE model of Fabian et al. (1989) simulated with $E_{\rm c} = 6.4\,{\rm keV}$, $r_{\rm in} = 6\,r_{\rm g}$, $r_{\rm out} = 300\,r_{\rm g}$, inclination $= 30°$ and $q = 2$. Middle panel: The PEXRAV model of Magdziarz & Zdziarski (1995) simulated with $\Gamma = 2$, $E_{\rm cut} = 300\,{\rm keV}$, inclination $= 30°$, $R = 1$ and solar abundances. Lower panel: The REFLIONX model of Ross & Fabian (2005) simulated with $\Gamma = 2$, $\xi = 300\,{\rm erg\,cm\,s^{-1}}$ and solar abundances. See Section 2.5.1 for model parameter details.

reflected spectrum.

- XSTAR: A code for calculating the physical conditions of a photoionised gas (Kallman & Bautista 2001; Kallman et al. 2004). It assumes a spherical shell of gas surrounding a central point-source of ionising radiation. The user assumes the shape and strength of the incident continuum on the shell along with the pressure or density of the gas, its turbulent velocity, $v_{\rm turb}$, assuming Gaussian broadening (in units of $\rm km\,s^{-1}$) and the abundances of elements within the gas itself. The code then computes the effects of the defined ionising continuum on this gas and calculates the re-radiated spectra. As such, it self-consistently models zones of emission or absorption including treatment of lines and continua with the following free parameters for the gas: column density, $N_{\rm H}$, in units of $\rm cm^{-2}$, ionisation parameter, ξ (equation 1.13), in units of $\rm erg\,cm\,s^{-1}$ and redshift, z (which may be used to infer velocity shifts). The default abundances are those of Grevesse, Noels & Sauval (1996).

2.6 NGC 7213 and NGC 4051 Data Reduction

This section describes the data reduction procedures for the *Suzaku* and *Chandra* observations of NGC 7213 (Section 3.1) and NGC 4051 (Section 4.1) which are analysed in detail in Chapters 3–5.

NGC 7213 is located at a redshift of $z = 0.005839$ with equatorial coordinates $R.A. = 22\,\rm h\,09\,m\,16.3\,s$ and $DEC. = -47\,\rm d\,10\,m\,00\,s$ and NGC 4051 is located at a redshift of $z = 0.002336$ with equatorial coordinates $R.A. = 12\,\rm h\,03\,m\,09.6\,s$ and $DEC. = +44\,\rm d\,31\,m\,53\,s$. The data reduction procedures for a 2006 *Suzaku* observation of NGC 7213 plus recent *Suzaku* and *Chandra* HETG observations of NGC 4051 are described below.

2.6.1 Suzaku Analysis

NGC 7213 was observed by *Suzaku* (see Section 2.2.1) in October 2006 with a net exposure of $\sim$90 ks (see Table 2.2). Here, data acquired with the four XIS (Koyama et al. 2007) CCDs

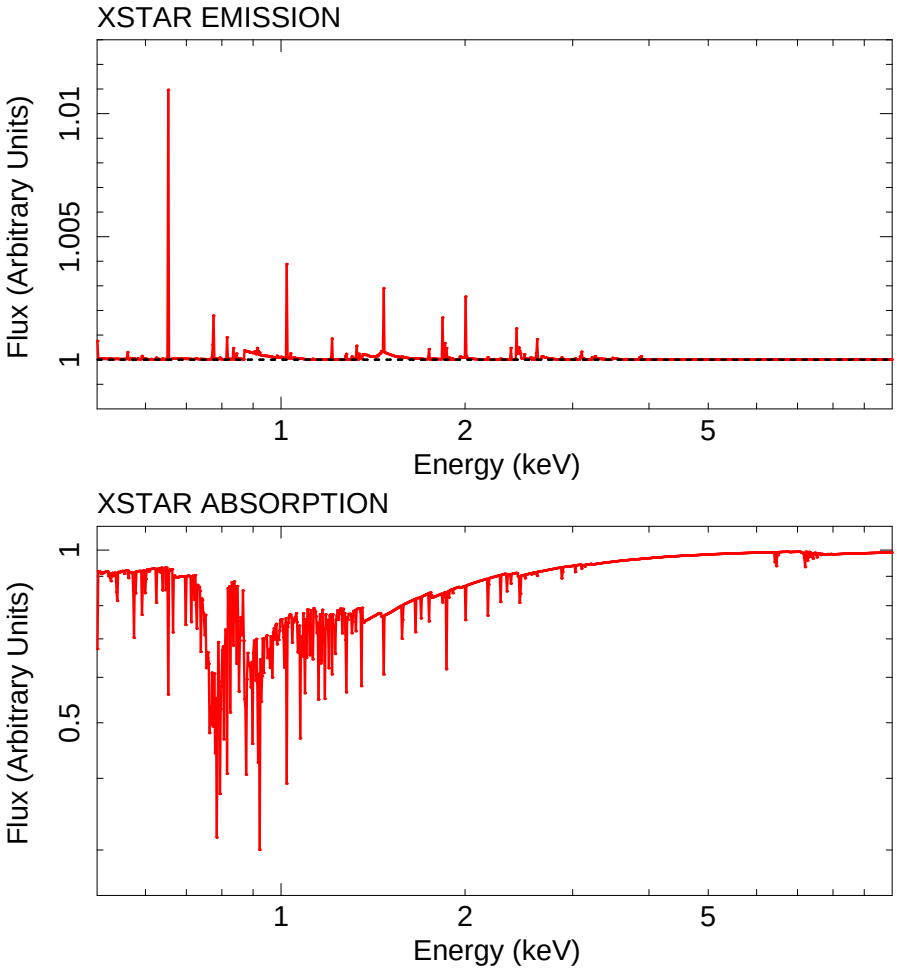

Figure 2.6: Examples of emission and absorption spectra from photoionised gas using the XSTAR code. Both spectra show the affect of a single zone on a power-law continuum of photon index $\Gamma = 2$. The upper and lower panels show zones of emission and absorption respectively. Both zones are simulated with $N_{\rm H} = 1 \times 10^{22}\,{\rm cm}^{-2}$, $\log \xi = 2$ and $v_{\rm turb} = 200\,{\rm km\,s}^{-1}$. See Section 2.5.1 for model parameter details.

and the PIN silicon diodes of the HXD (Takahashi et al. 2007) are discussed using events files from version 2.2.11.22 of the *Suzaku* pipeline processing. NGC 4051 was observed with *Suzaku* in November 2005 and again in November 2008 with respective net exposure times of 120 and 350 ks[12] (see Table 2.2 for an observation log). The 2005 data have been described previously by Terashima et al. (2009). Here, data taken with the *Suzaku* XIS (Koyama et al. 2007) instruments will be discussed along with the silicon PIN diodes of the non-imaging HXD (Takahashi et al. 2007). Events files from versions 2.2.11.22 of the *Suzaku* pipeline processing were used for all NGC 4051 observations and all data were reduced using HEASOFT version 6.4.1. Note that both sources are too faint to be detected with the HXD GSO instrument.

All data were screened within XSELECT to exclude periods when the spacecraft passed through the South Atlantic Anomaly plus the following 500 s of such a passage. Data acquired with Earth elevation angles (ELV) $< 10^{\circ}$ and Earth day-time elevation angles (DYE_ELV) $< 20^{\circ}$ were also excluded. A cut-off rigidity (COR) criterion of >6 GeV/c for the XIS was applied. Only good events with grades $0, 2, 3, 4$ and 6 were used, while hot and flickering pixels were removed from the XIS images using the CLEANSIS script. Time intervals affected by telemetry saturation (when the number of events detected in a single frame exceeds a threshold such that the instrument's ability to process the information is compromised) were also removed.

2.6.1.1 Suzaku XIS Data Reduction

Source spectra from the XIS CCDs were extracted from circular regions of $2.3'$ and $2.9'$ radii centered on the source for NGC 7213 and NGC 4051 respectively. In principle, an extraction radius of $4.3'$ should encircle 99% of the point-source flux. However, recent calibration releases allow radii as small as $1'$ to be used[13]. The extraction radii of $2.3'$ and $2.9'$ used here differ slightly because for fainter sources, such as NGC 7213, minimising the contribution of the background can be more important in optimising the signal-to-noise. In both instances, the

[12]Note that the 2008 *Suzaku* observation was split into two separate observations due to scheduling constraints with respective exposure times of 275 and 78 ks.

[13]http://heasarc.nasa.gov/docs/suzaku/analysis/abc/node9.html

extraction regions are greater than the half-power diameter[14] of the PSF and the size of the extraction region is always accounted for in the ancillary response file, which accounts for any energy dependence of the PSF and the fraction of photons that are enclosed (i.e. via the XISSIMARFGEN routine, which performs ray tracing of the individual photons through the telescope).

Background spectra were extracted from same-size circular regions but offset from the source region while avoiding the calibration sources on the corners of the CCD chips. Note that extracting background regions from an annulus around the source produces identical results for both NGC 7213 and NGC 4051. An example of the XIS background spectrum is shown in Figure 2.7 in the case of NGC 7213. The XIS background is mainly shaped by: (i) the non-X-ray-background (NXB) consisting of a continuum and several emission lines (e.g. Kα transitions from Mn, Ni and Au at $\sim$5.90, $\sim$7.47 and $\sim$9.67 keV respectively) produced by interactions between cosmic rays and the CCD chip / sensor housing, (ii) the cosmic X-ray background (CXB) consisting of diffuse X-ray radiation from all directions of the sky forming a power law of photon index $\Gamma \sim 1.49$, and (iii) diffuse X-rays from the Local Hot Bubble which is dominant at energies < 1 keV (Yamaguchi et al. 2006).

The NGC 7213 and NGC 4051 2008 data were acquired in the on-axis XIS nominal pointing position whereas the HXD instrument was the on-axis instrument during the NGC 4051 2005 observation. XIS response files (RMFs) and ancillary response files (ARFs) were generated using the XISRMFGEN and XISSIMARFGEN FTOOLS respectively including correction for the hydrocarbon contamination on the optical blocking filter (Ishisaki et al. 2007). For NGC 7213, a net XIS source exposure of 90.7 ks was obtained for each of the four XIS chips. In the case of NGC 4051, net source exposures of 120, 275 and 78 ks were obtained for the XIS chips in the 2005 and two 2008 observations respectively.

The three FI XIS chips (XIS $0, 2, 3$) were found to produce consistent spectra within the statistical errors in the NGC 7213 and 2005 NGC 4051 data and so the spectra and responses were combined (for each observation) to maximise signal-to-noise, as recommended by the

[14]The half-power diameter is the diameter within which half of the focused X-rays are enclosed.

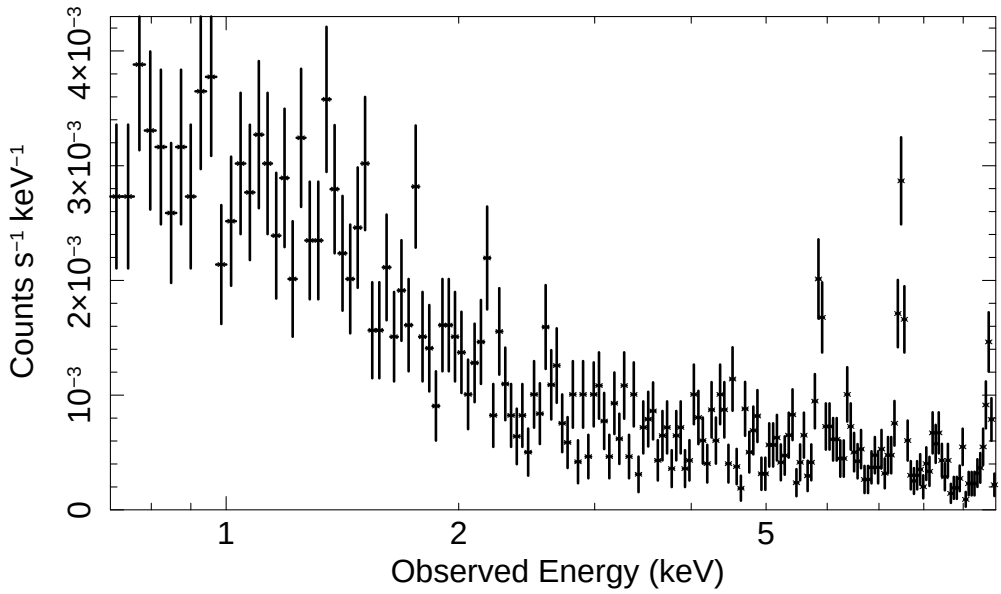

Figure 2.7: The FI XIS background spectrum of NGC 7213 which is shaped by the NXB (i.e. cosmic rays), the CXB and diffuse emission from the Local Hot Bubble. The count rate is typically $< 1\%$ of the source rate.

XIS team to increase the speed and efficiency of spectral fitting[15]. The same was done for the two active FI XIS detectors during the 2008 NGC 4051 observation. Upon combining the spectra, the individual responses matrices for the FI XIS detectors were also correctly weighted for exposure time in the summed spectra.

For NGC 7213, the net source count rate for the three FI XIS spectra combined was $1.563 \pm 0.002\,\mathrm{cts\,s^{-1}}$ per XIS, with the background rate only 0.7% of the source rate. This count rate corresponds to an observed flux of $F_{0.5-10} = 3.83 \times 10^{-11}\,\mathrm{erg\,cm^{-2}\,s^{-1}}$ and a luminosity of $L_{0.5-10} = 2.82 \times 10^{42}\,\mathrm{erg\,s^{-1}}$ over the 0.5–10 keV energy range. For NGC 4051, the net source count rates corresponding to the 2005 Nov 10, 2008 Nov 6 and 2008 Nov 23 observations respectively over the 0.5–10 keV energy range were found to be 0.451 ± 0.001, 2.07 ± 0.002 and $1.42 \pm 0.002\,\mathrm{cts\,s^{-1}}$ per FI XIS with the background rates corresponding to

[15]http://heasarc.gsfc.nasa.gov/docs/suzaku/analysis/fasterfit.html

Observation Date (Start Date)	Object	Mission	Sequence Number	Exposure (ks)
2005/11/10	NGC 4051	*Suzaku*	700004010	120
2006/10/22	NGC 7213	*Suzaku*	701029010	90
2008/11/06	NGC 4051	*Suzaku*	703023010	275
2008/11/06	NGC 4051	*Chandra*	10777	27.8
2008/11/08	NGC 4051	*Chandra*	10775	30.9
2008/11/09	NGC 4051	*Chandra*	10403	38.2
2008/11/11	NGC 4051	*Chandra*	10778	34.1
2008/11/11	NGC 4051	*Chandra*	10776	25.2
2008/11/12	NGC 4051	*Chandra*	10404	20.1
2008/11/13	NGC 4051	*Chandra*	10801	26.1
2008/11/20	NGC 4051	*Chandra*	10779	27.8
2008/11/23	NGC 4051	*Suzaku*	703023020	78
2008/11/25	NGC 4051	*Chandra*	10780	26.4
2008/11/26	NGC 4051	*Chandra*	10781	24.1
2008/11/29	NGC 4051	*Chandra*	10782	23.7
2008/11/30	NGC 4051	*Chandra*	10824	9.2

Table 2.2: Log of the *Suzaku* and *Chandra* HETG observations of NGC 7213 and NGC 4051 analysed in Chapters 3–5.

$\sim$2.4%, $\sim$0.9% and $\sim$0.9% of the respective source count rates. These count rates correspond to fluxes of $F_{0.5-10} = 1.32\times10^{-11}$, 5.03×10^{-11} and 3.53×10^{-11} erg cm^{-2} s^{-1} and luminosities of $L_{0.5-10} = 3.66\times10^{41}$, 1.39×10^{42} and 9.76×10^{41} erg s^{-1} for the three respective observations (see Table 2.3).

2.6.1.2 Suzaku HXD Data Reduction

As NGC 7213 and NGC 4051 are below the detection threshold of the HXD Gadolinium Silicate (GSO) instrument, only data from the HXD PIN were used, which provides useful data over the 15–70 keV energy range. The source spectra were extracted from cleaned HXD-PIN events files and, since the PIN background rate varies significantly around the orbit of the spacecraft, they were processed with the screening criteria described above. The resulting time filters were applied to the background model files to produce model-background data for the PIN for the same time intervals covered by the on-source data (i.e. 'good time intervals'; GTIs). The HXD-PIN instrumental non-X-ray-background (NXB) spectra were generated

from "tuned" time-dependent models provided by the HXD instrument team (Fukazawa et al. 2009) and the source exposures were corrected for the detector deadtime (which is $\approx 6.7\%$) using the HXDDTCOR script (version 2007 May). A detailed description of the PIN detector deadtime is given in Kokubun et al. (2007). Note that the background spectral models that are supplied to the user by the instrument team are generated with 10 times the actual background count rate in order to suppress the photon noise on the simulated background data. This has been accounted for by increasing the effective exposure times of the background spectra by a factor of 10. HXD-PIN response files are made available by the instrument team whenever significant changes are made to the instrumental settings (e.g. changes in bias voltages). Each response file covers a specific epoch and so the appropriate response file should be chosen such that its corresponding epoch covers the date of the observation. The HXD-PIN response file dated 2008/01/29 (epoch 3; 2006 Oct 02 - 2007 Jul 28; XIS-nominal position) was used for all subsequent spectral fits for NGC 7213 whereas the response files dated 2008/01/29 (epoch 1; 2005 Aug 17 - 2006 May 13; HXD-nominal position) and 2008/07/16 (epoch 5; 2008 Sep 01 - 2009 Sep 30; XIS-nominal position) were used for the 2005 and 2008 observations of NGC 4051 respectively. After deadtime correction, the net exposure times of the PIN source spectrum were 84.3 ks for NGC 7213 and 112, 204 and 59 ks for the 2005 Nov 10, 2008 Nov 6 and 2008 Nov 23 observations of NGC 4051 respectively.

To account for the cosmic X-ray background (CXB; Boldt 1987; Gruber et al. 1999), background spectra were simulated which were taken from a model of the form $9.0 \times 10^{-9}(E/3\,\mathrm{keV})^{-0.29}\exp(-E/40\,\mathrm{keV})\,\mathrm{erg\,cm^{-2}\,s^{-1}\,sr^{-1}\,keV^{-1}}$. This was normalised to the FOV of the HXD PIN instrument for each observation using a flat-field response and combined with the instrumental background file to produce a total background file. The effective flux of the CXB component was $F_{15-50} = 8.49 \times 10^{-12}\,\mathrm{erg\,cm^{-2}\,s^{-1}}$ in the 15–50 keV band corresponding to a count rate of $\sim$0.017 cts s^{-1} for NGC 7213. After background subtraction (including both the instrumental and CXB components), the net PIN source count rate for NGC 7213 was found to be $0.062 \pm 0.002\,\mathrm{cts\,s^{-1}}$ from 15–50 keV corresponding to a net flux of $F_{15-50} = 3.58 \times 10^{-11}\,\mathrm{erg\,cm^{-2}\,s^{-1}}$. Therefore, the CXB component represents $\sim$24% of the net source flux measured by the HXD PIN. For NGC 4051, the net PIN source count rates from 15–50 keV are found to be 0.043 ± 0.001, 0.068 ± 0.001 and $0.053 \pm 0.001\,\mathrm{cts\,s^{-1}}$ for the

three respective observations corresponding to fluxes of $F_{15-50} = 1.73 \times 10^{-11}$, 3.06×10^{-11} and 2.66×10^{-11} erg cm^{-2} s^{-1}. The respective effective CXB fluxes are $F_{15-50} = 7.83 \times 10^{-12}$, $F_{15-50} = 8.64 \times 10^{-12}$ and $F_{15-50} = 8.35 \times 10^{-12}$ erg cm^{-2} s^{-1}. The mean net count rates and fluxes are summarised in Table 2.3.

Note that there may be some uncertainty in the absolute flux level of the CXB component measured between missions; for instance, Churazov, Sunyaev & Revnivtsev (2007) find the CXB normalisation from *INTEGRAL* (*International Gamma-Ray Astrophysics Laboratory*) to be about 10% higher than that measured by Gruber et al. (1999) from *HEAO-1* (High Energy Astronomy Observatory - 1) data. A factor of ±10% uncertainty in the CXB normalisation would result in an uncertainty of ±2.4% in the HXD flux for NGC 7213, for example. Therefore a systematic uncertainty of ±10% in the CXB level was included within the error bars in all spectral fitting. Finally, note that the total background count rate for NGC 7213 was found to be ∼0.350 cts s^{-1} (15–50 keV) with a typical 1σ systematic uncertainty of ±1.3% (i.e. ±0.0043 cts s^{-1} and ±0.0022 cts s^{-1} for the NXB and CXB components respectively, corresponding to $< 10\%$ of the source count rate). The total background count rates for NGC 4051 were found to be ∼0.352, ∼0.305 and ∼0.316 cts s^{-1}.

2.6.2 NGC 4051 Chandra HETG Data Reduction

NGC 4051 was observed with the *Chandra* X-ray Observatory (Weisskopf et al. 2000) on twelve different occasions dating from November 6 2008 to November 30 2008 with a total net exposure of ∼300 ks. A log of the separate observations and their corresponding exposures is shown in Table 2.2. The *Chandra* observations were performed with the HETGS (Markert et al. 1994; Canizares et al. 2005) in the focal plane of the ACIS–S (Garmire et al. 2003) which consists of two separate gratings: the medium energy grating (MEG; 0.4–5 keV) and the high energy grating (HEG; 0.8–10 keV). The *Chandra* HETG data were reduced using version 4.1 of both the CIAO software package (Fruscione et al. 2006) and the corresponding CALDB. See Section 2.2.2 for a description of the satellite.

First order MEG and HEG spectra were extracted for the source and background for each individual observation. Spectral redistribution matrix (RMF) files were created using

Date	Object	Mission	Instrument	Exposure	Count Rate	Flux	Luminosity
2005-11-10	NGC 4051	*Suzaku*	XIS	120	0.45	1.32	3.66
			HXD	112	0.04	1.73	4.78
2006-10-22	NGC 7213	*Suzaku*	XIS	90	1.56	3.83	28.2
			HXD	84	0.06	3.58	26.8
2008-11-06	NGC 4051	*Suzaku*	XIS	275	2.07	5.03	13.9
			HXD	204	0.07	3.06	8.46
2008-11-06	NGC 4051	*Chandra*	HETG	314	0.83	5.08	14.1
2008-11-23	NGC 4051	*Suzaku*	XIS	78	1.42	3.53	9.76
			HXD	59	0.05	2.66	7.35

Table 2.3: Mean count rates ($\mathrm{cts\,s^{-1}}$), fluxes ($\times 10^{-11}\,\mathrm{erg\,cm^{-2}\,s^{-1}}$) and luminosities ($\times 10^{41}\,\mathrm{erg\,s^{-1}}$) for the time-averaged *Suzaku* and *Chandra* HETG observations of NGC 7213 and NGC 4051 described in Chapters 3–5. All XIS and HETG (MEG + HEG combined) count rates, fluxes and luminosities are given in the 0.5–10.0 keV energy band while the HXD values are given from 15–50 keV. The net exposure times for each instrument are also shown in ks. The *Suzaku* and *Chandra* satellites are described in Sections 2.2.1 and 2.2.2 respectively.

the MKGRMF script for each first order grating arm (-1 and +1) for both the MEG and HEG. Telescope effective area files were also created using the FULLGARF script incorporating the CIAO tool MKGARF. Events files were extracted from the negative and positive first order grating arms of the MEG and HEG allowing lightcurves and spectra to be extracted. The first order spectra were then combined for each individual exposure using combined response files (with appropriate weighting) for the MEG and HEG. The background was not subtracted however as, for bright X-ray point sources, it has a negligible effect in the energy ranges of interest here due *Chandra*'s very small PSF (i.e typically $< 1\%$ of the source rate). The total count rates in the first-order energy spectra (0.5–10 keV) are 0.602 ± 0.001 and $0.250\pm0.001\,\mathrm{ct\,s^{-1}}$ for the MEG and HEG respectively (or 0.583 ± 0.001 and $0.233\pm0.001\,\mathrm{ct\,s^{-1}}$ for the respective 0.5–5 and 1–8 keV energy bands for the MEG and HEG which are adopted here). These count rates correspond to fluxes of $F_{0.5-5} = 3.99 \times 10^{-11}$ and $F_{1-8} = 3.29 \times 10^{-11}\,\mathrm{erg\,cm^{-2}\,s^{-1}}$ and luminosities of $L_{0.5-5} = 1.11 \times 10^{42}$ and $L_{1-8} = 9.12 \times 10^{41}\,\mathrm{erg\,s^{-1}}$ for the respective 0.5–5 and 1–8 keV energy bands for the MEG and HEG (see Table 2.3).

3 X-Ray Spectroscopy of NGC 7213

This chapter is based on published work entitled *'Evidence for a Truncated Accretion Disc in the Low-Luminosity Seyfert Galaxy, NGC 7213?'; Lobban, A.P., Reeves, J.N., Porquet, D., Braito, V., Markowitz, A., Miller, L., Turner, T.J., 2010, MNRAS, 408, 551-564.*

All data reduction, analysis and spectral modelling was conducted by the author. All co-authors assisted with scientific interpretation and discussion and participated in review of the aforementioned manuscript.

3.1 Introduction

NGC 7213 is a nearby low-luminosity AGN ($z = 0.005839$), often classified as an intermediate between a type-1 Seyfert and a LINER galaxy due to its optical spectrum (Filippenko & Halpern 1984). Its X-ray spectral properties also appear to lie between those of weak AGN (e.g. M81) and 'classical' higher-luminosity broad-line Seyferts. The UV flux measured by Wu, Boggess & Gull (1983) was higher than would be expected from an extrapolation of the optical flux, indicating that NGC 7213 may have a BBB, although weak compared to most Seyferts. This object has a high black hole mass of $M_{\rm BH} \sim 10^8\,{\rm M}_{\odot}$ as estimated from the stellar velocity dispersion (Nelson & Whittle 1995; Woo & Urry 2002) and a low bolometric luminosity of $L_{\rm bol} \sim 9 \times 10^{42}\,{\rm erg\,s^{-1}}$ (Starling et al. 2005).

NGC 7213 has a very low accretion rate of $\sim$0.07% $L_{\rm Edd}$; a value which is intermediate between those usually found in local type-1 Seyfert galaxies (e.g. Padovani & Rafanelli 1988; Wandel 1999; Page 2001) and LINERs (e.g. Ho 1999). Interestingly, this is much less than the predicted 2% $L_{\rm Edd}$ 'critical' rate whereby the high-/soft-state in black hole X-ray binaries can be observed (Maccarone 2003). Furthermore, this object exhibits another interesting characteristic since it is part of a class of Seyfert galaxies which have radio properties that are intermediate between those of radio-loud and radio-quiet active galaxies (e.g. Blank, Harnett & Jones 2005 and references therein). It is there conceivable that NGC 7213 is an analogue of the Galactic low-/hard-state sources.

A simultaneous *XMM-Newton* (net EPIC-pn exposure ∼30 ks) and *BeppoSAX* observation in May 2001 revealed further peculiar characteristics of NGC 7213. The low S/N (signal-to-noise) RGS spectrum showed the presence of several weak emission features with no absorption lines (Starling et al. 2005) contrary to what is usually found in type-1 Seyfert galaxies. Moreover, the emission lines appeared to be the signature of a collisionally-ionised thermal plasma ($k_{\rm B}T \sim 0.18$ keV), while in Seyfert galaxies, only emission and/or absorption lines from a photo-ionised warm absorber / emitter have before been observed (e.g. NGC 3783, Kaspi et al. 2001; NGC 4151, Schurch & Warwick 2002; NGC 1068, Kinkhabwala et al. 2002; Brinkman et al. 2002; Mrk 3, Pounds & Page 2005). Such emission lines from collisionally-ionised thermal plasmas have, however, been observed in the soft X-ray spectra of LINERs, such as M81 (Page et al. 2003). Interestingly, no significant Compton-reflection signature was detected in this simultaneous *XMM-Newton* and *BeppoSAX* observation (reflection component: $R = \Omega/2\pi < 0.2$, where a value $R = 1$ corresponds to reflection off material subtending 2π sr; Bianchi et al. 2003), though the presence of a significant Fe K complex could be explained by three narrow emission lines: neutral Fe at $E_{\rm c} \sim 6.40$ keV with an equivalent width (EW) of ∼80 eV, Fe XXV at $E_{\rm c} \sim 6.66$ keV and Fe XXVI at $E_{\rm c} \sim 6.94$ keV (see also Starling et al. 2005).

Bianchi et al. (2003) deduced from the absence of the reflection component that the neutral Fe Kα emission line is most likely produced in a Compton-thin torus or the BLR. Indeed, according to Matt, Perola & Pirlo (1991) and George & Fabian (1991), a line with an EW of ∼80 eV would require a reflection component of $R \sim 0.6$; a value larger than that found for this object ($R < 0.2$). Furthermore, Bianchi et al. (2008) reported the data analysis of a long *Chandra* HETG observation of NGC 7213 finding that the neutral Fe Kα line is resolved with a FWHM of $2\,400^{+1100}_{-600}$ km s^{-1}, fully consistent with the Hα line width (FWHM $= 2\,640^{+110}_{-90}$ km s^{-1}) measured with the *European Southern Observatory* (ESO) *New Technology Telescope* (NTT). They therefore inferred that the neutral Fe K line seen in this object originates in the Compton-thin BLR explaining the lack of evidence for Compton reflection. They also confirmed the presence of two ionised Fe lines at $E_{\rm c} \sim 6.72$ keV and $E_{\rm c} \sim 6.99$ keV which they associate most probably with the resonance transition of the Fe XXV triplet and the Lyα transition of Fe XXVI, respectively. Comparing the line energies found

with their rest-frame values, a blueshift of $\sim$900 km s^{-1} is inferred. If the dominant line at $\sim$6.72 keV is indeed the resonance line of the Fe XXV triplet, this means that the line may be associated with a collisionally-ionised thermal plasma (Porquet & Dubau 2000; Bautista & Kallman 2000).

Here the results of a 90 ks *Suzaku* observation of NGC 7213 are reported on. The overall goal is to understand accretion in an AGN at low rates compared to Eddington through a high signal-to-noise, broad-band observation of this source. Specifically, the objectives are to parameterise the Fe-line complex with an analysis of the XIS spectra in order to constrain the individual properties of the lines before considering the complete broad-band spectrum from 0.6–150 keV with a combined analysis of the *Suzaku* XIS and HXD data with those from the time-averaged *Swift*-BAT 58-month survey (see Section 3.3). The aims are to obtain better constraints on the origin of both the Fe-line complex and any observed soft excess while simultaneously testing for the presence (or absence) of a Compton-reflection component (see Section 3.4). Finally, by considering more recent *XMM-Newton* data, the nature of the spectral variability exhibited by this source is discussed.

3.2 Spectral Analysis

The NGC 7213 *Suzaku* data reduction is described in Section 2.6.1. Data in the 0.6–10 keV energy range from both the FI- and BI-XIS spectra were used. XSPEC uses the source-spectrum file and the background-spectrum file to derive the set of background-subtracted spectra[1]. Note that for the XIS the background uncertainty is negligible as NGC 7213 has, for example, an XIS background rate that is $< 1\%$ of the total count rate. The XIS data are dominated by the statistical uncertainties although a significant systematic uncertainty exists from $\sim$1.7–1.9 keV due to $\pm 10\%$ calibration uncertainties around the Si K edge[2]. Consequently, data in the 1.7–1.9 keV band in the co-added FI-XIS spectrum and the individual BI-XIS spectrum were ignored. In all fits, a constant multiplicative factor was included to account for relative

[1] https://heasarc.gsfc.nasa.gov/xanadu/xspec/manual/XspecSpectralFitting.html
[2] http://heasarc.gsfc.nasa.gov/docs/suzaku/analysis/sical.html

instrument normalisations. The relative BI-XIS/FI-XIS normalisation was also allowed to vary, but best-fitting values were always within 1% of each other. The XIS source spectrum was binned at the half-width at half-maximum (HWHM) resolution of the detector due to the high photon statistics. This enabled the use of χ^2 minimisation as there were >50 counts per resolution bin. Errors are quoted to 90% confidence for 1 parameter (i.e. $\Delta\chi^2 = 2.71$) unless otherwise stated.

A visual analysis of the lightcurves was undertaken to determine whether any detailed timing analysis was necessary. It can be seen from Figure 3.1 that the amplitude of the FI-XIS lightcurve varies only by a factor of ∼10% throughout the entire observation indicating little intrinsic variability below 10 keV. From Figure 3.2 it can be seen that the HXD-PIN lightcurve, too, shows little evidence of any substantial variability in the hard X-ray band. Note that the XIS and HXD lightcurves are displayed over the same time period. Therefore, due to the lack of any strong evidence of short-timescale spectral variability, the time-averaged spectrum was analysed.

The XSPEC V12.7 software package (Arnaud 1996) was used for spectral analysis of the background-subtracted spectrum. In all fits, a Galactic column density ($N_{\rm H}^{\rm Gal}$ = 1.1 $\times 10^{20}$ cm^{-2}, obtained from the FTOOL NH using the compilations of Dickey & Lockman 1990 and Kalberla et al. 2005 from 21 cm Galactic hydrogen studies) was included and the cross-sections for X-ray absorption by the interstellar medium from Morrison & McCammon (1983) were used. Absorption due to other elements such as O and Si are included assuming solar abundances for the given hydrogen column. Note that all fit parameters are given in the rest frame of the host galaxy, assuming a distance of 25 Mpc to NGC 7213 (Mould et al. 2000). Abundances are those of Anders & Grevesse (1989) unless otherwise stated.

The cross-normalisation between the HXD-PIN (where this object is detected at the 13 σ level relative to the background) and XIS detectors was accounted for by the addition of a fixed constant component at a value of 1.16 for the XIS nominal pointing position; a value derived using *Suzaku* observations of the Crab (Ishida, Suzuki & Someya 2007[3]). Note that the XIS and HXD-PIN data were fitted simultaneously (unless stated otherwise) and that

[3]ftp://legacy.gsfc.nasa.gov/suzaku/doc/xrt/suzakumemo-2007-11.pdf

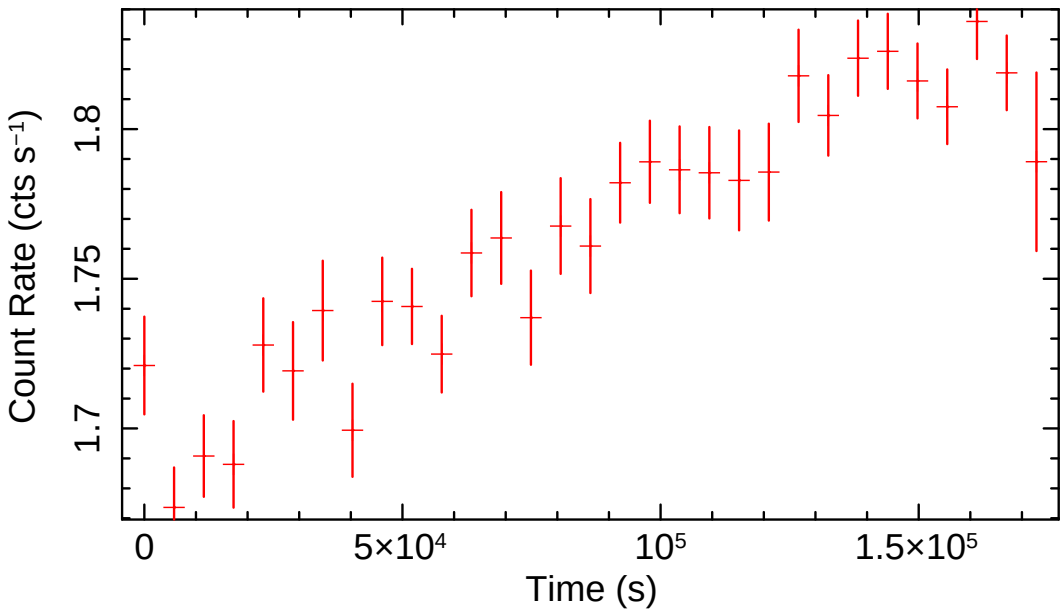

Figure 3.1: Background-subtracted lightcurve of NGC 7213 from 0.5–10 keV FI-XIS data in 5760 s orbital bins.

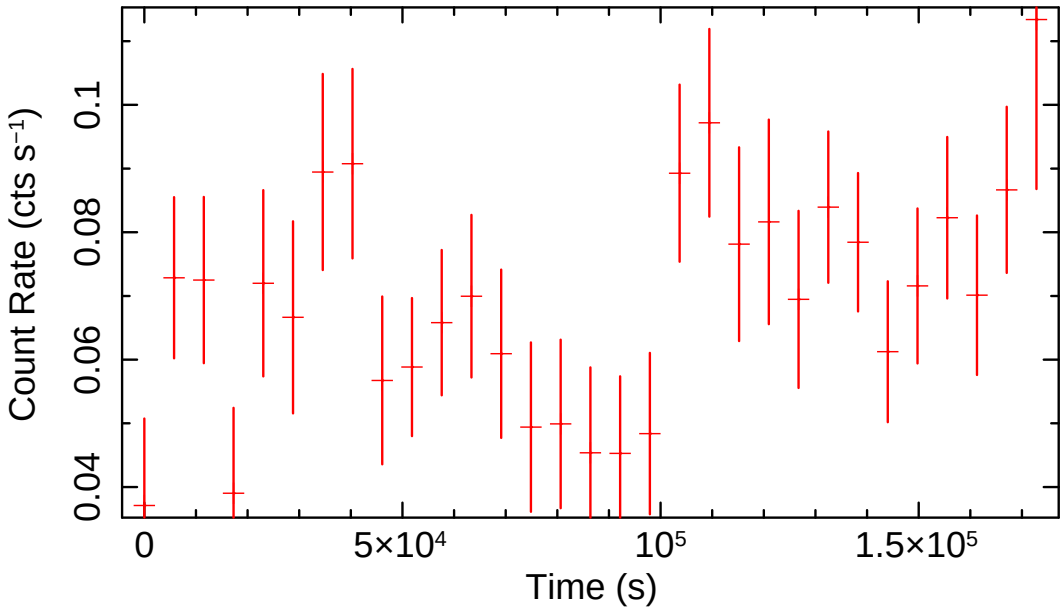

Figure 3.2: Net background-subtracted HXD-PIN lightcurve of NGC 7213 from 15–50 keV in 5760 s orbital bins.

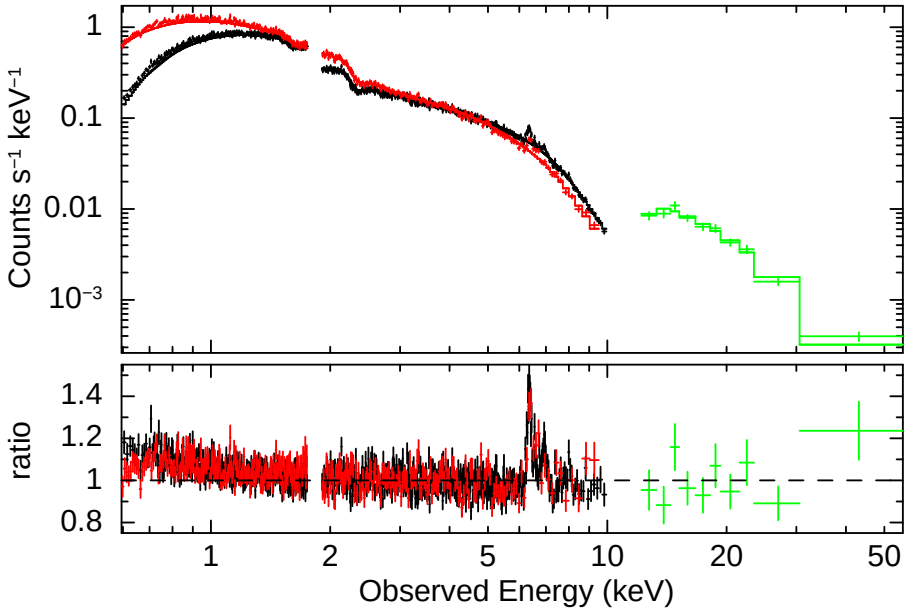

Figure 3.3: The *Suzaku* spectra of NGC 7213 (in the observed frame) showing the FI-XIS (black), BI-XIS (red) and HXD-PIN (green) data. An absorbed (Galactic column density) power law has been fitted to the broad-band spectrum. A significant positive residual is observed in the Fe K complex energy range, as well as a weak excess < 1 keV. The upper panel shows the observed data whereas the lower panel shows the ratio of the remaining residuals (i.e. data / model).

the PIN data were binned to a minimum of 5σ above the background level.

3.3 Results

3.3.1 The Fe K Line Profile

The X-ray spectrum was initially checked over the 0.6–50 keV band using the FI-XIS, BI-XIS and HXD-PIN data. A power law with Galactic absorption of column density $N_{\rm H} = 1.1 \times 10^{20}\,{\rm cm}^{-2}$ was fitted to the data revealing a slight soft excess at energies < 1 keV as shown in Figure 3.3[4], where the excess is seen in the data / model residuals in the lower panel.

[4]The observed data are plotted in the standard way; i.e. counts s^{-1} keV^{-1} which is essentially equivalent to counts s^{-1} channel^{-1} except that the y-axis counts are divided by the width of a channel in keV. This

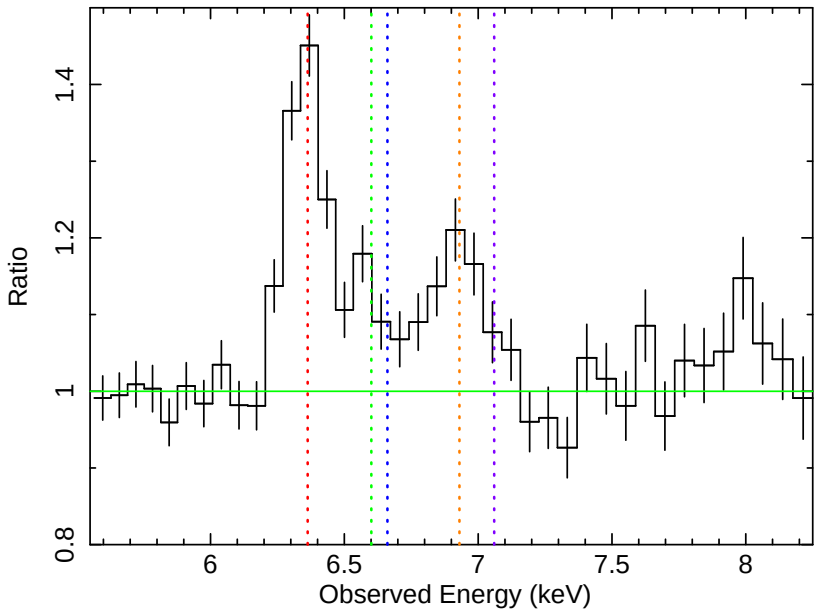

Figure 3.4: The ratio of the residuals for the FI-XIS data for the Fe-line complex compared to the power-law continuum. The spectra are binned relative to the HWHM of the detector resolution. The vertical dotted lines show the expected line energies of, from left to right, Fe Kα (red), Fe XXV forbidden (green), Fe XXV $1s$–$2p$ resonance (blue), Fe XXVI $1s$–$2p$ Lyα (orange) and Fe Kβ (magenta) in the observed frame.

For clarity, the HXD data were binned to 10σ per spectral bin relative to the background. The hard X-ray data are seen to extrapolate quite well to the XIS data with very few residuals in excess of the power-law continuum indicating little or no reflection component ($R \sim 0.2$; see Section 3.3.2). Line emission is clearly present with a strong but seemingly relatively narrow Fe Kα line at $\sim$6.4 keV.

The Fe K emission profile was subsequently analysed. As the BI-XIS data have a lower effective area than the FI-XIS data at higher energies (i.e. > 2 keV), these data are now excluded from the analysis that follows. Likewise, the HXD data are excluded in the following analysis as the lack of any apparent Compton-reflection hump suggests that the Fe K emission lines can be modelled independently. The HXD-PIN and BI-XIS data are re-introduced in the

information is contained within the response matrix file (RMF) which steps in bins of 2 eV.

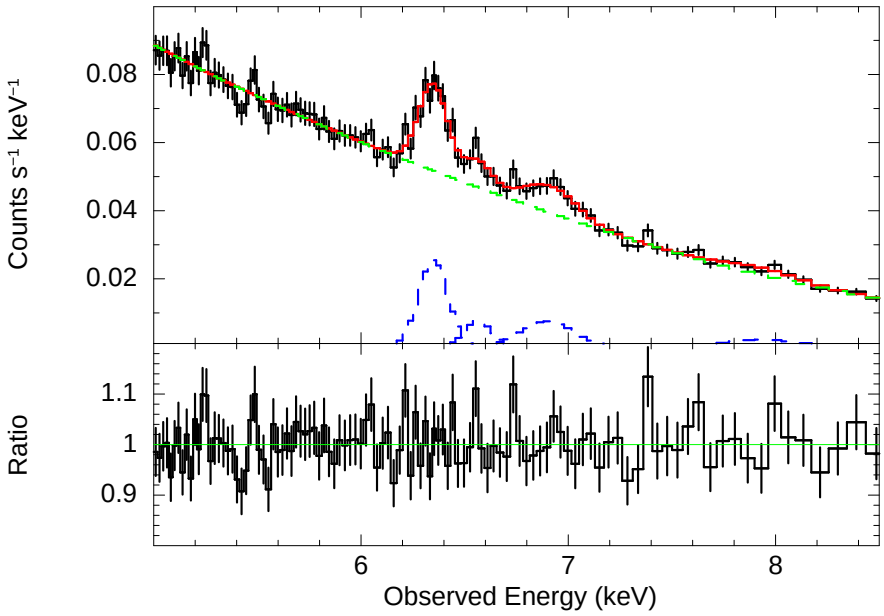

Figure 3.5: The NGC 7213 FI-XIS data in the Fe K band. The continuum is modelled with an absorbed power law while the emission lines are modelled with individual Gaussians. Upper panel: The data from 5–8.5 keV with the model superimposed. The additive Gaussians are shown in navy. Lower panel: The ratio of the residuals. The model is described in Section 3.3.1 and the best-fitting parameters are shown in Table 3.1.

broad-band fits in Section 3.3.2. Finally, the FI-XIS data are now analysed from 2.5–10 keV to allow the Fe K emission lines to drive the spectral fitting.

A simple power-law model of $\Gamma = 1.75 \pm 0.02$ with Galactic absorption resulted in a poor fit to the FI-XIS data ($\chi^2/d.o.f. = 739/316$), highlighted by a low null hypothesis probability of 6.67×10^{-36}, where this is the probability that these data could be drawn from this model assuming that the model is correct. A plot of the ratio of the residuals with respect to the power-law continuum from 5.0–8.5 keV (Figure 3.4) clearly shows X-ray line emission which requires modelling; the most apparent being the Fe Kα line from near-neutral material at $\sim$6.4 keV, plus additional higher-energy lines. These lines were modelled with Gaussian profiles, each consisting of three free parameters: line energy, E_c, line width, σ and line intensity. All line and continuum (i.e. the power law) parameters were allowed to be free

during the fitting procedure. Note that the best-fitting parameters quoted in the text are those obtained from the final model once all of the emission components have been accounted for. These are shown in Table 3.1 along with the change in χ^2 upon removing the component from the final model. The model fit to the lines in shown in Figure 3.5.

The strongest line has a best-fitting energy of $E_{\rm c} = 6.39 \pm 0.01\,{\rm keV}$ with an intrinsic width of $\sigma < 43\,{\rm eV}$, and an observed flux of $F_{{\rm K}\alpha} = 2.18^{+0.28}_{-0.29} \times 10^{-5}\,{\rm photons\,cm^{-2}\,s^{-1}}$. Its equivalent width against the observed continuum is ${\rm EW} = 83.1^{+11.0}_{-10.7}\,{\rm eV}$ and sequentially modelling this line improves the fit significantly to $\chi^2/d.o.f. = 422/313$ (compared to $\chi^2/d.o.f. = 739/316$ for the simple absorbed power law). This line most likely corresponds to Fe Kα emission from near-neutral material. However, even upon modelling the strong Fe Kα line at 6.39 keV, the fit remains unacceptable (null probability $= 3.70 \times 10^{-5}$) with further residuals still present between 6.5–7.0 keV indicating K-shell emission from ionised Fe.

Further Gaussian profiles were added to fit other prominent emission lines starting with the $1s$–$2p$ doublet from H-like Fe (Fe XXVI) at $E_{\rm c} = 6.95 \pm 0.03\,{\rm keV}$ which improves the fit to $\chi^2/d.o.f. = 365/310$. Unlike the 6.39 keV line, this line is resolved compared to the detector resolution with an intrinsic width of $\sigma = 0.10^{+0.05}_{-0.04}\,{\rm keV}$ (FWHM $\sim 10\,000\,{\rm km\,s^{-1}}$), an equivalent width of ${\rm EW} = 62.3^{+16.0}_{-14.2}\,{\rm eV}$ and an observed flux of $F_{\rm line} = (1.40^{+0.36}_{-0.32}) \times 10^{-5}\,{\rm photons\,cm^{-2}\,s^{-1}}$. A third narrow component at a line energy of $E_{\rm c} = 6.60 \pm 0.03\,{\rm keV}$ was also modelled, resulting in a fit statistic of $\chi^2/d.o.f. = 332/307$. A line-energy vs. line-flux contour plot (Figure 3.6) shows that this line energy can be rejected at the 99.9% confidence level (for two interesting parameters) as being associated with the resonance line of He-like Fe (Fe XXV) at 6.700 keV ($\Delta\chi^2 \sim 14$) and is just acceptable (rejected at only 90% confidence) as the forbidden line at 6.637 keV (also see Section 3.3.3.2).[5] The fact that this indicates that the line at 6.60 keV is more consistent with the forbidden transition of Fe XXV is an interesting discovery since the resonance line is expected to dominate over the forbidden line in a collisionally-ionised plasma (Porquet & Dubau 2000; Bautista & Kallman 2000).

[5] An analysis of the spectrum produced by the XIS Fe-55 calibration source, which produces emission lines from Mn Kα and Mn Kβ, shows that the absolute XIS energy scale is accurate to within $\pm 10\,{\rm eV}$.

Model Component	Parameter	Value	$\Delta\chi^2$
Power-law continuum[a]	Γ	$1.75^{+0.02}_{-0.02}$	
	Normalisation	$6.25^{+0.02}_{-0.06}$	
	$F_{2.5-10\,\mathrm{keV}}$	2.18×10^{-11}	
Galactic absorption[b]	N_H	1.10×10^{20}	
Fe Kα Line[c]	E_c	$6.39^{+0.01}_{-0.01}$	
	σ	$< 4.30 \times 10^{-2}$	
	EW	$83.1^{+11.0}_{-10.7}$	277
	FWHM	$< 4\,600$	
	Line flux	$2.18^{+0.28}_{-0.29}$	
Fe XXVI Line[c]	E_c	$6.95^{+0.03}_{-0.03}$	
	σ	$0.10^{+0.05}_{-0.04}$	
	EW	$62.3^{+16.0}_{-14.2}$	37
	FWHM	$10\,000^{+5\,000}_{-4\,000}$	
	Line flux	$1.40^{+0.36}_{-0.32}$	
Fe XXV Line[c]	E_c	$6.60^{+0.03}_{-0.03}$	
	σ	< 0.30	
	EW	$24.4^{+8.0}_{-8.0}$	24
	FWHM	$< 32\,000$	
	Line flux	$0.67^{+0.22}_{-0.22}$	
8.00 keV Line[c]	E_c	$8.00^{+0.10}_{-0.14}$	
	σ	< 0.28	
	EW	$45.9^{+33.5}_{-27.7}$	12
	FWHM	$< 25\,000$	
	Line flux	$0.78^{+0.57}_{-0.47}$	
Fe Kβ Line[c]	E_c	7.06	
	σ	$< 4.30 \times 10^{-2}$	
	EW	< 29.3	0.5
	FWHM	$< 4\,600$	
	Line flux	< 0.67	
Fit statistics[d]	χ^2/d.o.f.	322/304	
	Null probability	0.36	

Table 3.1: Spectral Parameters for the *Suzaku* XIS data for NGC 7213 in the Fe K band. [a] Γ, photon index; Normalisation in units $\times 10^{-3}$ photons cm^{-2} s^{-1} at 1 keV; $F_{2.5-10\,\mathrm{keV}}$, absorbed continuum flux from 2.5–10 keV in units erg cm^{-2} s^{-1}. [b] Local Galactic absorption (at $z = 0$), units cm^{-2}. [c] E_line, line energy in units keV; σ, 1σ line width in units keV; EW, equivalent width in units eV; FWHM, full-width at half-maximum in units km s^{-1}; Line Flux in units $\times 10^{-5}$ photons cm^{-2} s^{-1}. [d] Reduced chi-squared (χ^2/dof) and null hypothesis probability for the spectral fit. Note that the $\Delta\chi^2$ values correspond to how much the fit worsens upon removing the component from the final overall model and all uncertainties correspond to $\Delta\chi^2 = 2.7$.

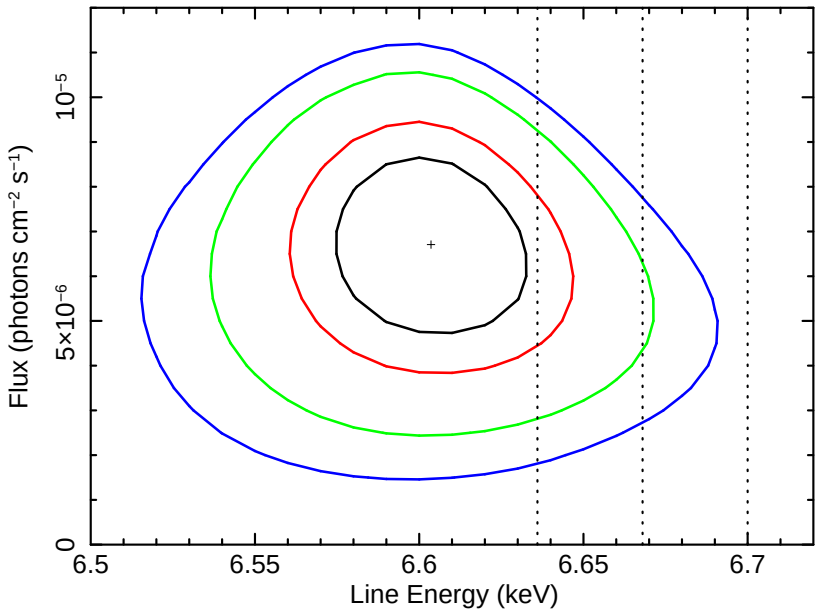

Figure 3.6: A two-dimensional contour plot between line-energy and flux of the 6.60 keV line at the 68%, 90%, 99% and 99.9% confidence intervals (inner to outer contours respectively) for 2 parameters of interest. The vertical dashed lines show the rest energies of forbidden, intercombination and resonance transitions of the Fe XXV triplet at 6.637, 6.668 and 6.700 keV respectively.

Further discussion regarding the origin of this emission can be found in Section 3.4.2.

A weak, narrow component also remains in the residuals at a line energy of $E_{\rm c} = 8.00^{+0.10}_{-0.14}$ keV with an intrinsic width of $\sigma < 0.28$ keV. However, the detection is more marginal; removing this extra line component from the final model only worsens the fit by $\Delta\chi^2 = 12$ for 3 parameters of interest. This putative line could possibly be associated with the $1s$–$3p$ transitions of Fe XXV or Fe XXVI (corresponding to rest energies of ∼7.88 and ∼8.25 keV respectively) or alternatively, it could be due to the $1s$–$2p$ transition of H-like nickel (corresponding to a rest energy of ∼8.10 keV).

Finally, no neutral Fe Kβ emission was apparent but was still modelled for consistency. Its line energy was fixed at $E_{\rm c} = 7.06$ keV and its intrinsic width, σ, was tied to that of the corresponding Kα line. All other parameters in the model were allowed to be free including the normalisation of the Kβ line which provided an upper limit on its flux of $F_{\rm K\beta} < 0.67 \times$

10^{-5} photons cm^{-2} s^{-1}. This corresponds to an upper limit on the Kβ/Kα flux ratio of 0.35. A value of $\Delta\chi^2 = 0.5$ with respect to the overall model revealed that the Kβ line is consistent with the fit to the data but in this instance is not required. Hereafter, the Kβ line is included in all subsequent fits, fixed at 13% of the Kα flux to remain representative of the range of theoretical and experimental values discussed in the literature (see Kaastra & Mewe 1993 and Palmeri et al. 2003).

An attempt was also made to model the neutral Fe Kα emission with a DISKLINE component (Fabian et al. 1989) to test for the presence of any broad, relativistic emission from the inner regions of the accretion disc. This model is described in Section 2.5.1. The width of the original narrow Gaussian at 6.39 keV was fixed to be narrow ($\sigma = 10$ eV) in order to model emission from distant material and a DISKLINE component was added to the model with the centroid energy fixed at $E_c = 6.39$ keV and the emissivity index fixed at a standard value of $q = 3$. The inner and outer radii of the emission were also fixed at 6 and 400 r_g from the black hole respectively (where 6 r_g corresponds to the ISCO for a Schwarzschild black hole) and the inclination angle of the source was fixed at $\theta = 30°$. Upon fitting, this returned a value for the flux of the line of $F_{\rm diskline} < 7.64 \times 10^{-6}$ photons cm^{-2} s^{-1} which corresponds to a 90% upper limit on the equivalent width of the line of EW <26.8 eV, whereas an equivalent width of ∼150 eV might be expected for an accretion disc covering 2π sr with a photon index $\Gamma = 1.7$ and a solar Fe abundance (George & Fabian 1991). This tight constraint excludes the presence of any Fe K emission from the inner accretion disc and is equivalent to a disc covering <18% of 2π sr. It was noted that no other significant emission or absorption lines are found in the Fe K band.

3.3.2 The Broad-Band Spectrum

The first stage of the broad-band spectral analysis was to model the spectra above 10 keV by including the *Suzaku* HXD-PIN data. To check for consistency, the 58-month time-averaged *Swift*-BAT spectrum (14–150 keV) was also included (Baumgartner et al. 2010). This provided an extension of the spectrum far beyond the high-energy limit of the HXD PIN. The energy range of the HXD was restricted to 15–50 keV and a constant multiplicative

factor of 1.16 was applied to account for the cross-normalisation at the XIS-nominal pointing position. The constant in front of the BAT data was allowed to be free as the 14–150 keV flux over the 58-month period (15/12/2004–10/10/2009) may have varied (time-averaged flux, $F_{14-150} = 4.01 \times 10^{-11}$ erg cm^{-2} s^{-1}). This provided a cross-normalisation factor of 0.75 ± 0.11 for the BAT compared to the *Suzaku* XIS data. The power-law component was replaced by an exponential cut-off power law and it is noted that no cut-off energy is required in these data. The 90% lower limit on the cut-off is constrained at $E_{\rm cut} > 350$ keV. A simultaneous *XMM-Newton* and *BeppoSAX* PDS observation published by Bianchi et al. (2004) required a high energy cut-off with a value of $E_{\rm cut} = 90^{+50}_{-20}$ keV. However, fixing the cut-off energy at 90 keV in the *Suzaku*+BAT spectrum results in a worse fit with $\Delta\chi^2 = 35$ supportive of the notion that the cut-off exists at significantly higher energy in these data. A simple test was also performed to see if the spectral shape varied between the *Suzaku* and BAT data by allowing the photon index to adjust in the BAT data. However, this resulted in a best-fitting value of $\Gamma = 1.77^{+0.18}_{-0.17}$ for the BAT spectrum compared to $\Gamma = 1.75 \pm 0.02$ for the *Suzaku* XIS+HXD data. As there was no requirement for any change in the spectral shape, the photon index was left tied between datasets.

The residuals in the hard X-ray band show very little excess flux above 10 keV when modelled with a power law indicating a lack of a Compton-reflection component. To test for this, the PEXRAV model of Magdziarz & Zdziarski (1995) was included which is an additive component incorporating the reflected continuum from a neutral slab (see Section 2.5.1). The photon index of the power law incident upon the reflector was tied to that of the power-law continuum and the elemental abundances were fixed to solar values (Anders & Grevesse 1989). The cosine of the inclination angle of the source was also fixed at 0.87 and the e-folding energy was tied to the cut-off energy of the power law at ∼1 000 keV, consistent with no cut-off as above. The inclusion of the PEXRAV component resulted in a reflection scaling factor value of $R = 0.18^{+0.23}_{-0.14}$, consistent with the *XMM-Newton*/*BeppoSAX* analysis of Bianchi et al. (2004) who find $R < 0.19$. The inclusion of this component corresponds to $\Delta\chi^2 \approx 5.0$ where R is the only additional free parameter. So although not a strong component, the reflector is still required by the data. This resulted in a fit statistic $\chi^2/d.o.f. = 486/446$, acceptable with a null hypothesis probability of 0.10.

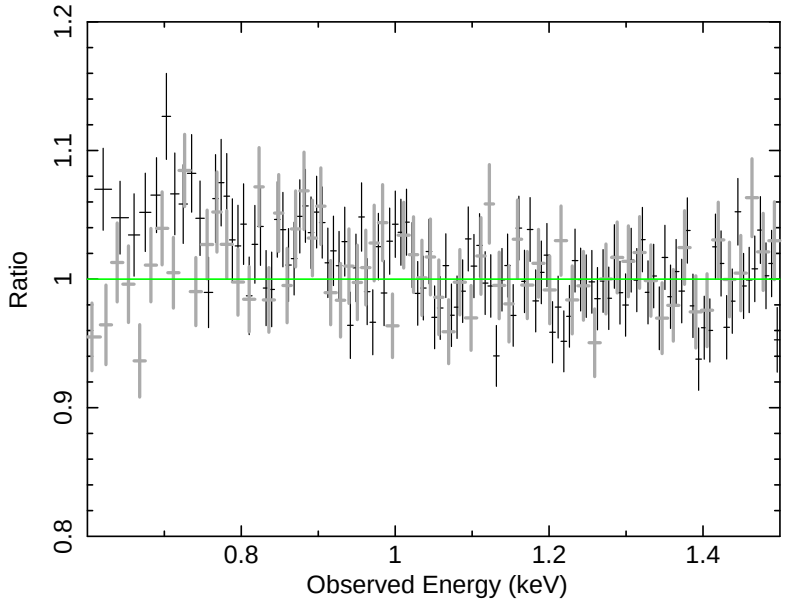

Figure 3.7: A ratio plot showing the residuals compared to the model described in Section 3.3.2 prior to the addition of the MEKAL component (i.e. a power-law, PEXRAV component and Gaussians modelling the Fe K emission, all absorbed by a Galactic column). The plot shows the divergence of the BI-XIS detector data (light grey) with that of the FI-XIS detectors (black) in the soft X-ray band (see Section 3.3.2).

The next step was to model the entire broad-band spectra by including the XIS data below 2.5 keV. The BI-XIS data were also re-included at this point. As the signal-to-noise ratio decreases at lower energies, the spectra were only considered down to 0.6 keV for each XIS. The data were also ignored from 1.7–1.9 keV so as not to include any uncertainties associated with the silicon absorption edge due to the detectors. The inclusion of these data resulted in a slightly worse fit with a null probability of 2.98×10^{-3}. Residuals were observed at energies < 2 keV hinting at the presence of a weak soft excess (e.g. Figure 3.3). Upon closer inspection of these residuals it was noted that the BI-XIS detector data slightly diverged with that of the remaining XIS detectors (Figure 3.7), even when the photon index of the power-law continuum was allowed to vary between detectors. As data from the three individual FI-XIS detectors were all self-consistent, this divergence was possibly caused by

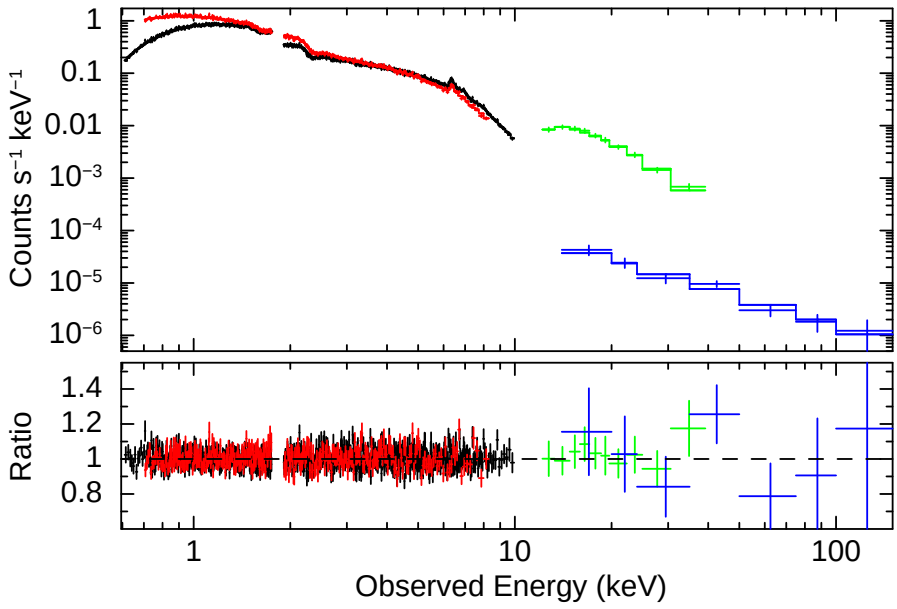

Figure 3.8: The broad-band *Suzaku* spectra of NGC 7213 (in the observed frame; FI XIS = black; BI XIS = red; HXD PIN = green) with the inclusion of the *Swift*-BAT spectra (blue). A plot of the ratio of the residuals to the best-fitting model described in Section 3.3.2 and Table 3.2 is shown in the lower panel. No further significant residuals are present.

calibration effects around the oxygen-K detector edge. To account for this, the data from the BI-XIS detector were ignored below 0.7 keV.

In an attempt to then model the observed soft excess, the neutral column of absorbing gas from Galactic hydrogen was firstly allowed to vary. However, this resulted in a column density that was consistent with zero with an upper limit of $N_{\rm H} < 7 \times 10^{18}\,{\rm cm}^{-2}$ while still leaving positive residuals in the soft X-ray band. Instead, a MEKAL (Mewe, Gronenschild & van den Oord 1985; Mewe, Lemen & van den Oord 1986; Kaastra 1992; Liedahl, Osterheld & Goldstein 1995) thermal plasma component was added to the model incorporating the emission spectrum from a collisionally-ionised hot diffuse gas (Starling et al. 2005). It is worth noting that a featureless blackbody component models the soft excess with an equally good fit as there are no strong lines. However, the blackbody model was not considered any further as the lack of evidence for a strong BBB (Wu, Boggess & Gull 1983) in the optical–UV SED

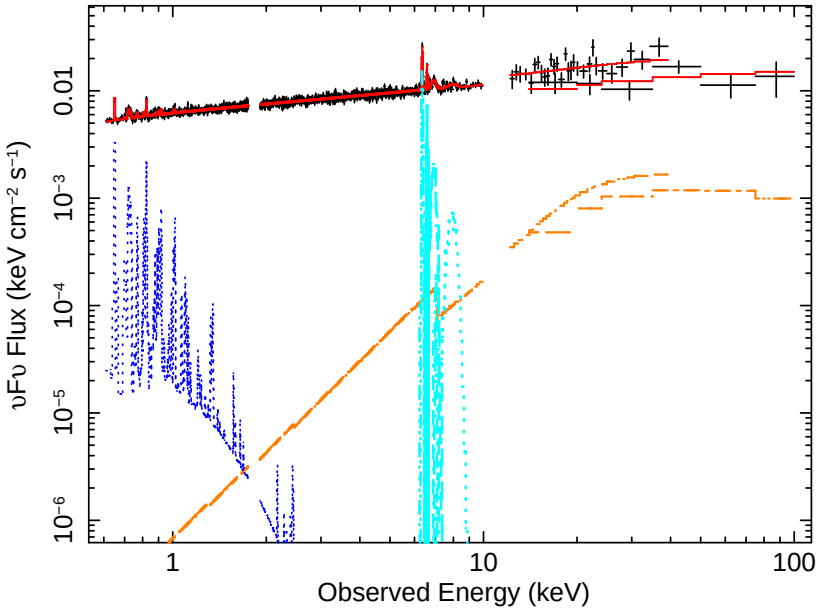

Figure 3.9: The relative contributions of the individual model components across the broad-band 0.6–100 keV *Suzaku*+BAT energy range for NGC 7213 (see Section 3.3.2 for details). The PEXRAV neutral reflection component is shown in orange over the 1–100 keV energy range while the soft collisionally-ionised MEKAL component (< 3 keV) is shown in navy blue. The emission in the Fe K complex is modelled with individual Gaussians and is shown in cyan. The red curve spanning the whole energy range shows the sum of all the model components (including the absorbed power-law continuum) superimposed on the data.

suggested little thermal emission directly from the disc (Starling et al. 2005). The addition of the MEKAL component gave a best-fitting thermal plasma temperature of $k_{\rm B}T = 0.27^{+0.05}_{-0.04}$ keV and resulted in an overall better fit with $\chi^2/d.o.f. = 1071/996$ compared to 1127/998 before the MEKAL component was added[6] (Figure 3.8). The luminosity of the MEKAL component was calculated to be $L = 2.14 \times 10^{40}\,{\rm erg\,s^{-1}}$ corresponding to only 1% of the the total luminosity in the 0.5–10 keV band. Note that with the MEKAL component included, the column density of the neutral absorber was found to have a best-fitting value of $N_{\rm H} = (9.3^{+2.8}_{-4.4}) \times 10^{19}\,{\rm cm^{-2}}$, consistent with the value of $N_{\rm H} = 1.1 \times 10^{20}\,{\rm cm^{-2}}$ derived from the 21 cm Galactic hydrogen

[6]Modelling the soft excess with an APEC component was also considered (http://hea-www.harvard.edu/APEC/; Smith et al. 2001) although at the *Suzaku* resolution here, the fit was identical to that obtained with the MEKAL thermal plasma.

Model Component	Fit Parameter	Value
Cut-off power law[a]	Γ	$1.74^{+0.01}_{-0.01}$
	High-energy cut-off	> 350
	Normalisation	$6.28^{+0.05}_{-0.03}$
Galactic absorption[b]	$N_{\rm H}$	1.10×10^{20}
PEXRAV[c]	$\|R\|$	$0.09^{+0.19}_{-0.08}$
MEKAL[d]	$k_{\rm B}T$	$0.27^{+0.05}_{-0.04}$
	Normalisation	$1.27^{+0.59}_{-0.38}$
	Luminosity	2.14×10^{40}
Fit statistics[e]	χ^2/d.o.f.	1071/996
	Null probability	4.98×10^{-2}

Table 3.2: Spectral parameters of the continuum fit to the broad-band *Suzaku* and *Swift*-BAT data in the 0.6–150 keV range for NGC 7213 (see Section 3.3.2 for details). [a] Γ, photon index; High-energy cut-off in units keV; Normalisation in units $\times 10^{-3}$ photons cm^{-2} s^{-1}. [b] Local Galactic absorption (at $z = 0$), units cm^{-2}. [c] $|R|$, reflection scaling factor, where a value $R = 1$ corresponds to reflection from neutral material subtending 2π sr. [d] $k_{\rm B}T$, plasma temperature in units keV; Normalisation (Emission Measure $= \int n_e n_{\rm H} dV$) in units $\times 10^{63}$ cm^{-3}. [e] Reduced chi-squared ($\chi^2/d.o.f.$) and null hypothesis probability for spectral fit.

studies of Dickey & Lockman (1990) and Kalberla et al. (2005). As no further significant residuals were observed in the spectra (Figure 3.8), this became the accepted broad-band model, the final parameters of which are summarised in Table 3.2. Note that the full broad-band model from 0.6–150 keV also resulted in a tighter constraint on the reflection scaling factor, R, the best-fitting value of which is shown in Table 3.2. However, the best-fitting parameters of the emission lines remained consistent within the errors with those quoted in Table 3.1. A plot of the relative unfolded model contributions is shown in Figure 3.9.

3.3.3 Comparison with Past Observations

3.3.3.1 XMM-Newton & BeppoSAX

Any long-term variations in the source were tested for by applying the best-fitting broad-band *Suzaku* model to the 2001 *XMM-Newton* (30 ks exposure; see Table 3.3) observation,

Date	Mission	Instrument	Exposure (ks)
2001-05-27	*BeppoSAX*	MECS	61
		PDS	38
2001-05-29	*XMM-Newton*	EPIC-pn	30
2004-12-15 - 2009-10-10	*Swift*	BAT	2300
2006-10-22	*Suzaku*	XIS + HXD	90
2007-08-06	*Chandra*	HETG	148
2009-11-11	*XMM-Newton*	EPIC-pn	83

Table 3.3: Observation log of NGC 7213. See Section 3.3.3 for details.

as published previously by Bianchi et al. (2003), Bianchi et al. (2004) and Starling et al. (2005). The ratio of the 2001 *XMM-Newton* EPIC-pn spectrum from 0.3–10 keV to the best-fitting *Suzaku* model, with continuum parameters described in Table 3.2, is shown in Figure 3.10. It can be seen that compared to the *Suzaku* XIS spectrum, the pn spectrum is steeper, while overall the flux was slightly lower in the *XMM-Newton* data with a value of $F = 2.19 \times 10^{-11}\,\mathrm{erg\,cm^{-2}\,s^{-1}}$ over the 2–10 keV energy range.

Simultaneous *BeppoSAX* PDS data (38 ks exposure; May 2001; see Table 3.3 and Bianchi et al. 2003) were then also included and fitted from 15–100 keV. The flux obtained from the *BeppoSAX* data was lower than that obtained with the *Suzaku* HXD over the 15–100 keV range (when the HXD model is extrapolated to higher energies; $F = 2.46 \times 10^{-11}$ compared to $F = 3.81 \times 10^{-11}\,\mathrm{erg\,cm^{-2}\,s^{-1}}$ respectively). Since the photon index of the power-law continuum is quite hard in this source, this difference could simply arise from small changes in the intrinsic power law. The model is generally in good agreement with the data although subtle changes in the continuum can be observed, with the spectral curvature being more apparent in the *XMM-Newton* data; e.g. with the spectrum being noticeably steeper below 2 keV, but somewhat flatter above 3 keV. No strong residuals are present in the Fe K band, which suggests that the Fe-line emission has remained constant between the 2001 *XMM-Newton* and 2006 *Suzaku* observations.

To quantify the changes in the spectrum, the single power-law continuum used to fit the *Suzaku* data in Sections 3.3.1 and 3.3.2 was replaced with a broken power law, breaking at $E_{\mathrm{break}} = 2.19^{+0.34}_{-0.30}$ keV with photon indices of $\Gamma = 1.84 \pm 0.01$ and $\Gamma = 1.71 \pm 0.02$ below

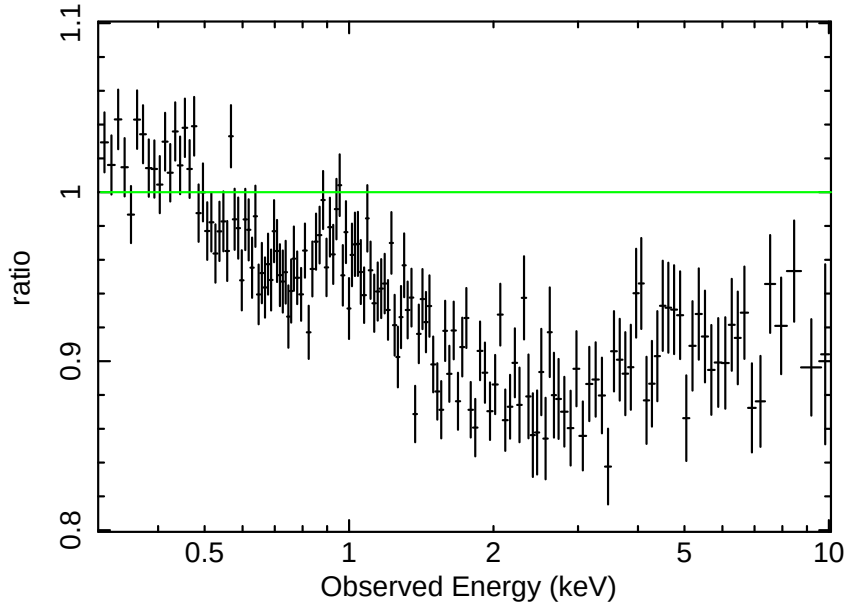

Figure 3.10: Data / model residuals of the 2001 *XMM-Newton* EPIC-pn data to the *Suzaku* model listed in Table 3.2 for NGC 7213. The *XMM-Newton* data show the source to have a slightly steeper spectrum compared to the *Suzaku* data at energies below 2 keV, while overall the continuum flux in the 2–10 keV band is lower in the *XMM-Newton* data in 2001 compared to in the *Suzaku* data in 2006. See Section 3.3.3 for details.

and above this energy break respectively. Furthermore, a slight softening of the spectrum below 1 keV in the *XMM-Newton* data, as suggested by the bump in the residuals at ∼0.9 keV (which may due to the Ne IX triplet or a blend of emission from Fe L-shell lines), indicates that the single temperature MEKAL component obtained from the *Suzaku* data was not sufficient to model the soft excess. Thus, a second MEKAL component was added to the model with a higher temperature of $k_{\rm B}T = 0.86^{+0.20}_{-0.14}$ keV, which significantly improved the fit ($\Delta\chi^2 = 19.2$) compared to the model with only a single temperature plasma. The parameters of this best-fitting model to the *XMM-Newton* + *BeppoSAX* data are summarised in Table 3.4 while Figures 3.11 and 3.12 show the data + residuals and the model components respectively.

For consistency, this two-temperature-MEKAL model was then applied to the 2006 *Suzaku* dataset (including data from all four XIS units and the HXD PIN). The temper-

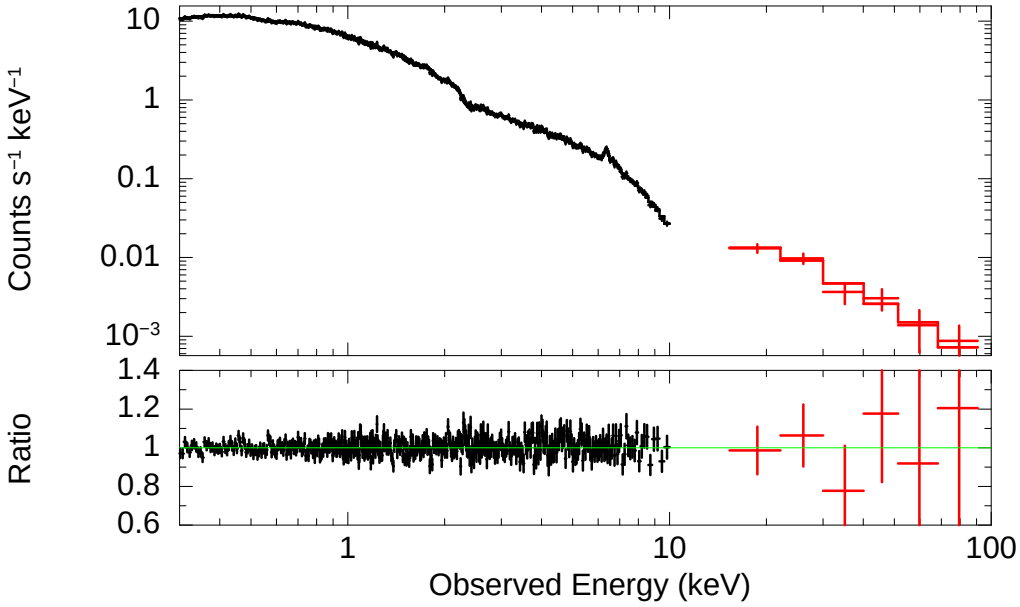

Figure 3.11: The broad-band *XMM-Newton* EPIC-pn (black) + *BeppoSAX* PDS (red) spectrum of NGC 7213 from 0.3–100 keV. The data are fitted with the model described in Section 3.3.3.1 and the residuals are shown in the lower panel.

atures and normalisations of the MEKAL were kept fixed at the best-fitting values acquired from the *XMM-Newton* + *BeppoSAX* data, as an extended diffuse collisional plasma may not be expected to vary significantly over time (note that if the parameters are allowed to vary, the values obtained from the *Suzaku* data are consistent with the *XMM-Newton* + *BeppoSAX* data, within the errors). The broken-power-law continuum parameterisation was also retained from the *XMM-Newton* + *BeppoSAX* fit, although the photon indices and normalisations were allowed to vary. A comparison of fit parameters for the *Suzaku* and *XMM-Newton* + *BeppoSAX* observations is shown in Table 3.4. No other significant variations were observed between the two observations; the Fe K line parameters are consistent with constant values (within the errors) for the centroid energy and line fluxes, while the 2001 *BeppoSAX* PDS data show no evidence for a reflection hump above 10 keV (with $R < 0.2$; see also Bianchi et al. 2004), consistent with what is found with the *Suzaku* HXD.

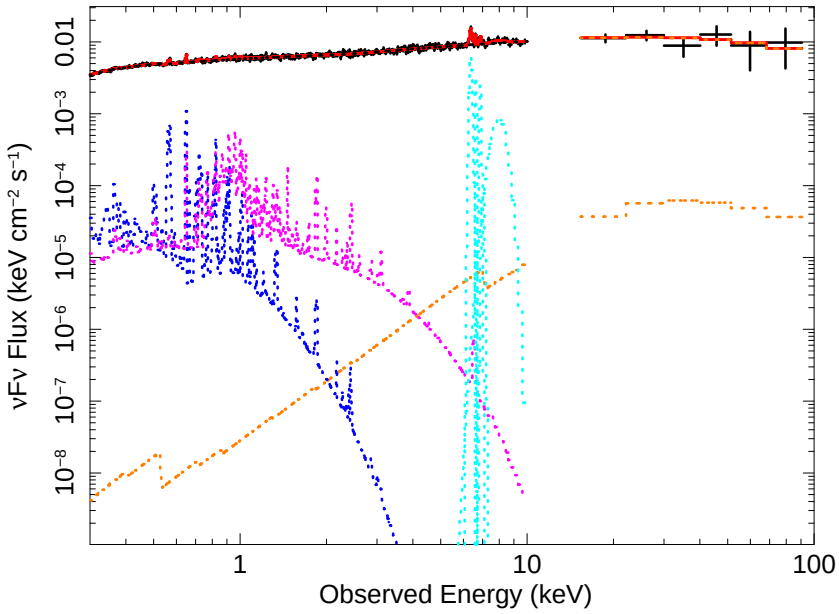

Figure 3.12: The relative contributions of the individual model components from the *XMM-Newton* + *BeppoSAX* fit described in Section 3.3.3.1. The PEXRAV reflection component is shown in orange and the lower- and higher-temperature MEKAL components are shown in navy and magenta respectively. The individual Gaussians are shown in cyan and the red curve shows the overall model (including the absorbed power law) superimposed on the data.

3.3.3.2 Chandra HETG

In Section 3.3.1, the emission line at 6.60 keV in the *Suzaku* XIS spectrum was found to be rejected at the $> 99.9\%$ confidence level as arising from the resonance transition of He-like Fe (see Figure 3.6). As a consistency check, the archival *Chandra* HETG spectrum was analysed (using the latest version of the calibration database; v.4.2.2). A comparison of the HETG spectrum to the best-fitting *Suzaku* model described in Section 3.3.1 is shown in Figure 3.13. The HETG Fe K band was then modelled with an absorbed power law and the emission lines were parameterised with simple Gaussians, consistent with the values found by Bianchi et al. (2008) (also see Table 3.4) with emission at 6.40, 6.72 and 6.99 keV (see Figure 3.14). Fixing an additional narrow line ($\sigma = 10$ eV) at 6.60 keV (as required by the *Suzaku* data) in the HETG spectrum was not required by the data but resulted in a value for the equivalent width

Model Component	Fit Parameter	*Suzaku*	*XMM-Newton* & *BeppoSAX*	*Chandra* HETG	*XMM-Newton*
Obs. Date	-	22-10-2006	29-05-2001	06-08-2007	11-11-2009
Flux[a]	$F_{0.5-2}$	1.37	1.29	-	0.71
	F_{2-10}	2.44	2.19	2.32	1.20
	F_{15-100}	3.81	2.46	-	-
Broken power law	Γ_1	$1.94^{+0.09}_{-0.06}$	$1.84^{+0.01}_{-0.01}$	$1.69^{+0.01}_{-0.01}$	$1.88^{+0.01}_{-0.01}$
	$E_{\rm break}$	$0.93^{+0.06}_{-0.07}$	$2.19^{+0.34}_{-0.30}$	-	$1.66^{+0.19}_{-0.12}$
	Γ_2	$1.74^{+0.01}_{-0.01}$	$1.71^{+0.02}_{-0.02}$	-	$1.71^{+0.01}_{-0.02}$
	Norm.	$6.11^{+0.09}_{-0.16}$	$5.92^{+0.03}_{-0.04}$	$5.65^{+0.03}_{-5.65}$	$3.21^{+0.02}_{-0.02}$
MEKAL[c]	$k_{\rm B}T_1$	FIXED	$0.24^{+0.07}_{-0.06}$	-	-
	Norm.$_1$	FIXED	$6.60^{+4.06}_{-3.81}$	-	-
	$k_{\rm B}T_2$	FIXED	$0.86^{+0.20}_{-0.14}$	-	$0.75^{+0.08}_{-0.09}$
	Norm.$_2$	FIXED	$7.63^{+2.74}_{-2.65}$	-	$3.65^{+0.35}_{-0.35}$
	$L_{\rm total}$	1.99	1.99	-	0.86
Fe Kα Line[d]	$E_{\rm c}$	$6.39^{+0.01}_{-0.01}$	$6.40^{+0.02}_{-0.02}$	$6.40^{+0.01}_{-0.01}$	$6.43^{+0.01}_{-0.01}$
	σ	< 0.05	< 0.07	$2.23^{+1.01}_{-0.56} \times 10^{-2}$	$4.94^{+2.22}_{-2.70} \times 10^{-2}$
	EW	$80.7^{+18.6}_{-15.4}$	$85.9^{+14.0}_{-14.4}$	120^{+40}_{-30}	141^{+16}_{-16}
	Line flux	$2.12^{+0.27}_{-0.32}$	$2.33^{+0.38}_{-0.39}$	$2.9^{+0.9}_{-0.7}$	$1.91^{+0.22}_{-0.22}$
Fe XXV Line[d]	$E_{\rm c}$	$6.60^{+0.03}_{-0.04}$	$6.66^{+0.04}_{-0.05}$	$6.72^{+0.01}_{-0.02}$	$6.72^{+0.03}_{-0.03}$
	σ	< 0.17	< 0.14	< 0.08	< 0.09
	EW	$23.0^{+10.5}_{-7.2}$	$27.4^{+11.6}_{-11.6}$	24^{+17}_{-17}	50^{+13}_{-13}
	Line flux	$0.64^{+0.20}_{-0.21}$	$0.78^{+0.33}_{-0.33}$	$0.7^{+0.5}_{-0.5}$	$0.72^{+0.18}_{-0.18}$
Fe XXVI Line[d]	$E_{\rm c}$	$6.95^{+0.03}_{-0.03}$	$6.91^{+0.08}_{-0.08}$	$6.99^{+0.02}_{-0.01}$	$7.01^{+0.04}_{-0.05}$
	σ	$0.10^{+0.04}_{-0.04}$	$0.07^{+0.06}_{-0.03}$	< 0.11	< 0.07
	EW	$55.9^{+13.2}_{-15.7}$	$37.1^{+18.8}_{-18.8}$	60^{+30}_{-30}	53^{+20}_{-16}
	Line flux	$1.28^{+0.32}_{-0.29}$	$0.89^{+0.45}_{-0.45}$	$1.3^{+0.6}_{-0.6}$	$0.63^{+0.24}_{-0.19}$
Statistics	$\chi^2/d.o.f.$	1061/991	846/872	-	1633/1571
	Null probability	0.06	0.73	-	0.14

Table 3.4: Spectral parameters of the broad-band fit in the 0.6–150 keV energy range for the 2006 *Suzaku*, 2001 simultaneous *XMM-Newton* and *BeppoSAX* and the 2009 *XMM-Newton* observations of NGC 7213 (see Section 3.3.3 for details). The Fe-line-complex parameters from the 2007 *Chandra* HETG observation (reported by Bianchi et al. 2008) are also shown for ease of comparison. [a] Continuum flux in the specified range in units $\times 10^{-11}\,{\rm erg\,cm^{-2}\,s^{-1}}$. [b] Γ, photon index; $E_{\rm break}$ in units keV; Normalisation in units $\times 10^{-3}$ photons $\rm cm^{-2}\,s^{-1}$. [c] $k_{\rm B}T$, plasma temperature in units keV; Normalisation ($= \int n_e n_{\rm H} dV$) in units $\times 10^{62}\,{\rm cm^{-3}}$; Total MEKAL luminosity from 0.5–10 keV in units $10^{40}\,{\rm erg\,s^{-1}}$. All MEKAL fit parameters in the *Suzaku* dataset are fixed at the best-fitting values from the *XMM-Newton* data. [d] $E_{\rm line}$, line energy in units keV; σ, intrinsic width in units keV; EW, equivalent width in units eV; Line Flux in units $\times 10^{-5}$ photons $\rm cm^{-2}\,s^{-1}$.

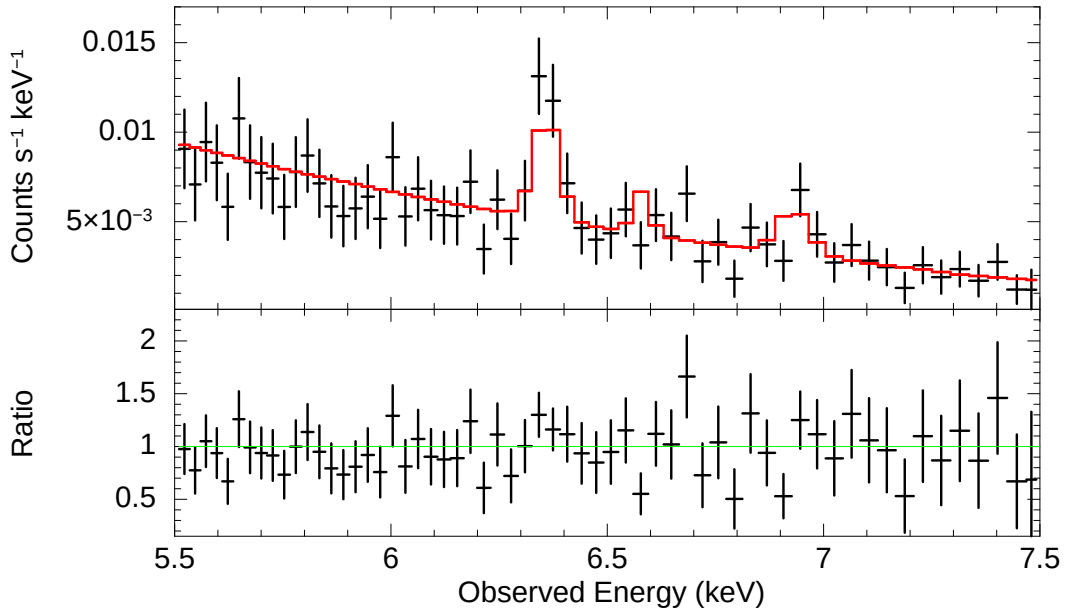

Figure 3.13: The 2007 *Chandra* HETG spectrum compared to the best-fitting *Suzaku* model described in Section 3.3.1. The HEG data are shown in black and are binned up by a factor of 2 for clarity. Note how the *Suzaku* model (red) slightly over-predicts the flux at ∼6.6 keV and slightly under-predicts the flux at ∼6.7 keV in the HETG data. The residuals are shown in the lower panel. See Section 3.3.3.2 for details.

of EW < 21.2 eV and an upper limit on the line-flux of $F_{\rm line} < 5.1 \times 10^{-6}$ photons cm^{-2} s^{-1}, which is consistent with the flux of $F_{\rm line} = (6.4^{+2.0}_{-2.1}) \times 10^{-6}$ photons cm^{-2} s^{-1} found with the *Suzaku* XIS. Likewise, including a narrow Gaussian in the *Suzaku* spectrum with the centroid energy fixed at 6.72 keV (as found with *Chandra*) is also not required by the XIS data but yields an upper limit on the equivalent width of EW < 14.3 eV and an upper limit on the line-flux of $F_{\rm line} < 5.7 \times 10^{-6}$ photons cm^{-2} s^{-1}, again consistent with the flux of $F_{\rm line} = (7 \pm 5) \times 10^{-6}$ photons cm^{-2} s^{-1} reported by Bianchi et al. (2008) with the *Chandra* HETG. Therefore, this suggests that the Fe K parameters in both datasets are consistent with each other with no evidence of variability detected within the errors.

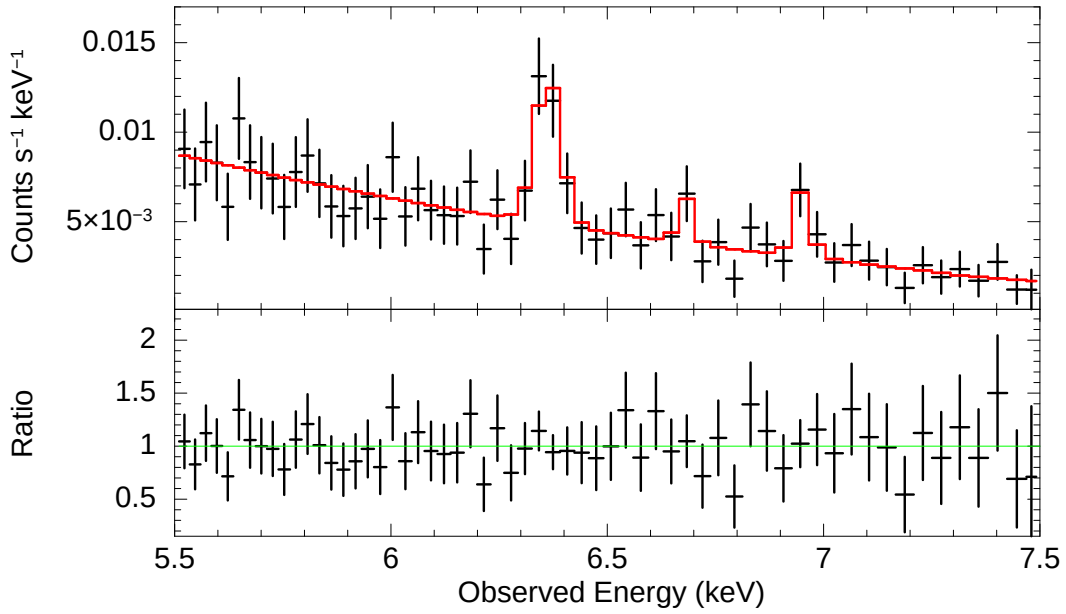

Figure 3.14: The 2007 *Chandra* HETG spectrum shown over the Fe K band in the 5.5–7.5 keV energy range. The HEG data are shown in black and are binned up by a factor of 2 for clarity. The best-fitting model is overplotted in red and shows emission from near-neutral Fe Kα, Fe XXV $1s$–$2p$ resonance and Fe XXVI Lyα (from left to right). The residuals are shown in the lower panel. See Section 3.3.3.2 for details.

3.3.3.3 A More Recent XMM-Newton Observation

NGC 7213 was also observed again with *XMM-Newton* in 2009 (Emmanoulopoulos et al. 2012; Emmanoulopoulos et al. 2013) with an EPIC-pn exposure time of ∼83 ks. The flux was found to have dropped by a factor of ∼2 in comparison with previous observations ($F_{2-10} = 1.20 \times 10^{-11}$ erg cm^{-2} s^{-1}; $L_{2-10} = 9.04 \times 10^{41}$ erg s^{-1}), as shown in Figure 3.15. The data again require a broken power law breaking at $E_{\rm break} = 1.66^{+0.19}_{-0.12}$ keV with photon indices of $\Gamma = 1.88 \pm 0.01$ and $\Gamma = 1.71^{+0.01}_{-0.02}$ at energies below and above the break respectively. To account for further softening of the spectrum at low energies, a thermal plasma component was included in the model again using the MEKAL code. This component requires a best-fitting temperature of $k_{\rm B}T = 0.75^{+0.08}_{-0.09}$ keV, consistent with previous datasets, and improves the fit statistic by $\Delta\chi^2 = 53$. However, including a second thermal plasma component with

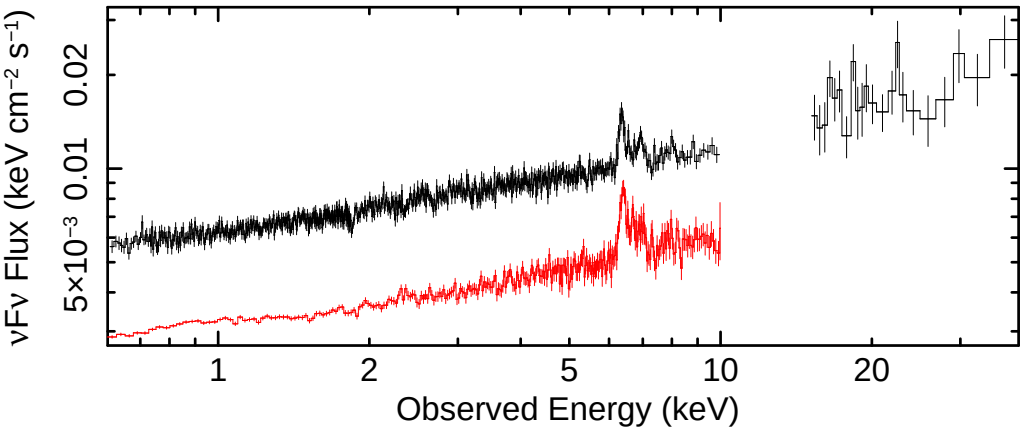

Figure 3.15: The 2006 *Suzaku* XIS + HXD data (black) and the 2009 *XMM-Newton* EPIC-pn data (red) for NGC 7213. The data are unfolded against a power law of photon index $\Gamma = 2$. Note that, while the spectral shape appears to have changed very little between observations, the flux of the *XMM-Newton* data at energies <10 keV is lower than that of the *Suzaku* data by a factor of ∼2.

a temperature of $k_{\rm B}T \sim 0.2$ keV, consistent with the best-fitting value from the 2001 *XMM-Newton* observation (Section 3.3.3.1), is not required here. This indicates that these data can be explained with a simple single-temperature component.

Regarding the Fe K profile, a ratio plot of the residuals in the Fe K band compared with those found with *Suzaku* is shown in Figure 3.16. The data can again be well-fitted with three narrow Gaussian emission lines (see Figures 3.17 and 3.18). The strongest of these lines is the Fe Kα emission line from near-neutral material ($E_{\rm c} = 6.43 \pm 0.01$ keV; FWHM $= 5\,300^{+2\,400}_{-2\,900}$; $\Delta\chi^2 = 300$). The flux of this line has remained unchanged within the errors between observations ($F = (1.91 \pm 0.22) \times 10^{-5}$ photons cm^{-2} s^{-1}; see Table 3.4) with its equivalent width increasing to EW $= 141 \pm 16$ eV against the observed continuum suggesting that the line is not responding to changes in the continuum. Note that the corresponding Fe Kβ line was also included for consistency at 7.06 keV with its flux fixed at 13% of the Fe Kα line (as per the expected branching ratio; see Kaastra & Mewe 1993), although it was not formally required by the data. A second line at $E_{\rm c} = 7.01^{+0.04}_{-0.05}$ keV was also modelled ($\Delta\chi^2 = 38$) and is most likely the emission signature of Fe XXVI. The parameters of this line

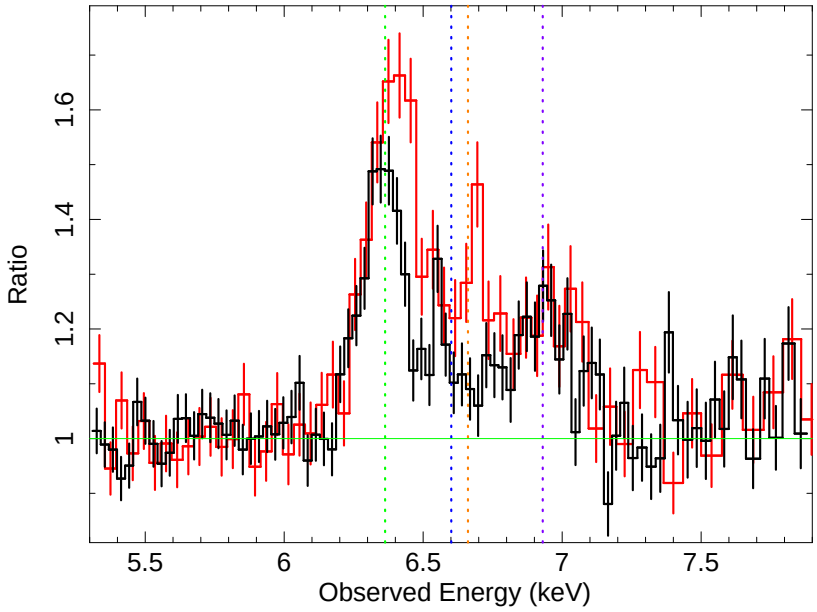

Figure 3.16: The ratio of the data-to-model residuals of the 2009 *XMM-Newton* EPIC-pn NGC 7213 data in the Fe K band compared to a power-law model are shown in red. For comparison, the *Suzaku* XIS data are shown in black. Both spectra are binned up by a factor of 5 for clarity. The vertical dotted lines show the expected line energies of, from left to right, Fe Kα (green), Fe XXV forbidden (navy), Fe XXV $1s$–$2p$ resonance (orange), Fe XXVI $1s$–$2p$ Lyα (orange) and Fe Kβ (magenta) in the observed frame.

are once again largely consistent with previous observations apart from the line flux which has dropped by a factor of $\sim$2 when compared to previous observations (i.e. with *Suzaku* and *Chandra*). Coupled with the fact that the continuum flux had also dropped by a factor of $\sim$2 when observed with *XMM-Newton* in 2009, it could be the case that this line responds to changes in the continuum.

A third strong emission line is also observed, most likely originating from Fe XXV. However, the line requires a best-fitting centroid energy of $E_{\rm c} = 6.72 \pm 0.03$ keV, implying that the line is consistent with the resonance transition but not the forbidden transition of Fe XXV which is in contrast with the result found with the *Suzaku* XIS ($E_{\rm c} = 6.60 \pm 0.03$ keV; Section 3.3.1), which appeared to rule out the resonance transition as the origin of the line (see Figure 3.6). A line energy vs. line-flux contour plot for this line in the EPIC-pn data

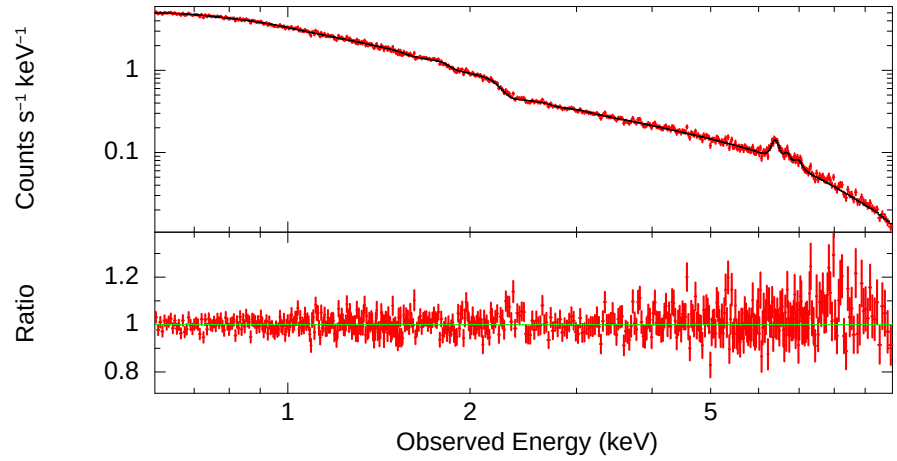

Figure 3.17: The 2009 *XMM-Newton* spectrum of NGC 7213 modelled with an absorbed power law, a soft thermal emission component and Gaussians to account for emission from Fe K (see Section 3.3.3.3 for details). The residuals against the model are shown in the lower panel.

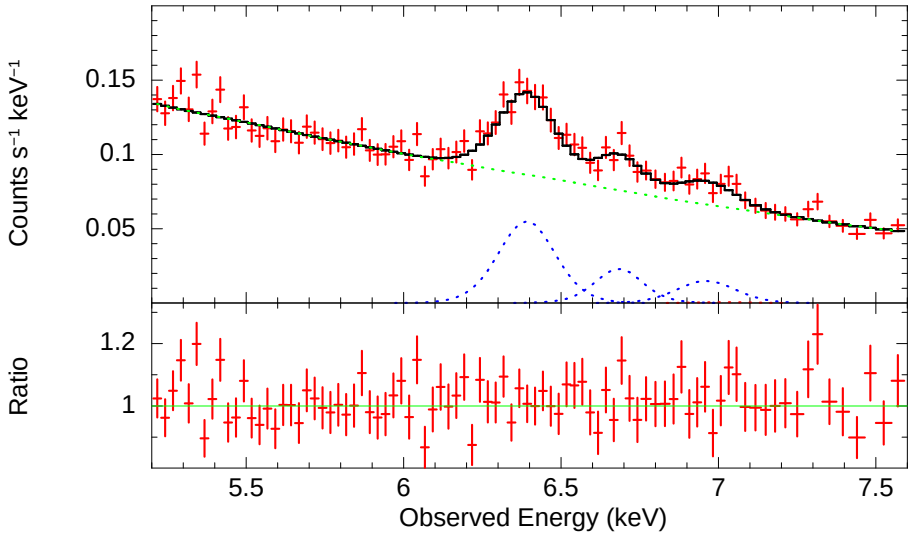

Figure 3.18: The 2009 *XMM-Newton* spectrum of NGC 7213 in the Fe K band modelled with an absorbed power law (green) and the emission lines (navy) described in Section 3.3.3.3 and Table 3.4.

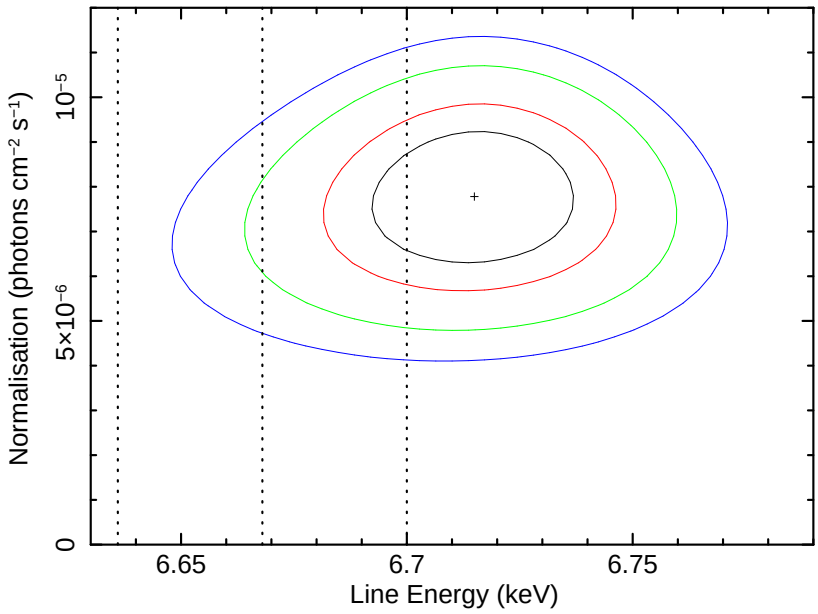

Figure 3.19: A two-dimensional contour plot between line-energy and normalisation of the 6.72 keV line in the *XMM-Newton* EPIC-pn NGC 7213 data at the 68%, 90%, 99% and 99.9% confidence intervals (inner to outer contours respectively) for 2 parameters of interest. The vertical dashed lines show the rest energies of the forbidden, intercombination and resonance transitions of the Fe XXV triplet at 6.637, 6.668 and 6.700 keV respectively. In the *Suzaku* XIS dataset, the corresponding line has an energy of ∼6.60 keV and is associated with the forbidden transition. In comparison, the line here (∼6.72 keV) is associated with the resonance transition. However, a common origin for the two lines cannot be ruled out, as shown in Section 3.3.3.3.

is shown in Figure 3.19 and shows that although the forbidden transition is ruled out by the data at the $> 99.9\%$ confidence level, a common origin for the line in the two datasets cannot be completely ruled out.

To test this further, the *XMM-Newton* EPIC-pn and *Suzaku* XIS datasets were modelled simultaneously over the 2.5–10 keV energy band with a power law and simple Gaussians to parameterise the emission lines. All the emission line parameters were left free except for the centroid energy and the intrinsic width of the Fe XXV emission line which were tied together between the two datasets. Upon fitting, the line was found to have a best-fitting centroid energy of $E_{\rm c} = 6.66^{+0.06}_{-0.09}$ keV, consistent with the rest-energies of both the resonance

and forbidden transitions. Furthermore, untying the parameters and allowing them to go free marginally improves the fit statistic by $\Delta\chi^2 \sim 5$ also indicating that a common origin for the line cannot be ruled out between datasets. It should be noted that it is also difficult to rule out any contribution from the intercombination lines of Fe XXV at $\sim$6.67 keV or a blend of emission from Fe of intermediate-ionisation states (e.g. Fe XXIII-XXIV). Finally, as a consistency check (as in Section 3.3.3.2), an additional narrow emission line ($\sigma = 10$ eV) was fixed at 6.60 keV (as required by the *Suzaku* XIS spectrum) in the EPIC-pn spectrum. This was not found to be statistically required by the data but resulted in a constraint on the flux of the line of $F_{\rm line} < 5.8 \times 10^{-6}$ photons cm^{-2} s^{-1}; a value consistent with the flux of the same line found with the *Suzaku* XIS (i.e. $F_{\rm line} = (6.4^{+2.0}_{-2.1}) \times 10^{-6}$ photons cm^{-2} s^{-1}). This suggests that no significant variability of this line can be detected within the errors between observations.

Note that the presence of the emission line at $\sim$8 keV detected with the *Suzaku* XIS (see Figure 3.4) was tested for in the EPIC-pn data. Although its inclusion in the model is significant ($\Delta\chi^2 = 12$), the line is unresolved and its parameters are very difficult to constrain (i.e. $E_{\rm c} = 7.92^{+0.72}_{-0.49}$). Therefore, its origin still remains somewhat ambiguous. So overall the Fe K emission line parameters are largely consistent with the values found from previous *Suzaku*, *Chandra* and *XMM-Newton* observations but with the equivalent widths against the observed continuum increasing as the source flux drops. The constancy in flux of the near-neutral Fe Kα emission line is strongly supportive of the notion of an origin in distant material (i.e. the dusty torus or BLR clouds). However, the Fe XXVI emission line is a possible exception as its flux may respond to changes in the continuum and so is perhaps the signature of material closer to the black hole.

The presence of a neutral reflection component was also tested for in the EPIC-pn data with the inclusion of a PEXRAV component with the photon index and normalisation tied to that of the intrinsic (illuminating) power law in the usual way (see Section 3.3.2). However, this component was not statistically required by the data and returned a best-fitting value for the reflection strength of $R < 0.67$. This again implies that NGC 7213 frequently exhibits no evidence for a significant reflection component, consistent with previous findings. The large errors on this component could perhaps be a result of not having simultaneous broad-

band coverage in this dataset; i.e. >10 keV. The *Swift*-BAT data are time-averaged over a 58-month period and so cannot be used to constrain a robust measurement of the reflection strength here; especially since the source flux from 0.5–10.0 keV has been observed to vary by a factor of ∼2 between observations. The presence of a high-energy cut-off was also tested for with the *XMM-Newton*+BAT data by including the HIGHECUT model within XSPEC. However, a high-energy cut-off is not required by these data with the 90% lower limit on the cut-off constrained to be $E_{\rm cut} > 200$ keV. This is largely consistent with the analysis of the broad-band *Suzaku* data in Section 3.3.2 where the 90% lower limit was constrained to be $E_{\rm cut} > 350$ keV.

An attempt was also made to account for the variability of the source by modelling the two *XMM-Newton* EPIC-pn datasets simultaneously (see Figure 3.20). The model consisted of a broken power law, Gaussians to model the Fe K emission (as described above) and two MEKAL thermal plasma components ($k_{\rm B}T_1 \sim 0.3$ keV; $k_{\rm B}T_2 \sim 0.7$ keV; although the normalisation of the lower-temperature component was set to 0 in the 2009 dataset as this component is not required by the data). This modelled the data well and it was found that the variability between the two spectra can be accounted for simply by tying together all model parameters between the two datasets except for the normalisation of the intrinsic power law which, when allowed to vary, drops from $(5.96^{+0.03}_{-0.04}) \times 10^{-3}$ to $(3.23^{+0.01}_{-0.02}) \times 10^{-3}$ photons cm^{-2} s^{-1} between the 2001 and 2009 *XMM-Newton* spectra respectively. This yields a good fit to the data with $\chi^2/d.o.f. = 3041/3007$ (null hypothesis probability = 0.33). It should also be noted that all other model parameters are consistent between the two datasets when untied and allowed to vary which strongly suggests that the long-term variability in this source can be accounted for simply by changes in the flux of the intrinsic power-law continuum, consistent with the trend for the X-ray flux in this source to have been gradually decreasing since 1980 (Bell et al. 2011).

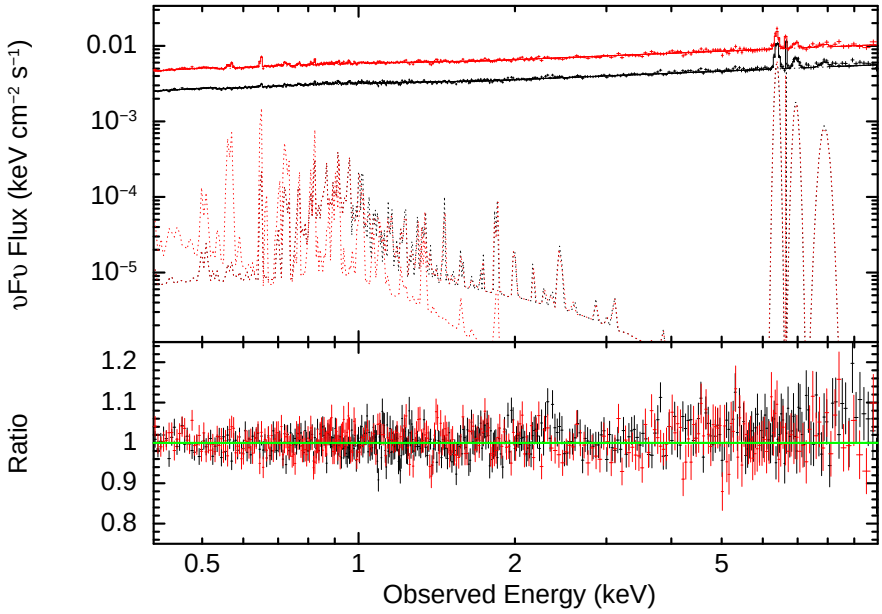

Figure 3.20: The contribution of the various model components to the two *XMM-Newton* NGC 7213 spectra in the observed frame. The 2001 data are shown in red and the 2009 data are shown in black. The long-term spectral variability can be accounted for by simple changes in the normalisation of the intrinsic power law with the other components remaining largely constant between observations.

3.4 Discussion

In this section the possible origin of both the neutral and ionised Fe K line emission from NGC 7213 will be discussed along with its implications for the nature of the central engine in this source.

3.4.1 The Origin of the Neutral Fe Kα Line

The possibility of whether a distant Compton-thick reflector, e.g. such as the pc-scale torus, could account for the neutral Fe Kα emission was firstly investigated. The tight constraint on the reflection fraction of $R = 0.09^{+0.19}_{-0.08}$, obtained in Section 3.3.2 (also see Table 3.2), may rule out the possibility of the 6.39 keV line originating via scattering off Compton-thick matter since, for an Fe Kα line with an EW $\sim$ 80 eV (as observed here), a strong

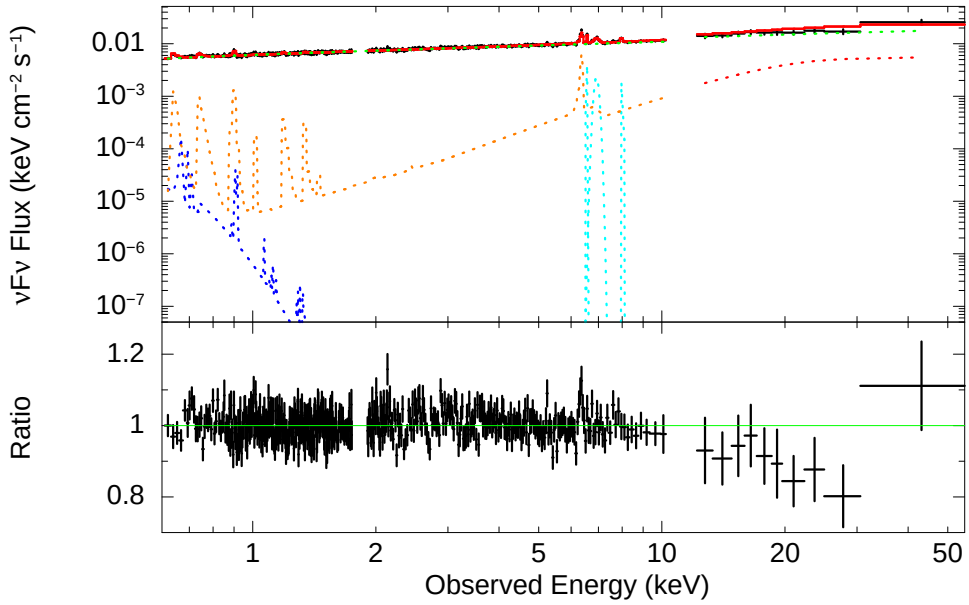

Figure 3.21: The additive model components described in Section 3.4.1 when modelling the broad-band *Suzaku* spectrum of NGC 7213. The components include a soft thermal plasma (MEKAL; blue), a neutral reflector (REFLIONX; orange) and Gaussians to model ionised emission (cyan). Without invoking highly super-solar abundances of Fe, the model under-predicts the flux from Fe Kα emission while over-predicting the hard X-ray flux. The residuals are shown in the lower panel.

reflection scaling factor value of $R \approx 0.6$ would be required (George & Fabian 1991). To test this further, the ionised reflection model REFLIONX (Ross & Fabian 2005) was used in place of the simple 6.39 keV Gaussian emission and PEXRAV model for the Compton-scattered continuum off neutral material and applied to the *Suzaku* XIS and HXD-PIN data (Figure 3.21). As in Section 3.3.1, the BI-XIS data are excluded from the following fits due to the lower effective area of the BI CCD in the Fe K band. The other model components, as described in Section 3.3.2 (also see Table 3.1 and Table 3.2), were adopted and are identical in the spectral fits. The REFLIONX model consists of the emergent spectrum for a photo-ionised optically-thick slab of gas when irradiated by a power-law spectrum, with a high-energy exponential cut-off at $E_{\rm cut} = 300$ keV, using the abundances of Anders & Ebihara (1982). The advantage of the REFLIONX model is that it self-consistently computes both the reflected

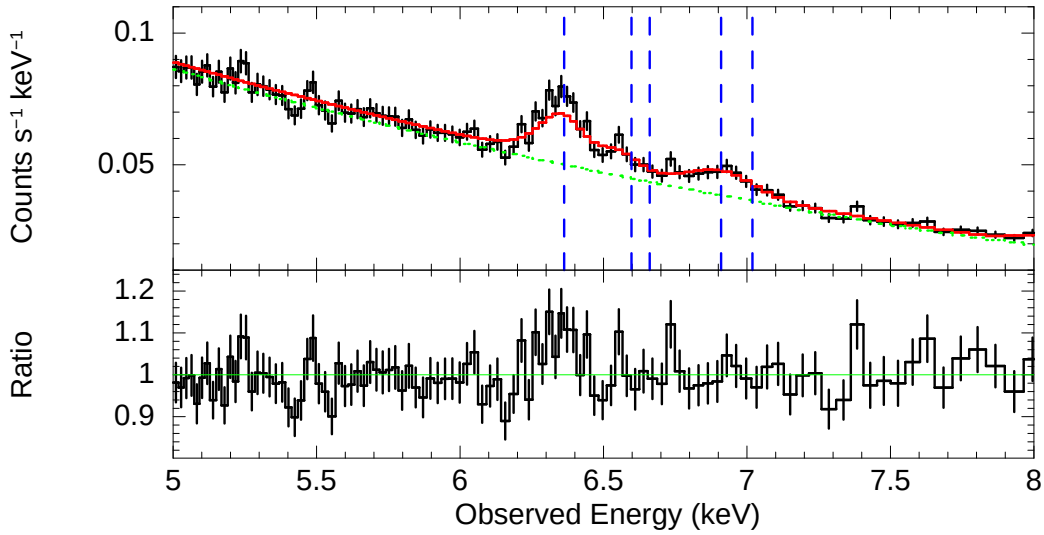

Figure 3.22: A plot showing the inability of the REFLIONX reflection component to account for the emission from near-neutral Fe Kα at $\sim$6.4 keV. The vertical dashed lines show the expected energies (in the observed frame) of, from left to right, Fe Kα, Fe XXV forbidden, Fe XXV 1s–2p resonance, Fe XXVI Lyα and Fe Kβ. See Section 3.4.1 for details.

continuum and line emission for the astrophysically abundant elements. The details of the REFLIONX model and its parameters are described in Section 2.5.1.

The Fe abundance was initially fixed to the solar value, while the redshift of the reflector was found to be consistent with the cosmological redshift of the source, with no net (e.g. gravitational) redshift. Since the Fe Kα emission line observed in the *Suzaku* spectrum was observed to be narrow and unresolved, no additional velocity broadening was applied to the reflected spectrum. The reflector ionisation parameter[7] was also fixed at a value of $\xi = 1\,\mathrm{erg\,cm\,s^{-1}}$ (the lowest value allowed by the model), corresponding to near-neutral Fe (i.e. Fe atoms typically in a low-ionisation state corresponding to Fe I–XVII). This model provides an upper limit on the reflection scaling factor of $R < 0.16$, consistent with what was found by the PEXRAV model in Section 3.3, but results in a relatively poor fit to the *Suzaku*

[7]Note that in the REFLIONX ionised reflection model the ionisation parameter is defined as $\xi = \frac{4\pi F}{n}$ and has units $\mathrm{erg\,cm\,s^{-1}}$, where F is the illuminating flux incident upon the reflector (integrated over the energy range 100 eV to 1 MeV) and n is the gas density in $\mathrm{cm^{-3}}$.

+ BAT data of $\chi^2/d.o.f. = 810/715$ (null probability $= 7.22 \times 10^{-3}$). This is due to the fact that the model over-predicts the hard-X-ray flux (i.e. in the HXD-PIN band) while it under-predicts the amount of Fe Kα emission, leaving a significant positive residual at $\sim$6.4 keV in the *Suzaku* XIS data (see Figures 3.21 and 3.22). Allowing the Fe abundance to vary to enhance the Fe K emission results in a better fit with $\chi^2/d.o.f. = 745/714$ corresponding to a null hypothesis probability of 0.21 (with $R < 0.06$). However, in order to adequately model the Fe Kα line, this requires an overabundance of Fe by a factor of ~ 10 with respect to the solar value (the 90% confidence lower limit on this value is still 4 times solar).

It therefore appears that the lack of an observed Compton-reflection hump in the data above 10 keV means that the reflection and Fe Kα emission cannot be simultaneously modelled in this way, seemingly ruling out a reflection origin for the Fe Kα emission, as also suggested by Bianchi et al. (2003) on the basis of the *BeppoSAX* data. Indeed, a more acceptable fit can only be obtained if the abundances are assumed to be greatly super-solar, at odds with the modest spread of values found by Perola et al. (2002) from a sample of nine bright type-1 Seyfert galaxies and narrow emission-line galaxies (NELGs) observed with *BeppoSAX*. Thus it is unlikely that the 6.39 keV emission originates via reflection off Compton-thick matter unless the material covers a very small solid angle (< 1 sr) and is extremely Fe-over-abundant.

Instead it is perhaps more likely that the near-neutral Fe Kα line originates in Compton-thin matter, covering a higher fraction of 4π sr solid angle. Indeed, an estimate of the column density of the Kα-emitting material can be made using the calculations of Yaqoob et al. (2010) where an analytic expression relating the efficiency of the Fe Kα line production and the column density of the emitting material is derived in the optically-thin limit. The production efficiency of the Fe Kα line is calculated by:

$$\chi_{\mathrm{Fe\,K}\alpha} = \frac{I_{\mathrm{Fe\,K}\alpha,\mathrm{n}}}{\int_{E_\mathrm{K}}^{\infty} E^{-\Gamma} dE}. \tag{3.1}$$

Here, E_K is the threshold energy for Fe K-shell absorption and $I_{\mathrm{Fe\,K}\alpha,\mathrm{n}}$ refers to the line flux renormalised to an incident continuum with a flux of 1 photon cm^{-2} s^{-1} keV^{-1} at 1 keV. Γ is the photon index assuming an incident power-law continuum. Adopting the Verner et al. (1996) value of $E_\mathrm{K} = 7.124$ keV, an Fe Kα line production efficiency of $\sim$1% can be calculated

for NGC 7213. In the Compton-thin case, it can be found that this results in an estimate of the column density of the Kα-emitting material of $N_{\rm H} \sim 2 \times 10^{23}\,{\rm cm}^{-2}$ using the analytic expression derived by Yaqoob et al. (2010):

$$\begin{aligned} \chi_{\rm Fe\,K\alpha} &= 0.00482 \left(\frac{\Delta\Omega}{4\pi}\right) \left(\frac{\omega_{\rm K}}{0.347}\right) \left(\frac{\omega_{\rm K\alpha}}{\omega_{\rm K}}\right) \left(\frac{A_{\rm Fe}}{4.68 \times 10^{-5}}\right) \\ &\times \left(\frac{\sigma_0}{3.37 \times 10^{-20}\,{\rm cm}^2}\right) N_{22} f\left(\Gamma\right) \quad (\Gamma > 1)\,, \end{aligned} \tag{3.2}$$

where

$$f\left(\Gamma\right) \equiv \frac{\Gamma - 1}{\Gamma + \alpha - 1}. \tag{3.3}$$

Here, the quantity $\Delta\Omega/4\pi$ is the covering fraction (i.e. the fractional solid angle that the line-emitting material subtends to the source), $\omega_{\rm K}$ and $\omega_{\rm K\alpha}$ are the respective fluorescence yields for the Fe K-shell and the Fe Kα line only and $A_{\rm Fe}$ is the abundance of Fe relative to hydrogen assuming the abundances of Anders & Grevesse (1989). The quantity σ_0 is the Fe K-shell absorption cross-section at $E_{\rm K}$ and α is the power-law index of the cross-section. Using the adopted values of Verner et al. (1996), $\sigma_0 = 3.37 \times 10^{-20}\,{\rm cm}^2$ and $\alpha = 2.67$. Finally, N_{22} is the column density in units $10^{22}\,{\rm cm}^{-2}$. Yaqoob et al. (2010) adopt a value of 0.135 for the Fe Kβ/Fe Kα branching ratio leading to $\omega_{\rm K\alpha}/\omega_{\rm K} = 0.881$.

Although the estimated value is consistent with that found by Bianchi et al. (2008), the expression is valid only in the Compton-thin limit which begins to break down for $N_{\rm H} > 2 \times 10^{22}\,{\rm cm}^{-2}$ as the optical depth of the Fe K line photons to absorption and scattering becomes non-negligible (see Figure 3.23). However, accounting for these effects, according to the calculations of Yaqoob et al. (2010) and Murphy & Yaqoob (2009), a column density of $N_{\rm H} \sim 3 - 4 \times 10^{23}\,{\rm cm}^{-2}$ can result in an Fe Kα line efficiency of 1% for a face-on geometry covering 2π sr in their toroidal X-ray reprocessor model. Thus the Fe Kα line may originate in a Compton-thin torus or perhaps the outer BLR clouds, as suggested by Bianchi et al. (2005), although the covering fraction would perhaps be slightly high in the latter case (Netzer & Laor 1993).

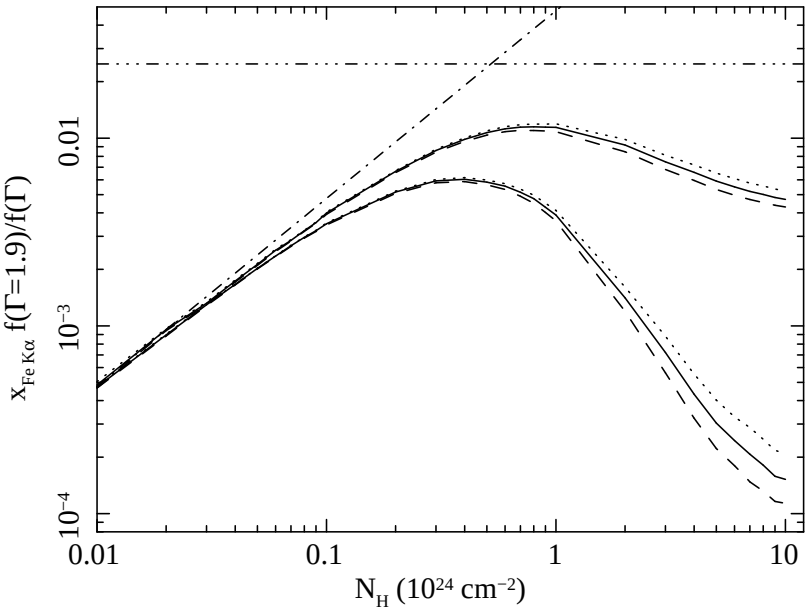

Figure 3.23: The Fe Kα line efficiency, $\chi_{\mathrm{FeK}\alpha}$, as a function of equatorial column density, N_{H}, for a toroidal reprocessor model (where $\Delta\Omega/4\pi = 0.5$). Solid curves correspond to a power-law incident continuum with $\Gamma = 1.9$. Dotted curves are for the same geometry but for $\Gamma = 1.5$, multiplied by the factor $f(\Gamma = 1.9)/f(\Gamma = 1.5)$, where $f(\Gamma)$ is given by equation 3.3. Dashed curves correspond to $\Gamma = 2.5$, multiplied by the factor $f(\Gamma = 1.9)/f(\Gamma = 2.5)$. For each pair of curves for a given value of Γ, the upper and lower curves correspond to the face-on and edge-on inclination-angle bins respectively. The dot-dashed line shows the relation for the optically-thin limit (for $\Gamma = 1.9$), from equation 3.2. The dashed, triple-dotted (horizontal) line shows the value of $\chi_{\mathrm{FeK}\alpha}$ for a standard, face-on, semi-infinite disk that has a Compton-depth > 10 ($N_H > 1.25 \times 10^{25}$ cm^{-2}). Figure taken from Yaqoob et al. (2010).

3.4.2 The Origin of the Highly-Ionised Fe

The possibility of an ionised accretion disc as a potential origin for the 6.60 and 6.95 keV emission lines was investigated. To test this scenario, an attempt was made to model the two ionised emission lines with a REFLIONX component with a high ionisation parameter of $\log \xi = 3.0^{+0.2}_{-0.1}$. The remainder of the *Suzaku* spectrum was modelled as before, i.e. a cut-off power law for the continuum emission, a single temperature thermal MEKAL component to account for the weak soft X-ray excess and a narrow Gaussian centered at 6.39 keV for the neutral Fe Kα emission. No relativistic blurring was applied. This resulted in a poor fit of

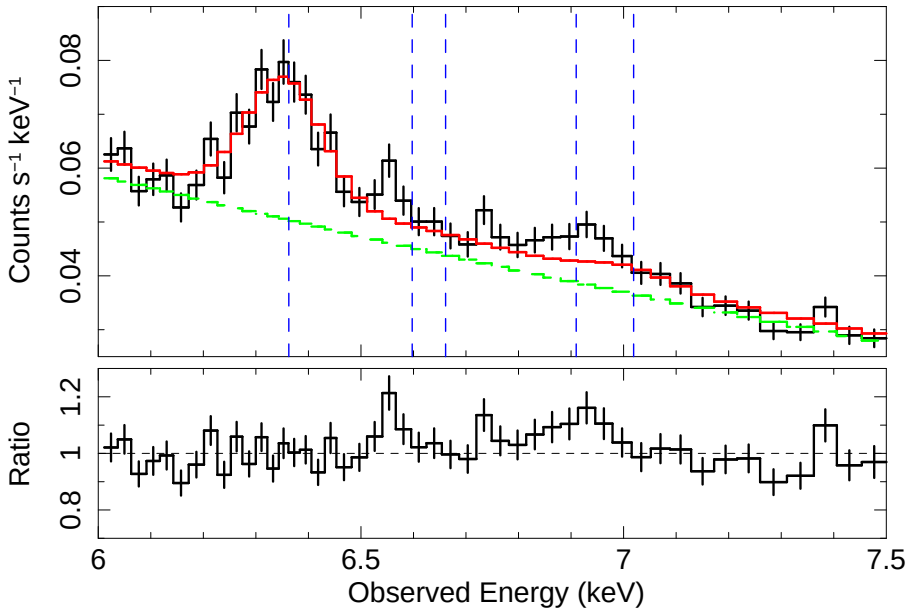

Figure 3.24: A plot showing the inability to model the highly-ionised Fe emission at 6.60 keV and 6.95 keV in NGC 7213 with an ionised reflector therefore suggesting a non-reflection origin for these lines (as described in Section 3.4.2). The continuum level is shown in green and the lower panel shows the ratio of the residuals to the model. The neutral Fe Kα line at 6.39 keV is modelled with a Gaussian. The vertical dotted lines show the expected line energies of, from left to right, Fe Kα, Fe XXV forbidden, Fe XXV $1s$–$2p$ resonance, Fe XXVI $1s$–$2p$ and Fe Kβ in the observed frame.

$\chi^2/d.o.f. = 791/717$ (null probability $= 2.79 \times 10^{-2}$) with the model unable to account for the ionised emission from either Fe XXV or Fe XXVI (see Figure 3.24). Indeed, due to the large intrinsic electron scattering depth at such high values of ξ, the lines in the reflection model become too broadened and so are unable to model the relatively narrow 6.60 and 6.95 keV lines that are observed in the *Suzaku* spectrum. Furthermore the 90% confidence upper-limit on the reflection fraction for the highly-ionised reflector is restricted to $R < 0.06$, which seemingly allows the presence of a highly-ionised Compton-thick medium in NGC 7213 (such as a highly-ionised, but Compton-thick inner accretion disc) to be rejected.

In addition, the inability to model the neutral Fe Kα emission with a low ionisation reflector (see Section 3.4.1) coupled with the apparent lack of a Compton hump > 10 keV means that this source exhibits no evidence at all for any Compton-thick material, either

neutral or ionised. Furthermore, the data do not show any relativistic signatures since the neutral and ionised Fe lines are narrow (or only moderately broad in the case of Fe XXVI), thus ruling out any emission from the inner-most regions around the black hole[8]. Combining the lack of evidence for any Compton-thick matter in this source with the lack of any relativistic signature seems to suggest the complete absence of an inner optically-thick accretion disc in NGC 7213. Instead, it may support the notion of an accretion disc which is truncated at some radius with the inner regions replaced by some form of Radiatively Inefficient Accretion Flow (RIAF; Narayan & Yi 1995), where the low efficiency of the inner, hot corona leads to much of the energy being advected into the black hole rather than radiated away.

3.4.2.1 Collisionally-Ionised Model

The possibility of a collisionally-ionised origin for the highly-ionised Fe K emission was investigated instead, which was modelled with a high-temperature broadened APEC component (Smith et al. 2001). This required a temperature of $k_{\rm B}T = 13.03^{+2.61}_{-2.86}$ keV and intrinsic velocity broadening, $\sigma \sim 2\,500\,{\rm km\,s^{-1}}$ (which is in addition to any small component of thermal broadening), resulting in a fit statistic of $\chi^2/d.o.f. = 788/716$ (see Figure 3.25). Inspection of the data around the Fe K band reveals that the collisionally-ionised model over-predicts the contribution of the resonance line compared to the forbidden line of Fe XXV, which leaves some excess line flux near 6.60 keV unmodelled, although the Fe XXVI line is modelled well. Thus, although the collisional model cannot be ruled out with high confidence in the present data, given that the energy of the 6.60 keV line is more consistent with the forbidden rather than resonance transition of Fe XXV, an additional photo-ionised component would perhaps be required to model this line (see Section 3.4.2.2).

An estimate of the density of the collisionally-ionised material can be calculated from the normalisation of the APEC code, which returns (emission measure) $\int n^2\,dV \sim 10^{64}\,{\rm cm^{-3}}$. If the observed broadening of the line is assumed to be due to a Keplerian orbit ($\sigma \sim$

[8]Indeed, assuming a Keplerian orbit viewed edge-on, line broadening on the order of several $10^4\,{\rm km\,s^{-1}}$ might be expected an accretion disc within a few tens of $r_{\rm g}$ from the black hole. The observed broadening may then increase further due to gravitational redshift.

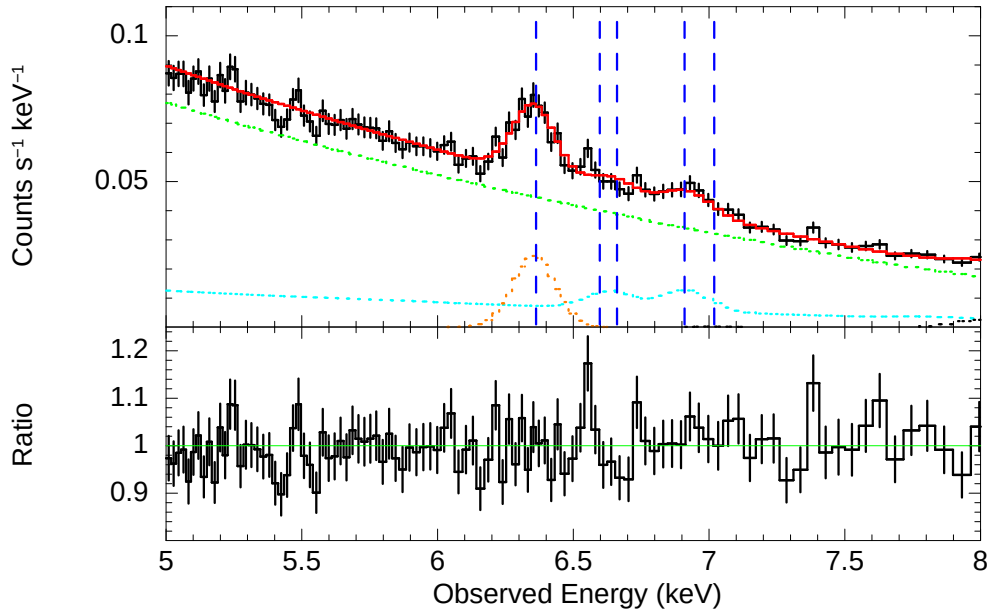

Figure 3.25: The *Suzaku* XIS spectrum of NGC 7213 in the Fe K band when attempting to model the highly-ionised Fe emission with a collisionally-ionised plasma. The model components include an absorbed power law (green), a Gaussian to model near-neutral Fe Kα emission (orange) and an APEC thermal plasma component (cyan). The vertical dashed lines show the expected energies (in the observed frame) of, from left to right, Fe Kα, Fe XXV forbidden, Fe XXV 1s–2p resonance, Fe XXVI Lyα and Fe Kβ. The residuals are shown in the lower panel. See Section 3.4.2.1 for details.

0.1 keV, corresponding to a few $10^3\,\mathrm{km\,s^{-1}}$; see Table 3.1), an estimate of the radius of the emitting material from the central black hole can be calculated of a few $10^4\,r_\mathrm{g}$, where $1\,r_\mathrm{g} = 1.5 \times 10^{13}\,\mathrm{cm}$ for a black hole mass of $M_\mathrm{BH} = 10^8\,\mathrm{M}_\odot$ (Nelson & Whittle 1995). Adopting this radius of $R \sim 1.5 \times 10^{17}\,\mathrm{cm}$ results in an estimate of $n \sim 10^6\,\mathrm{cm^{-3}}$ for the density of the emitting material, assuming a spherical cloud distribution.

If the collisional gas is indeed responsible for some of the highly-ionised Fe emission then it should be noted that the conditions of the gas must be different from those in the lower-temperature gas used to model the weak soft excess at energies $< 1\,\mathrm{keV}$ (see Section 3.3.2). The two components require very different temperatures ($0.27^{+0.05}_{-0.04}$ and $13.03^{+2.61}_{-2.86}\,\mathrm{keV}$ for the low- and high-temperature gases respectively) and it is noted that any contribution from one distinct zone of emission to the other is negligible (i.e. no significant emission from the lower

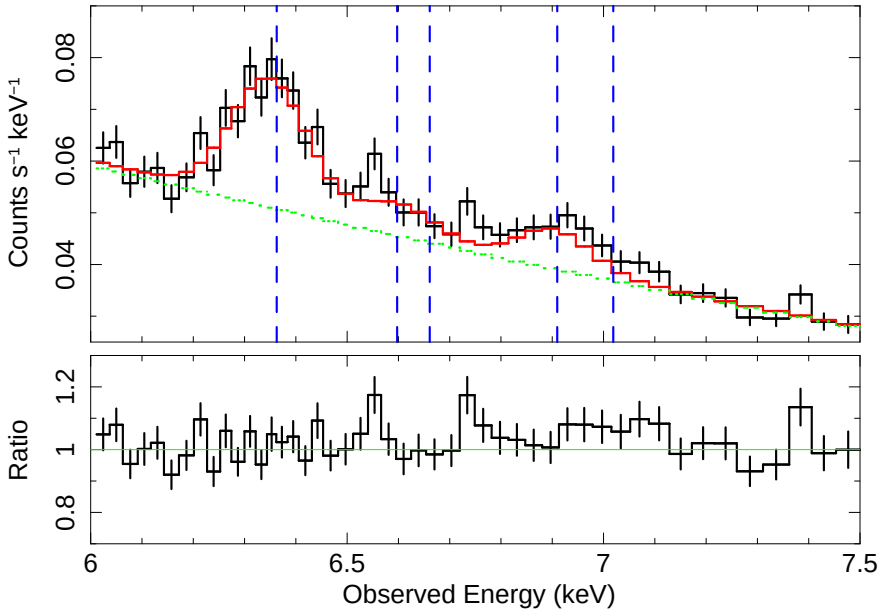

Figure 3.26: A plot showing the fit obtained when the highly-ionised Fe emission in NGC 7213 is modelled with a photo-ionised XSTAR grid with $v_{\rm turb} = 200\,{\rm km\,s^{-1}}$ and $\log\xi = 3.7$ (as described in Section 3.4.2.2). The continuum level is shown in green and the lower panel shows the ratio of the residuals to the model. The neutral Fe Kα line at 6.39 keV is modelled with a Gaussian. The vertical dotted lines show the expected line energies of, from left to right, Fe Kα, Fe XXV forbidden, Fe XXV $1s$–$2p$ resonance, Fe XXVI $1s$–$2p$ and Fe Kβ in the observed frame.

temperature zone is found to be contributing the emission at Fe K and vice-versa). However, the two zones of gas could be linked by their origin albeit on completely different scales with the emission from the lower-temperature gas originating at a much greater distance from the black hole.

3.4.2.2 A Photo-Ionisation Model for the Ionised Fe K Emission

An alternative origin for the lines could be emission from a photo-ionised, but Compton-thin plasma. This scenario was modelled using the XSTAR 2.1ln11 code (Kallman & McCray 1982), which incorporates the abundances of Grevesse, Noels & Sauval (1996). The XSTAR code is described in Section 2.5.1. The lines were initially modelled using a single zone of

emission with solar abundances and a turbulent velocity width of $v_{\rm turb} = 200\,{\rm km\,s^{-1}}$ where the free parameters were the ionisation parameter, ξ, column density, $N_{\rm H}$ and normalisation (see Section 3.4.2.3 for constraints on the column density). The best-fitting value of the ionisation parameter was $\log\xi = 3.7 \pm 0.3$ (where the ionisation parameter in XSTAR is defined as in equation 3.5), which resulted in an acceptable fit with $\chi^2/d.o.f. = 779/715$ (null probability $= 4.73 \times 10^{-2}$). Even so, some slight excess residuals were apparent (as shown in Figure 3.26), particularly around the 6.95 keV line, which might suggest there is some intrinsic velocity broadening of the ionised lines. For instance, as measured from Section 3.3.1, the H-like line has a FWHM of $\sim$10 000 km s^{-1}.

Thus an alternative XSTAR grid was used with a higher turbulence velocity of $v_{\rm turb} = 3\,000\,{\rm km\,s^{-1}}$. This resulted in a slightly better fit of $\chi^2/d.o.f. = 765/715$ (null probability $= 8.50 \times 10^{-2}$), with an ionisation parameter of $\log\xi = 4.4 \pm 0.1$ (see Section 3.4.2.1 for a calculation of the lower limit on the column density). This fit is significantly better than the one obtained with the collisionally-ionised model (Section 3.4.2.1) with $\Delta\chi^2 = 23$ between the two models. A plot of this model superimposed on the data is shown in Figure 3.27. The 90% uncertainty on the redshift of the zone was also calculated allowing constraints to be made on the net velocity shift of the ionised emitter of $v = +650^{+1650}_{-1500}\,{\rm km\,s^{-1}}$, where a positive velocity denotes redshifted / infalling material. Thus the data do not formally require a velocity shift in this model. Further zones of ionised matter are also not statistically required by the data.

Both high- and low-turbulence models give good fits over the Fe K band, with the 6.95 keV emission line originating from the Fe XXVI Lyα doublet and the 6.60 keV He-like line arising due to a blend of the forbidden and intercombination lines at 6.637 and 6.668 keV respectively. In the low-density limit assumed in the XSTAR model here (where $n < 10^{16}\,{\rm cm^{-3}}$), the He-like emission is from an approximately equal mixture of the forbidden and intercombination lines, with a negligible contribution from the resonance line at 6.700 keV. Note that some weak emission via satellite lines of lower-ionisation Fe (i.e. Fe XXIII-XXIV) could also be contributing to this blend of emission although at the high ionisation parameter inferred here (of $\log\xi \sim 4$), this contribution is likely to be negligible (Kallman & McCray 1982). However, future calorimeter-based spectroscopy, e.g. with *Astro–H*, will be required to spectrally resolve all the line emission components associated with the He-like triplet of Fe and

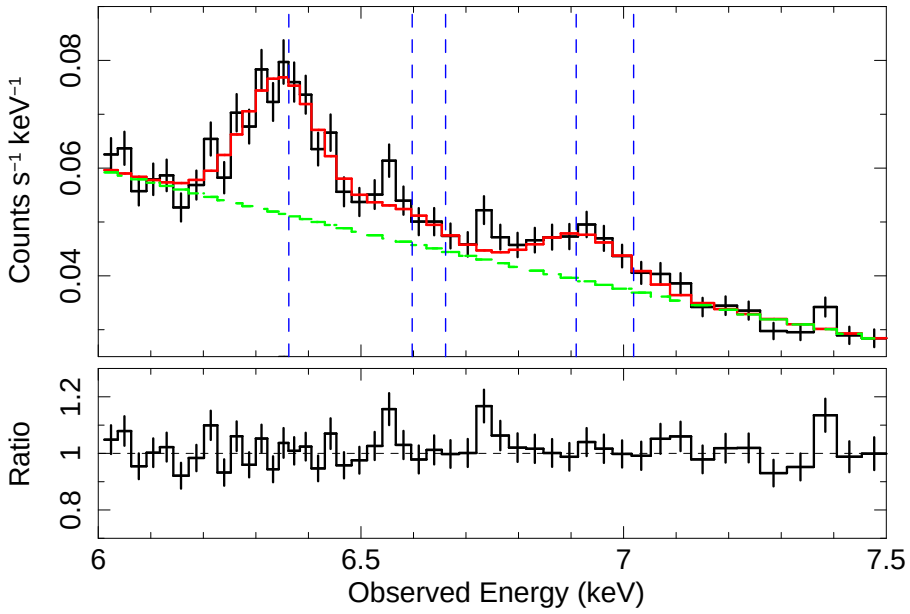

Figure 3.27: A plot showing the fit obtained when the highly-ionised Fe emission in NGC 7213 is modelled with a photo-ionised XSTAR grid with $v_{\rm turb} = 3\,000\,{\rm km\,s^{-1}}$ and $\log\xi = 4.4$ (as described in Section 3.4.2.2). The continuum level is shown in green and the lower panel shows the ratio of the residuals to the model. The neutral Fe Kα line at 6.39 keV is modelled with a Gaussian. The vertical dotted lines show the expected line energies of, from left to right, Fe Kα, Fe XXV forbidden, Fe XXV $1s$–$2p$ resonance, Fe XXVI $1s$–$2p$ and Fe Kβ in the observed frame.

to constrain the intrinsic velocity broadening.

It is also noted that if the highly-ionised Fe lines are originating in photo-ionised gas then the possibility remains that a similar photo-ionised gas but with a much lower ionisation parameter could be responsible for the weak soft X-ray lines observed at energies < 1 keV. However, Starling et al. (2005) analysed the results of an *XMM-Newton* RGS observation of NGC 7213 and found that a collisionally-ionised thermal plasma was preferred by the data from consideration of the 'G' ratio[9] (Porquet & Dubau 2000) of the O VII triplet.

[9]The 'G' ratio is given by $G(T_{\rm e}) = \frac{z+(x+y)}{w}$, where w is the intensity of the resonance line, z is the intensity of the forbidden line and x and y are the intensities of the intercombination lines (Porquet & Dubau 2000).

3.4.2.3 The Location of the Highly-Ionised Gas

From consideration of various photo-ionised and collisionally-ionised models, it seems that the 6.60 and 6.95 keV lines are consistent with originating in a photo-ionised medium, although the H-like Lyα line is quite strong with an equivalent width of $\sim$60 eV. Bianchi & Matt (2002) calculate the equivalent widths of Fe XXV and Fe XXVI lines with respect to both the reflected and total continua and show that an equivalent width of $\sim$15 eV for H-like Fe would be expected if it originated in material of column density, $N_{\rm H} \sim 10^{23}\,{\rm cm}^{-2}$, with an ionisation parameter of $\log \xi \sim 3.5$, photon index of $\Gamma = 1.7$ and a covering fraction, $f_{\rm cov} = 1$. To test whether the equivalent width of $\sim$60 eV measure here was feasible, a lower limit on the column density of the photo-ionised material was calculated in the case of one single zone of emission.

For a uniform, spherical, Compton-thin shell, the normalisation of the photo-ionised emission component is defined within the XSTAR code by[10]:

$$k = f_{\rm cov} \frac{L_{\rm ion}}{D^2} \tag{3.4}$$

where $f_{\rm cov}$ is the covering fraction of the material (i.e. $f_{\rm cov} = 1$ for matter covering 4π sr), $L_{\rm ion}$ is the ionising luminosity in units $10^{38}\,{\rm erg\,s^{-1}}$ from 1 to 1 000 Rydberg and D is the distance to the source in kpc. Physically, the XSTAR normalisation is simply proportional to the observed X-ray flux of the source multiplied by the covering fraction of the photo-ionised gas. Thus, the appropriate value of this normalisation, k, for NGC 7213 can be calculated assuming $f_{\rm cov} = 1$. For the luminosity of and distance to NGC 7213, this results in a value of $k = 9.0 \times 10^{-5}$ in units $10^{38}\,{\rm erg\,s^{-1}\,kpc^{-2}}$, where a distance of 25 000 kpc has been adopted to NGC 7213 (Mould et al. 2000). The value used for the ionising luminosity was derived from an extrapolation of the broken power-law continuum given in Table 3.4, integrated from 1 to 1 000 Rydberg and is found to be $L_{\rm ion} = 5.61 \times 10^{42}\,{\rm erg\,s^{-1}}$, comparable to the estimate of the bolometric luminosity of $L_{\rm bol} \sim 9 \times 10^{42}\,{\rm erg\,s^{-1}}$ given by Starling et al. (2005).

In the model described in Section 3.4.2.2, the normalisation of the additive XSTAR

[10] see http://heasarc.gsfc.nasa.gov/docs/software/xstar/docs/html/node94.html

emission component was fixed to the above value and thus a fully covering shell of gas around NGC 7213 was assumed, with the appropriate source luminosity and distance from above. The column density was then allowed to vary within the XSTAR model in order to fit the ionised Fe K emission lines. This provided a best-fitting value for the column density of $N_{\rm H} = 4.0^{+0.5}_{-0.8} \times 10^{23}\,{\rm cm}^{-2}$. The 90% confidence lower limit on the column density is $N_{\rm H} > 3.2 \times 10^{23}\,{\rm cm}^{-2}$ for a fully-covering spherical shell of gas, with an ionisation parameter of $\log \xi \sim 4$, as above. For a shell that does not fully cover the source, the column density will need to be higher to compensate for the lower covering fraction. This is in good agreement with the calculations of Bianchi & Matt (2002), who predict an equivalent width for the Fe XXVI Lyα line of 15 eV for a column density of $N_{\rm H} = 10^{23}\,{\rm cm}^{-2}$, compared to the observed equivalent width of 60 eV in the case of NGC 7213, but for a column density approximately 3–4 times higher.

In order to better constrain the origin of the Fe XXVI Lyα line it is important to estimate a value for the distance of the emitting material. Assuming a uniformly ionised, spherical shell of gas, the ionisation parameter in XSTAR is defined as:

$$\xi = \frac{L_{\rm ion}}{nR^2} \tag{3.5}$$

and has units erg cm s^{-1} where $L_{\rm ion}$ is the ionising luminosity from 1 to 1 000 Rydberg, n is the gas density in cm^{-3} and R is the radius of the absorbing / emitting material from the central source of X-rays. Combining this with the column density, which is given by:

$$N_{\rm H} = \int_{R_{\rm in}}^{\infty} n\, dR, \tag{3.6}$$

yields an estimate of the inner radius of the emitting material:

$$R_{\rm in} \sim \frac{L_{\rm ion}}{N_{\rm H}\xi}. \tag{3.7}$$

Assuming values of $L_{\rm ion} \sim 6 \times 10^{42}\,{\rm erg\,s}^{-1}$ (derived above), $\xi \sim 10^4\,{\rm erg\,cm\,s}^{-1}$ and $N_{\rm H} \sim 3 \times 10^{23}\,{\rm cm}^{-2}$ then gives a lower limit on the radius of $R \sim 2 \times 10^{15}$ cm corresponding to a value of $\sim$130 $r_{\rm g}$ (assuming a black hole mass of $M_{\rm BH} = 10^8\,{\rm M}_\odot$; Nelson & Whittle 1995) and implies an electron density of $n_e \sim 10^8\,{\rm cm}^{-3}$ (equation 3.5). As this radius is a lower

limit, this could still be consistent with the FWHM of $\sim 10\,000\,\mathrm{km\,s^{-1}}$ of the H-like Fe line which, if the broadening is assumed to be the intrinsic broadening due to a Keplerian orbit, provides an estimate of the line-emitting radius of a few $10^3\,r_\mathrm{g}$.

3.4.3 NGC 7213 as a Low-Luminosity AGN

3.4.3.1 The Inner Advective Flow in NGC 7213

From 2–10 keV, the X-ray spectrum of NGC 7213 resembles that of a typical type-1 Seyfert galaxy where the spectrum is dominated by a power-law continuum of $\Gamma = 1.75$ and near-neutral Fe Kα emission at 6.39 keV. This neutral Fe Kα emission may originate from Compton-thin material of $N_\mathrm{H} \sim 3 - 4 \times 10^{23}\,\mathrm{cm^{-2}}$ possibly in the outer BLR or a Compton-thin torus (Bianchi et al. 2008). Significant emission is also detected from highly-ionised material located close to the central source with the Fe XXV and Fe XXVI lines perhaps originating in a photo-ionised medium with a column density $N_\mathrm{H} \gtrsim 3 \times 10^{23}\,\mathrm{cm^{-2}}$ invoked to match the high observed EW of ∼60 eV. This emission is likely to originate at a distance of $R \sim 10^3 - 10^4\,r_\mathrm{g}$ from the black hole / X-ray source.

Given the tight constraints on reflection from both neutral and ionised material ($R < 0.16$ and $R < 0.06$ respectively), the lack of any relativistic signatures and the very weak BBB (Wu, Boggess & Gull 1983; often interpreted as thermal emission from the disc), this may rule out the presence of an inner, 'classic' optically-thick, geometrically-thin accretion disc (Shakura & Sunyaev 1973) envisaged in the unification scheme of AGN (Antonucci 1993). Instead, one suggestion is that the accretion disc is maybe truncated at some radius on the order of $10^3 - 10^4\,r_\mathrm{g}$ (∼0.01 pc) from the black hole with the inner regions perhaps replaced by a Radiatively Inefficient Accretion Flow (RIAF; Narayan & Yi 1995) consisting of highly-ionised, low-density ($n \sim 10^6\,\mathrm{cm^{-3}}$), Compton-thin gas covering some significant fraction of 4π sr. In this scenario, the low accretion rate of the source (0.07% L_Edd), perhaps due to a lack of available accreting material, may not allow the infalling material to cool sufficiently in order for a standard thin accretion disc to form. Instead, a stable accretion flow can still occur if the material takes on the form of an optically-thin, hot corona, where most of the material is advected across the event horizon as opposed to radiating away the energy it has

acquired in moving close to the black hole.

Such a hot, inner flow is expected to comprise of a low-density plasma whereby collisional processes dominate over photo-ionisation due to the high temperature. At radii below about $100\,r_{\rm g}$, the ion and electron temperatures diverge forming a two-temperature medium with $T_{\rm e} \sim 10^9 - 10^{10}\,{\rm K}$ and $T_{\rm ion}$ approaching $10^{12}\,{\rm K}$ in the inner-most regions (Narayan & Yi 1995). The electron temperature, $T_{\rm e}$, is then expected to fall as $10^{12}\,({\rm K})/R$ for $R > 10^2$, where R is in Schwarzschild units (i.e. $1\,r_{\rm S} = 2\,r_{\rm g}$). However, further out at $R \sim 10^3 - 10^4\,r_{\rm S}$, a plasma temperature of a few $10^8\,{\rm K}$ (i.e. $K_{\rm B}T \sim 13\,{\rm keV}$, as observed in the collisional APEC model), corresponding to $R \sim 10^4\,r_{\rm S}$, would produce emission from both He-like and H-like Fe, as observed. However, while the Fe XXVI emission could plausibly originate in such a plasma, the presence of the Fe XXV forbidden line suggests that the He-like Fe cannot be solely produced in such a collisionally-ionised medium. Thus, an alternative picture could instead be that both the Fe XXV and Fe XXVI emission lines originate in photo-ionised gas, perhaps at the transition region between the RIAF and the cold, outer accretion disc at a radius $R \sim 10^3 - 10^4\,r_{\rm g}$ from the black hole. Alternatively, the Fe XXV / XXVI emission lines may arise from a hybrid of photo- and collisionally-ionised processes (e.g. with the Fe XXVI emission associated with the RIAF and the Fe XXV emission arising from more distant photo-ionised gas).

3.4.3.2 NGC 7213 as a Low-/Hard-State Source

The accretion rate of NGC 7213 is much lower than the predicted "critical" value of $\sim$2% $L_{\rm Edd}$ (Maccarone 2003) whereby the high-/soft-state in black hole X-ray binaries can be observed. As a result, one interesting possibility is that NGC 7213 is an AGN analogue of the low-/hard-state observed in GBHCs. Long-term monitoring of NGC 7213 with *RXTE* (Bell et al. 2011) shows that the AGN is only slowly variable, indicating a relatively low-frequency power spectral density (PSD) break. This would be consistent with NGC 7213 having a relatively high black hole mass (e.g. $M_{\rm BH} = 10^8\,{\rm M}_{\odot}$; Nelson & Whittle 1995; Woo & Urry 2002) but a low accretion rate compared to Eddington, consistent with the scaling relations in the timing properties seen between AGN and GBHCs (McHardy et al. 2006). This is further supported

by the SED of NGC 7213 which suggests that this object has interesting radio properties lying between those of radio-loud and radio-quiet quasars. Indeed, taking the 5 GHz radio flux and B-band flux (host-galaxy-subtracted) of Sadler (1984) and Halpern & Filippenko (1984) respectively and using the equation for radio-loudness[11] of Wilkes & Elvis (1986) gives a value of $R_{\rm L} \sim 2$ suggesting that NGC 7213 is intermediate between radio-quiet AGN and radio-loud AGN such as radio galaxies and blazars. However, Panessa et al. (2007) also find that a radio-loudness of $\sim$2 is not so uncommon in Seyfert galaxies.

The inability to constrain the high-energy cut-off of the X-ray emission (i.e. $E_{\rm cut} > 350\,{\rm keV}$) could indicate that the continuum emission may be of non-thermal origin with one possibility being that some of the hard X-ray emission observed with *Suzaku* originates from the base of a jet[12]. Hameed et al. (2001) imaged NGC 7213 in the optical band and discovered a giant Hα filament approximately 19 kpc from the nucleus. They suggest that such a filament could be the signature of neutral gas shock-ionised by the interactions of a jet. A more recent 8.4 GHz Long Baseline Array (LBA) radio study of NGC 7213 (Blank, Harnett & Jones 2005) reports that the source is unresolved on the scale of $\sim$3 milli-arcseconds (corresponding to $\sim 10^4\,r_{\rm g}$ at the distance and black hole mass of NGC 7213), just showing a core, indicating that the jet could be orientated face-on. At lower frequencies, there is also evidence for a large-scale structure ($9'$; Blank, Harnett & Jones 2005 and reference therein) which could possibly be a signature of the extended radio lobes. Consequently, NGC 7213 is perhaps consistent with the hypothesis of Falcke, Patnaik & Sherwood (1996) whereby the radio-intermediate objects are similar to radio-quiet AGN but with moderate beaming from pc-scale jets orientated face-on to the observer.

[11] $R_{\rm L} = \log_{10}(F_{5\,{\rm GHz}}/F_{\rm B})$, where $F_{5\,{\rm GHz}}$ and $F_{\rm B}$ are the 5 GHz and B-band fluxes respectively. Typically, a value of $R_{\rm L} \geq 1$ signifies a radio-loud object.

[12] Note that the high-energy cut-off was measured with *BeppoSAX* in 2001 and found to be $E_{\rm cut} = 90^{+50}_{-20}\,{\rm keV}$ (Bianchi et al. 2004). However, no evidence is found for a cut-off energy $< 350\,{\rm keV}$ with the combined *Suzaku* XIS, HXD and *Swift*-BAT spectra.

3.4.3.3 The Origin of the High-Energy Continuum

NGC 7213 is not detected to date with the *Fermi* LAT gamma-ray instrument at ∼GeV energies (Abdo et al. 2010b) where the inverse-Compton emission from the jet would be expected to dominate. The *Fermi*-LAT flux limit corresponding to the detection threshold of Abdo et al. (2010b) at the galactic co-ordinates of NGC 7213 and for $\Gamma = 1.75$ is $F_{0.1-100\,\mathrm{GeV}} < 3 \times 10^{-9}\,\mathrm{photons\,cm^{-2}\,s^{-1}}$. Extrapolating the best-fitting broad-band *Suzaku* model to GeV energies over-predicts the γ-ray flux by a factor of ∼100 returning a predicted photon flux of $F_{0.1-100\,\mathrm{GeV}} \sim 3 \times 10^{-7}\,\mathrm{photons\,cm^{-2}\,s^{-1}}$. This implies that the hard X-ray / γ-ray continuum does in fact roll over at energies $> 350\,\mathrm{keV}$.

In order to be consistent with the 0.1–100 GeV flux limit from *Fermi*, it requires that the e-folding energy of the power-law component must be $E_{\mathrm{cut}} < 25\,\mathrm{MeV}$. This, combined with the lower limit on the high-energy cut-off from the combined *Suzaku* and *Swift* data means that $350\,\mathrm{keV} < E_{\mathrm{cut}} < 25\,\mathrm{MeV}$, consistent with the predicted electron temperature of the hot, inner flow (see Section 3.4.3.1). This suggests that thermal Comptonisation is responsible for the X-ray continuum and that any non-thermal contribution from the inverse-Compton component associated with a jet may be negligible in this source.

Furthermore, the high EW of the observed emission lines may also suggest that there is very little dilution of the X-ray continuum by a jet. It is noted that other radio-loud sources such as the BLRGs 3C 120 and 3C 390.3 do also show fairly strong Fe K line emission with EWs on the order of 50–100 eV. However, in the case of 3C 390.3, Sambruna et al. (2009) argue from the *Suzaku* data and the overall radio–γ-ray SED that the jet makes a minimal contribution to the X-ray continuum emission. Likewise, Kataoka et al. (2007) argue a similar case from the *Suzaku* observation of 3C 120 and conclude that the putative jet component does not dilute the Fe K emission. In addition, comparing the ratio of the 1–100 GeV γ-ray flux from *Fermi* to the 2–10 keV X-ray flux for NGC 7213 with that of 3C 111 (the only BLRG detected by *Fermi* to date) and 3C 273, it is found that the ratio is higher by a factor of > 6 for the two radio-loud AGN. By comparison, like for NGC 7213, none of the X-ray bright type-1 Seyfert galaxies has been detected with *Fermi* to date.

As a further test, an attempt was made to model the X-ray continuum with a double

power-law component consisting of a hard spectrum to model any possible emission from a jet and a much softer, Seyfert-like spectrum to model the photo-ionising nuclear X-ray emission. Statistically speaking, this fit is not required by the data as it only yields an improvement of $\Delta\chi^2 \sim 2$ for an additional two parameters of interest. Upon fixing the photon index of the softer power law at $\Gamma = 2$, the normalisation of the harder, jet-like component becomes very small with an upper-limit corresponding to just 10% of the normalisation of the main power law. So it seems that a double power-law model is not required by the data and that the X-ray continuum is best represented by a single power-law component.

The photon index of the X-ray continuum has a best-fitting value of $\Gamma = 1.75 \pm 0.02$ over 2–10 keV and therefore has only a slightly flatter spectrum than the typical values usually associated with radio-quiet quasars (RQQs) and type-1 Seyfert galaxies. For example, Reeves & Turner (2000) find a mean value of $\Gamma = 1.89 \pm 0.05$ from a sample of 27 RQQs observed with *ASCA* and Nandra & Pounds (1994) find a mean value of $\Gamma = 1.95$ with a dispersion of $\sigma = 0.15$ from their sample of Seyfert galaxies observed with *Ginga*. Porquet et al. (2004b) also find a mean value of $\Gamma = 1.90$ with a dispersion of $\sigma = 0.27$ from a sample of 14 RQQs observed with *XMM-Newton*. The photon index of NGC 7213 is, however, consistent with those found in other low-luminosity AGN such as M81 (Young et al. 2007) and NGC 4579 (Dewangan et al. 2004). Interestingly, the spectrum in NGC 7213 is somewhat steeper than the predicted photon index of $\Gamma = 1.4$ from the relation between mass accretion rate and photon index of Papadakis et al. (2009) given its calculated accretion rate of $0.07\% L_{\rm Edd}$ (an accretion rate of $\sim 2\% L_{\rm Edd}$ would be required to obtain $\Gamma = 1.75$). So it seems that NGC 7213 may not strictly follow the positive correlation between spectral steepness and accretion rate in AGN and X-ray Binaries suggested by Shemmer et al. (2006) although the high-energy cut-off of the X-ray continuum (i.e. $350\,{\rm keV} < E_{\rm cut} < 25\,{\rm MeV}$) observed here may suggest that the hard X-ray emission observed with *Suzaku* and *Swift* could be consistent with a very hot inner-flow, compatible with NGC 7213 having a low mass accretion rate.

3.5 Conclusions

NGC 7213 is an unusual AGN as it consistently exhibits no evidence for a Compton-reflection component unlike in other type-1 Seyfert galaxies (Perola et al. 2002; Dadina 2008). The time-averaged continuum emission is well fitted by a single power law of $\Gamma = 1.75$ and from consideration of the combined *Suzaku* and *Swift*-BAT data and the *Fermi* flux limit the high-energy cut-off is constrained to be $350\,\mathrm{keV} < E_{\mathrm{cut}} < 25\,\mathrm{MeV}$. The limits on reflection for the neutral and ionised cases from the REFLIONX model are $R < 0.16$ and $R < 0.06$ respectively suggesting that a significant Compton-thick reflector (e.g. from the inner disc or Compton-thick torus) is absent in this source, consistent with previous findings (e.g. Bianchi et al. 2003). Nonetheless, a significant Fe K complex is observed above 6 keV appearing only in emission. The line from neutral Fe Kα dominates ($E_{\mathrm{c}} \sim 6.39\,\mathrm{keV}$; EW $\sim 80\,\mathrm{eV}$) with further contributions from Fe XXV and Fe XXVI Lyα ($E_{\mathrm{c}} \sim 6.60$ and $E_{\mathrm{c}} \sim 6.95\,\mathrm{keV}$ respectively; also see Starling et al. 2005 and Bianchi et al. 2008). Furthermore, in this observation it is also found that the Fe XXVI Lyα emission is somewhat resolved in the *Suzaku* spectrum with a FWHM $\sim 10\,000\,\mathrm{km\,s^{-1}}$ and that the emission from Fe XXV is consistent with the forbidden transition from He-like Fe at $E_{\mathrm{c}} \sim 6.64\,\mathrm{keV}$ as opposed to the resonance transition at $E_{\mathrm{c}} \sim 6.70\,\mathrm{keV}$.

The neutral Fe Kα emission cannot be modelled via reflection off Compton-thick matter. However, an origin in a Compton-thin plasma covering a significant fraction of 4π sr is feasible with an inferred column density of $N_{\mathrm{H}} \sim 3-4\times10^{23}\,\mathrm{cm^{-2}}$, again consistent with the findings of previous observations with *Chandra* and *XMM-Newton*. Likewise here, the emission from highly-ionised Fe can also be modelled with a substantial column ($N_{\mathrm{H}} \gtrsim 3\times10^{23}\,\mathrm{cm^{-2}}$) of photo-ionised matter if a location close to the central engine is invoked to explain the inherent broadening and the high ionisation state. Given the lack of either neutral or ionised reflection coupled with the apparent absence of any relativistic signature in the spectrum, an inner, optically-thick accretion disc may be absent in this source. Instead, the accretion disc in NGC 7213 is most likely truncated at some radius with the inner regions perhaps replaced by an advective accretion flow (e.g. RIAF; Narayan & Yi 1995). The Fe XXV / XXVI emission could then be the ionised signature of such a hot, optically-thin plasma originating

in material a few $10^3\,r_{\rm g}$ from the central X-ray source.

Finally, NGC 7213 displays no evidence for any short-term X-ray variability on ks timescales. By comparing the broad-band *Suzaku* data from 2006 with more recent *XMM-Newton* data from 2009, the 2–10 keV flux was found to have fallen by a factor of $\sim$2 between observations. The spectral shape, however, was found to be largely invariant (e.g. constant Γ) and the long-term spectral variability could be accounted for simply by allowing the normalisation of the intrinsic power-law component to vary. Since NGC 7213 exhibits no evidence for any substantial amount of reprocessing material near to the black hole, either in absorption or reflection (most likely due to the low accretion rate of the source), it is likely that the observed variations are simply intrinsic to the source, consistent with the continuing trend noted by Bell et al. (2011) for the source to have been gradually decreasing in X-ray flux since 1980.

4 X-Ray Spectroscopy of NGC 4051

This chapter is based on published work entitled *'Contemporaneous Chandra HETG and Suzaku X-ray Observations of NGC 4051'; Lobban, A.P., Reeves, J.N., Miller, L., Turner, T.J., Braito, V., Kraemer, S.B., Crenshaw, D.M., 2011, MNRAS, 414, 1965-1986.*

As in Chapter 3, all data reduction, analysis and spectral modelling was conducted by the author. All co-authors assisted with scientific interpretation and discussion and participated in review of the aforementioned manuscript.

4.1 Introduction

NGC 4051 is a nearby ($z = 0.002336$; Verheijen & Sancisi 2001) NLS1 at a distance of 15.2 Mpc (Russell 2004) obtained from the Tully-Fisher relation for nearby galaxies (Tully & Fisher 1977). It has a black hole mass of $M_{\rm BH} = (1.73^{+0.55}_{-0.52}) \times 10^6\,{\rm M}_{\odot}$ determined via optical reverberation mapping (Denney et al. 2009) and is well known for its extreme X-ray variability both on short and long timescales with the X-ray spectrum hardening as the source flux becomes lower (Lamer et al. 2003), as seen in many other type-1 Seyfert galaxies (e.g. NGC 5506, Lamer, Uttley & McHardy 2000; MCG–6-30-15, Vaughan & Edelson 2001).

The warm absorber in NGC 4051 was studied by Collinge et al. (2001) with a simultaneous *Chandra* HETG and *Hubble Space Telescope* (*HST*) Imaging Spectrograph observation where they discovered two separate X-ray absorption systems corresponding to outflow velocities of $v_{\rm out} = 2\,340 \pm 130$ and $v_{\rm out} = 600 \pm 130\,{\rm km\,s^{-1}}$. Nine separate absorption systems were detected in the *HST* UV spectrum with one of the zones possibly corresponding to the lower velocity zone detected in the X-ray band. A further RGS observation with *XMM-Newton* was analysed by Ogle et al. (2004) who claimed the presence of a relativistically broadened O VIII Lyα emission line (EW ~ 90 eV) at $\sim$655 eV and suggested that this emission, along with its associated radiative recombination continuum (RRC), could be responsible for the weak soft excess. However, they found no evidence of the high-velocity outflow detected by Collinge et al. (2001). The RGS data from *XMM-Newton* observations in 2001 and 2002 were also anal-

ysed by Pounds et al. (2004a) and Nucita et al. (2010). They note that the 2002 observation caught the source during an extended period of low flux ($F_{2-10} = 5.8 \times 10^{-12}\,\mathrm{erg\,cm^{-2}\,s^{-1}}$). Pounds et al. (2004a) concluded that the hard X-ray spectral shape observed during this period of low flux was due to an increase in opacity of a substantial column of gas in the line-of-sight causing the spectrum to become dominated by a quasi-constant cold reflection component.

A more recent study by Krongold et al. (2007) showed the presence of two distinct ionisation components for the absorber through a 100 ks *XMM-Newton* exposure (from 2001). By measuring the electron densities through the absorber variability, they inferred that the absorbing components must be compact with the high- and low-ionisation zones existing at distances of 0.5–1 light-days and <3.5 light-days from the central engine respectively, well within the dusty torus and strongly suggestive of an accretion-disc origin for the warm-absorber wind. They calculated that the implied mass outflow-rate of the warm-absorber wind corresponds to approximately 2–5% of the mass accretion-rate of the source. They also detected several narrow emission lines in the RGS spectrum from C VI, N VI, O VII, O VIII, Ne IX and Fe XVII.

A further study of the warm absorber was also undertaken by Steenbrugge et al. (2009) through high-resolution X-ray spectroscopy using the *Chandra* LETG. They discovered that this object contains an outflowing wind consisting of four separate absorbing components ranging in ionisation parameter, $\log\xi$, from 0.07 to 3.19. They found that the absorbing zone with $\log\xi = 3.19$ requires a high outflow-velocity of $v_{\mathrm{out}} = 4\,760\,\mathrm{km\,s^{-1}}$ and from a study of the variability of the warm absorber, they inferred that three of the four absorbing zones are located in the range of 0.02–1 pc (∼24–1 200 light-days) from the black hole. This is more distant than the radial locations calculated by Krongold et al. (2007). Steenbrugge et al. (2009) suggest that the disagreement may arise from variability of the absorber between the observations or from the fact that Krongold et al. (2007) did not allow the shape of the continuum to vary in their analysis.

NGC 4051 was observed in 2005 with *Suzaku* when it was found to have fallen into an extended period of historically low flux (Terashima et al. 2009). A strong excess of emission was seen at energies >10 keV suggesting that the primary power-law continuum

had largely disappeared and that the bulk of the observed emission was reflection-dominated (e.g. Guainazzi et al. 1998; Pounds et al. 2004a). However, Terashima et al. (2009) were able to describe the data using a partial-covering model whereby the reflection-dominated emission and the intrinsic power-law emission are independently absorbed by gas covering some significant fraction of 4π sr. In this scenario, changes in the covering fraction of the partially-covered power-law component can account for the changes in the spectral shape at low energies whereas changes in the normalisation of the power-law component overlaid on a nearly constant hard component can account for the variability at energies >3.5 keV. This interpretation of the long-term spectral variability being caused by the primary X-ray continuum disappearing from view leaving behind a constant, hard, reflection-dominated component was supported by the results of Miller et al. (2010b) through principal components analysis (PCA) of the 2005 and 2008 *Suzaku* data (see Chapter 5). Miller et al. (2010b) also suggested that the periods of low flux are caused by variable partial-covering obscuring the central engine which also explains the constancy of the narrow Fe Kα emission-line flux.

Finally, the presence of an additional absorption feature at ∼7.1 keV was reported by Pounds et al. (2004a) indicating that a highly-ionised, high-velocity outflow could be apparent in this source. Further observations with *Suzaku* and *XMM-Newton* have confirmed the presence of this feature along with an additional absorption line at ∼6.8 keV (Terashima et al. 2009; Pounds & Vaughan 2011). If the two absorption lines are associated with K-shell transitions from Fe XXV and Fe XXVI then their blueshift would imply that the material is outflowing with a velocity of $v_{\rm out} \sim 0.02c$.

Here a ∼300 ks *Chandra* HETG observation of NGC 4051 is reported on where the soft X-ray warm-absorber is studied in detail (Section 4.3). A contemporaneous 350 ks *Suzaku* observation is also reported on (Section 4.5), where the Fe K band is studied including the blueshifted Fe K absorption lines as the signature of the highest-ionisation component of the outflowing wind (Section 4.6.1).

4.2 Spectral Analysis

The NGC 4051 *Chandra* and *Suzaku* data reduction is described in Section 2.6.1. For all spectral analysis, the XSPEC V12.7 software package (Arnaud 1996) was used. All fits include Galactic absorption with a column density $N_{\rm H}^{\rm Gal} = 1.35 \times 10^{20}\,{\rm cm}^{-2}$, obtained using the FTOOL NH with the compilations of Dickey & Lockman (1990). Absorption due to other elements such as O and Si are included assuming solar abundances for the given hydrogen column. The cross-sections for X-ray absorption by the interstellar medium obtained by Morrison & McCammon (1983) were also used by utilising WABS within XSPEC. Note that allowing the neutral absorption column to vary in the full broad-band fits always returns a value consistent with the column density of $N_{\rm H} = 1.35 \times 10^{20}\,{\rm cm}^{-2}$ derived from the 21 cm Galactic hydrogen maps of Dickey & Lockman (1990). Abundances are those of Anders & Grevesse (1989) unless otherwise stated. Both the *Chandra* HETG and *Suzaku* XIS spectra were binned at the HWHM resolution of the corresponding detector. To maximise the use of *Chandra*'s excellent spectral resolution, the spectrum was not binned up further such that χ^2 minimisation could be performed. Instead, due to the low number of counts per channel (i.e. <50 counts per resolution bin in some channels) in the HETG data, fit statistics were checked in the *Chandra* spectra using the C-statistic (Cash 1979; defined in Section 2.4.1.1). However, due to the higher photon statistics in the *Suzaku* spectra, the HWHM-resolution-binning enabled all goodness-of-fit values to be calculated using χ^2 minimisation as there were >50 counts per resolution bin. The HXD-PIN data were binned to a minimum of 5σ above the background level for all spectral fitting and were modelled simultaneously (in the 15–50 keV energy range) with the XIS data. Note that all errors quoted correspond to 90% confidence for one interesting parameter ($\Delta C = \Delta\chi^2 = 2.71$) unless stated otherwise. Where ΔC or $\Delta\chi^2$ values are quoted in tables, these values have been determined by removing the component from the final model and re-fitting. All fit parameters are given in the rest frame of the host galaxy having been corrected for the cosmological redshift ($z = 0.002336$) and assuming a distance of 15.2 Mpc to NGC 4051 (Russell 2004) obtained from the Tully-Fisher relation for nearby galaxies (Tully & Fisher 1977).

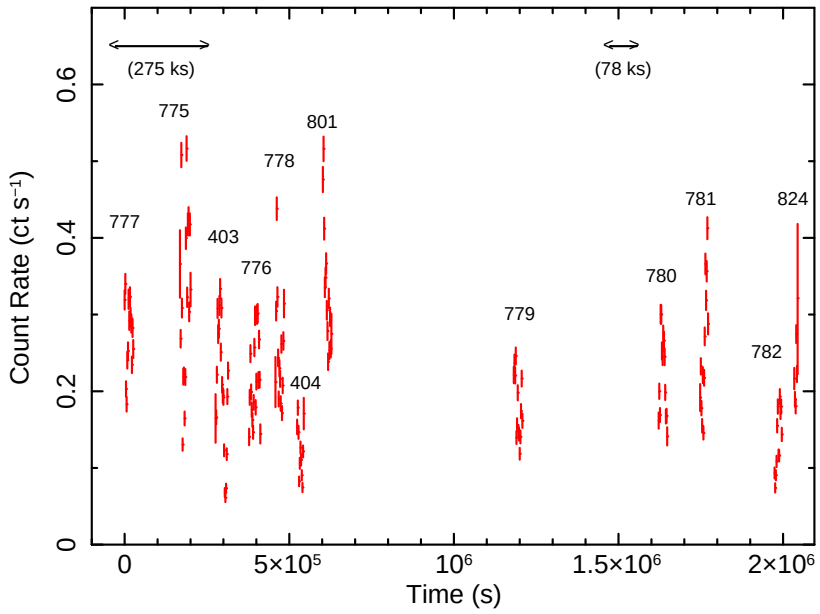

Figure 4.1: The summed HEG and MEG lightcurve showing the count rates of the twelve individual *Chandra* HETG observations of NGC 4051 over the 1.0–6.0 keV energy range. The labels refer to the sequence numbers of the observations listed in Table 2.2. The data are binned up in 2 ks bins and the horizontal lines show the duration and overlap of the two contemporaneous *Suzaku* observations.

4.3 The Chandra HETG Spectrum at Low Energies

The twelve separate HETG observations were initially considered (see Table 2.2) and it was found that the flux varies by a factor of ∼2 over the course of this 24-day period. A lightcurve showing the twelve individual observations with 2 ks binning over the 1.0–6.0 keV range (including both the MEG and HEG) is shown in Figure 4.1. The short-term variability is consistent with bright NLS1 galaxies in that the X-ray continuum softens as the flux increases (e.g. Lamer et al. 2003; Taylor, Uttley & McHardy 2003). This can be demonstrated by fitting an absorbed (Galactic column) power-law continuum to the individual exposures. Indeed, fitting a power law to a high-, medium- and low-flux exposure (sequence numbers 801, 824 and 782 respectively) from 1–6 keV returns best-fitting photon indices of $\Gamma = 2.11 \pm 0.04$, $\Gamma = 1.94 \pm 0.08$ and $\Gamma = 1.76 \pm 0.06$ respectively. However, to maximise signal-to-noise

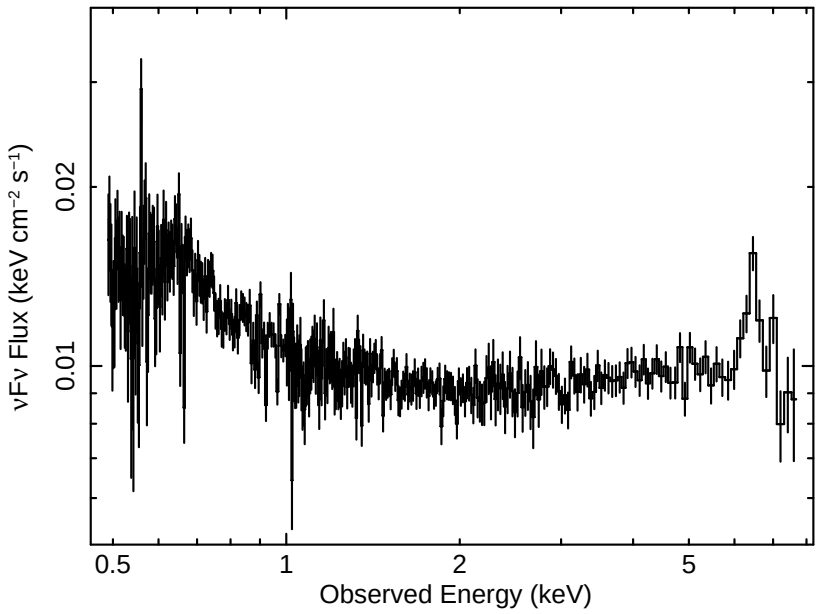

Figure 4.2: The NGC 4051 *Chandra* HETG spectrum from 0.5–8.0 keV unfolded against a power law with $\Gamma = 2$. Strong emission at energies >6 keV is most likely due to significant Fe K emission and positive spectral curvature can also be observed at energies <1 keV suggestive of the presence of a weak soft excess. The MEG and HEG are fitted over the 0.5–5.0 and 1.0–8.0 keV bands respectively (in the observed frame) and are binned by a factor of 10 for clarity.

so as to significantly determine the parameters of the warm absorber and detect individual absorption lines, the entire 300 ks time-averaged HETG spectrum was analysed. The MEG and HEG data were binned to a constant resolution of $\Delta\lambda = 0.01$ Å and $\Delta\lambda = 0.005$ Å respectively, representing the approximate HWHM resolution of the corresponding detector, and in all subsequent fits the MEG and HEG are considered over the respective 0.5–5.0 keV and 1.0–8.0 keV energy bands.

4.3.1 Continuum

A simple parameterisation was fitted to the continuum using the MEG and HEG in order to allow the warm absorber to be studied in detail. The continuum emission was fitted over the 0.5–8.0 keV range with an absorbed power law with a Galactic column density

$N_{\rm H}^{\rm Gal} = 1.35 \times 10^{20}\,{\rm cm}^{-2}$ (Dickey & Lockman 1990) and a photon index $\Gamma = 2.12 \pm 0.01$. This gave a poor fit to the data with $C/d.o.f. = 6082/4396$ (null probability < 0.01). The fluxed HETG spectrum unfolded against a power law with $\Gamma = 2$ is shown in Figure 4.2 where significant emission can be observed >6 keV due to the Fe K emission complex and positive spectral curvature can also be seen below 1 keV indicating that an additional steepening of the spectrum is present in this source. This was parameterised in the model with the addition of a simple featureless blackbody ($k_{\rm B}T = 0.10 \pm 0.01$ keV) which improved the fit by $\Delta C = 197$. The purpose of the blackbody component was not to model the data in a physical sense but to simply parameterise the soft excess with a smooth continuum, therefore allowing the individual lines from the warm absorber to be studied in detail. This yields a decent fit to the low-energy continuum and, as no evidence for any emission / absorption features >2 keV can be seen (apart from at Fe K), the MEG and HEG data >2 keV were excluded and the soft, ionised absorption lines in the 0.5–2.0 keV band were analysed and identified. A plot of the σ residuals <2 keV at full (HWHM) resolution is shown in Figure 4.3 revealing a number of absorption and emission lines.

4.3.2 Absorption Lines

The time-averaged 300 ks spectrum reveals 21 significant (>99.9%) soft X-ray absorption lines below 2 keV (20 of which are identified) originating from material with a range of ionisation states and column densities. The lines are fitted locally with simple Gaussian profiles with the line energy, line width and intensity as free parameters. The continuum was simultaneously allowed to re-adjust and also form part of the fit and the statistical significance of a line was determined by comparing the final model (i.e. with all lines fitted; see Table 4.1) with the fit achieved when the line is removed. Several of the lines are somewhat resolved in the HETG spectrum (e.g. O VII $1s$–$2p$, O VIII $1s$–$2p$, Fe XVIII $2p$–$3d$) with FWHM on the order of a few hundred to $\sim$1 000 km s^{-1}. Indeed, a mean value is found for the FWHM of 580 ± 59 km s^{-1} with a dispersion of $\sigma = 210$ km s^{-1} for the 13 absorption lines which are resolved in the spectrum. Note that the FWHM resolution of the MEG and the HEG at 1 keV is $\sim$500 km s^{-1} and $\sim$300 km s^{-1} respectively. The spectrum reveals absorption primarily from

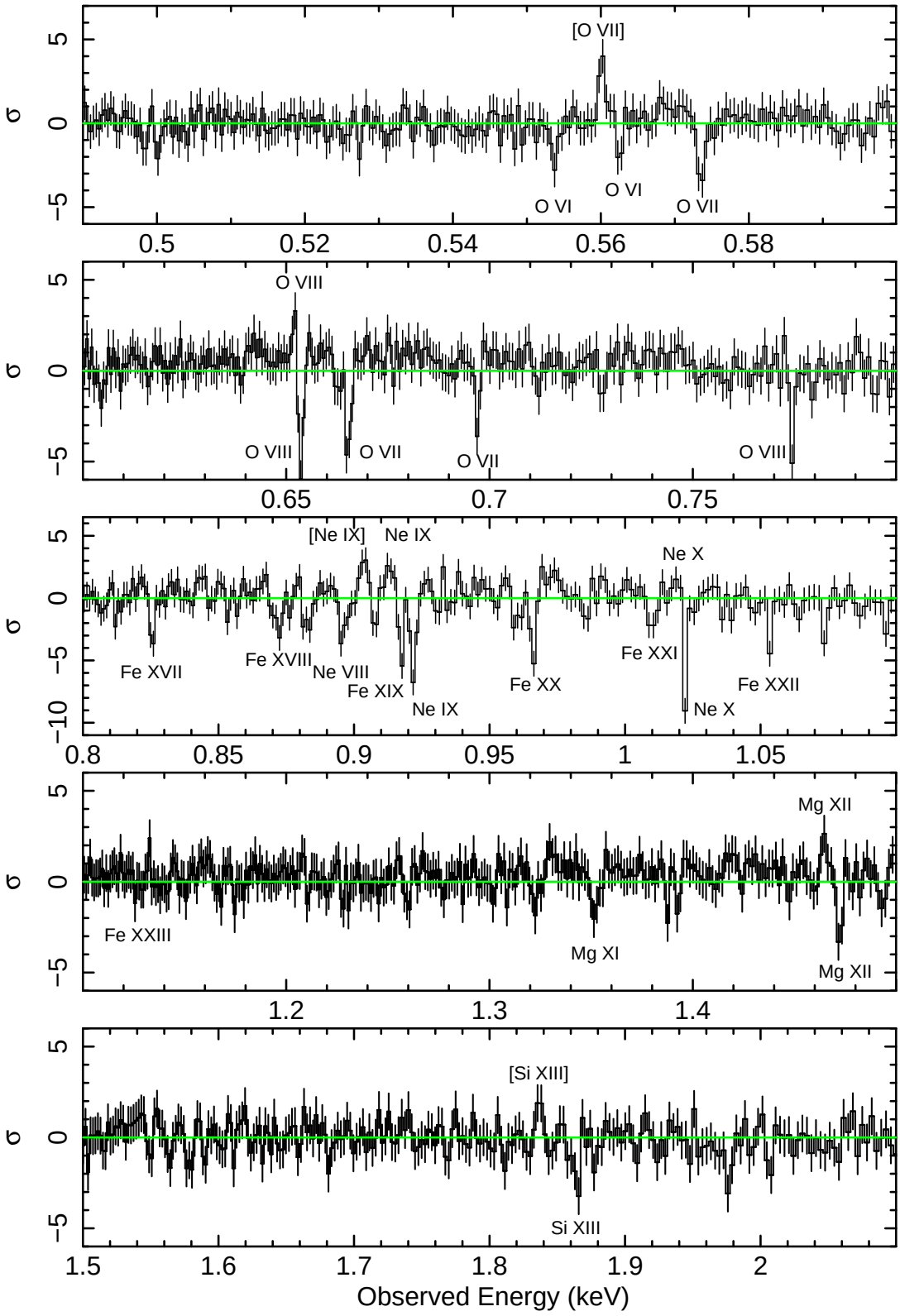

Figure 4.3: The σ residuals of the NGC 4051 *Chandra* HETG spectrum from 0.5–2.0 keV when fitted with a single absorbed power law and a featureless blackbody as described in Section 4.3.1. Significant residuals can be observed throughout the spectrum indicating the presence of several absorption and emission features. The statistically significant features which are able to be identified are labelled on the plot. All spectra are binned up by a factor of 2 for clarity and are plotted in the observed frame.

H-like and He-like ions of O, Ne, Mg and Si along with lines from less-ionised ions such as O VI. Several L-shell transitions of Fe XVII-Fe XXII are also detected. After taking into account the systemic redshift of NGC 4051, it should be noted that the observed centroid energies of the absorption lines are all blueshifted on the order of a couple of eV. This blueshift implies that the absorbing material in our line-of-sight is outflowing with calculated velocity shifts on the order of a few hundred to $\sim$1 000 km s^{-1} (e.g. the O VII, O VIII $1s$–$2p$ lines) relative to the host galaxy. A mean value for the outflow velocity of $v_{\rm out} = 620 \pm 34\,{\rm km\,s^{-1}}$ with a dispersion of $\sigma = 150\,{\rm km\,s^{-1}}$ is calculated for the 20 absorption lines that are able to be identified[1]. The line parameters and their likely identifications are summarised in Table 4.1. All lines were detected at the >99.9% significance level for three interesting parameters (i.e. $\Delta C \geq 16.3$) where ΔC is the difference in the fit statistic upon removing the component from the final model.

4.3.3 Emission Lines

In addition to a wealth of absorption features, the HETG spectrum also reveals 7 narrow emission lines at energies <2 keV which were again initially parameterised with simple symmetric Gaussians (see Table 4.1). Their identifications are largely consistent with the narrow emission lines found in the *XMM-Newton* RGS spectrum of NGC 4051 by Pounds et al. (2004a) and also with those detected by Terashima et al. (2009). These lines primarily originate from He-like ions of O, Ne and Si due to their associated forbidden transitions. The Ne IX intercombination lines are also identified at $\sim$915 eV[2]. Furthermore, Lyα transitions from H-like species of O and Mg are also observed at $\sim$653 eV and $\sim$1 472 eV respectively. It is noted that the O VIII Lyα emission observed here is narrow (FWHM <400 km s^{-1}; see Figure 4.4) and that no additional relativistically broadened Lyα feature, such as the one claimed by Ogle

[1]Note that the uncertainties quoted in $v_{\rm out}$ correspond to the statistical uncertainties only. The absolute wavelength accuracy of the MEG and the HEG is $\pm$0.011 Åand $\pm$0.006 Årespectively. The HEG uncertainty would correspond to an uncertainty of $\sim \pm 145\,{\rm km\,s^{-1}}$ at 1 keV but $v_{\rm out}$ is still significant.

[2]Interestingly, the forbidden and intercombination lines from Ne IX are observed to have similar strengths; this could be due to the presence of the Ne VIII $1s$–$2p$ absorption line at $\sim$895 eV reducing the observed flux of the Ne IX forbidden transition, thus making it appear to be weaker than it really is.

Line Energy (eV)	Line Width (eV)	FWHM ($\mathrm{km\,s^{-1}}$)	EW (eV)	Line Flux ($10^{-6}\,\mathrm{ph\,cm^{-2}\,s^{-1}}$)	Transition (Rest-Frame Energy) (eV)	Velocity Shift ($\mathrm{km\,s^{-1}}$)	ΔC
$555.17^{+0.03}_{-0.01}$	< 0.16	< 190	$-(0.95^{+0.17}_{-0.08})$	$-(49.3^{+8.6}_{-4.3})$	O VI $1s$–$2p$ (554.25)	$-(500^{+20}_{-10})$	33.3
$561.42^{+0.10}_{-0.09}$	< 0.34	< 290	$2.38^{+0.70}_{-0.60}$	$125.4^{+37.0}_{-31.9}$	[O VII] $1s$–$2s$ (560.98)	$-(230^{+50}_{-50})$	88.2
$563.87^{+0.14}_{-0.19}$	$0.17^{+0.17}_{-0.16}$	310^{+210}_{-200}	$-(0.71^{+0.16}_{-0.17})$	$-(34.5^{+8.0}_{-8.4})$	O VI $1s$–$2p$ (563.05)	$-(440^{+70}_{-100})$	17.2
$575.00^{+0.16}_{-0.17}$	$0.50^{+0.19}_{-0.05}$	610^{+230}_{-57}	$-(1.26^{+0.32}_{-0.10})$	$-(65.6^{+16.5}_{-5.3})$	O VII $1s$–$2p$ (573.95)	$-(550^{+80}_{-90})$	43.4
$652.09^{+0.18}_{-0.22}$	< 0.38	< 400	$0.97^{+0.43}_{-0.33}$	$33.2^{+14.9}_{-11.2}$	O VIII $1s$–$2p$ (653.49)	650^{+100}_{-80}	30.1
$653.62^{+0.14}_{-0.19}$	$0.54^{+0.21}_{-0.11}$	570^{+140}_{-110}	$-(1.41^{+0.30}_{-0.21})$	$-(50.2^{+10.8}_{-7.6})$	O VIII $1s$–$2p$ (653.49)	$-(740^{+70}_{-90})$	69.1
$666.84^{+0.24}_{-0.24}$	$0.68^{+0.27}_{-0.22}$	700^{+280}_{-230}	$-(1.30^{+0.31}_{-0.43})$	$-(43.8^{+10.6}_{-14.7})$	O VII $1s$–$3p$ (665.62)	$-(550^{+110}_{-110})$	48.7
$698.63^{+0.16}_{-0.13}$	< 0.50	< 490	$-(0.57^{+0.18}_{-0.16})$	$-(16.6^{+5.3}_{-4.7})$	O VII $1s$–$4p$ (697.80)	$-(360^{+70}_{-50})$	19.0
$776.26^{+0.19}_{-0.19}$	$0.37^{+0.24}_{-0.36}$	< 530	$-(0.88^{+0.23}_{-0.25})$	$-(19.7^{+5.2}_{-5.5})$	O VIII $1s$–$3p$ (774.58)	$-(650^{+70}_{-80})$	38.5
$827.49^{+0.18}_{-0.25}$	< 0.71	< 360	$-(0.88^{+0.25}_{-0.35})$	$-(15.9^{+4.5}_{-6.3})$	Fe XVII $2p$–$3d$ (825.73)	$-(640^{+70}_{-90})$	36.0
$874.45^{+0.58}_{-0.85}$	$1.13^{+1.09}_{-0.75}$	890^{+860}_{-590}	$-(1.37^{+0.58}_{-0.70})$	$-(22.0^{+9.3}_{-11.2})$	Fe XVIII $2p$–$3d$ (872.65)	$-(620^{+200}_{-290})$	23.7
$885.14^{+0.72}_{-0.35}$	$1.28^{+0.59}_{-0.50}$	$1\,000^{+460}_{-390}$	$-(1.2^{+0.50}_{-0.50})$	$-(18.7^{+7.0}_{-7.0})$	Unidentified		20.5
$897.89^{+0.14}_{-0.28}$	< 0.55	< 420	$-(0.91^{+0.20}_{-0.31})$	$-(13.2^{+2.8}_{-4.6})$	Ne VIII $1s$–$2p$ (895.89)	$-(670^{+50}_{-90})$	41.0
$906.07^{+0.38}_{-0.42}$	$0.72^{+0.49}_{-0.66}$	550^{+370}_{-500}	$1.39^{+0.52}_{-0.48}$	$19.5^{+7.3}_{-6.7}$	[Ne IX] $1s$–$2s$ (905.08)	$-(330^{+130}_{-140})$	35.5
$915.19^{+0.60}_{-0.83}$	< 1.72	< 1300	$1.12^{+0.55}_{-0.53}$	$15.3^{+7.5}_{-7.3}$	Ne IX $1s$–$2p$ (914.80)	$-(130^{+200}_{-270})$	21.1
$919.72^{+0.26}_{-0.29}$	$0.58^{+0.43}_{-0.53}$	440^{+310}_{-400}	$-(1.15^{+0.44}_{-0.34})$	$-(15.8^{+6.1}_{-4.6})$	Fe XIX $2p$–$3d$ (918.10)	$-(530^{+90}_{-100})$	41.8
$924.01^{+0.28}_{-0.25}$	$0.85^{+0.29}_{-0.29}$	640^{+220}_{-210}	$-(1.67^{+0.35}_{-0.36})$	$-(22.6^{+4.7}_{-4.8})$	Ne IX $1s$–$2p$ (922.02)	$-(650^{+90}_{-80})$	72.1
$968.29^{+0.54}_{-0.22}$	$0.78^{+0.35}_{-0.53}$	550^{+250}_{-390}	$-(1.09^{+0.38}_{-0.35})$	$-(12.9^{+4.5}_{-4.1})$	Fe XX $2p$–$3d$ (967.33)	$-(300^{+170}_{-70})$	38.1
$1\,011.91^{+0.14}_{-0.19}$	< 0.36	< 250	$-(0.81^{+0.08}_{-0.19})$	$-(8.7^{+0.9}_{-2.1})$	Fe XXI $2p$–$3d$ (1 009.23)	$-(790^{+40}_{-60})$	46.7
$1\,022.48^{+0.87}_{-0.30}$	< 1.14	< 770	$0.73^{+0.99}_{-0.28}$	$7.6^{+10.3}_{-2.9}$	Ne X $1s$–$2p$ (1 021.50)	$-(290^{+250}_{-90})$	24.7
$1\,024.56^{+0.18}_{-0.22}$	$0.53^{+0.17}_{-0.11}$	350^{+120}_{-71}	$-(1.48^{+0.31}_{-0.17})$	$-(15.6^{+3.2}_{-1.8})$	Ne X $1s$–$2p$ (1 021.50)	$-(900^{+50}_{-60})$	129.3
$1\,055.91^{+0.21}_{-0.20}$	< 0.63	< 410	$-(0.73^{+0.20}_{-0.23})$	$-(7.0^{+2.0}_{-2.2})$	Fe XXII $2p$–$3d$ (1 053.62)	$-(650^{+60}_{-60})$	35.9
$1\,129.91^{+0.96}_{-0.95}$	$1.17^{+0.80}_{-0.51}$	720^{+490}_{-310}	$-(0.59^{+0.41}_{-0.24})$	$-(4.9^{+3.4}_{-2.0})$	Fe XXIII $2s$–$3p$ (1 127.20)	$-(720^{+250}_{-250})$	25.6
$1\,354.80^{+0.78}_{-0.66}$	$0.87^{+0.84}_{-0.49}$	450^{+430}_{-250}	$-(0.74^{+0.20}_{-0.59})$	$-(4.0^{+1.1}_{-3.2})$	Mg XI $1s$–$2p$ (1 352.25)	$-(570^{+170}_{-150})$	20.6
$1\,468.07^{+1.19}_{-0.71}$	< 2.31	< 750	$0.65^{+0.33}_{-0.26}$	$3.0^{+1.5}_{-1.2}$	Mg XII $1s$–$2p$ (1 471.69)	740^{+150}_{-240}	18.4
$1\,475.94^{+0.23}_{-0.09}$	< 0.92	< 430	$-(0.81^{+0.16}_{-0.24})$	$-(3.7^{+0.8}_{-1.1})$	Mg XII $1s$–$2p$ (1 471.69)	$-(860^{+50}_{-20})$	41.0
$1\,841.75^{+1.56}_{-1.61}$	$2.66^{+2.11}_{-1.20}$	$1\,000^{+790}_{-450}$	$1.93^{+0.91}_{-0.62}$	$5.5^{+2.6}_{-1.8}$	[Si XIII] $1s$–$2s$ (1 839.42)	$-(380^{+250}_{-260})$	40.7
$1\,869.17^{+0.57}_{-0.44}$	< 1.06	< 400	$-(1.39^{+0.33}_{-0.31})$	$-(3.9^{+0.9}_{-0.9})$	Si XIII $1s$–$2p$ (1 864.98)	$-(670^{+90}_{-70})$	40.8

Table 4.1: The best-fitting parameters of the absorption and emission lines detected in the *Chandra* HETG spectrum of NGC 4051 <2 keV. Several of the absorption lines are spectrally resolved with FWHM corresponding to a few hundred to $\sim$1 000 $\mathrm{km\,s^{-1}}$. ΔC corresponds to the change in the C-statistic upon removing the feature from the final model. All parameters are given in the rest frame of the host galaxy. See Sections 4.3.2 and 4.3.3 for further details.

et al. (2004), is required. The emission lines detected here have a mean velocity shift, $v_{\rm out}$, within $\pm 200\,{\rm km\,s^{-1}}$ of the systemic shift and are unresolved except for the forbidden emission lines from Ne IX (FWHM $= 550^{+370}_{-500}\,{\rm km\,s^{-1}}$) and Si XIII (FWHM $= 1\,000^{+790}_{-450}\,{\rm km\,s^{-1}}$). The Ly$\alpha$ transitions of O VIII and Mg XII are also observed to be redshifted on the order of a few $100\,{\rm km\,s^{-1}}$ relative to their rest-frame centroid energies. This is most likely due to the P-Cygni-like profiles in which the lines appear with their corresponding blueshifted absorption lines (see Figure 4.4). Like the absorption features, all of the emission lines were also detected at the >99.9% significance level for three interesting parameters (i.e. $\Delta C \geq 16.3$ upon removing the component from the overall final model).

4.4 The Broad-Band HETG Spectrum

In order to model the broad-band HETG spectrum, the data above 2 keV were included in the spectral fits so that the full 0.5–8.0 keV energy range was being considered. The model from Section 4.3 was carried forward consisting of a simple baseline power-law continuum, a featureless blackbody to parameterise the soft spectral steepening (i.e. the soft X-ray excess) and symmetric Gaussians to model the soft absorption and emission features. Figure 4.2 shows that a significant excess can be observed in the Fe K band at energies >6 keV (see Section 4.4.2). However, a more physical parameterisation of the warm absorber is firstly considered.

4.4.1 The Warm Absorber

The simple Gaussian profiles parameterising the absorption lines (see Table 4.1) were removed from the model and an attempt was made to model the warm absorber using the XSTAR 2.1ln11 code (Kallman & Bautista 2001; also see Kallman et al. 2004), incorporating the abundances of Grevesse, Noels & Sauval (1996). The XSTAR code is described in Section 2.5.1 and assumes thin shells of absorbing gas, self-consistently modelling zones of absorption whose free parameters are the column density, $N_{\rm H}$, redshift, z and ionisation parameter, ξ, which is defined as:

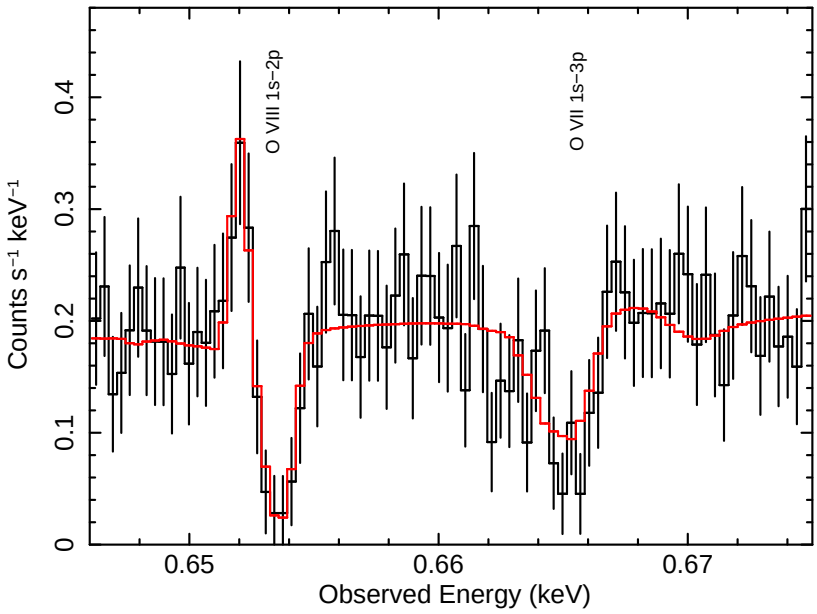

Figure 4.4: The relatively narrow O VIII Lyα emission at ∼652 eV in the observed frame of NGC 4051. This line, along with its corresponding absorption feature at ∼653 eV is observed to be P-Cygni-like in appearance. The model is superimposed on the data and is shown in red; the O VIII Lyα emission at ∼652 eV is modelled with a Gaussian and the corresponding absorption line at ∼653 eV is modelled with XSTAR as described in Section 4.4.1. A turbulence velocity of $v_{\rm turb} = 500\,{\rm km\,s^{-1}}$ in the warm absorber model (zone 2) is required to model the absorption line at ∼666 eV which likely corresponds to the $1s$–$3p$ transition from O VII. Note that this model does leave some excess absorption unmodelled from ∼662–666 eV although this could be a higher-velocity contribution from O VIII.

$$\xi = \frac{L_{\rm ion}}{nR^2} \tag{4.1}$$

and has units erg cm s^{-1}, where $L_{\rm ion}$ is the ionising luminosity from 1 to 1 000 Rydberg in units erg s^{-1}, n is the gas density in cm^{-3} and R is the radial distance in cm of the absorbing gas from the central source of X-rays. For the SED of the XSTAR models assumed here a simple illuminating power law with $\Gamma = 2.5$, consistent with that obtained from modelling the broad-band *Suzaku* spectrum (see Section 4.5), was used although this is difficult to compare with the observed SED of NGC 4051 since the UV data from the *HST* were acquired a year later and so are not simultaneous. The absorption lines were initially modelled using solar

Absorption Component	Model Parameter	Value	ΔC
Zone 1[a]	$N_{\rm H}\,({\rm cm}^{-2})$	$(3.06^{+1.04}_{-0.78})\times10^{20}$	149
	$\log\xi$	$-(0.86^{+0.14}_{-0.30})$	
	$v_{\rm out}\,({\rm km\,s}^{-1})$	180^{+100}_{-100}	
Zone 2[a]	$N_{\rm H}\,({\rm cm}^{-2})$	$(1.52^{+0.54}_{-0.37})\times10^{20}$	56
	$\log\xi$	$0.60^{+0.30}_{-0.22}$	
	$v_{\rm out}\,({\rm km\,s}^{-1})$	220^{+40}_{-60}	
Zone 3a[a]	$N_{\rm H}\,({\rm cm}^{-2})$	$(1.10^{+0.84}_{-0.51})\times10^{21}$	106
	$\log\xi$	$2.16^{+0.09}_{-0.21}$	
	$v_{\rm out}\,({\rm km\,s}^{-1})$	550^{+60}_{-60}	
Zone 3b[a]	$N_{\rm H}\,({\rm cm}^{-2})$	$(4.96^{+2.26}_{-1.48})\times10^{20}$	143
	$\log\xi$	$1.96^{+0.17}_{-0.06}$	
	$v_{\rm out}\,({\rm km\,s}^{-1})$	820^{+30}_{-30}	
Zone 4[a]	$N_{\rm H}\,({\rm cm}^{-2})$	$(2.74^{+0.58}_{-0.66})\times10^{21}$	127
	$\log\xi$	$2.97^{+0.10}_{-0.05}$	
	$v_{\rm out}\,({\rm km\,s}^{-1})$	710^{+20}_{-40}	
Partial-Coverer[b]	$N_{\rm H}\,({\rm cm}^{-2})$	$(2.00^{+0.68}_{-0.53})\times10^{23}$	286
	$\log\xi$	<2.40	
	$f_{\rm cov}$	30%	

Table 4.2: The best-fitting parameters for the four individual zones of absorption in the *Chandra* HETG data for NGC 4051. [a]XSTAR zone: $N_{\rm H}$, column density; ξ, ionisation parameter; $v_{\rm out}$, outflow velocity. [b]Partial-coverer: $f_{\rm cov}$, covering fraction. Zones 1, 3 and 4 require a turbulent velocity width of $v_{\rm turb} = 200\,{\rm km\,s}^{-1}$ whereas zone 2 is better modelled with a turbulent velocity width of $v_{\rm turb} = 500\,{\rm km\,s}^{-1}$.

abundances and a turbulent velocity width of $v_{\rm turb} = 200\,{\rm km\,s}^{-1}$, a value largely comparable to the observed velocity widths from the Gaussian line fits (see Table 4.1).

As shown in Table 4.2, it was found that the data statistically require five individual XSTAR zones of absorbing gas to model the data covering four distinct levels of ionisation. Each zone is significant at the >99.9% confidence level for three parameters of interest where the significance of each zone is assessed upon removing it from the final model. A plot of the warm-absorber model superimposed on the data is shown in Figure 4.5. The column densities are found to be on the order of $N_{\rm H} \sim 10^{20}$–$10^{21}\,{\rm cm}^{-2}$ and the zones cover a range

in ionisation parameter of $\log \xi = -0.86$ to $\log \xi = 2.97$. All the zones are observed to be blueshifted implying that the material is outflowing with velocities on the order of a few $100\,\mathrm{km\,s^{-1}}$ with the general trend being that v_{out} increases with increasing ξ. Two of the zones can be modelled with no statistically significant change in N_{H} or ξ but with two distinct outflow velocities ($v_{\mathrm{out}} \sim 500\,\mathrm{km\,s^{-1}}$ and $v_{\mathrm{out}} \sim 800\,\mathrm{km\,s^{-1}}$; see zones 3a and 3b in Table 4.2). Replacing zones 3a and 3b with one zone of higher turbulence velocity significantly worsens the fit (i.e. $\Delta C = 116$ for $v_{\mathrm{turb}} = 500\,\mathrm{km\,s^{-1}}$). Therefore, the inclusion of the two separate zones with $v_{\mathrm{turb}} = 200\,\mathrm{km\,s^{-1}}$ and differing outflow velocities is preferred by the data. Note that zones 3a and 3b are subsequently referred to as one single zone due to their consistent column densities and levels of ionisation (i.e. the HETG data are described as being modelled by four fully-covering warm-absorber zones). Note that the underlying continuum was free in the fit and the best-fitting photon index re-adjusted slightly to $\Gamma = 2.14 \pm 0.01$.

A plot showing the individual contribution of each of the four zones is shown in Figure 4.6. Regarding the transitions modelled by each XSTAR zone, it was found that the first zone (ultra-low ionisation) is mainly responsible for the absorption of O VI and lower-ionisation O ions. The second zone, with a slightly higher ionisation parameter, models absorption primarily from O VII. An inspection of the residuals reveals that this zone underpredicts the amount of absorption at ∼666 eV which is likely due to the turbulence velocity of $v_{\mathrm{turb}} = 200\,\mathrm{km\,s^{-1}}$ being too low. This has the effect of saturating the O VII $1s$–$3p$ line and hence underpredicting its EW. Increasing the turbulence velocity of this zone to $v_{\mathrm{turb}} = 500\,\mathrm{km\,s^{-1}}$ significantly improves the fit ($\Delta C = 34$) and better models the residuals at ∼666 eV (see Figure 4.4). However, increasing the turbulence velocity of the remaining warm absorber zones to $v_{\mathrm{turb}} = 500\,\mathrm{km\,s^{-1}}$ significantly worsens the fit and so these zones are better modelled with $v_{\mathrm{turb}} = 200\,\mathrm{km\,s^{-1}}$. Zones 3a and 3b are observed to adequately model the absorption from ions such as Ne IX, O VIII and the various L-shell transitions from Fe XVII - XXII and finally, the highest-ionisation zone corresponds to absorption from ions such as Ne X, Mg XI - XII and Si XIII.

It should be noted that there are no detected absorption lines associated with a fifth warm-absorber zone. However, the presence of a partially-covering zone of absorption, imparting bound-free absorption on the continuum, was allowed for by including an additional

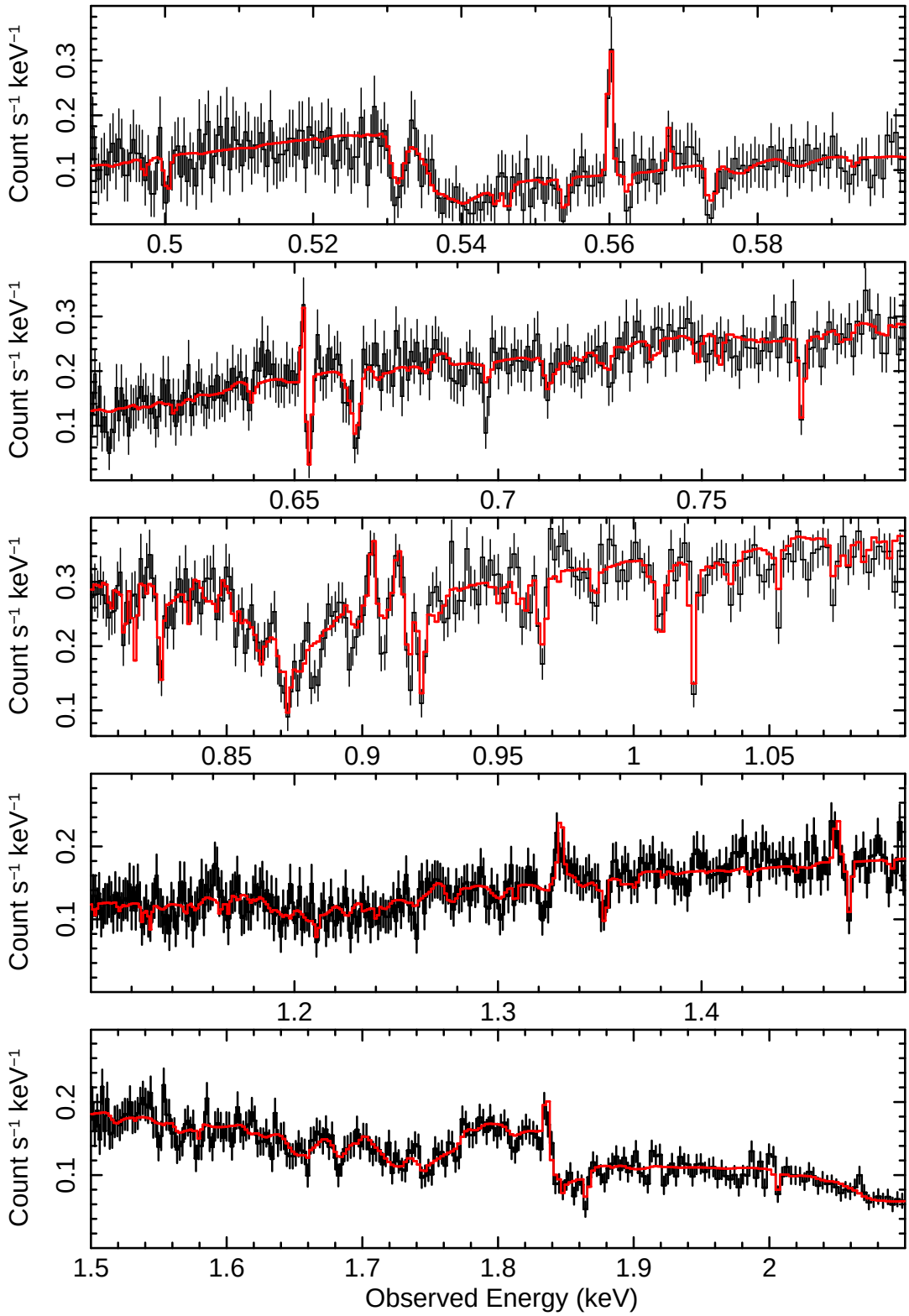

Figure 4.5: The HETG spectrum from 0.5–2.0 keV with the best-fitting warm-absorber model superimposed. The emission lines are modelled with simple Gaussians. All spectra are binned up by a factor of 2 for clarity and are plotted in the observed frame. Note that an additional Gaussian with a negative flux was included in the fit to model the excess residuals at ∼666 eV (see Section 4.4.1 for further details). It is noted that some unmodelled residuals remain in the data at ∼0.87 keV; these are likely due to inner-shell Ne transitions (e.g. Ne VIII) which are not included in the XSTAR models.

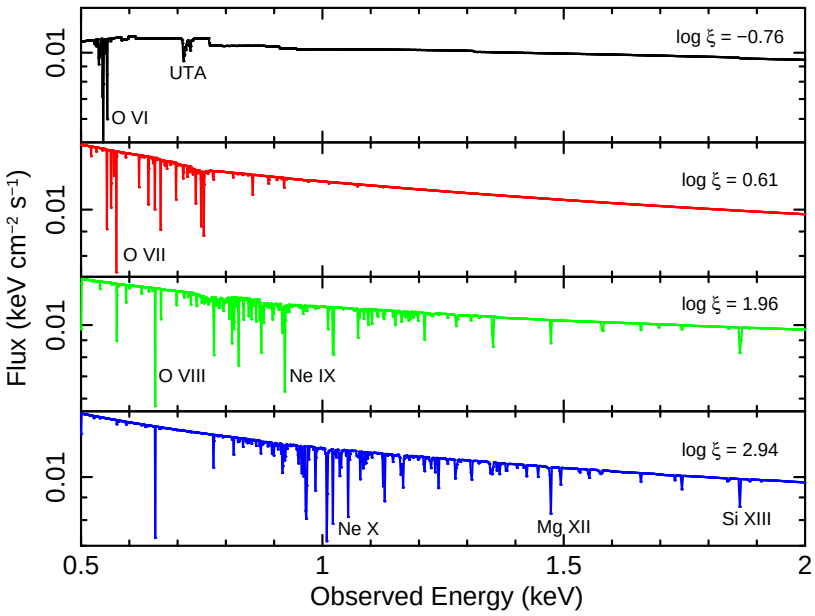

Figure 4.6: Plot showing the contribution of each of the four warm-absorber zones to the power-law continuum. The lowest- to highest-ionisation zones (zones 1 to 4) are shown from the upper to lower panels respectively. The ions contributing to the most significant absorption lines are marked on the plot.

power-law component absorbed by a further shell of gas. The photon indices of the two power-law components (one absorbed by the partial-coverer, the other left unattenuated) were tied together leaving just one of the components absorbed by an XSTAR zone. Zones 1–4 of the warm absorber and a column of Galactic hydrogen were retained in the model absorbing the entire continuum. It was found that this additional partial-coverer improves the fit significantly with $\Delta C = 286$ and is important in modelling additional curvature in the continuum at energies below $\sim$5 keV. The best-fitting parameters of the partial-coverer indicate that the material is partially-ionised with $\log \xi < 2.40$ and has a substantial line-of-sight column density, $N_{\rm H} = (2.00^{+0.68}_{-0.53}) \times 10^{23}\,{\rm cm}^{-2}$. The addition of this component also allows the temperature of the blackbody component to re-adjust slightly to $k_{\rm B}T = 0.12 \pm 0.01$ keV (a value consistent with Terashima et al. 2009) and the best-fitting photon index of the power-law continuum to steepen to $\Gamma = 2.25^{+0.02}_{-0.01}$. Indeed, without the partial-coverer, the

photon index of $\Gamma \sim 2.1$ may be slightly too low for this source when the flux is high (e.g. Lamer et al. 2003; Miller et al. 2010b). The covering fraction of the partial-coverer is given by the normalisation ratio of the absorbed to total power-law components at 1 keV; i.e. $4.98 \times 10^{-3} / 1.67 \times 10^{-2} \approx 0.30$ which suggests that the partial-coverer corresponds to a line-of-sight covering fraction of ∼30% of the nuclear X-ray source. The best-fitting parameters of the partial-coverer are also noted in Table 4.2.

Furthermore, replacing the blackbody with the REFLIONX reflection model (Section 2.5.1) of Ross & Fabian (2005) provides an equally good parameterisation of the soft excess. It was found that no relativistic blurring is required and that the addition of this component allows the photon index of the power law to steepen further with $\Gamma = 2.45 \pm 0.02$, a value consistent with that found from a quasi-simultaneous broad-band *Suzaku* observation in 2008 (see Section 4.5 where this is discussed in more detail). The REFLIONX component has a best-fitting value for the ionisation parameter of $\log \xi = 3.3 \pm 0.1$ and corresponds to a ratio of reflected-flux to incident-flux of ∼0.8 over the 0.5–8.0 keV energy range. However, the ionised reflector is unable to account for some of the soft X-ray emission lines, particularly the forbidden transitions from O VII, Ne IX and Si XIII which indicates that these lines could have an alternative origin. There have been previous claims in the literature of detections of RRC associated with H-like and He-like ions of C, N, O and Ne (e.g. Ogle et al. 2004; Pounds et al. 2004a) using the RGS on-board *XMM-Newton* which suggests that the soft X-ray emission lines could instead be the signature of a photo-ionised plasma. Indeed it has been somewhat well established that such soft X-ray lines are commonly formed either in the NLR or as part of the photo-ionised outflow (e.g. Bianchi, Guainazzi & Chiaberge 2006).

A subsequent paper (Kraemer et al. 2012) discusses the results of a UV observation of NGC 4051 made with the Cosmic Origins Spectrograph (COS) on-board the *HST* in December 2009. By comparing kinematic profiles of the strongest X-ray absorption lines (e.g. O VII and O VIII) with the strongest found in the UV data (e.g. N V and C IV), a visual correlation can be seen. The results suggest that the high-ionisation / high-velocity components detected in the UV band (three separate components) likely overlap with the lower-ionisation X-ray absorbers detected with the *Chandra* HETG (i.e. zones 1 and 2) but not the higher-ionisation X-ray absorption (i.e. O VIII).

4.4.1.1 Comparison with Recent RGS Data

The warm absorber in NGC 4051 was also recently studied by Pounds & Vaughan (2011) through *XMM-Newton* RGS observations in May–June 2009 (∼6 months after the *Suzaku* and *Chandra* observations from 2008) with an overall exposure of ∼600 ks. The data revealed significant absorption features primarily from H-like and He-like ions of C, N, O, Ne, Mg, Si, Ar and Fe. When modelled with XSTAR, the RGS data require five separate line-of-sight outflow velocity components ranging in velocity from $v_{\rm out} \sim 500\,{\rm km\,s^{-1}}$ to $v_{\rm out} \sim 30\,000\,{\rm km\,s^{-1}}$. With the HETG data analysed here, it is possible to confirm the presence of the lowest-velocity zone (on the order of a few hundred $\rm km\,s^{-1}$). The third zone ($v_{\rm out} \sim 6\,000\,{\rm km\,s^{-1}}$) can also be confirmed in the Fe K band with the *Suzaku* XIS (see Section 4.5.2 for more details). However, it is found that there is no requirement for the highest-velocity zone at Fe K ($v_{\rm out} \sim 30\,000\,{\rm km\,s^{-1}}$; Section 4.5.2); nor does there appear to be any evidence for the second and fourth intermediate zones claimed by Pounds & Vaughan (2011) which have velocities on the order of $v_{\rm out} \sim 4\,000\,{\rm km\,s^{-1}}$ and $v_{\rm out} \sim 7\,000$–$9\,000\,{\rm km\,s^{-1}}$ respectively.

To demonstrate this, the parameters of the model suggested by Pounds & Vaughan (2011) were compared to the HETG data. Regarding the zone with $v_{\rm out} \sim 4\,000\,{\rm km\,s^{-1}}$, Pounds & Vaughan (2011) model this with a single XSTAR zone with $\log\xi = 2.52 \pm 0.07$ and $N_{\rm H} = (1.9 \pm 0.4) \times 10^{21}\,{\rm cm^{-2}}$. Including a zone fixed at the best-fitting parameters from Pounds & Vaughan (2011) in the HETG spectrum worsens the fit with $\Delta C = 45$ even when the rest of the fit is free to re-adjust. Allowing this new zone to also vary results in the column density becoming consistent with zero with an upper limit of $N_{\rm H} < 7.6 \times 10^{19}\,{\rm cm^{-2}}$. The remaining free parameters remain unchanged and the inclusion of the new zone is found to be not required with $\Delta C < 1$.

Regarding the zone with $v_{\rm out} \sim 7\,000$–$9\,000\,{\rm km\,s^{-1}}$, Pounds & Vaughan (2011) do not model this with an XSTAR zone. Instead they focus on modelling discrete absorption features at observed energies, $E_{\rm c}$, of 997.5, 1 436 and 1 954 eV which they identify with Lyα transitions of Ne X, Mg XII and Si XIV respectively. Including a negative Gaussian to model each of these absorption lines in the HETG spectrum (where the width and intensity are the free parameters) is not statistically required with $\Delta C < 1$ in each case. Pounds & Vaughan (2011)

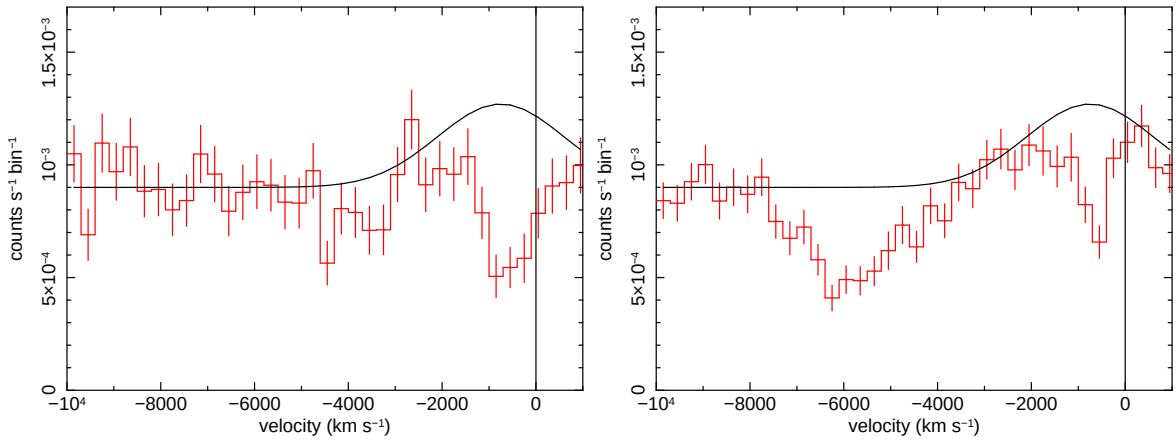

Figure 4.7: Radial velocity profiles centred on the O VII $1s$–$2p$ resonance transition at ∼574 eV (left panel) and the O VIII Lyα transition at ∼653 eV (right panel) taken from the RGS analysis of Pounds & Vaughan (2011). The plots are taken from the high-flux absorption-line-dominated RGS data and the solid black curves correspond to the emission profiles modelled by Pounds & Vaughan (2011) in the corresponding low-flux RGS data.

don't quote the strengths of these lines but upper limits on the magnitudes of the line fluxes, $F_{\rm line}$, are found to be $< 3.9 \times 10^{-6}$, $< 7.6 \times 10^{-7}$ and $< 1.2 \times 10^{-6}$ photons cm^{-2} s^{-1} for the three lines in the HETG spectrum respectively.

Pounds & Vaughan (2011) also report that the O VII $1s$–$2p$ resonance transition is detected with two separate velocity components (∼400 km s^{-1} and ∼4 000 km s^{-1}; Figure 4.7; left panel). However, only the presence of the lowest-velocity component is able to be confirmed with the HETG for this transition (see Figure 4.8; upper panel). Pounds & Vaughan (2011) also report three separate velocity components for the O VIII Lyα absorption line (see Figure 4.7; right panel). However, it is possible to only confidently confirm the lowest-velocity component in the HETG data (see Figure 4.8; lower panel). Interestingly, additional residuals are observed at ∼666 eV in the HETG spectrum which could potentially be the signature of a higher-velocity component of the O VIII Lyα transition with $v_{\rm out} \sim 6\,000$ km s^{-1} (Figure 4.8; lower panel), consistent with the value of $v_{\rm out} \sim 5\,600$ km s^{-1} found in the RGS spectrum (note that this velocity component is confirmed in the Fe K band with the *Suzaku* XIS; see Section 4.5.2). However, as this residual feature coincides with the expected energy of the

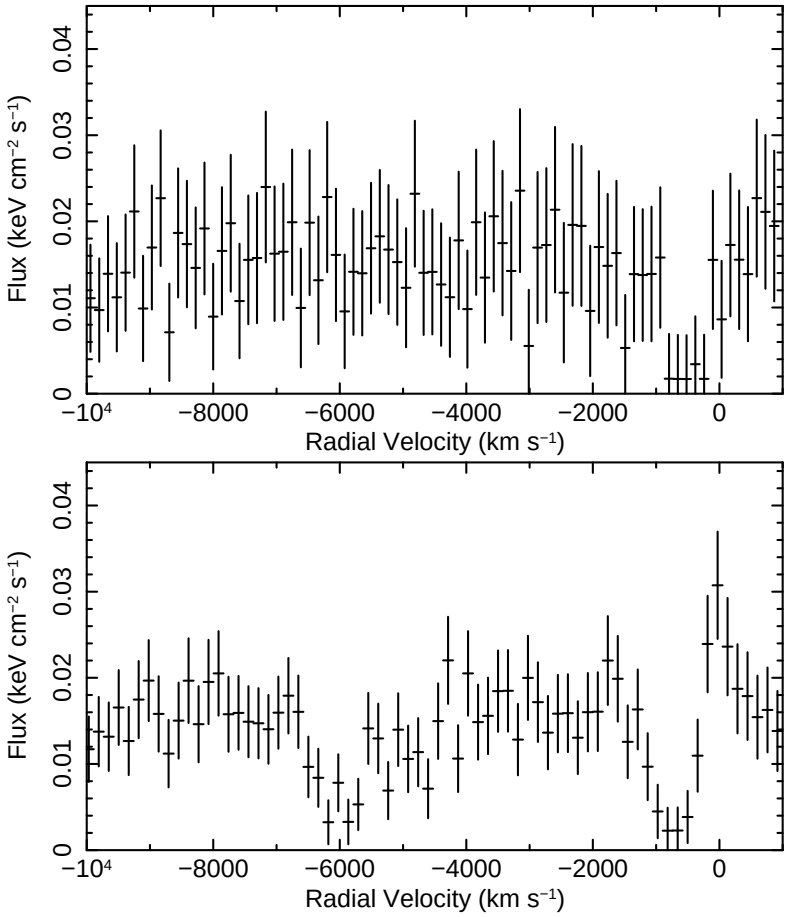

Figure 4.8: Upper panel: Plot showing a radial-velocity profile centred on the O VII $1s$–$2p$ resonance transition at ∼574 eV. Note that evidence is seen for an associated absorption component with an outflow velocity of a few hundred $\mathrm{km\,s^{-1}}$ but there is no requirement for the higher-velocity components reported by Pounds & Vaughan (2011). Lower panel: Plot showing a radial velocity profile centred on the O VIII Lyα transition at ∼653 eV. Again, evidence is seen for the lowest-velocity absorption-component with $v_{\mathrm{out}} < 1,000\,\mathrm{km\,s^{-1}}$. An absorption feature is seen which may correspond to O VIII Lyα blueshifted by $v_{\mathrm{out}} \sim 6\,000\,\mathrm{km\,s^{-1}}$; however, this feature may also be associated with the $1s$–$3p$ transition from O VII.

$1s$–$3p$ transition from O VII, it may also be possible to account for this with a slightly higher turbulence-velocity ($v_{\mathrm{turb}} = 500\,\mathrm{km\,s^{-1}}$) in the XSTAR model (as mentioned in Section 4.4.1) so its interpretation remains open. It should also be noted that no significant requirement is found in the HETG data for the additional velocity-component associated with the O VIII

transition at $v_{\rm out} \sim 4\,100\,{\rm km\,s^{-1}}$ from the RGS data. Therefore, the presence of only two of the five velocity components associated with the *XMM-Newton* data can be confirmed here which suggests that the absorber may have varied over the six-month period between observations.

4.4.2 The Fe K Complex

A ratio plot of the residuals to the absorbed baseline-HETG-continuum from 5.5–7.5 keV is shown in Figure 4.9. Line emission is clearly present suggestive of a significant Fe K complex (see Table 4.3). The most prominent line originates from Fe Kα fluorescent emission from near-neutral material at a centroid energy of $E_{\rm c} = 6.41 \pm 0.03\,{\rm keV}$. Modelling this with a Gaussian reveals that this line has an intrinsic width of $\sigma = 0.12^{+0.04}_{-0.01}\,{\rm keV}$ (FWHM $= 13\,000^{+4\,000}_{-1\,000}\,{\rm km\,s^{-1}}$) and an associated equivalent width of ${\rm EW} = 185^{+58}_{-19}\,{\rm eV}$. The addition of this line results in a fit statistic of $C/d.o.f. = 4819/4434$. However, the fit statistic is improved further by incorporating an additional unresolved narrow component ($\sigma = 0\,{\rm eV}$) centered at 6.40 keV to model any Fe Kα emission from distant material. This component has an equivalent width of ${\rm EW} = 50^{+18}_{-16}\,{\rm eV}$ and results in an improvement of the fit statistic to $C/d.o.f. = 4800/4432$. Upon the addition of this component, the parameters of the underlying broader Kα component adjust slightly to compensate but are still consistent within the errors (see Table 4.3 for the final best-fitting values). The presence of a Compton shoulder[3] was also tested for by including an additional Gaussian centred around ∼6.3 keV. This feature is not statistically required by the data and an upper limit on the equivalent width is found to be ${\rm EW} < 6\,{\rm eV}$. Including this component did not result in any changes to the parameters of the broad and narrow Fe Kα components at ∼6.4 keV. So although the near-neutral Fe Kα emission appeared to then be well modelled, further residuals were still present indicating additional K-shell emission from ionised Fe.

Additional Gaussians were adopted to model the remaining emission. A line at $E_{\rm c} = 6.97 \pm 0.02\,{\rm keV}$ is required by the data with an intrinsic width of $\sigma = 32^{+34}_{-17}\,{\rm eV}$ (FWHM

[3]The "Compton shoulder" results from scattered line photons from Fe Kα emission.

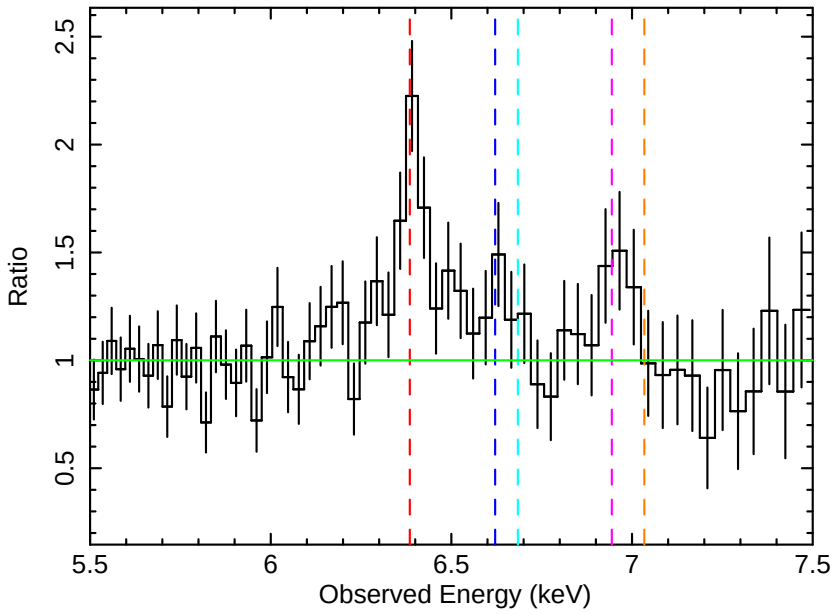

Figure 4.9: Ratio plot showing the residuals of the HEG data from 5.5–7.5 keV to a power law absorbed by Galactic hydrogen and a partial-coverer (as described in Section 4.4.1). Significant Fe K line emission is clearly present. The data are binned by a factor of 2 for clarity. The vertical dotted lines show the expected line energies of, from left to right, Fe I-XVII Kα (red), Fe XXV forbidden (blue), Fe XXV Kα resonance (cyan), Fe XXVI Lyα (magenta) and Fe I-XVII Kβ (orange) in the observed frame.

Line ID	E_c (keV)	σ (eV)	FWHM (km s^{-1})	F_{line} (10^{-5} ph cm^{-2} s^{-1})	EW (eV)	ΔC
Fe Kα_{broad}	$6.43^{+0.06}_{-0.06}$	150^{+60}_{-43}	$16\,000^{+7\,000}_{-4\,000}$	$3.17^{+0.91}_{-0.89}$	156^{+45}_{-44}	36
Fe Kα_{narrow}	$6.40^{+0.01}_{-0.01}$	0_{fixed}	-	$1.16^{+0.41}_{-0.37}$	50^{+18}_{-16}	25
[Fe XXV] $1s$–$2s$	$6.64^{+0.02}_{-0.02}$	< 52	$< 5\,400$	$0.43^{+0.37}_{-0.30}$	19^{+16}_{-13}	6
Fe XXVI $1s$–$2p$	$6.97^{+0.02}_{-0.02}$	32^{+34}_{-17}	$3\,100^{+3\,400}_{-1\,600}$	$1.01^{+0.51}_{-0.47}$	63^{+32}_{-29}	15

Table 4.3: The best-fitting Fe K parameters from the *Chandra* HETG spectrum of NGC 4051. All values are given in the rest frame of the source. See Section 4.4.2 for details.

$= 3\,100^{+3\,400}_{-1\,600}$ km s^{-1}) and an associated equivalent width of EW $= 63^{+32}_{-29}$ eV. This line is most likely due to the $1s$–$2p$ doublet from H-like iron (Fe XXVI) and improves the fit to $C/d.o.f. = 4785/4429$. A third component with a centroid energy of $E_c = 6.64 \pm 0.02$ keV is also required by the data. This line has an intrinsic width of $\sigma < 52$ eV (FWHM $<$

5 400 km s^{-1}) and corresponds to an equivalent width of EW = 19^{+16}_{-13} eV. This line improves the fit statistic by $\Delta C = 6$ (i.e. only ∼95% significant) and is most likely associated with being the forbidden transition of the He-like iron (Fe XXV) triplet at 6.636 keV, suggesting that this emission line may be consistent with an origin in photo-ionised gas (Bautista & Kallman 2000; Porquet & Dubau 2000). No further emission or absorption features are observed around the Fe K complex in the HETG data. In Table 4.3, the ΔC values refer to the change in the fit statistic upon removing the line from the final model. The overall fit statistic corresponds to $C/d.o.f. = 4779/4426$.

With the parameterisation of the baseline continuum, the warm absorber and the Fe K components complete, this is considered to be the final best-fitting model to the time-averaged *Chandra* HETG data. This model is then applied to the 2008 contemporaneous *Suzaku* data.

4.5 Suzaku Spectral Analysis

The first thing to be considered was the time-averaged 2008 *Suzaku* spectrum. In all subsequent fits, data acquired in the 0.6–10.0 and 15.0–50.0 keV energy bands for the XIS and HXD respectively were used. The cross-normalisation between the HXD-PIN and the XIS detectors was accounted for by the addition of a fixed constant component at a value of 1.18 for the HXD nominal pointing position (2005 observation) and 1.16 for the XIS nominal pointing position (2008 observations); values derived using *Suzaku* observations of the Crab (Ishida, Suzuki & Someya 2007). All data from 1.7–2.0 keV were also ignored so as to avoid any contamination from the K-shell absorption edge due to silicon in the detectors. Since the XIS data were binned up at the HWHM of the resolution of the detector, a 2% systematic error was included in all fits to account for the high statistical weight of the bins at low energies.

4.5.1 The Broad-Band Suzaku Model

Firstly, the best-fitting HETG continuum model (from Section 4.4) consisting of a power-law continuum, a partial-coverer, the fully-covering warm absorber (zones 1–4), Fe K emission

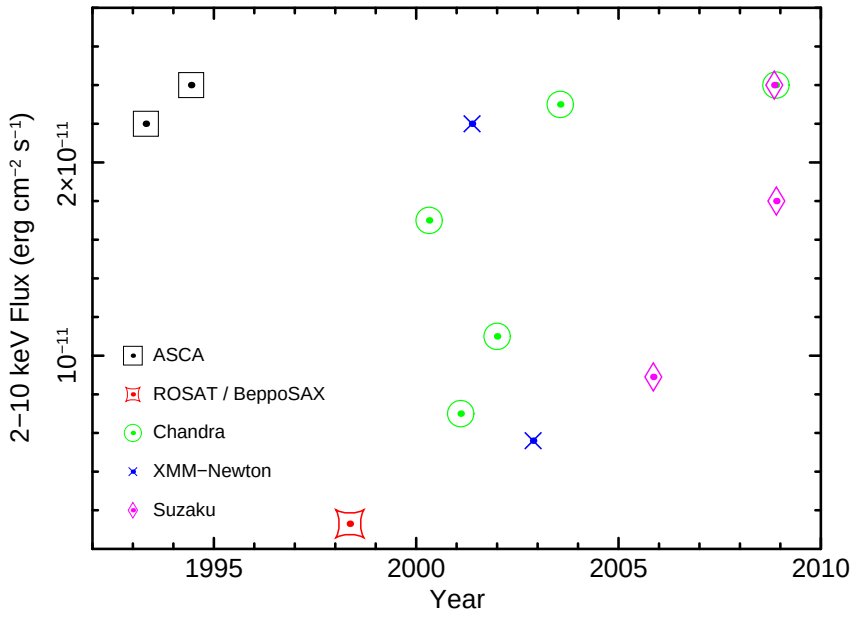

Figure 4.10: A historical lightcurve showing the 2–10 keV flux from all observations of NGC 4051 with *ASCA*, *BeppoSAX* (simultaneously with *ROSAT*), *Chandra*, *XMM-Newton* and *Suzaku*. The lightcurve shows that the flux of this source varies significantly over time and that the 2008 *Chandra* and *Suzaku* observations described here (top-right) were made during a period of high flux. Note that the 2005 *Suzaku* data modelled in Section 5.2.3.2 as well as previously by Terashima et al. (2009) were taken during a period of much lower flux. Data for the lightcurve were obtained from Guainazzi et al. (1996), Guainazzi et al. (1998), Uttley et al. (1999), Collinge et al. (2001), Uttley et al. (2003), Ogle et al. (2004), Steenbrugge et al. (2009), Terashima et al. (2009), Shu, Yaqoob & Wang (2010) and Turner et al. (2010).

lines and a blackbody to parameterise the soft excess was applied to the time-averaged 2008 broad-band *Suzaku* data from 0.6–50.0 keV when the source was observed to be in a period of high flux ($F_{0.5-10.0} = 5.03 \times 10^{-11}$ erg cm^{-2} s^{-1}). A historical lightcurve of NGC 4051 in the X-ray band is shown in Figure 4.10 where it can be seen that the 2008 observations were made during a period of relatively high flux for this source. Since the 2008 data were obtained in two separate observations due to scheduling constraints, the much longer ∼275 ks exposure is initially only considered. All of the soft X-ray, fully-covering absorption zones required by the HETG data (including the soft emission lines) were included and the parameters were fixed at the best-fitting values listed in Table 4.2 since the 2008 *Chandra* and *Suzaku* data

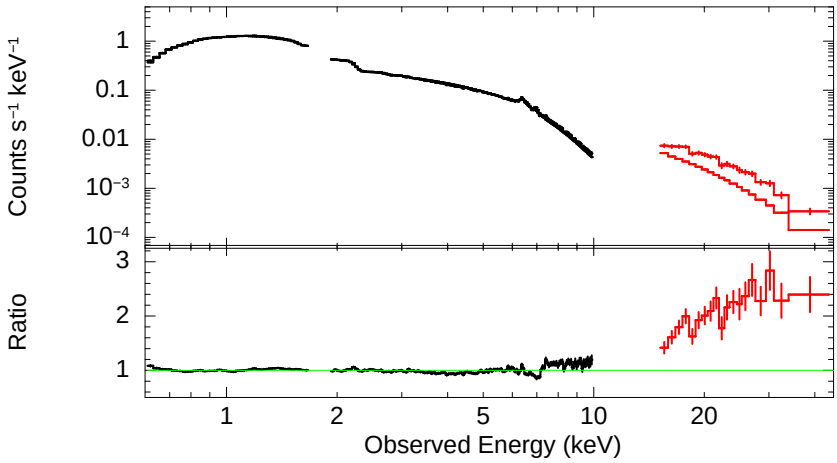

Figure 4.11: Plot showing the long (275 ks) 2008 *Suzaku* observation of NGC 4051 where the time-averaged broad-band (XIS + HXD) spectrum from 0.5–50 keV is compared with the best-fitting *Chandra* HETG continuum model (Section 4.4). Note the significant hard excess at energies >10 keV and negative residuals at ∼7 keV arising from absorption from highly-ionised Fe (see Section 4.5.2).

were quasi-simultaneous. This results in a very poor fit with $\chi^2/d.o.f. = 1351/188$. Allowing the model to renormalise slightly improves the fit but still returns a poor fit statistic of $\chi^2/d.o.f. = 1165/188$ with the main contribution to the residuals arising from the significant hard excess seen most notably at energies >10 keV. This hard excess can be seen in Figure 4.11 (also see Section 5.2.3.2) where the broad-band *Suzaku* spectrum is shown compared to the *Chandra* HETG model, which is extrapolated to higher energies (i.e. into the HXD-PIN band).

4.5.2 The Suzaku Fe K Profile: Emission and Highly-Ionised Absorption

In order to accurately analyse the *Suzaku* Fe K profile, it was important to firstly parameterise the broad-band continuum emission using both the XIS and HXD data. To do this, the hard excess was modelled by including the PEXRAV model (Magdziarz & Zdziarski 1995; see Section 2.5.1); an additive component incorporating the Compton-reflected continuum from a neutral slab. The photon index and the normalisation of the unabsorbed power-law

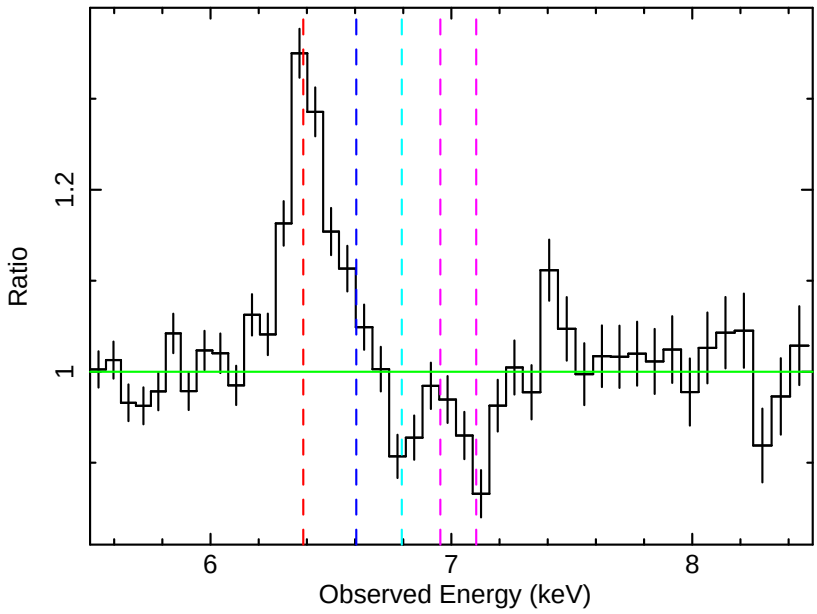

Figure 4.12: Plot showing the ratio of the data-to-model residuals of the 2008 *Suzaku* XIS data in the Fe K band in the observed frame. The dotted lines show the best-fitting centroid energies of the five significant emission / absorption lines required by the data: from left to right, neutral Fe Kα emission at 6.41 keV (red), Fe XXV forbidden emission at 6.62 keV (blue), blueshifted absorption most likely from Fe XXV at 6.81 keV (cyan) and emission and blueshifted absorption from Fe XXVI Lyα at 6.97 keV and 7.12 keV respectively (both magenta).

continuum were tied to that of the power-law component incident upon the reflector and the elemental abundances were fixed to solar values (Anders & Grevesse 1989). The cosine of the inclination angle of the source was fixed to 0.87 (corresponding to 30°; consistent with its classification as a type-1 Seyfert) and the folding energy was tied to the cut-off energy of the power law at 300 keV, consistent with no cut-off in the HXD-PIN band below 50 keV. It was found that the combination of the PEXRAV and blackbody models (to account for the hard- and soft-excess respectively) with the partial-coverer from the HETG model (to account for the additional spectral curvature) was able to smoothly paramaterise the broad-band continuum well.

The data-to-model residuals in the Fe K band are shown in Figure 4.12. The Fe K profile was parameterised with four significant lines modelled with Gaussians; two in emission and

two in absorption. The most prominent emission line corresponds to Kα emission from near-neutral Fe ($\Delta\chi^2 = 228$) and has a best-fitting centroid energy of $E_c = 6.41 \pm 0.01$ keV in the *Suzaku* data and an intrinsic width of $\sigma < 53$ eV (FWHM $<5\,700$ km s^{-1}). It also has an associated equivalent width of EW $= 75^{+14}_{-9}$ eV against the observed continuum. The second emission line ($\Delta\chi^2 = 12$) is manifested in the slight blue wing of the Fe Kα line shown in Figure 4.12 and corresponds to the forbidden transition from Fe XXV found in Section 4.4.2. The line width was fixed at $\sigma = 0$ eV (intrinsically narrow) and although the centroid energy was difficult to constrain, it was found to have a best-fitting value of $E_c = 6.62^{+0.09}_{-0.02}$ keV. The best-fitting values of the line flux and associated equivalent width ($F_{\rm line} = (5.51^{+1.29}_{-2.39}) \times 10^{-6}$ photons cm^{-2} s^{-1} and EW$= 25^{+6}_{-11}$ eV respectively) are also largely consistent with the corresponding values found in the *Chandra* HETG data.

The significant negative residuals apparent in the data at $\sim$7 keV are suggestive of the presence of highly-ionised absorption lines (also see Figure 4.13). At a first glance, the inferred blueshift of these lines could suggest that these lines are the absorption signature of a high-velocity outflow, such as that detected by Pounds et al. (2004a). These absorption lines were initially parameterised with Gaussians with negative fluxes. The first line ($\Delta\chi^2 = 26$) is found to have a centroid energy of $E_c = 6.81^{+0.04}_{-0.05}$ keV. Its intrinsic width was initially fixed at a value of $\sigma = 0$ eV. This absorption line has an associated equivalent width of EW $= -(28^{+31}_{-11})$ eV and is most likely due to absorption from the Fe XXV resonance line at 6.70 keV (rest-frame). If so, the blueshift of the line would suggest that the absorbing material is outflowing with a velocity of $v_{\rm out} = 5\,500^{+1\,800}_{-2\,100}$ km s^{-1} relative to the host galaxy, consistent with the value found by Terashima et al. (2009) and Pounds & Vaughan (2011). The second line ($\Delta\chi^2 = 56$) has a best-fitting centroid energy of $E_c = 7.12 \pm 0.04$ keV with a corresponding equivalent width of EW $= -(43^{+9}_{-11})$ eV (also see Figure 4.13). Again the intrinsic width of the line was fixed at $\sigma = 0$ eV. If this line is associated with the $1s$–$2p$ Lyα doublet from Fe XXVI at $\sim$6.97 keV (rest-frame) then it would correspond to an outflow velocity of $v_{\rm out} = 7\,500^{+1\,600}_{-1\,700}$ km s^{-1} again consistent with the findings of Pounds et al. (2004a) and Terashima et al. (2009).

In Section 4.4.2, an emission line from the Fe XXVI $1s$–$2p$ Lyα transition was also detected. To test for its presence in the XIS spectrum, including an additional line fixed at

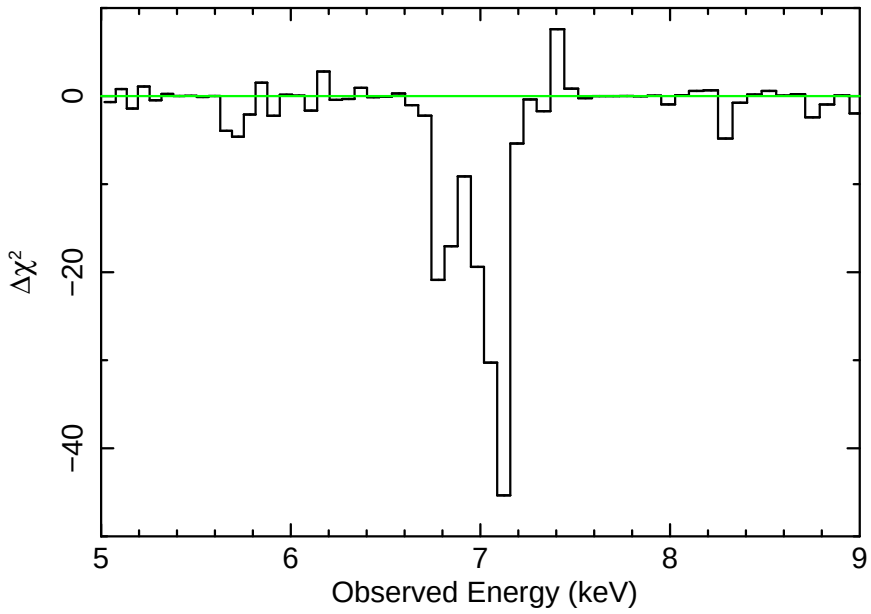

Figure 4.13: Plot (in the observed frame) showing the significant contribution to the χ^2 value of the two highly-ionised absorption lines at ∼6.8 and ∼7.1 keV most likely originating from Fe XXV and Fe XXVI respectively. The Fe K emission lines are modelled in this plot. See Section 4.5.2

the best-fitting value found in the HETG data of $E_c = 6.97$ keV with an intrinsically narrow width of $\sigma = 0$ eV (see Table 4.3) corresponds to an equivalent width of EW $= 9.9^{+9.3}_{-7.8}$ eV against the observed continuum. However, it is barely required by the data ($\Delta\chi^2 \sim 5$) and so is less significant in the *Suzaku* XIS data than in the *Chandra* HETG data. This could possibly be due to the strength of the two strong absorption lines with blueshifted centroid energies of ∼6.8 keV and ∼7.1 keV (in the observed frame) which are possibly masking some of the emission from the $1s$–$2p$ transition of H-like Fe in the XIS data. Note that a slight positive residual can also be observed at ∼7.5 keV (see Figure 4.12) which is likely due to Kα fluorescence from near-neutral Ni which has a rest-frame centroid energy of ∼7.47 keV. However, modelling this feature with a Gaussian is not statistically required by the data.

Finally, although no neutral Fe Kβ emission was statistically required by the data ($\Delta\chi^2 \sim 2$), it was modelled for consistency with the addition of a further Gaussian. The line

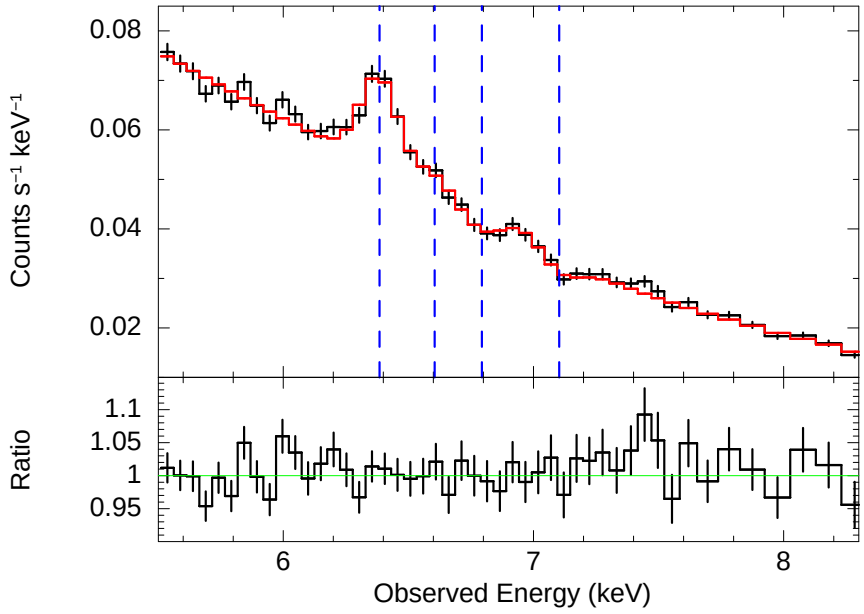

Figure 4.14: Plot showing the Fe K region of the 2008 *Suzaku* spectrum of NGC 4051. The model described in Section 4.5.2 is superimposed on the data. The vertical blue dashed lines denote the energies of the emission lines at ∼6.4 and ∼6.6 keV and the absorption lines at ∼6.8 and ∼7.1 keV. Note that no evidence is seen of any additional absorption features at ∼7.8 and ∼8.0 keV (indicative of a zone of high-velocity outflowing gas with $v_{\rm out} \sim 0.13c$) such as those reported by Pounds & Vaughan (2012) as part of their analysis of the *XMM-Newton* EPIC-pn data.

energy was fixed at 7.06 keV, the intrinsic width was tied to that of the corresponding Fe Kα line and the line flux was fixed at 13% of the Kα flux, consistent with the theoretical flux ratio for near-neutral iron (Kaastra & Mewe 1993). This line is retained in all subsequent fits.

After parameterising the absorption lines with simple Gaussians, an attempt was made to self-consistently model the lines with the addition of a photo-ionised grid of absorbing gas using the XSTAR code of Kallman & Bautista (2001). The XSTAR code is described in Section 2.5.1. This fit is shown in Figure 4.14 (also see Table 4.4). A turbulence velocity of $v_{\rm turb} = 3\,000\,{\rm km\,s^{-1}}$ was adopted so as not to saturate the absorption lines and to explain their high observed equivalent widths. The addition of this zone of gas improves the fit by $\Delta\chi^2 = 113$ and requires a best-fitting column density of $N_{\rm H} = (8.4^{+1.9}_{-2.0}) \times 10^{22}\,{\rm cm^{-2}}$

Component	Parameter	Value	$\Delta\chi^2$
Power law[a]	Γ	$2.20^{+0.01^{l_1}}_{-0.01}$	
	Norm. ($\mathrm{ph\,cm^{-2}\,s^{-1}}$)	$(1.14^{+0.01}_{-0.01}) \times 10^{-2}$	
Power law$^{b}_{\mathrm{abs.}}$	Γ	l_1	
	Norm. ($\mathrm{ph\,cm^{-2}\,s^{-1}}$)	$(5.19^{+0.56}_{-0.69}) \times 10^{-3}$	
PEXRAV[c]	R	$1.23^{+0.13}_{-0.06}$	
	A_{Fe}	$0.37^{+0.08}_{-0.11}$	
Blackbody[d]	$k_{\mathrm{B}}T$ (keV)	$0.11^{+0.01}_{-0.01}$	
	Norm. (L_{39}/D_{10}^2)	$(2.34^{+0.18}_{-0.26}) \times 10^{-4}$	
Fe Kα[e]	E_{c} (keV)	$6.41^{+0.01}_{-0.01}$	228
	σ (eV)	< 53	
	F_{line} ($\mathrm{ph\,cm^{-2}\,s^{-1}}$)	$(1.69^{+0.32}_{-0.20}) \times 10^{-5}$	
	EW (eV)	75^{+14}_{-9}	
Fe XXV[e]	E_{c} (keV)	$6.62^{+0.09}_{-0.02}$	12
	σ (eV)	0_{fixed}	
	F_{line} ($\mathrm{ph\,cm^{-2}\,s^{-1}}$)	$(5.51^{+1.29}_{-2.39}) \times 10^{-6}$	
	EW (eV)	25^{+6}_{-11}	
Fe XXV$^{e}_{\mathrm{abs.}}$	E_{c} (keV)	$6.81^{+0.04}_{-0.05}$	26
	σ (eV)	0_{fixed}	
	F_{line} ($\mathrm{ph\,cm^{-2}\,s^{-1}}$)	$-(5.14^{+5.74}_{-1.95}) \times 10^{-6}$	
	EW (eV)	$-(28^{+31}_{-11})$	
Fe XXVI$^{e}_{\mathrm{abs.}}$	E_{c} (keV)	$7.12^{+0.04}_{-0.04}$	56
	σ (eV)	0_{fixed}	
	F_{line} ($\mathrm{ph\,cm^{-2}\,s^{-1}}$)	$-(6.95^{+1.41}_{-1.81}) \times 10^{-6}$	
	EW (eV)	$-(43^{+9}_{-11})$	
High ξ abs.[f]	N_{H} ($\mathrm{cm^{-2}}$)	$(8.36^{+1.89}_{-2.01}) \times 10^{22}$	113
	$\log \xi$	$4.10^{+0.18}_{-0.11}$	
	v_{out} ($\mathrm{km\,s^{-1}}$)	$5\,800^{+860}_{-1\,200}$	

Table 4.4: The best-fitting rest-frame parameters of the broad-band *Suzaku* XIS + HXD model described in Section 4.5 for NGC 4051. [a]Primary power-law continuum: Γ, photon index; Normalisation. [b]Absorbed power law. [c]PEXRAV neutral reflector: R, reflection scaling factor; A_{Fe}, iron abundance with respect to solar values. [d]Blackbody: $k_{\mathrm{B}}T$, temperature; Normalisation defined as L_{39}/D_{10}^2 where L_{39} is the source luminosity in units of $10^{39}\,\mathrm{erg\,s^{-1}}$ and D_{10} is the distance to the source in units of 10 kpc. [e]Emission/Absorption lines: E_{c}, centroid energy; σ, intrinsic width; F_{line}, line flux; EW, equivalent width. [f]Highly-ionised absorption: N_{H}, column density; ξ, ionisation parameter; v_{out}, velocity shift. The symbol l signifies that the parameter is linked to all parameters with the corresponding number. Note that the high ξ XSTAR zone replaced the highly-ionised absorption lines and they were not modelled simultaneously.

and a best-fitting value for the ionisation parameter of $\log \xi = 4.1^{+0.2}_{-0.1}$. The blueshift of the zone corresponds to an outflow velocity of $v_{\rm out} = 5\,800^{+860}_{-1\,200}\,{\rm km\,s^{-1}}$ ($\sim$0.02c), consistent with the values found by Pounds et al. (2004a) and Terashima et al. (2009) for the highly-ionised outflow. No further zones of absorption are statistically required by the data to model the absorption in the Fe K band and it should be noted that no evidence is seen of the higher-velocity ($v_{\rm out} \sim 0.13c$) component reported by Pounds & Vaughan (2012). Indeed, by fixing two additional Gaussians centred on energies of 7.8 and 8.0 keV (corresponding to the observed energies reported by Pounds & Vaughan 2011), it was found that these are not statistically required by the data ($\Delta\chi^2 < 1$ in each case) and have upper limits on the magnitudes of their line fluxes of $F_{\rm line} < 8.4 \times 10^{-7}$ and $F_{\rm line} < 6.3 \times 10^{-7}\,{\rm photons\,cm^{-2}\,s^{-1}}$ respectively. Fixing the fluxes at the best-fitting values from the *XMM-Newton* data analysed by Pounds & Vaughan (2011) of $F_{\rm line} = -4.8 \times 10^{-6}$ and $F_{\rm line} = -3.1 \times 10^{-6}\,{\rm photons\,cm^{-2}\,s^{-1}}$ worsens the fit by $\Delta\chi^2 = 13$ and $\Delta\chi^2 = 18$ for the 7.8 and 8.0 keV lines respectively. So, although this high-velocity component is not required in the *Suzaku* spectrum it could be due to variations in the line-of-sight absorber between observations.

Upon modelling the Fe K emission and the highly-ionised absorption, the reflection scaling factor of the PEXRAV component was found to have a best-fitting value of $R = 1.23^{+0.13}_{-0.06}$. It is noted that a sub-solar Fe abundance is preferred by the data with the value dropping to $A_{\rm Fe} = 0.37^{+0.08}_{-0.11}$ times solar (where the abundances used are those of Anders & Grevesse 1989). However, this could simply be due to the limitations of fitting the spectrum with a simple neutral slab. It is also noted that the ratio of the normalisations of the absorbed to total power-law components at 1 keV ($\sim$0.3) is consistent with the best-fitting values obtained from the HETG spectrum (i.e. still suggestive of a $\sim$30% covering fraction for the partial-covering zone; also see Section 4.4.1). The final best-fitting parameters of the broad-band model to the *Suzaku* XIS + HXD data are shown in Table 4.4. The overall fit statistic corresponds to $\chi^2/d.o.f. = 218/187$.

Finally, as a consistency check, the presence of the two highly-ionised absorption lines which are detected with *Suzaku* was tested for in the *Chandra* HETG data. A direct comparison of the Fe K regions is shown in Figure 4.15. Taking the best-fitting HETG model from Section 4.4, two Gaussian profiles with negative fluxes were added, fixing the centroid

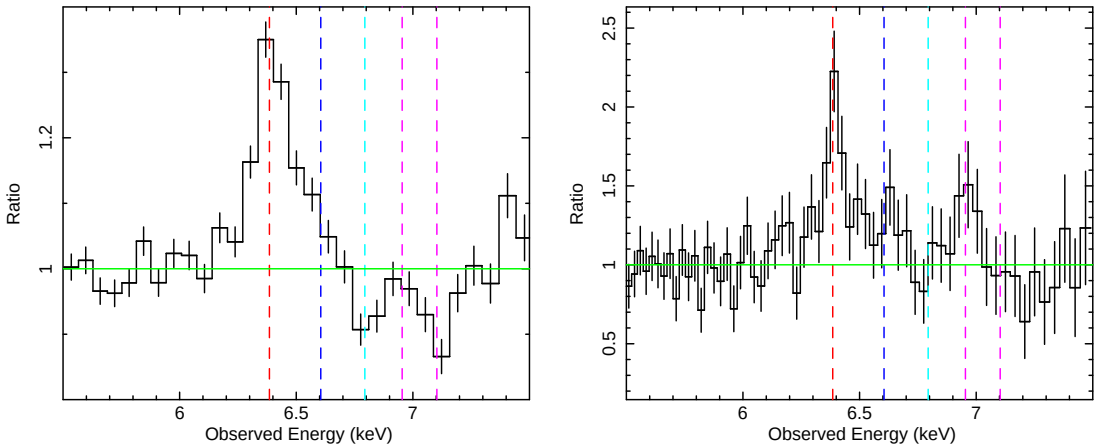

Figure 4.15: Ratio plots against an absorbed power-law continuum of the Fe K region in the 2008 *Suzaku* XIS (left) and *Chandra* HETG (right) data. The dotted lines show the best-fitting centroid energies of the five significant emission / absorption lines required by the data: from left to right, neutral Fe Kα emission at 6.41 keV (red), Fe XXV forbidden emission at 6.62 keV (blue), blueshifted absorption most likely from Fe XXV at 6.81 keV (cyan) and emission and blueshifted absorption from Fe XXVI Lyα at 6.97 keV and 7.12 keV respectively (both magenta).

energies at $E_c = 6.81\,\mathrm{keV}$ and $E_c = 7.12\,\mathrm{keV}$ respectively and the intrinsic width of the two lines at $\sigma = 0\,\mathrm{eV}$, consistent with the *Suzaku* data. Neither of the two lines were statistically required by the HETG data but upper limits are found on the magnitudes of the line fluxes of $F_{\mathrm{line}} < 3.9 \times 10^{-6}$ and $F_{\mathrm{line}} < 6.3 \times 10^{-6}\,\mathrm{photons\,cm^{-2}\,s^{-1}}$ for the two respective lines, indicating that they are consistent with the values that are found with the *Suzaku* data.

4.6 Discussion

4.6.1 Highly-Ionised Outflow

The *Suzaku* XIS spectrum of NGC 4051 reveals two absorption lines with centroid energies at ∼6.8 and ∼7.1 keV, as described in Section 4.5.2. This suggests that the absorption is significantly blueshifted and could be the signature of a highly-ionised, high-velocity outflow. Modelling with an XSTAR grid with a turbulence velocity of $v_{\mathrm{turb}} = 3\,000\,\mathrm{km\,s^{-1}}$ requires

one zone of absorption with a best-fitting column density of $N_{\rm H} = 8.4^{+1.9}_{-2.0} \times 10^{22}\,{\rm cm}^{-2}$ and an ionisation parameter of $\log \xi = 4.1^{+0.2}_{-0.1}$ (as per Section 4.5.2). Assuming that the lines correspond to K-shell absorption of Fe XXV and Fe XXVI, the blueshift of the zone corresponds to an outflow velocity of $v_{\rm out} = 5\,800^{+860}_{-1200}\,{\rm km\,s}^{-1}$, largely consistent with the findings of Pounds et al. (2004a) and Terashima et al. (2009). It is also conceivable that this is the highly-ionised signature of the high-velocity outflow detected by Steenbrugge et al. (2009) with the *Chandra* LETG which they deduce to have a comparable outflow velocity of $v_{\rm out} \sim 4\,500\,{\rm km\,s}^{-1}$ although with an ionisation parameter $\sim$10 times lower (i.e. $\log \xi \sim 3.1$).

4.6.1.1 The Kinematics of the Highly-Ionised Absorption

For a homogeneous, radial, outflowing wind, the column density along the line-of-sight is given by $N_{\rm H} = \int_{R_{\rm in}}^{R_{\rm out}} n_{\rm e}(R) dR$, where $R_{\rm in}$ and $R_{\rm out}$ are the inner and outer radii along the line-of-sight through the wind respectively. Under the assumption that one is looking down a spherically-symmetric homogeneous wind towards the inner radius, then $R_{\rm out}$ tends to ∞. So, combining this with the definition of the ionisation parameter (equation 4.1) leads to $R_{\rm in} = L_{\rm ion}/N_{\rm H}\xi$. However, if the thickness of the wind is defined as $\Delta R = R_{\rm out} - R_{\rm in}$ then the inner radius may extend inwards if the wind is clumpy (i.e. if $R_{\rm in} \gg \Delta R$). This yields:

$$R_{\rm in} \lesssim \frac{L_{\rm ion}}{N_{\rm H}\xi}. \tag{4.2}$$

A value for the ionising luminosity can be calculated by extrapolating the total power-law continuum of the broad-band *Suzaku* model from the 2008 data and integrating from 1 to 1 000 Rydberg. This gives a value of $L_{\rm ion} \sim 1.4 \times 10^{43}\,{\rm erg\,s}^{-1}$. Combining this with the best-fitting values of the column density and the ionisation parameter from the XSTAR model (Table 4.4) then yields a value for the radius of the absorbing material of $R_{\rm in} \lesssim 1.3 \times 10^{16}$ cm which is of the order of $\lesssim 0.004$ pc or $\lesssim 5$ light-days from the central engine. Assuming that the material escapes to infinity then a lower limit on the radius can also be calculated by considering the outflowing material's escape velocity where $v_{\rm esc} = \sqrt{\frac{2GM}{R}}$. Rearranging for R gives a lower limit of $R > 1.4 \times 10^{15}$ cm placing the constraints on the radius of the highly-ionised absorber to be $0.5 < R \lesssim 5$ light-days from the central source and implies that

the electron density can be constrained to $7 \times 10^6 \lesssim n_\mathrm{e} < 6 \times 10^8\,\mathrm{cm}^{-3}$ (equation 4.1). The constraints on the radius derived here are consistent with the radius of 0.5–1 light-days found by Krongold et al. (2007) for their highly-ionised zone of absorption found in the *XMM-Newton* RGS spectrum. This is well within the 10–15 light-day dust sublimation radius in NGC 4051 (see Krongold et al. 2007 fig.10) and so cannot have an origin in the dusty molecular torus. Instead, as the location of the highly-ionised absorber also appears to be contained within the location of the He II broad emission line region (BELR; Krongold et al. 2007), an accretion-disc wind is perhaps a more likely origin for this absorption signature.

By considering the case of a homogeneous, spherical flow under the assumption that the outflow velocity remains approximately constant on the compact scales observed here (although likely decelerating at some larger radius), an estimate of the mass outflow-rate of the highly-ionised zone can be calculated from the simple conservation of mass:

$$\dot{M}_\mathrm{out} = 4\pi b \frac{L_\mathrm{ion}}{\xi} v_\mathrm{out} m_\mathrm{p}, \tag{4.3}$$

where $L_\mathrm{ion}/\xi = n_\mathrm{e} R^2$. Here, $\dot{M}_\mathrm{out}$ is the mass-outflow rate in units $\mathrm{g\,s}^{-1}$ subtending a solid angle, $4\pi b$ (where $0 \leq b \leq 1$), where L_ion is is the ionising luminosity from 1 to 1 000 Rydberg in units $\mathrm{erg\,s}^{-1}$, ξ is the ionisation parameter in units $\mathrm{erg\,cm\,s}^{-1}$, v_out is the outflow velocity in units $\mathrm{cm\,s}^{-1}$ and m_p is the rest-mass of a proton. Initially assuming that the absorber is fully covering (i.e. $b = 1$) and taking the best-fitting values of the ionisation parameter and outflow velocity given in Table 4.4 and the value for the ionising luminosity derived above yields an estimate of the mass-outflow rate of $\dot{M}_\mathrm{out} \sim 0.2\,\mathrm{M}_\odot\,\mathrm{yr}^{-1}$. This value then translates into an estimate of the kinetic output of the outflow via:

$$\dot{E}_\mathrm{out} = \frac{1}{2} \dot{M}_\mathrm{out} v_\mathrm{out}^2, \tag{4.4}$$

which corresponds to a value of $\dot{E}_\mathrm{out} \sim 2 \times 10^{42}\,\mathrm{erg\,s}^{-1}$, which is approximately 3–4% of the bolometric output of the AGN ($L_\mathrm{bol} \sim 7 \times 10^{43}\,\mathrm{erg\,s}^{-1}$; Ogle et al. 2004). The momentum-rate of the outflow is then $\dot{M}_\mathrm{out} v_\mathrm{out} \sim 8 \times 10^{33}\,\mathrm{g\,cm\,s}^{-2}$.

For a momentum-driven outflow whereby $\tau \sim 1$ (i.e. where the photons scatter once before escaping and so all momentum is transferred to the outflow) accreting at near-Eddington

(i.e. $\dot{M}_{\rm out} \sim \dot{M}_{\rm Edd}$), the total wind-momentum flux must be of the same order as the photon-momentum flux (King 2010), i.e.:

$$\dot{M}_{\rm out} v_{\rm out} \approx \frac{L_{\rm Edd}}{c}. \tag{4.5}$$

Assuming a black hole mass of $M_{\rm BH} = 1.73 \times 10^6\,{\rm M}_\odot$ (Denney et al. 2009) for NGC 4051, the Eddington luminosity is found to be $L_{\rm Edd} \sim 2.2 \times 10^{44}\,{\rm erg\,s^{-1}}$ which yields $L_{\rm Edd}/c \sim 7.5 \times 10^{33}\,{\rm erg\,cm^{-1}}$; a value comparable to the calculated outflow momentum rate of $\dot{M}_{\rm out} v_{\rm out} \sim 8 \times 10^{33}\,{\rm g\,cm\,s^{-2}}$. So it can be seen that equation 4.5 is largely satisfied if one assumes that the highly-ionised outflow is momentum-driven by Thomson scattering such as in the similar case of the QSO PG 1211+143 (King & Pounds 2003; Pounds et al. 2003a).

Furthermore, the Eddington luminosity is also defined by:

$$L_{\rm Edd} = \eta \dot{M}_{\rm Edd} c^2, \tag{4.6}$$

where η is the efficiency of mass-to-energy conversion and takes a value between 0 and 1. Combining this with equation 4.5 yields an expression for the wind velocity (King 2010):

$$v_{\rm out} \approx \frac{\eta}{\dot{m}} c, \tag{4.7}$$

where $\dot{m} = \dot{M}_{\rm acc}/\dot{M}_{\rm Edd}$ is the accretion rate in Eddington units. Since $v_{\rm out} = 0.02c$ here, a value of $\eta \sim 0.02$ would be required to sustain the Eddington luminosity of this source if it were accreting at the Eddington rate (i.e. $\dot{m} \sim 1$). Note that the maximum value of η is 0.06 for a non-rotating, Schwarzschild black hole (although this increases to $\eta = 0.36$ for a Kerr black hole).

The bolometric luminosity of NGC 4051 calculated by Ogle et al. (2004) and corrected for the distance of 15.2 Mpc assumed here is $L_{\rm bol} \sim 7 \times 10^{43}\,{\rm erg\,s^{-1}}$. Comparing this to the Eddington luminosity suggests that this object has an accretion rate of ~30% of $\dot{M}_{\rm Edd}$ which would correspond to an observed mass accretion-rate of $\dot{M}_{\rm acc} = L_{\rm bol}/\eta c^2 \sim 0.06\,{\rm M}_\odot\,{\rm yr^{-1}}$ assuming an efficiency of $\eta = 0.02$. However, the observed luminosity of the system with respect to Eddington may be underestimated if some of the emission is obscured by a Compton-thick wind and scattered out of the line-of-sight (an idea perhaps supported by the apparent pres-

ence of high column densities towards this source; also see Chapter 5). So it is perhaps conceivable that NGC 4051 is accreting at an appreciable fraction of the Eddington rate. Furthermore, Sim et al. (2010) show that radiatively-driven accretion-disc winds can exist with similar properties to those that are observed here for sources with luminosities of a few tens of per cent of $L_{\rm Edd}$.

4.6.1.2 The Covering Fraction

From the consideration of mass conservation (equation 4.3), it can be seen that the mass-outflow rate is dependent upon the covering factor, b, which is likely to be some significant fraction of 4π sr. The calculations in Section 4.6.1.1 were based on the assumption that the outflow is a radial flow in a spherical geometry with $b = 1$. However, if the outflow takes the form of a bi-conical geometry (Elvis 2000), as proposed by Krongold et al. (2007) for this source then the covering fraction may be lower.

The *Chandra* HETG data reveal the presence of two highly-ionised Fe K emission lines most likely originating from Fe XXV and Fe XXVI. The former line is also observed in the *Suzaku* XIS spectrum although testing for the presence of the Fe XXVI line shows that it is barely required by the XIS data. If these lines are the signature of the same ions associated with the highly-ionised, high-velocity outflow, an attempt can be made to obtain an estimate of the covering fraction of the material. Bianchi & Matt (2002) calculate the predicted equivalent widths of the Fe XXV and Fe XXVI emission lines against the total (primary + reprocessed) continuum for a given photon index and column density. Figures 8 and 9 of Bianchi & Matt (2002) show that for a column density of $N_{\rm H} = 10^{23}\,{\rm cm}^{-2}$ and a photon index of $\Gamma = 2.4$, the expected equivalent widths are $\sim$50 eV and $\sim$15 eV for the Fe XXV and Fe XXVI emission lines respectively. As the column density of the highly-ionised absorption observed here with *Suzaku* is $N_{\rm H} \sim 8 \times 10^{22}\,{\rm cm}^{-2}$ (see Section 4.5.2) and the best-fitting photon index is $\Gamma \sim 2.5$ (see Section 5.2.3.1) in the 2008 data, a direct comparison can be made. No robust comparison can be made for the Fe XXVI emission since it is only significant in the *Chandra* HETG data yet not really required in the *Suzaku* XIS spectrum (which has a higher effective area in the Fe K band than the HETG). However, within the errors, the

equivalent width of ∼25 eV obtained for the Fe XXV emission line in the *Suzaku* data (see Table 4.4) suggests that it is on the order of ∼50% lower than the predicted maximum values perhaps implying that the covering factor is on the order of $b \sim 0.5$.

Furthermore, Tombesi et al. (2010) analysed a sample of 42 radio-quiet AGN observed with *XMM-Newton*. They detected 22 absorption lines at rest-frame energies >7.1 keV, implying that high-velocity outflows may be a common phenomenon in radio-quiet AGN. The fraction of AGN having at least one feature with a blue-shifted velocity in their sample is 17/42, corresponding to ∼40% of the objects. They also find that the global covering-fraction of the absorbers that they detect is estimated to be in the range $C \sim 0.4$–0.6, suggesting that the outflowing winds generally have large opening angles (also see Gofford et al. 2012 for a similar study with *Suzaku* data).

A rough estimate of b can also be obtained by comparing the observed accretion rate of the source ($\dot{M}_{\rm acc} \sim 0.06\,{\rm M}_{\odot}\,{\rm yr}^{-1}$; see Section 4.6.1.1) with the calculated spherical-outflow rate from equation 4.3 ($\dot{M}_{\rm out} \sim 0.2\,{\rm M}_{\odot}\,{\rm yr}^{-1}$) under the assumption that the mass-outflow rate either does either not exceed or is of the same order as the mass-accretion rate (i.e. $\dot{M}_{\rm out} \lesssim \dot{M}_{\rm acc}$). This suggests a covering fraction of $b \lesssim 0.3$ although this could be higher if the observed luminosity with respect to Eddington is underestimated somewhat perhaps due to partially-covering Compton-thick clouds in the line-of-sight. So it seems that although the absorption component is unlikely to be fully covering, the observational evidence suggests that the outflow is not highly collimated with b still likely to correspond to a significant fraction of 1 which is consistent with the detailed reverberation analysis of Miller et al. (2010b) who state that a global covering fraction of $\gtrsim 40\%$ is required to match the observations.

4.6.1.3 Implications for Feedback

Given the high accretion-rates required for the growth of supermassive black holes, significant outflows may be a consequence of near-Eddington accretion (King 2010). If so, they could be an important factor in galaxy evolution and in establishing the observed M–σ and M–$M_{\rm bulge}$ relations between the supermassive black hole and its host galaxy (Magorrian et al. 1998; Ferrarese & Merritt 2000; Gebhardt et al. 2000).

Taking the bolometric luminosity of $L_{\rm bol} \sim 7 \times 10^{43}\,{\rm erg\,s^{-1}}$ of NGC 4051, an estimate for the mass accretion rate can be calculated of $\dot{M}_{\rm acc} \sim 0.06\,{\rm M_\odot\,yr^{-1}}$. Thus, for the black hole to accrete a mass of $M_{\rm BH} = 1.73 \times 10^6\,{\rm M_\odot}$ (Denney et al. 2009), the Salpeter e-folding time would be $\sim 3 \times 10^7\,{\rm yr}$. As calculated in Section 4.6.1.1, the energy output of the high-velocity outflow is $\dot{E}_{\rm out} \sim 2 \times 10^{42}\,{\rm erg\,s^{-1}}$ assuming that $b \sim 1$. Integrating this over the e-folding time of the AGN gives a total energy output of $E_{\rm tot} \sim 10^{57}\,{\rm erg}$ (even if a conservative value of $b = 0.1$ is assumed, this still provides a total output of $E_{\rm tot} \sim 10^{56}\,{\rm erg}$). This value can then be compared with the binding energy of the bulge of the host galaxy. Marconi & Hunt (2003) and Häring & Rix (2004) provide an observable relationship between the mass of the central object and the mass of the galaxy bulge, i.e. $M_{\rm BH} \sim 10^{-3} M_{\rm bulge}$. This can then be used to calculate the binding energy of NGC 4051 whereby $B.E. \sim \sigma^2 M_{\rm bulge}$. Nelson & Whittle (1995) provide a value for the velocity dispersion of NGC 4051 of $\sigma = 88\,{\rm km\,s^{-1}}$ which then yields an estimate of the binding energy of $B.E. \sim 3 \times 10^{56}\,{\rm erg}$, comparable with the likely total energy deposited by the wind (assuming that the wind persists for at least one e-folding time). Therefore, it can be seen that the total energy output of the high-velocity outflow could have a considerable influence on its host galaxy environment (e.g. King 2003; King 2010; McQuillin & McLaughlin 2012). Indeed it may be conceivable that NGC 4051 is a low-mass analogue of the QSOs PG 1211+143 (Pounds & Reeves 2009) and PDS 456 (Reeves et al. 2009) which may deposit as much as $10^{60}\,{\rm erg}$ throughout the lifetime of the AGN.

4.6.2 The Soft X-ray Absorption / Emission

The HETG spectrum shows evidence for a wealth of absorption lines in the soft X-ray band. Modelling this warm absorber with XSTAR requires four distinct ionisation-zones of gas with the ionisation parameter ranging from $\log \xi = -0.86$ to $\log \xi = 2.97$ and column densities on the order of 10^{20}–$10^{21}\,{\rm cm^{-2}}$ (see Table 4.2). The zones are observed to be outflowing with velocities on the order of a few $100\,{\rm km\,s^{-1}}$ with the general trend appearing to be that the larger outflow velocities correspond to more highly-ionised zones. This is perhaps suggestive of a geometry whereby all of the zones form part of the same extended outflowing

wind with the higher velocity, more highly-ionised components originating much closer to the central source. Indeed, as the mass outflow-rate (equation 4.3) and the ionisation parameter (equation 4.1) combine to give:

$$\dot{M}_{\rm out} \propto \frac{L_{\rm ion} v_{\rm out}}{\xi} = const. \tag{4.8}$$

(King 2010), such a trend between ionisation parameter and outflow velocity would be expected to be observed if the mass outflow-rate is to be conserved. Such a correlation has previously been noted in NGC 4051 by Pounds et al. (2004a) and, if confirmed, could provide strong evidence of a cooling shock (King 2010).

Using equation 4.2, it is possible obtain upper limits for the radius of the absorbing zones of gas (see Table 4.5). However, these values are largely unconstrained and result in very conservative upper limits on the order of kpc for the two most lowly-ionised zones. The constraints on the medium- and higher-ionisation zones are a little tighter with the radius of the material falling within $\sim$70 and $\sim$2 pc from the central source respectively. It should be noted that the absorbers could exist at smaller radii still if the material is somewhat clumpy or filamentary.

Calculations of the mass-outflow rate of zones 1–4 using equation 4.3 prove to significantly exceed the Eddington accretion-rate of the source by several orders of magnitude since they assume that the absorber forms part of a fully-covering, homogeneous, radial flow. However, if the assumption is made that the mass-outflow rate does not exceed the observed mass accretion-rate since the energy required to accelerate the outflow must come from the infalling gas (i.e. $\dot{M}_{\rm out} \lesssim 0.06\,{\rm M}_{\odot}\,{\rm yr}^{-1}$), the soft zones can be scaled accordingly and upper limits can be placed on the covering fraction (see Table 4.5). This results in values ranging from $b \lesssim 4.4 \times 10^{-4}$ to $b \lesssim 0.56$ for the lowest- and highest-ionisation zones in the HETG data respectively. The values for the lower-ionisation zones are generally consistent with the opening angles of the warm absorber components detected by Steenbrugge et al. (2009) with the *Chandra* LETG. Upper limits were also calculated for the kinetic output of the outflow using the assumption about the mass outflow-rate stated above and equation 4.4. This resulted in values ranging from $\dot{E}_{\rm out} \lesssim 1.8 \times 10^{39}\,{\rm erg\,s}^{-1}$ to $\dot{E}_{\rm out} \lesssim 2.9 \times 10^{40}\,{\rm erg\,s}^{-1}$ for the

Absorption Component	R (pc)	$E_{\rm K}$ ($\rm erg\,s^{-1}$)	b
Zone 1	$\lesssim 8.7\times10^{4}$	$\lesssim 1.8\times10^{39}$	$\lesssim 4.4\times10^{-4}$
Zone 2	$\lesssim 1.2\times10^{4}$	$\lesssim 7.4\times10^{39}$	$\lesssim 5.2\times10^{-3}$
Zone 3a	$\lesssim 75$	$\lesssim 1.7\times10^{40}$	$\lesssim 0.10$
Zone 3b	$\lesssim 65$	$\lesssim 3.8\times10^{40}$	$\lesssim 0.05$
Zone 4	$\lesssim 1.8$	$\lesssim 2.9\times10^{40}$	$\lesssim 0.56$
High ξ	$0.0004 < R \lesssim 0.004$	$\sim 2\times10^{42}$	~ 0.5

Table 4.5: The upper limits of the radius, R, kinetic energy output, $E_{\rm K}$, and covering fraction, b, obtained for the five individual zones of absorption detected in the *Chandra* HETG data for NGC 4051 (see Section 5.1) assuming that the mass outflow-rates for each zone does not exceed or is on the order of $\sim 0.1\,\rm M_{\odot}\,yr^{-1}$. The absorption zones directly correspond to those listed in Table 4.2. The highly-ionised zone of absorption detected with *Suzaku* is also included for ease of comparison.

five zones of absorption, i.e. very small fractions of the total bolometric output of the AGN in contrast to the high-velocity outflow observed with *Suzaku* which has a kinetic output at least two orders of magnitude higher and could potentially be highly significant in terms of galactic feedback.

Several narrow emission features are also detected at energies <2 keV. The ionised reflector is unable to model all of the emission lines and, in particular, cannot account for the forbidden transitions from O VII, Ne IX and Si XIII. Previous studies with the RGS on-board *XMM-Newton* have claimed the presence of RRC (Ogle et al. 2004; Pounds et al. 2004a) associated with H-like and He-like ions of elements such as O and Ne, especially when the source is found to have fallen into an extended period of low flux, suggesting that the soft X-ray emission lines may have a photo-ionised origin. Indeed an origin in photo-ionised gas (either formed in the NLR or in an extended photo-ionised outflow) has been claimed for soft X-ray lines in many other objects (e.g. Bianchi, Guainazzi & Chiaberge 2006). If the emission lines detected here do indeed originate in a photo-ionised plasma, an estimate of the electron density of the O VII emission (the strongest soft X-ray emission line detected here) can be calculated using the 'R' ratio for He-like ions of Porquet & Dubau (2000), which is defined as $R(n_{\rm e}) = \frac{z}{x+y}$ where z is the intensity of the forbidden line and x and y are the intensities of the intercombination lines. An upper limit on the flux of the O VII intercombination line(s)

can be found by including an additional Gaussian in the HETG spectrum with the centroid energy fixed at 568.5 eV and the intrinsic width of the line tied to that of the associated forbidden transition. There is no statistical requirement for this component by the data and it returns an upper limit of the line flux of $F_{\rm line} < 2.85 \times 10^{-5}$ photons cm^{-2} s^{-1}. Combining this with the flux of the O VII forbidden line of $F_{\rm line} = 1.25^{+0.37}_{-0.32} \times 10^{-4}$ photons cm s^{-1} (see Table 4.1) provides a lower limit on the value of the R ratio[4] of $R > 3$. Then, by considering the relationship between the R ratio and electron density for O VII shown in fig.8 of Porquet & Dubau (2000), an upper limit on the electron density for the O VII emission can be obtained which is on the order of $n_{\rm e} < 10^{11}$ cm^{-3}. If the majority of O VII absorption is being modelled by zone 2 (see Table 4.2 and Figure 4.6), then by assuming that the emission has an ionisation parameter of $\log \xi \sim 0.6$, equation 4.1 allows a lower limit to be placed on the radius of this emission of $R > 3.8 \times 10^{15}$ cm, which is on the order of $\sim 10^4\, r_{\rm g}$ or $\sim$1.5 light-days. This radius is largely consistent with the value of $R < 100$ light-days found by Steenbrugge et al. (2009) and the value of $R < 3.5$ light-days for the lowly-ionised component detected by Krongold et al. (2007).

4.7 Conclusions

Through a detailed analysis of the time-averaged X-ray spectrum of NGC 4051 with the *Chandra* HETG and the *Suzaku* XIS and HXD instruments, it is possible to fully parameterise the warm absorber with zones of absorption ranging in ionisation parameter from $\log \xi = -0.86$ to $\log \xi = 4.1$ and ranging in column density from $N_{\rm H} \sim 10^{20}$ cm^{-2} to $N_{\rm H} \sim 10^{23}$ cm^{-2}. The soft X-ray absorber zones are observed to be outflowing with velocities on the order of a few 100 km s^{-1} with the general trend being that the outflow velocity increases with ionisation parameter. The kinetic output of the zones are then calculated to be on the order of $\dot{E}_{\rm out} \lesssim 10^{39}$–$10^{40}$ erg s^{-1}; values which correspond to very small fractions of the total bolometric output of the AGN and are negligible with respect to the binding energy

[4]One caveat to this is that densities obtained with the R ratio are also dependant upon photo-excitation of the associated resonance line and optical-depth effects.

of the galactic bulge (although such kinetic luminosities could still significantly influence the interstellar medium; Hopkins & Elvis 2010).

Regarding the 2008 *Suzaku* spectrum of NGC 4051, the presence of two statistically significant absorption lines at ∼6.8 and ∼7.1 keV is detected. If these lines are the signature of He-like and H-like Fe respectively then their blueshift suggests that they are the ionised signature of the high-velocity outflowing wind previously detected by Pounds et al. (2004a) and Terashima et al. (2009). The absorption lines can be modelled with a single absorber with a turbulence velocity of $v_{\rm turb} = 3\,000\,{\rm km\,s^{-1}}$ and best-fitting parameters of $\log\xi \sim 4.1$ and $N_{\rm H} \sim 8.4 \times 10^{22}\,{\rm cm^{-2}}$. The zone has an outflow velocity of $v_{\rm out} \sim 5\,800\,{\rm km\,s^{-1}}$ (∼-0.02c) and is perhaps the highly-ionised signature of the high-velocity outflowing zones of gas detected by Collinge et al. (2001) and Steenbrugge et al. (2009). The location of the material is constrained to be on the order of a few (0.5–5) light-days from the black hole, well within the putative inner radius of the dusty torus for this object and may originate in an accretion-disc wind perhaps depositing up to 10^{56-57} erg throughout the lifetime of the AGN. It should be noted, however, that no requirement is found in these data for the higher-velocity outflow ($v_{\rm out} \sim 0.13c$) at Fe K reported by Pounds & Vaughan (2012) from the results of their recent *XMM-Newton* observation.

5 X-Ray Spectral Variability of NGC 4051

This chapter is based on the following published work (plus additional research):

'Contemporaneous Chandra HETG and Suzaku X-ray Observations of NGC 4051'; Lobban, A.P., Reeves, J.N., Miller, L., Turner, T.J., Braito, V., Kraemer, S.B., Crenshaw, D.M., 2011, MNRAS, 414, 1965-1986;

'Spectral Variability and Reverberation Time Delays in the Suzaku X-ray Spectrum of NGC 4051'; Miller, L., Turner, T.J., Reeves, J.N., Lobban, A.P., Kraemer, S.B., Crenshaw, D.M., 2010, MNRAS, 403, 196-210;

'Significant X-ray Line Emission in the 5–6 keV Band of NGC 4051'; Turner, T.J., Miller, L., Reeves, J.N., Lobban, A.P., Braito, V., Kraemer, S.B., Crenshaw, D.M., 2010, 712, 209-217.

All work was conducted by the author except for the results discussed in Sections 5.2.1, 5.3.1 and 5.3.3.3 where collaborators were responsible for part of the research. See the text for details.

5.1 Introduction

NGC 4051 is a highly variable X-ray source showing significant variations on both short (<day) and long (years) timescales. The rapid, short-term variability (down to hundreds of seconds) has been studied for many years since observations were made with such X-ray satellites as *EXOSAT* (*European X-Ray Observatory Satellite*) and *Ginga* (e.g. Lawrence et al. 1985; Matsuoka et al. 1990) and NGC 4051 has been the subject of various observations made with *XMM-Newton*, *Chandra* and *Suzaku* plus an extensive long-term monitoring campaign with *RXTE* (Uttley et al. 1999; Markowitz & Edelson 2004).

In terms of the X-ray spectral variability, the general observed trend appears to be that the photon index of the continuum emission is somewhat correlated with the source flux; that is to say that the spectrum becomes harder when the source flux drops. When the flux is high, the spectrum resembles that of a typical type-1 Seyfert galaxy and can be explained with an intrinsic steep power-law component ($\Gamma \gtrsim 2$), Fe K emission from near-neutral material, a standard reflection component from cold matter, a soft excess and ionised warm absorbers (e.g. Pounds et al. 2004a). However, when the source becomes fainter, the spectrum at energies $\gtrsim 2$ keV significantly flattens, becoming more convex in shape. The origin of this flat spectral shape has been the focus of much debate in the literature (e.g. Uttley et al. 2004; Ponti et al. 2006).

One popular interpretation for the observed spectral variations is that the slope of the intrinsic power-law component changes, perhaps pivoting about some relatively high energy (e.g. $\gtrsim 60$ keV). Such a model was proposed by Guainazzi et al. (1998) who analysed *ASCA* data and found that if the strength of the reflection component is constant (or inversely proportional to the strength of the power-law component), the apparent power-law slope changes by $\Delta\Gamma = 0.4$ to account for the spectral variations. Lamer et al. (2003) came to a similar conclusion when they found that the photon index also varies even when the contribution from the reflection component (which is assumed to be constant) is subtracted from the spectrum. Flux-flux analysis was performed on *RXTE* data by Taylor, Uttley & McHardy (2003) and they concluded that, by comparing the 2–5 keV and 7–15 keV energy bands, the spectral variability could best be described by a changing power-law slope superimposed on a constant hard component. Finally, a similar conclusion was also arrived at by Uttley et al. (2004) who also performed flux-flux analysis on *XMM-Newton* data (this time using the 0.1–0.5 keV and 2–10 keV energy bands) both when the source flux was high and low and suggested that the pivoting power law was superimposed on constant thermal and reflection components. As described in Section 1.4, spectral pivoting could conceivably occur via Compton-cooling of the corona by seed photons from the disc (Zdziarski et al. 2002).

A second interpretation to account for the spectral variability consists of a proposed two-component model whereby the variations are caused by significant changes in a variable soft component which is superimposed on a constant hard component. Then, when the

source flux drops, the soft component effectively disappears from view leaving behind a reflection-dominated hard component of flat spectral index. However, the cause of these variations is unknown and there are currently two popular models in the literature which attempt to explain it (e.g. Miniutti et al. 2007; Miller et al. 2007). Firstly, a reflection-dominated model was proposed by Ponti et al. (2006) in the case of NGC 4051 where the spectrum was modelled with a variable power-law component with fixed photon index ($\Gamma = 2.2$) superimposed on a combination of blurred, ionised reflection (see Laor 1991) and neutral reflection from distant matter as the constant component. However, the two-component model has also been interpreted as arising from an absorption-dominated spectrum. Using the same 2001 and 2002 *XMM-Newton* spectra as Ponti et al. (2006), this approach was taken by Pounds et al. (2004a) who successfully modelled the spectrum with a two-component model combined with an absorbed component. They assumed that the photon index of the power law and the strength of the reflection component were invariant between observations and interpreted the very hard spectrum in 2002 as arising from a significant neutral reflection component from distant matter and a substantial increase in the column density of the lowly-ionised absorber. Terashima et al. (2009) were also able to model the 2005 *Suzaku* observation in a similar way. They found that they were unable to model the spectrum purely with reflection since the observed strength of the Fe K emission (EW ~ 140 eV) is far too weak for the strong reflection component required by the data ($R \sim 7$). Therefore, they accounted for the spectral variations at low energies by allowing for changes in the covering fraction of a partially-covering absorber.

It should also be noted that the X-ray flux of NGC 4051 occasionally drops dramatically, as discovered when the source was observed by *RXTE* and *BeppoSAX* in 1998 (Guainazzi et al. 1998; Uttley et al. 1999). From 2–10 keV, the source flux was found to be as low as $F_{2-10} = 1.3 \times 10^{-12}\,\mathrm{erg\,cm^{-2}\,s^{-1}}$ and was accompanied by a very flat spectrum ($\Gamma \sim 0.8$). The shape of the spectrum appeared to be reflection-dominated with a very strong narrow Fe Kα line (EW ~ 600 eV). Modelling of the spectrum suggested that the central engine had effectively switched off at this time and so the observed X-ray emission was in fact reflection from very distant matter such as the dusty, molecular torus delayed from an earlier epoch when the source was brighter. However, an alternative explanation could be that the source

was very strongly absorbed.

Here, the X-ray spectral variability of the 2005 and 2008 *Suzaku* observations is investigated. The results of the PCA of Miller et al. (2010b) are firstly summarised before the broad-band spectra are modelled in a physical way with an attempt made to account for the long-term spectral changes. Such studies are important since spectral variability may provide a powerful diagnostic tool for extracting valuable information regarding various emission components.

5.2 Spectral Analysis

5.2.1 Summary of Principal Components and Timing Analyses

Due to signal-to-noise limitations, many X-ray spectral analyses of AGN have tended to consist of fitting simple composite models to mean, time-averaged spectra and numerous timing analysis studies have investigated the variability on short timescales but over broad energy ranges. However, information may often be lost when only the mean spectra are considered. For this reason, it has been crucial to obtain long-exposure observations of bright AGN so that the extra information contained in the variability of the source may be accessed. Section 5.2.1 summarises the work of Miller et al. (2010b) which analysed the same *Suzaku* datasets from 2005 and 2008 described in this thesis. The author of the thesis assisted in scientific interpretation and discussion of the results, relating them directly to the spectral modelling described in Chapter 4 and subsequent sections in Chapter 5.

5.2.1.1 Principal Components Analysis

In the case of NGC 4051, Miller et al. (2010b) investigated the nature of the spectral variability by performing PCA on the data. PCA is a method whereby the spectral variations are decomposed into orthogonal components revealing the primary modes of variation and is particularly effective when dealing with variations which are additive in nature. It assumes that spectrally-invariant components of emission exist whose amplitude may vary with time. Linearly combining these components then produces the observed spectra. Miller et al. (2010b)

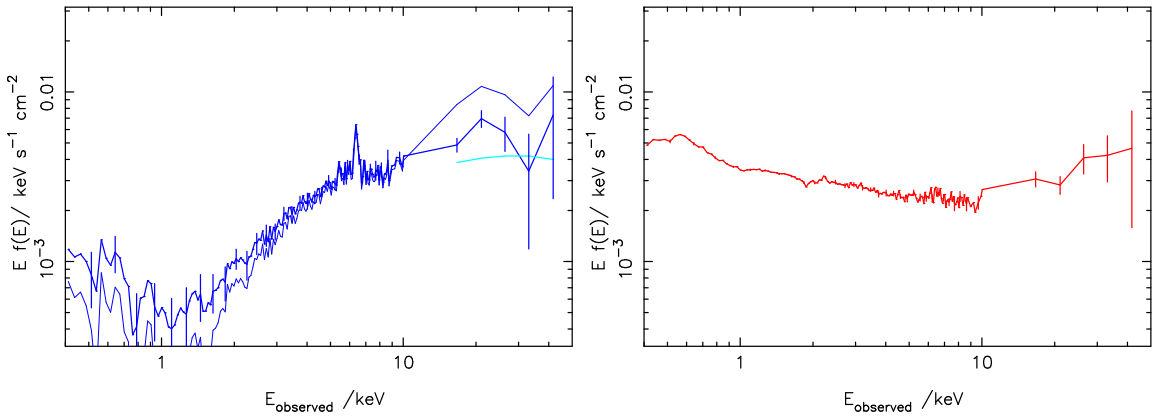

Figure 5.1: The PCA of NGC 4051 observed with *Suzaku* in 2005 and 2008. Left panel: the quasi-constant offset component. This is the shape of the invariant component of emission which is steady in time. It essentially describes the source during its period of lowest observed flux (i.e. what the spectrum looks like as the amplitude of the variable components tend to zero). The two curves show the possible range of this component. Right panel: eigenvector one. This is the shape of the principal mode of variation which varies in amplitude over time super-imposed on the hard, offset component (left panel). It is power-law-like in shape and accounts for 81% of the variance in the 0.4–50 keV energy band. For clarity, errors are only shown at every fifth point. Figures taken from Miller et al. (2010b).

used the method described in Miller et al. (2007) to decompose the spectra. The results of previous studies with other AGN (e.g. Mrk 766, Miller et al. 2007; MCG–6-30-15, Miller et al. 2008) have indicated that only a small number of variable components are usually required to explain the observed variations. What is generally produced is a component called "eigenvector one", which describes the primary source variations, and an "offset" component which usually remains quasi-constant over time. Then, by adding or subtracting arbitrary amounts of eigenvector one to or from the constant offset component, the resultant observed spectrum may be produced.

The primary components of the PCA from 0.4–50 keV (using both XIS and PIN data) are shown in Figure 5.1 for the combined 2005 and 2008 *Suzaku* datasets using a sampling time of 20 ks, where each time-resolved spectrum was identically binned to the HWHM of the detector resolution. This allows the data to be thought of as an $m \times n$ matrix where m is the number of photon-energy bins and n is the number of measurements. By considering the

flux in each bin, each spectrum is then described by one point in m-dimensional space with the full dataset described by n points. For a completely invariant source, all the points would lie at the same location. However, if a single component of varying emission were to exist, the points would be distributed in a straight line passing through the origin. For further varying components, the points would be confined to a p-dimensional surface where p is the number of such components. PCA allows the number of dimensions required to explain the variability to be evaluated. It also enables the presence of a component of invariant emission to be tested for since this would allow the p-dimensional surface to be embedded in $p - 1$ dimensions with a shifted origin. Mathematically, PCA defines a new coordinate system such that one axis in the rotated m-dimensional space lies in the same direction for which the variance of the distribution is largest. This direction is the first principal component (i.e. eigenvector one). The second principal component would then mark the direction with the second largest variance. In essence, the principal components are the eigenvectors of the data-covariance matrix and each component's variance is its eigenvalue.

In the case of NGC 4051, Miller et al. (2010b) found that eigenvector one (Figure 5.1; right panel) accounts for 81% of the variations in the 0.4–50 keV energy band and that the generic features of the PCA appear to take on the same form as other type-1 AGN such as Mrk 766 (Miller et al. 2007) and MCG–6-30-15 (Miller et al. 2008). A hard, constant offset component is also observed (Figure 5.1; left panel) which dominates the PIN band above 15 keV and, interestingly, is also seen to carry various atomic features such as the Fe K edge and the Fe Kα emission line at $\sim$6.4 keV. Eigenvector one, however, appears to take on the form of a power law but with (multiplicative) warm absorber features apparent in the soft band. Eigenvector one also shows evidence for a variable component at energies >20 keV plus a weak but slightly broadened component of Fe Kα emission (EW = 66^{+43}_{-37} eV), consistent with that found with the *Chandra* HETG in Section 4.4.2.

Miller et al. (2010b) interpret eigenvector one to imply that the primary continuum takes the form of a power law of invariant photon index but which varies in amplitude. Such variations in amplitude could arise from modification by absorption due to Compton-thick clouds of variable covering-fraction or from something more intrinsic to the source such as coronal flickering / variations. The variable component of hard excess in eigenvector one

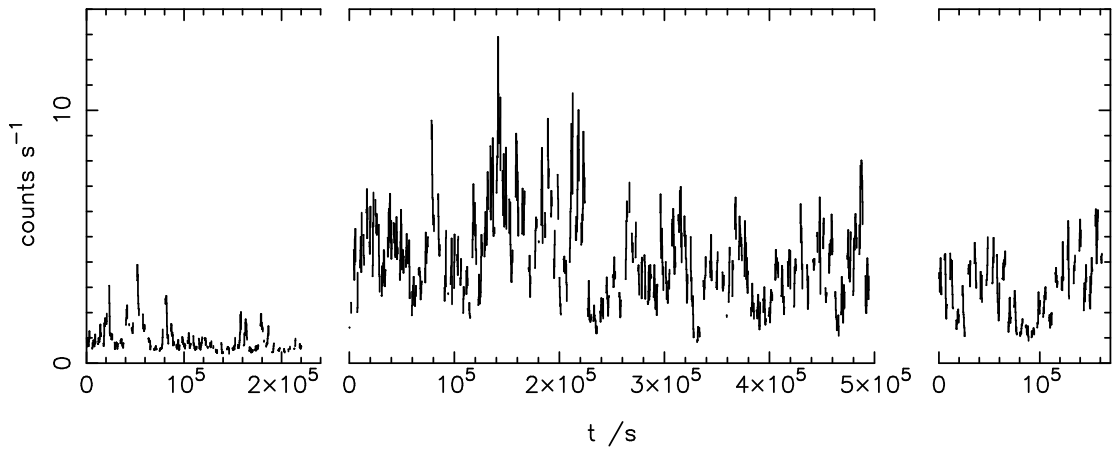

Figure 5.2: The *Suzaku* XIS lightcurve of NGC 4051 over the 0.3–10 keV energy range sampled at 256 s. From left to right, the 2005 and the two 2008 observations are shown. Since XIS 0, 2 and 3 were all operational in 2005, this lightcurve has been scaled to the flux expected from just XIS 0 and 3 which were the only FI detectors operational in 2008. Figure taken from Miller et al. (2010b).

could then arise from the flux transmitted through a partial-coverer of substantial column density (such as in the case of PDS 456; Reeves et al. 2009 and 1H 0419-577; Turner et al. 2009) or from reflection off optically-thick material. The authors then interpret the quasi-constant offset component to be the spectrum of the source when observed at its lowest flux level (i.e. when the primary power-law continuum has disappeared from view). This component could be explained as being either purely reflection-dominated or as the residual signal arising from variations of a partially-covering absorber. Finally, Miller et al. (2010b) note that the narrow component of the near-neutral Fe Kα emission line at 6.4 keV only appears in the constant offset component and is consistent with having an invariant flux between 2005 and 2008 despite large changes in the observed continuum flux of the source. This implies that the material responsible for producing the emission line must have received an invariant ionising continuum in 2005 and 2008 despite a change in flux from 7–10 keV of a factor of $\sim$2.5 between the two observations.

5.2.1.2 Power Spectra and Reverberation Time Delays

Miller et al. (2010b) also considered NGC 4051 in the timing domain. The complete *Suzaku*

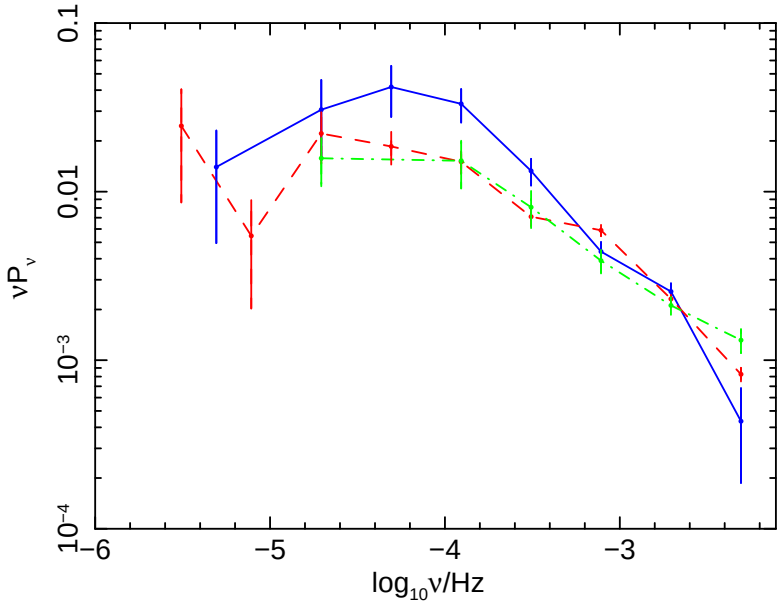

Figure 5.3: Comparison of the PSDs of NGC 4051 taken from the three *Suzaku* observations. The 2005 data are shown in blue (solid curve) and the data from the two 2008 observations are shown in red (dashed) and green (dot-dashed) respectively. Points with error bars are plotted at the mid-point in $\log \nu$ of each bandpower. Figure taken from Miller et al. (2010b).

lightcurve of NGC 4051 is shown in Figure 5.2. The gaps in the time series arise from the filtering of events and the short orbital timescale of the satellite. However, even by eye, the variability of the source is clear and appears to take on different characteristics between the 2005 and 2008 observations. Miller et al. (2010b) attempted to quantify this by comparing power spectral density (PSD) from the three observations to test for any non-stationarity within the variations. The PSDs over the 0.3–10 keV energy range using each XIS dataset are shown in Figure 5.3. Note that due to the steep source spectrum and the higher effective area at lower energies, the spectra are dominated by the soft band. Also, since the 2005 and 2008 observations had significantly different mean fluxes, the mean levels used to normalise the fluctuations are different whereas if the two spectra were scaled to the same mean, their amplitudes would differ. This could occur if some of the intrinsic fluctuations have been modulated by a secondary effect (such as absorption) or it could imply that the fluctuations

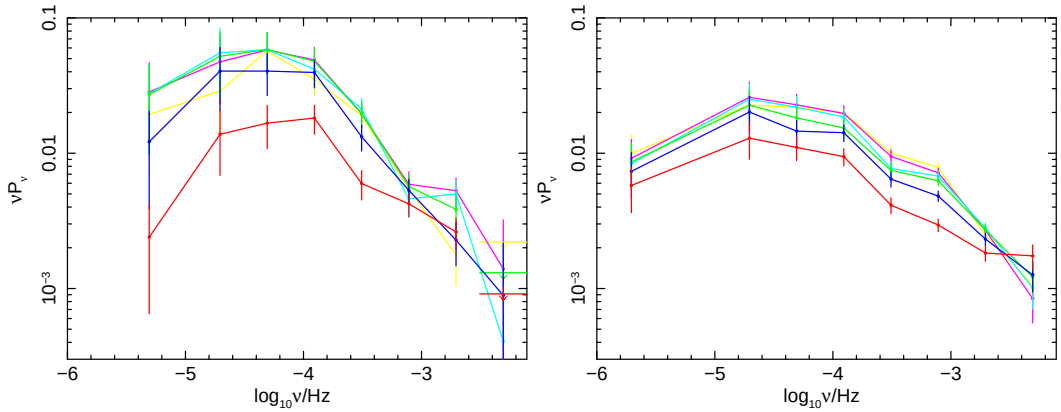

Figure 5.4: PSDs of NGC 4051 plotted as νP_ν from the 2005 (left) and 2008 (right) *Suzaku* observations. The six energy bands correspond to 0.3–0.94 (yellow), 0.94–1.2 (magenta), 1.2–1.5 (cyan), 1.5–2.1 (green), 2.1–3.8 (blue) and 3.8–10 keV (red). Figures taken from Miller et al. (2010b).

are fractional in nature, as previously suggested by Uttley & McHardy (2001) and Uttley, McHardy & Vaughan (2005). Nevertheless, the PSD appears to be significantly different in 2005 than in 2008 with more power in the mid-frequency range and a steeper spectrum to higher frequencies. Miller et al. (2010b) quantified this by adopting a minimum-χ^2-fitting method and found best-fitting slopes of $\alpha = 2.00 \pm 0.08$, $\alpha = 1.78 \pm 0.03$ and $\alpha = 1.67 \pm 0.08$ for the three observations chronologically, where $P_\nu \propto \nu^{-\alpha}$. Indeed, the 2005 PSD was seen to differ by 2.7σ and 3σ from the PSDs from the first and second 2008 observations respectively.

Miller et al. (2010b) also searched for any dependence of the PSD on photon energy. They divided the XIS bandpass into six energy bands (0.3–0.94, 0.94–1.2, 1.2–1.5, 1.5–2.1, 2.1–3.8 and 3.8–10 keV) such that each band had the same count rate. The resultant PSDs are shown in Figure 5.4. It appears that the harder bands show less overall variability, consistent with the findings of McHardy et al. (2004) with *XMM-Newton*, and the hardest energy band (3.8–10 keV) has a significantly flatter PSD than the softer bands, to the point that it has the highest power in 2008 of any energy band at the highest frequency measured despite having much less power than other bands at lower frequencies.

Finally Miller et al. (2010b) searched for any evidence of time lags between energy

bands. These are assessed by computing the cross-spectral properties between two evenly sampled time series (e.g. soft and hard energy bands), where the cross-spectrum is the complex-valued product of the Fourier transforms of the two series. The phase of the cross-spectrum is then converted into a time lag which records the average delay between two time series. In many AGN, time lags between different spectral bands have now been observed. The lags occur in the sense that hard-band photons lag behind soft-band photons and these are usually found in the range of tens to thousands of seconds (Papadakis, Nandra & Kazanas 2001; Vaughan, Fabian & Nandra 2003; McHardy et al. 2004; Markowitz et al. 2007). Interestingly, the lags are dependent on the frequency of the source variation (i.e. a relationship will be observed if the time lags between two time series are plotted as a function of the frequency of the source variation). For example, if the variations of a source are decomposed into Fourier modes, the lag between the hard band and the soft band will increase both with the period of those modes and with the separation of the energy bands considered. The frequency-dependence of the lags has been explained with a model whereby perturbations in the accretion flow propagate inwards with the harder X-ray emission arising from smaller radii (Arévalo & Uttley 2006). However, more complex behaviour has been observed in the sense that the relationship with Fourier period may not always be linear and so a new hypothesis has been proposed whereby the fluctuations arise in multiple components (McHardy et al. 2007).

Although the shape of the PSD was observed to vary between 2005 and 2008, the derived time lags show no significant evidence to have varied between epochs (within the statistical uncertainties) and so the 2005 and 2008 data were combined to maximise signal-to-noise. Miller et al. (2010b) found significant time lags between energy bands with the hard bands lagging behind the soft bands with the lag increasing with the difference in energy between the two bands (possibly as evidence of reprocessing by circumnuclear material). With respect to the softest band (0.3–0.94 keV), time lags of up to 970 ± 225 s were detected, which increase with the energy of the band and the period of the fluctuation, again consistent with McHardy et al. (2004). Miller et al. (2010b) did also investigate the time lags between the *Suzaku* XIS and PIN bands but found that the PIN data were too noisy for any accurate measurements to be taken, although they were consistent with the lags found for the hardest XIS band but

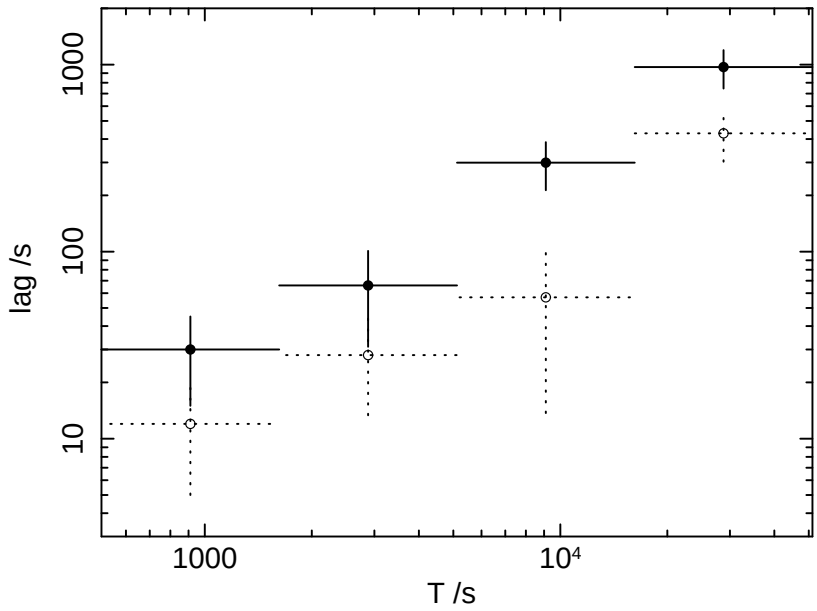

Figure 5.5: Time lags between the 0.3–0.94 keV energy band and the 6–10 keV (solid points and error bars) and 2.1–3.8 keV (open points and dotted error bars) energy bands, as a function of time period T for the combined 2005–2008 NGC 4051 dataset. The lags are derived by computing the cross-spectral properties between two time series (i.e. different energy bands) which then allows the magnitude and significance of characteristic lag times between the two series to be calculated. Vertical error bars show the 68% confidence regions. Horizontal bars show the range of time periods included in each bandpower. Figure taken from Miller et al. (2010b).

with large uncertainties. The measured time lags between the 0.3–0.94 keV and the 2.1–3.8 and 6–10 keV bands are shown in Figure 5.5.

5.2.2 Flux-Flux Analysis

The nature of the X-ray spectral variability can also, in principle, be investigated in a model-independent way by comparing the total fluxes measured in soft and hard energy bands. Following the method detailed by Taylor, Uttley & McHardy (2003), the fluxes in these bands can be expressed as:

$$F_{\rm s} = f_{\rm s} + C_{\rm s} \tag{5.1}$$

and

$$F_{\rm h} = f_{\rm h} + C_{\rm h}, \tag{5.2}$$

where $F_{\rm s}$ and $F_{\rm h}$ are the total fluxes in the soft and hard bands, $f_{\rm s}$ and $f_{\rm h}$ are the fluxes of the variable components in the soft and hard bands and $C_{\rm s}$ and $C_{\rm h}$ are the fluxes of the constant components in the soft and hard bands respectively. The relationship between the hard and soft variable fluxes can simply be parameterised by $f_{\rm h} = k f_{\rm s}^{\alpha}$, where k and α are constants. If $\alpha < 1$, the spectral variability can be described by a power law which pivots about some large energy, $E_{\rm p}$ (while the flux density at $E_{\rm p}$ remains constant). As $E_{\rm p}$ increases, α will asymptotically approach 1. If $\alpha = 1$, this describes a situation whereby the shape of the varying component remains constant with a hardness ratio of the varying component, k. Finally, if $\alpha > 1$, this corresponds to a pivoting power law whereby $E_{\rm p}$ lies at energies below the soft band. Combining this with equations 5.1 and 5.2 yields:

$$F_{\rm h} = k(F_{\rm s} - C_{\rm s})^{\alpha} + C_{\rm h}. \tag{5.3}$$

If one then plots the directly measurable fluxes, $F_{\rm s}$ versus $F_{\rm h}$, the resultant shape of the graph can reveal important information about the nature of the spectral variability. Essentially, if the varying component has a constant spectral shape, the relationship will be linear with gradient, k, and intercept, $C = C_{\rm h} - kC_{\rm s}$. Alternatively, if the spectral shape of the variable component changes with flux, the relationship will be non-linear. Indeed, if the variability is due to a simple pivoting power law, with no constant components, the relationship should be well-fitted with a power law of intercept $C = 0$. It should be noted that other non-linear shapes would suggest either more complex variability or a scenario whereby the varying spectral component is not a power law.

To test these scenarios, flux-flux plots were created enabling several energy bands to be compared. Since the cause of the spectral variability in NGC 4051 is expected to be the same in 2005 as in 2008, data were combined from all three *Suzaku* observations of NGC 4051 to maximise signal-to-noise. Data were combined from all four XIS units for the 2005 *Suzaku* data and all three available units for the 2008 data in the 0.4–2, 2–4 and 4–10 keV

energy bands and then normalised (per XIS). The HXD data from each observation was considered over the 15–50 keV energy range. Orbital bin-sizes were used for all XIS data (5 760 s) but this was increased to a two-orbital bin size for the HXD data (11 520 ks) to maximise signal-to-noise. The plots along with their best-fitting model superimposed are shown in Figure 5.6.

The flux-flux plots were initially fitted with a linear function to test for the case where the varying component has a constant spectral shape. It was found that a constant offset was always required in the hard band (e.g. $\sim$0.045 cts s^{-1} in the 4–10 keV band when compared to the 2–4 keV band; see Table 5.1) suggesting that a constant hard component may be present in the spectrum. If the linear model is correct, then this would be consistent with a soft component varying in normalisation (but not spectral shape) superimposed on the constant hard component, consistent with Ponti et al. (2006) and Miller et al. (2010b).

Power-law models were also fitted to the data, both with and without a constant offset. Only when comparing the 0.4–2 and 2–4 keV energy bands does the power-law model with no offset statistically produce a better fit than the linear + offset model, with an improvement in the variance of $\sim$400 (see Table 5.1 for a summary of the fits). In all other cases, the linear + offset model is statistically superior suggesting that the two-component model is a better description of the data than a pivoting power law. However, when allowing the power-law model to have a non-zero offset, the fit improves each time, regardless of the energy bands considered. It appears that when comparing softer energy bands (i.e. $<$10 keV), the power-law + offset model is statistically the best of the three models. However, when comparing softer bands with much harder bands (i.e. bands below 10 keV with the 15–50 keV HXD band), it becomes very difficult to distinguish between linear + offset and power-law + offset models (perhaps suggesting that the power law is not required here; see Table 5.1 for all values). This suggests that the inferred cause of spectral variability may depend upon the energy bands chosen when performing a flux-flux analysis. For example, the hard X-rays may be dominated by a constant offset whereas the variability of the soft X-rays may be dominated by another process such as spectral pivoting or variable absorption.

Taylor, Uttley & McHardy (2003) and Uttley et al. (2004) applied power-law models to their flux-flux plots for NGC 4051 and inferred that spectral pivoting is the primary cause of

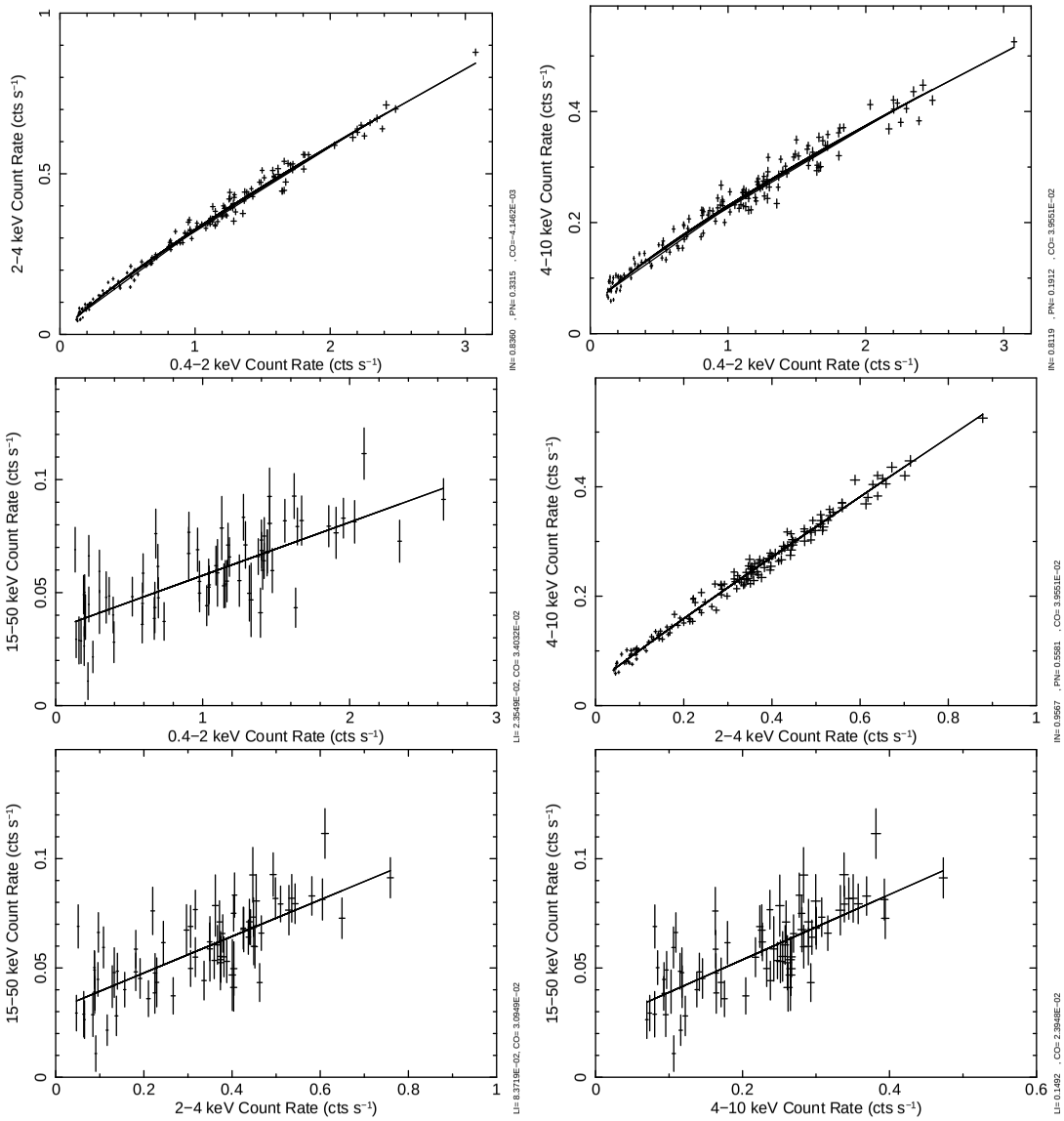

Figure 5.6: Flux-Flux Plots comparing the count rates of NGC 4051 in the 0.4–2, 2–4, 4–10 and 15–50 keV energy ranges. The best-fitting models are superimposed. See Section 5.2.2 and Table 5.1 for details.

Energy Bands (keV)	Model Linear		
	k_{lin}	C	Var/d.o.f.
0.4-2 vs 2-4	0.2898 ± 0.0008	0.0266 ± 0.0005	1676/149
0.4-2 vs 4-10	0.1617 ± 0.0007	0.0619 ± 0.0006	1641/149
2-4 vs 4-10	0.5660 ± 0.0025	0.0446 ± 0.0007	685.1/149
0.4-2 vs 15-50	0.0235 ± 0.0018	0.0340 ± 0.0020	136.1/72
2-4 vs 15-50	0.0837 ± 0.0063	0.0309 ± 0.0022	134.3/73
4-10 vs 15-50	0.1492 ± 0.0111	0.0239 ± 0.0027	131.2/73
Energy Bands (keV)	Model Power Law		
	k_{pow}	α	Var/d.o.f.
0.4-2 vs 2-4	0.3263 ± 0.0006	0.8525 ± 0.0027	1237/149
0.4-2 vs 4-10	0.2374 ± 0.0005	0.6225 ± 0.0030	1663/149
2-4 vs 4-10	0.5397 ± 0.0024	0.7334 ± 0.0036	967.1/149
0.4-2 vs 15-50	0.0607 ± 0.0011	0.3352 ± 0.0285	144.7/72
2-4 vs 15-50	0.0943 ± 0.0038	0.3950 ± 0.0335	144.5/73
4-10 vs 15-50	0.1340 ± 0.0087	0.5508 ± 0.0448	136.5/73

Energy Bands (keV)	Model Power Law + Offset			
	k_{pow}	α	C	Var/d.o.f.
0.4-2 vs 2-4	0.3315 ± 0.0024	0.8360 ± 0.0077	-0.0041 ± 0.0019	1232/148
0.4-2 vs 4-10	0.1912 ± 0.0024	0.8119 ± 0.0122	0.0395 ± 0.0019	1405/148
2-4 vs 4-10	0.5581 ± 0.0034	0.9567 ± 0.0137	0.0395 ± 0.0018	675.2/148
0.4-2 vs 15-50	0.0247 ± 0.0056	0.9492 ± 0.2234	0.0331 ± 0.0047	136.0/71
2-4 vs 15-50	0.0869 ± 0.0102	1.1910 ± 0.2610	0.0341 ± 0.0042	133.7/72
4-10 vs 15-50	0.1934 ± 0.0507	1.3830 ± 0.3327	0.0317 ± 0.0054	129.7/72

Table 5.1: The best-fitting parameters of the linear + offset, power law and power-law + offset models applied to the NGC 4051 2005 and 2008 summed *Suzaku* datasets.

the spectral variability. One particular issue with this interpretation is that NGC 4051 shows very large variability amplitudes on all timescales making it difficult to achieve purely by changes in the seed photon flux. Taylor, Uttley & McHardy (2003) reconcile this by stating that such variability could conceivably be observed in a scenario whereby the seed photon luminosity is dominated by internal viscous heating in the disc but the corona dissipates most of the accretion power. In this case, relatively small changes in the dissipation rate in the

corona could, if fed back to the disc, result in large changes in the seed photon luminosity while leaving the luminosity of the corona relatively unchanged. This could then produce the conditions required for spectral pivoting. However, by combining all *Suzaku* data from 2005 and 2008, the flux-flux analysis outlined here suggests that, while a spectral variability model consisting of a two-component model plus some variations in the spectral shape in the soft band cannot be ruled out, it generally seems to be that neither linear + offset or power-law + offset models offer a complete description of the data. This extra complexity may arise due to the numerous, possibly variable, absorption components present in the X-ray spectra (e.g. Section 4.4.1). Indeed, while a linear + offset model dominates the hardest band (15–50 keV; consistent with a constant offset component as per the PCA described in Section 5.2.1.1), the variations in the softest bands appear to be mostly non-linear, consistent with changes in the spectral shape.

5.2.3 Long-Term Broad-Band Spectral Variability

5.2.3.1 Absorbed-Reflection Model

In this section, a return is made to the detailed spectral analysis with the aim of developing a model to account for the spectral variability between all three *Suzaku* datasets. Initially, the long 2008 observation is considered. Since the neutral reflection (PEXRAV) and blackbody components featuring in the model described in Section 4.5 served as simple parameterisations of the Compton-scattered reflection hump off neutral material at energies >10 keV and the soft excess at energies <2 keV respectively, an attempt was made to model these features using a more physical approach.

Firstly, the PEXRAV component, the blackbody and the Gaussians modelling emission from near-neutral Fe Kα and highly-ionised Fe were removed. These components were then replaced with two absorbed-reflection models (consistent with the full broad-band model described in Turner et al. 2010) using the REFLIONX code of Ross & Fabian (2005); one low ξ (near-neutral) component to model the near-neutral Fe Kα emission line and the hard excess and one highly-ionised component to account for the spectral curvature in the soft band (i.e. the soft excess) plus the highly-ionised Fe K-shell emission lines.

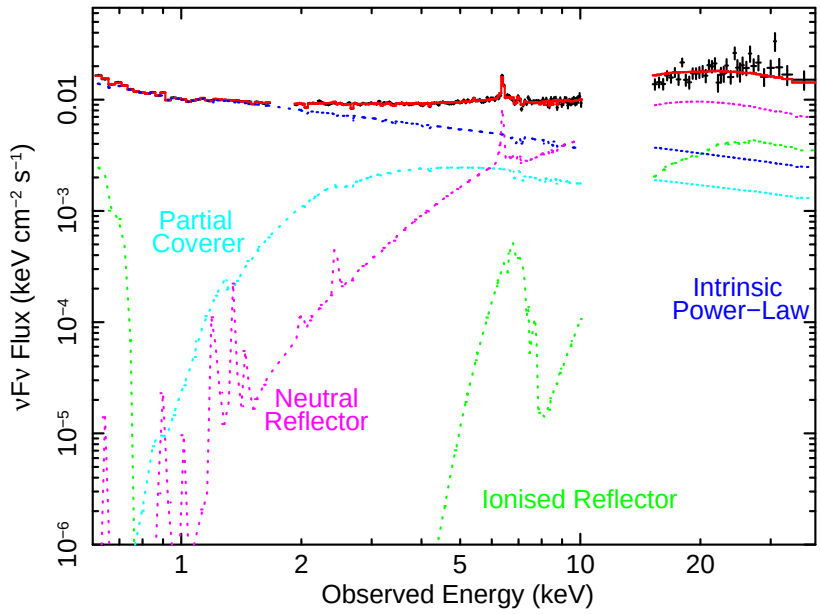

Figure 5.7: The relative model contributions to the best-fitting model for NGC 4051 described in Section 5.2.3.1 in the observed frame. The (obs. 2) data are shown in black with the sum of all model components superimposed in red. The absorbed- and unabsorbed-power-law components are shown in cyan and navy blue respectively. The absorbed neutral- and ionised-reflectors are shown in magenta and green respectively.

The REFLIONX code is described in Section 2.5.1 and models the emergent spectrum from a photo-ionised optically-thick slab of gas when irradiated by a power-law spectrum and consists of both the reflected continuum and line emission for the astrophysically abundant elements. It assumes a high-energy exponential cut-off of $E_{\rm cut} = 300\,{\rm keV}$ and uses the solar abundances of Anders & Ebihara (1982). All absorption was again modelled using the XSTAR 2.1ln11 code of Kallman & Bautista (2001) with the soft X-ray absorption fixed at the best-fitting values from the HETG data (Table 4.1) and the zone of highly-ionised absorption detected with *Suzaku* consistent with the values obtained in Section 4.5.2. Any soft X-ray emission lines unable to be accounted for by the ionised reflector were modelled with Gaussians as required. The relative contributions of the model components are shown in Figure 5.7 and the model can be expressed as:

$$
\begin{aligned}
F(E) \;=\; & \textsc{wabs} \times (\textsc{xstar}_{\rm HETG} \times \textsc{xstar}_{\rm Fe\,K} \times [{\rm PL}_{\rm int.} \\
& + ({\rm PL} \times \textsc{xstar}_{\rm pc}) + (\textsc{reflionx}_{{\rm low}\,\xi} \times \textsc{xstar}) \\
& + (\textsc{reflionx}_{{\rm high}\,\xi} \times \textsc{xstar})] + {\rm GA}^{\rm soft}_{\rm ems.}), \qquad (5.4)
\end{aligned}
$$

where WABS is the absorption due to Galactic hydrogen in our line-of-sight, $\textsc{xstar}_{\rm HETG}$ corresponds to the four fully-covering warm absorber zones (distant and outflowing) in the soft X-ray band fixed at the best-fitting values from the HETG data (see Table 4.2), $\textsc{xstar}_{\rm Fe\,K}$ is the zone of highly-ionised Fe-K absorption forming the high-velocity component of the outflow (see Section 4.5.2), $\rm PL_{int.}$ is the intrinsic ('unabsorbed') power-law continuum, PL × $\textsc{xstar}_{\rm pc}$ corresponds to the partial-coverer (possibly a clumpy absorber; see Section 5.2.3.2), the REFLIONX components are the near-neutral (distant; e.g. the torus) and highly-ionised (closer in; e.g. a disc wind or the outer accretion disc) absorbed reflectors (each of which is absorbed by a layer of gas within XSTAR, without which the soft excess cannot be modelled; see below) and $\rm GA^{soft}_{ems.}$ corresponds to the soft photoionised emission lines which the reflector is unable to account for (also see Section 4.3.3); primarily the forbidden transitions from O VII, Ne IX and Si XIII, which presumably originate from more distant, pc-scale photo-ionised gas. These lines were fixed at the best-fitting values from the HETG data (listed in Table 4.1). This forms a highly complex model since a complex ionised scattering-spectrum is being modelled with components that cannot necessarily account for all of the physical effects that one would expect to be present. Therefore, its apparent complexity may simply be an artefact of the limitations of the current physical models available, e.g. compared to physically realistic disc wind models (see Sim et al. 2008; Sim et al. 2010).

The best-fitting values of the reflection components and their associated zones of absorption are shown in Table 5.2. The redshift values of the two reflectors were fixed to that of the host galaxy (i.e. $z = 0.002336$), the iron abundances were tied together and the photon indices were tied to that of the incident power-law continuum (i.e. the intrinsic '$\rm PL_{int.}$' component in equation 5.4). No additional velocity broadening was applied to the reflected spectrum. It was found that the photon index steepens to $\Gamma = 2.50 \pm 0.02$. The ionisation parameter of the low ξ reflector pegs at a value of $\xi = 1\,{\rm erg\,cm\,s^{-1}}$ (the lowest value allowed

Component	Parameter	Value
Power law^a	Γ	2.50 ± 0.02^{l_1}
	Norm. ($\mathrm{ph\,cm^{-2}\,s^{-1}}$)	$(1.24 \pm 0.01) \times 10^{-2}$
Power law$^b_{\mathrm{abs.}}$	Γ	l_1
	Norm. ($\mathrm{ph\,cm^{-2}\,s^{-1}}$)	$(6.48^{+1.16}_{-1.10}) \times 10^{-3}$
	N_{H} ($\mathrm{cm^{-2}}$)	$(1.15^{+0.30}_{-0.14}) \times 10^{23}$
	$\log \xi$	< 0.50
REFLIONX$^c_{\mathrm{abs.}}$ (low ξ)	Γ	l_1
	ξ ($\mathrm{erg\,cm\,s^{-1}}$)	1_p
	A_{Fe}	0.23 ± 0.04^{l_2}
	$\mathrm{Flux}_{0.5-100}$ ($\mathrm{erg\,cm^{-2}\,s^{-1}}$)	$(2.12^{+0.11}_{-0.24}) \times 10^{-11}$
Absorber^d	N_{H} ($\mathrm{cm^{-2}}$)	$(5.64^{+0.84}_{-0.65}) \times 10^{22}$
	$\log \xi$	< 1.12
REFLIONX$^e_{\mathrm{abs.}}$ (high ξ)	Γ	l_1
	$\log \xi$	$3.8^{+0.2}_{-0.1}$
	A_{Fe}	l_2
	$\mathrm{Flux}_{0.5-100}$ ($\mathrm{erg\,cm^{-2}\,s^{-1}}$)	$(5.27^{+0.70}_{-0.70}) \times 10^{-11}$
Absorber^d	N_{H} ($\mathrm{cm^{-2}}$)	$(5.00^{+0.00\,p}_{-0.44}) \times 10^{24}$
	$\log \xi$	2.55 ± 0.03
Statistics	$\chi^2/d.o.f.$	181/187

Table 5.2: The best-fitting rest-frame parameters of the broad-band *Suzaku* XIS + HXD absorbed-reflection model described in Section 5.2.3.1 fitted to the 2008 *Suzaku* data (obs. 2) for NGC 4051. [a]Primary power-law continuum: Γ, photon index; Normalisation. [b]Absorbed power law: N_{H}, column density; ξ, ionisation parameter. [c]Neutral reflector: A_{Fe}, iron abundance with respect to solar values. [d]Zone of absorption. The redshift of the zone was fixed at the same value as that of the host galaxy (i.e. $z = 0.002336$). [e]Ionised reflector. The symbol p signifies that the parameter has pegged at the maximum / minimum value allowed by the model and the symbol l signifies that the parameter is linked to all parameters with the corresponding number.

by the model) whereas the highly-ionised reflector modelling the soft excess requires a best-fitting value of $\log \xi = 3.8^{+0.2}_{-0.1}$. Note that the highly-ionised reflector is able to account for the soft excess due to its enhanced reflectivity in the soft band at high levels of ionisation although it should stressed that the soft excess cannot be modelled by the REFLIONX component alone without introducing a zone of absorption (in addition to the soft X-ray warm absorbers, the partial-coverer and the Galactic absorption). The absorber in front of the reflector is responsible for producing deep bound-free edges which reduce the observed reflected

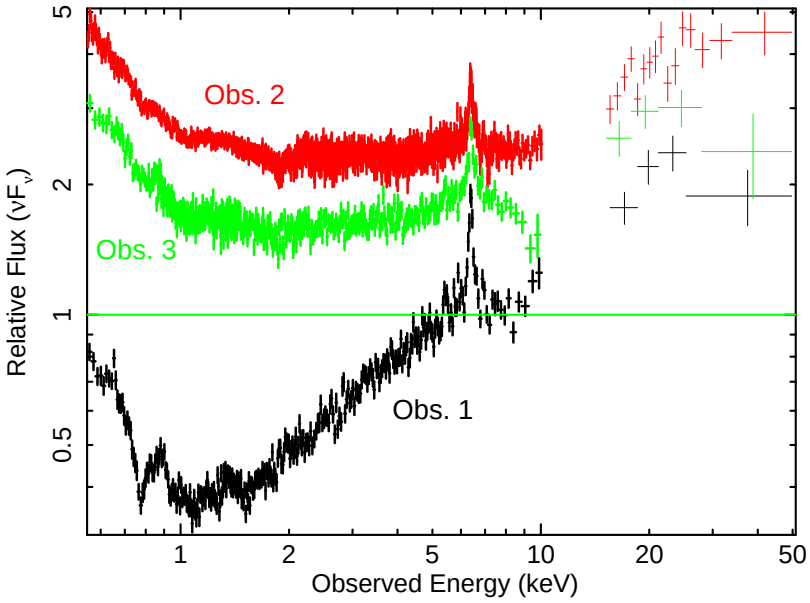

Figure 5.8: The relative fluxes of the combined *Suzaku* XIS and HXD-PIN data for NGC 4051 in the observed frame. The data are unfolded against a power law with photon index $\Gamma = 2$. The 2005 data are shown in black. The two separate 2008 observations are shown in red and green corresponding to the 275 and 78 ks exposures respectively.

flux at higher energies, thus revealing positive spectral curvature in the soft band. Such a component may be representative of scattering off a disc wind (e.g. Sim et al. 2008; Sim et al. 2010). The highly-ionised reflector also removes the residuals at Fe K and well models the ionised emission from Fe XXV. This model leaves very few residuals in the data and forms the final best-fitting model to the time-averaged 2008 *Suzaku* data, statistically giving a good fit with $\chi^2/d.o.f. = 181/187$; a significant improvement over the phenomenological model described in Section 4.5.2 ($\chi^2/d.o.f. = 218/187$).

5.2.3.2 Long-Term Spectral Variability

In order to assess the nature of the long-term X-ray spectral variability of NGC 4051, an attempt was made to simultaneously model the 2008 data with the 2005 *Suzaku* data over

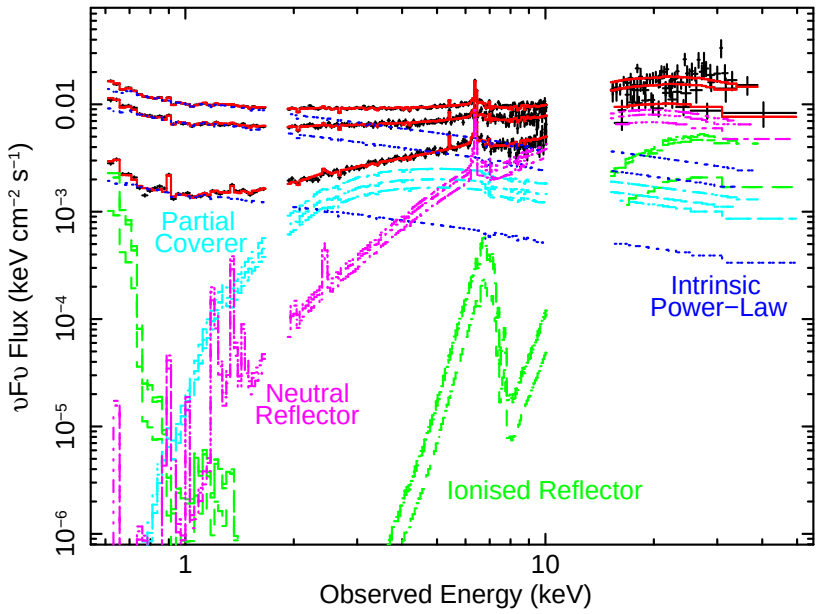

Figure 5.9: The relative contributions of the individual model components to the three broad-band 0.6–50.0 keV *Suzaku* spectra of NGC 4051 in the observed frame. The data are shown in black with the sum of all model components superimposed in red. The absorbed- and unabsorbed-power-law components are shown in cyan and navy blue respectively. The absorbed neutral- and ionised-reflectors are shown in magenta and green respectively. Note that the absorbed power-law component and the reflection components remain largely constant in flux across the three observations with the changes in spectral shape instead accounted for by significant variations in the normalisation of the intrinsic unabsorbed power-law component, which indicates that the covering fraction of the partial-coverer has varied.

the broad-band 0.6–50.0 keV energy range. The 2005 data have previously been described in detail by Terashima et al. (2009) where NGC 4051 was found to have fallen into an extended period of low flux with a 0.5–10.0 keV flux of $F = 1.32 \times 10^{-11}$ erg cm^{-2} s^{-1} ($F_{2-10} = 8.70 \times 10^{-12}$ erg cm^{-2} s^{-1}) compared to the much higher flux of $F = 5.03 \times 10^{-11}$ erg cm^{-2} s^{-1} ($F_{2-10} = 2.42 \times 10^{-11}$ erg cm^{-2} s^{-1}) in 2008. The spectrum was observed to be much harder in the 2005 observation with a significant excess compared to an intrinsic power-law fit at energies >10 keV. Figure 5.8 shows the relative fluxes of the three observations. The large changes in spectral shape can be well described by a two-component model consisting of a soft variable component superimposed over a hard constant component (Miller et al. 2010b).

Absorption Component	Model Parameter	Value Obs. 1	Value Obs. 2	Value Obs. 3
Zone 1[a]	$N_{\rm H}\,({\rm cm}^{-2})$	$(3.89^{+1.37}_{-1.64})\times10^{20}$	$(3.24^{+0.98}_{-1.10})\times10^{20}$	$(2.87^{+1.36}_{-1.29})\times10^{20}$
	$\log\xi$	$-(0.72^{+0.29}_{-0.24})$	$-(0.79^{+0.24}_{-0.24})$	$-(0.85^{+0.32}_{-0.21})$
	$v_{\rm out}\,({\rm km\,s}^{-1})$	200^{+150}_{-140}	190^{+120}_{-100}	160^{+130}_{-110}
Zone 2[a]	$N_{\rm H}\,({\rm cm}^{-2})$	$(1.68^{+0.71}_{-0.59})\times10^{20}$	$(1.80^{+0.62}_{-0.58})\times10^{20}$	$(1.49^{+0.68}_{-0.58})\times10^{20}$
	$\log\xi$	$0.71^{+0.40}_{-0.35}$	$0.64^{+0.36}_{-0.36}$	$0.54^{+0.38}_{-0.39}$
	$v_{\rm out}\,({\rm km\,s}^{-1})$	180^{+80}_{-70}	240^{+70}_{-60}	230^{+70}_{-70}
Zone 3a[a]	$N_{\rm H}\,({\rm cm}^{-2})$	$(1.62^{+1.09}_{-1.15})\times10^{21}$	$(1.34^{+0.97}_{-1.09})\times10^{21}$	$(1.35^{+1.14}_{-1.22})\times10^{21}$
	$\log\xi$	$2.08^{+0.23}_{-0.20}$	$2.14^{+0.11}_{-0.17}$	$2.07^{+0.25}_{-0.22}$
	$v_{\rm out}\,({\rm km\,s}^{-1})$	500^{+100}_{-90}	540^{+80}_{-90}	520^{+100}_{-100}
Zone 3b[a]	$N_{\rm H}\,({\rm cm}^{-2})$	$(5.87^{+2.79}_{-2.60})\times10^{20}$	$(5.13^{+2.42}_{-2.19})\times10^{20}$	$(6.00^{+2.31}_{-2.29})\times10^{20}$
	$\log\xi$	$1.99^{+0.29}_{-0.26}$	$2.08^{+0.25}_{-0.19}$	$2.01^{+0.17}_{-0.23}$
	$v_{\rm out}\,({\rm km\,s}^{-1})$	820^{+90}_{-100}	840^{+70}_{-80}	860^{+90}_{-90}
Zone 4[a]	$N_{\rm H}\,({\rm cm}^{-2})$	$(2.28^{+0.88}_{-0.84})\times10^{21}$	$(2.69^{+0.72}_{-0.77})\times10^{21}$	$(2.50^{+0.75}_{-0.76})\times10^{21}$
	$\log\xi$	$3.03^{+0.15}_{-0.15}$	$3.00^{+0.12}_{-0.13}$	$2.93^{+0.16}_{-0.15}$
	$v_{\rm out}\,({\rm km\,s}^{-1})$	770^{+90}_{-100}	730^{+60}_{-70}	780^{+80}_{-100}

Table 5.3: The best-fitting parameters for the fully-covering warm-absorber zones in the three *Suzaku* spectra. [a]XSTAR zone: $N_{\rm H}$, column density; ξ, ionisation parameter; $v_{\rm out}$, outflow velocity. Zones 1, 3 and 4 have a turbulent velocity width of $v_{\rm turb} = 200\,{\rm km\,s}^{-1}$ whereas zone 2 is better modelled with a turbulent velocity width of $v_{\rm turb} = 500\,{\rm km\,s}^{-1}$ (as required by the high-resolution *Chandra* HETG data.

The best-fitting model described in Section 5.2.3.1 was simultaneously applied to the 2005 and 2008 XIS and HXD *Suzaku* data. The second, shorter exposure (78 ks) observation from 2008 was also included in this joint-analysis. A plot of the relative contributions of the individual model components to the joint-fit is shown in Figure 5.9. The parameters of the fully-covering warm absorber were tested to see if they had varied between observations but the best-fitting values were consistent within the errors across the 2005 and 2008 data (see Table 5.3). All model parameters were tied between the three observations except for the relative normalisations of the absorbed- (i.e. the partial-coverer) and intrinsic-power-law components and the near-neutral and ionised-reflection components (REFLIONX) which were allowed to vary to account for the long-term spectral variability. The 0.5–100 keV fluxes

corresponding to the relative normalisations of the power-law and reflection components are given in Table 5.4. It was found that the normalisations of the absorbed power law and the near-neutral reflection component are largely constant across the three observations (see Table 5.5), consistent with the findings of Miller et al. (2010b). It should be noted that some changes in the flux of the highly-ionised reflector can be observed between 2005 and 2008. However, it was found that the spectral variability can ultimately be described by large changes in the normalisation of the intrinsic, unabsorbed power-law component which increases by a factor of $\sim$7 from the low-flux data in 2005 to the high-flux observation in 2008. The covering fraction of the partial-coverer is then given by the ratio between the normalisation of the absorbed and total power-law components which reveals a high covering fraction of $f_{\rm cov} = 71^{+1}_{-1}\%$ in the 2005 low-flux data compared to a much lower covering fraction of $f_{\rm cov} = 34^{+2}_{-1}\%$ when the source flux is higher. This supports of the notion of an empirical two-component model whereby the constant reflection-component contributes to the majority of the hard X-ray flux whereas changes in the normalisation of the intrinsic power law (i.e. changes in the covering fraction) account for the variations in spectral shape at lower energies.

Alternatively, an attempt was also made to account for the spectra with a reflection-dominated model. In this instance, the soft excess is accounted for by an independent COMPTT component (Titarchuk 1994) to represent inverse-Compton scattering of EUV seed photons from the disc. This is to ensure that the main features driving the fit of the reflector are any broad residuals in the Fe K region and not the soft excess (see Patrick et al. 2011b). The partial-coverer was replaced with an additional REFLIONX component convolved with the RELCONV kernel of Dauser et al. (2010). The RELCONV code is a convolution model used to calculate the effects of relativistic smearing; i.e. a blurred reflection component from the inner regions of the accretion disc which may account for the hard excess and spectral curvature. The free parameters of the RELCONV model are the unitless spin of the black hole, a, the inclination of the disc in units of degrees and the radial emissivity profile, q, where the emission profile of the disc scales as r^{-q}. The intrinsic power-law continuum (free to vary, along with a and q) and the fully-covering warm absorber zones remained in the fit. This model was applied to all three *Suzaku* spectra simultaneously but produced a significantly worse fit than with the partial-covering model by $\Delta\chi^2 = 833$ for 3 fewer degrees of

Component	$\mathrm{Flux}_{0.5-100\,\mathrm{keV}}$ ($\times 10^{-12}\,\mathrm{erg\,cm^{-2}\,s^{-1}}$) Obs. 1 (2005)	Obs. 2 (2008)	Obs. 3 (2008)
Power law	$6.63^{+0.11}_{-0.16}$	$47.39^{+0.39}_{-0.77}$	$31.25^{+0.26}_{-0.54}$
Power law$_{\mathrm{abs.}}$	$6.66^{+0.17}_{-0.13}$	$10.01^{+0.50}_{-0.47}$	$8.03^{+0.46}_{-0.44}$
REFLIONX$_{\mathrm{neutral}}$	$17.31^{+0.54}_{-0.79}$	$23.98^{+0.91}_{-1.76}$	$21.25^{+1.00}_{-1.24}$
REFLIONX$_{\mathrm{ionised}}$	$3.90^{+1.07}_{-1.17}$	$10.41^{+1.57}_{-1.52}$	$9.23^{+2.22}_{-1.99}$
Fe Kα	$0.21^{+0.12}_{-0.03}$	$0.25^{+0.04}_{-0.04}$	$0.30^{+0.06}_{-0.05}$
f_{cov}	$70^{+3}_{-2}\%$	$30^{+2}_{-2}\%$	$40^{+2}_{-2}\%$
Component	Ratio Obs. 1 (2005)	Obs. 2 (2008)	Obs. 3 (2008)
Power law	1	$7.15^{+0.23}_{-0.23}$	$4.71^{+0.16}_{-0.15}$
Power law$_{\mathrm{abs.}}$	1	$1.50^{+0.11}_{-0.10}$	$1.21^{+0.09}_{-0.10}$
REFLIONX$_{\mathrm{neutral}}$	1	$1.39^{+0.12}_{-0.15}$	$1.23^{+0.12}_{-0.11}$
REFLIONX$_{\mathrm{ionised}}$	1	$2.67^{+1.72}_{-0.88}$	$2.34^{+1.85}_{-0.88}$
Fe Kα	1	$1.19^{+0.42}_{-0.55}$	$1.43^{+0.57}_{-0.67}$

Table 5.4: Upper panel: the observed fluxes corresponding to the best-fitting values for the power law (both absorbed and unabsorbed), reflected continua and Fe Kα components in NGC 4051 obtained in Section 5.2.3.2 from 0.5–100 keV. The covering fraction of the partial-coverer is also shown for each observation. Lower panel: these values expressed as a ratio compared to the values obtained for the 2005 *Suzaku* data. It can be seen that the fluxes of the reflection components, the absorbed power law and the neutral Fe Kα emission line are consistent with remaining largely constant across all epochs whereas large variations in the flux of the intrinsic unabsorbed power law are apparent between observations with the flux considerably lower in 2005 when the source was found to have fallen into an extended period of low flux.

freedom. The emissivity and SMBH spin parameters are also forced to extreme values; $q > 7$ (implying that the primary emission is extremely centrally concentrated) and $a = 0.998$ (i.e. maximal spin) respectively. Furthermore, the 2-100 keV blurred reflector flux is found to be $\sim$3 times higher in the 2005 data than in the 2008 data, despite the spectroscopic evidence for the source being more strongly absorbed (along our line-of-sight) in 2005. As a result, the partial-covering fit is preferred on both statistical and physical grounds. A similar conclusion was also reached by Terashima et al. (2009) who were unable to account for the 2005 *Suzaku* data with a reflection-dominated model due to the relatively weak Fe Kα emission component.

The partial-covering fit is then considered to be the final, best-fitting model which describes the data well with all remaining free parameters across all three observations consistent

Component	Parameter	Value Obs. 1 (2005)	Obs. 2 (2008)	Obs. 3 (2008)
Power law[a]	Γ	$2.49^{+0.02\,l_1}_{-0.01}$	l_1	l_1
	Norm. ($\mathrm{ph\,cm^{-2}\,s^{-1}}$)	$(1.72^{+0.03}_{-0.04}) \times 10^{-3}$	$(1.23^{+0.02}_{-0.02}) \times 10^{-2}$	$(8.11^{+0.07}_{-0.14}) \times 10^{-3}$
Power law$^b_{\mathrm{abs.}}$	Γ	l_1	l_1	l_1
	Norm. ($\mathrm{ph\,cm^{-2}\,s^{-1}}$)	$(4.25^{+0.11}_{-0.08}) \times 10^{-3}$	$(6.39^{+0.32}_{-0.30}) \times 10^{-3}$	$(5.13^{+0.29}_{-0.28}) \times 10^{-3}$
Partial-coverer[c]	N_{H} ($\mathrm{cm^{-2}}$)	$(1.18^{+0.08}_{-0.09}) \times 10^{23\,l_2}$	l_2	l_2
	$\log \xi$	$0.51^{+0.11\,l_3}_{-0.16}$	l_3	l_3
	f_{cov}	$71^{+1}_{-1}\%$	$34^{+2}_{-1}\%$	$39^{+1}_{-1}\%$
REFLIONX$^d_{\mathrm{abs.}}$ (low ξ)	Γ	l_1	l_1	l_1
	ξ ($\mathrm{erg\,cm\,s^{-1}}$)	$1^{\,l_4}_{p}$	l_4	l_4
	A_{Fe}	$0.27^{+0.03\,l_5}_{-0.02}$	l_5	l_5
	$F_{0.5-100}$ ($\mathrm{erg\,cm^{-2}\,s^{-1}}$)	$(1.73^{+0.05}_{-0.08}) \times 10^{-11}$	$(2.40^{+0.09}_{-0.18}) \times 10^{-11}$	$(2.13^{+0.10}_{-0.12}) \times 10^{-11}$
Absorber[e]	N_{H} ($\mathrm{cm^{-2}}$)	$(1.36^{+2.27}_{-1.75}) \times 10^{22\,l_6}$	l_6	l_6
	$\log \xi$	$0.60^{+0.24\,l_7}_{-0.30}$	l_7	l_7
REFLIONX$^f_{\mathrm{abs.}}$ (high ξ)	Γ	l_1	l_1	l_1
	$\log \xi$	$3.5^{+0.1\,l_8}_{-0.1}$	l_8	l_8
	A_{Fe}	l_5	l_5	l_5
	$F_{0.5-100}$ ($\mathrm{erg\,cm^{-2}\,s^{-1}}$)	$(3.90^{+1.07}_{-1.17}) \times 10^{-12}$	$(1.04^{+0.16}_{-0.16}) \times 10^{-11}$	$(9.23^{+2.22}_{-1.99}) \times 10^{-12}$
Absorber[e]	N_{H} ($\mathrm{cm^{-2}}$)	$(4.84^{+0.16\,p}_{-0.17}) \times 10^{24\,l_9}$	l_9	l_9
	$\log \xi$	$2.53^{+0.02\,l_{10}}_{-0.02}$	l_{10}	l_{10}
High ξ abs.[g]	N_{H} ($\mathrm{cm^{-2}}$)	$(5.49^{+0.71}_{-0.49\,p}) \times 10^{22\,l_{11}}$	l_{11}	l_{11}
	$\log \xi$	$3.9^{+0.1\,l_{12}}_{-0.1}$	l_{12}	l_{12}
	v_{out} ($\mathrm{km\,s^{-1}}$)	$-(5\,400^{+600}_{-900})^{\,l_{13}}$	l_{13}	l_{13}
Fe Kα^h	E_{line} (keV)	$6.40^{+0.01}_{-0.02}$	$6.40^{+0.02}_{-0.01}$	$6.41^{+0.02}_{-0.02}$
	σ (eV)	71^{+19}_{-23}	68^{+33}_{-33}	< 55.3
	F_{line} ($\mathrm{ph\,cm^{-2}\,s^{-1}}$)	$2.06^{+0.22}_{-0.26}$	$2.46^{+0.41}_{-0.36}$	$1.70^{+0.43}_{-0.28}$
	EW (eV)	201^{+22}_{-25}	102^{+17}_{-15}	93^{+24}_{-15}

Table 5.5: The spectral parameters in the rest frame of the best-fitting model simultaneously fit to the 2005 (obs. 1) and 2008 (obs. 2 and obs. 3) broad-band 0.6–50.0 keV *Suzaku* data for NGC 4051 described in Section 5.2.3.2. [a]Primary power-law continuum: Γ, photon index; Normalisation. [b]Absorbed power law. [c]Partial-coverer: N_{H}, column density; ξ, ionisation parameter; f_{cov}, covering fraction expressed as a percentage. [d]Neutral reflector: A_{Fe}, iron abundance with respect to solar values; $F_{0.5-100}$, observed flux from 0.5–100 keV. [e]Zone of absorption. The redshift of the zone was fixed at the same value as that of the host galaxy (i.e. $z = 0.002336$). [f]Ionised reflector. [g]Highly-ionised absorption: v_{out}, velocity shift. [h]Fe Kα emission: E_{line}, centroid energy; σ, intrinsic width; F_{line}, line flux; EW, equivalent width (against the total observed continuum). The symbol p signifies that the parameter has pegged at the maximum / minimum value allowed by the model and the symbol l signifies that the parameter is linked to all parameters with the corresponding number. Note that the Fe Kα emission line parameters were obtained by replacing the neutral REFLIONX component with a PEXRAV component and a Gaussian.

with the values listed in Table 5.2 resulting in a final fit statistic of $\chi^2/d.o.f. = 560/549$.

5.2.4 Variability in the Fe K Band

The Fe K profile of NGC 4051 was analysed and parameterised in Section 4.5.2 with the time-averaged data from the long observation made in 2008. It was found that the Fe K emission complex could be parameterised with two statistically significant Gaussians centred at $E_c = 6.41 \pm 0.01$ and $E_c = 6.62^{+0.09}_{-0.02}$ keV corresponding to emission from near-neutral Fe Kα (EW $= 75^{+14}_{-9}$ eV) and Fe XXV (EW $= 25^{+6}_{-11}$ eV) respectively. Negative residuals were also observed in the data at blueshifted energies which were initially parameterised with two additional Gaussian absorption lines at $E_c = 6.81^{+0.04}_{-0.05}$ keV and $E_c = 7.12 \pm 0.04$ keV and ultimately modelled with a single zone of absorption using XSTAR with a best-fitting column density of $N_H = (8.4^{+1.9}_{-2.0}) \times 10^{22}\,cm^{-2}$, and an ionisation parameter of $\log \xi = 4.1^{+0.2}_{-0.1}$ for a turbulence velocity of $v_{turb} = 3\,000\,km\,s^{-1}$. If the two absorption lines correspond to Fe XXV and Fe XXVI respectively, then this is most the likely the signature of a highly-ionised outflow with a velocity of $v_{out} = 5\,800^{+860}_{-1\,200}\,km\,s^{-1}$.

A test was performed to see whether the parameters of the near-neutral Fe Kα emission line had varied between observations. Figure 5.10 shows the residuals in the Fe K band for all three *Suzaku* observations against the absorbed power-law continuum (with the emission and absorption lines removed). The model described in Section 4.5.2 was then fitted to the time-averaged 2005 *Suzaku* observation of NGC 4051, where the flux in the XIS band was found to be approximately 5 times lower. Fitting from 3–10 keV revealed that the parameters of the Fe Kα line are consistent with those found in the 2008 data within the errors (and also consistent with the analysis of the 2005 data by Terashima et al. 2009). Indeed, the flux of the line was found to be $F_{line} = (2.2 \pm 0.2) \times 10^{-5}$ photons cm^{-2} s^{-1} in 2008 compared to $F_{line} = (1.9 \pm 0.2) \times 10^{-5}$ photons cm^{-2} s^{-1} in 2005 but with an equivalent width increasing from EW $= 75^{+14}_{-9}$ eV to EW $= 155 \pm 24$ eV against the observed continuum as the source flux drops. The variability test was extended by applying the model to the second, shorter *Suzaku* observation made in 2008 along with two archival *XMM-Newton* EPIC-pn datasets which were acquired in 2001 and 2002. Once again, the flux of the line was found to be largely

invariable, with the best-fitting values reported in Table 5.6. A plot of the three *Suzaku* mean spectra in the Fe K band is shown in Figure 5.11. Alternatively, fixing the normalisation of the line at the best-fitting values from the long 2008 *Suzaku* observation and re-fitting in the subsequent datasets resulted in a change in the fit statistic of $\Delta\chi^2 < 1$ in each case, strongly suggesting that the emission line from near-neutral Fe does not respond to large changes in the continuum.

However, NGC 4051 is intrinsically a highly-variable source on short timescales and so it was conceivable that the Fe Kα parameters could vary within individual observations. As a further test, the two long *Suzaku* observations in 2005 and 2008 were split up into four 55 ks (duration) segments and six 80 ks (duration) segments respectively (to guarantee enough S/N to measure the Fe Kα parameters) and the shorter 2008 observation was split up into two 80 ks (duration) segments. The Fe Kα line was again parameterised in the same way as before and the results of the time-sliced fits are shown in Table 5.6 along with the mean fits.

Finally, the 2005 and 2008 long exposures were sub-divided to sample the line more finely in flux. The 2005 *Suzaku* data were split into high- and low-flux spectra (to avoid periods when the source was flaring) with an intensity selection of $0.47\,\mathrm{cts\,s^{-1}}$ over the 0.5–10 keV energy band. The long 2008 observation (made when the source was much brighter) was split into three intensity-selected spectra with count rates $<2.0\,\mathrm{cts\,s^{-1}}$, 2.0–$3.0\,\mathrm{cts\,s^{-1}}$ and $>3.0\,\mathrm{cts\,s^{-1}}$, again over the 0.5–10 keV energy range. The results are shown in Table 5.7, again alongside the results of the mean fits for ease of comparison.

So the flux of the Kα emission line from near-neutral Fe is observed to be largely constant on both long and short timescales and is invariant despite large changes in the flux of the observed continuum, with its equivalent width increasing as the source flux drops and vice-versa. To test this, the measured fluxes of the 6.4 keV line from *XMM-Newton* and *Suzaku* data were compared to a constant model yielding $\chi^2/d.o.f. = 4.5/7$ and $\chi^2/d.o.f. = 10.8/13$ for the intensity-sliced and time-sliced data respectively. So, overall, there is strong evidence to suggest that the line is consistent with having a constant flux over the 7-year time-period considered and does not respond to changes in the continuum flux. This is perhaps suggestive of a distant origin for the emitting material. However, a slightly variable, but weaker, broad

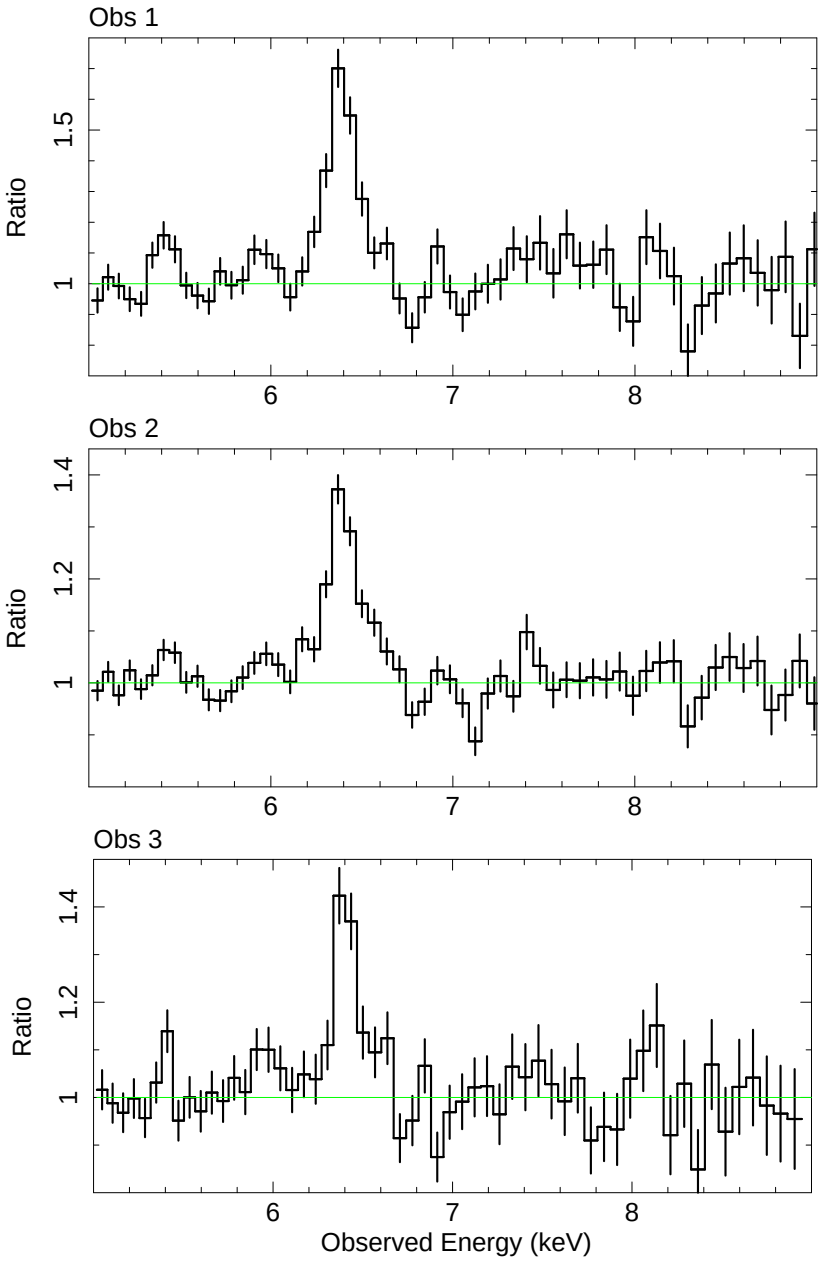

Figure 5.10: The Fe K region for the three *Suzaku* observations of NGC 4051 plotted as ratios against a simple absorbed power-law continuum displaying evidence for emission from Fe Kα ($\sim$6.4 keV) plus a highly-ionised outflow with $v_{\rm out} \sim 6\,000\,{\rm km\,s^{-1}}$, as reported in Section 4.5.2. Note that slight residuals at $\sim$8.0 and $\sim$8.3 keV can be seen (mainly in the 2005 data; obs. 1); these are likely due to the $1s$–$3p$ transitions of Fe XXV and Fe XXVI respectively but are not statistically significant detections. Residuals are also present at $\sim$5.4 and $\sim$5.9 keV which are discussed in Section 5.2.4.1.

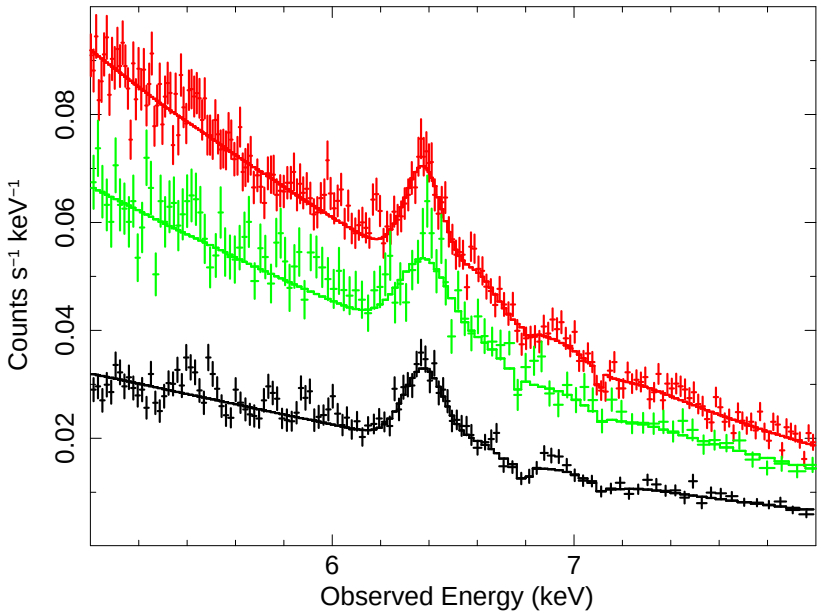

Figure 5.11: The modelled Fe K region of the three mean *Suzaku* spectra from 2005 (black) and 2008 (red and green; obs. 2 and 3 respectively). The Fe-line parameters are largely consistent between all three observations, as discussed in Section 5.2.4. The binning criteria were relaxed slightly in the plot to allow the spectral features to appear clearer in counts space. Residuals are also present at ∼5.4 and ∼5.9 keV which are discussed in Section 5.2.4.1.

component of the Fe Kα line may also be present. This component was first observed in the 2008 *Chandra* HETG spectrum (see Section 4.4.2) with an intrinsic width of $\sigma = 150^{+60}_{-43}$ eV (corresponding to FWHM $= 16\,000^{+7\,000}_{-4\,000}$ km s^{-1}). These results are supported by the PCA of Miller et al. (2010b) (see Section 5.2.1.1) where a narrow component of the Fe Kα emission line is observed in the constant offset component whereas a moderately broad component at ∼6.4 keV is observed in eigenvector one suggesting that it is variable in nature.

5.2.4.1 Significant Line Emission in the 5–6 keV Band

Upon performing a simple parameterisation of the Fe K band (as in Section 5.2.4), it was also found that additional residuals are present in the 5–6 keV energy band, as shown in Figure 5.10. An emission line at $E_c = 5.44 \pm 0.03$ keV is statistically required in the 2005

Observation	F_{2-10} [a]	$E_{6.40}$ [b]	$F_{6.40}$ [c]	$\mathrm{EW}_{6.40}$ [d]	$\Delta\chi^2$	$\chi^2/d.o.f.$
XMM 2001	2.31	$6.40^{+0.02}_{-0.02}$	$23.8^{+3.3}_{-3.3}$	95^{+15}_{-15}	143	117/109
XMM 2002	0.56	$6.41^{+0.01}_{-0.01}$	$18.1^{+2.6}_{-2.2}$	205^{+16}_{-16}	158	146/108
Suzaku 2005	0.87	$6.40^{+0.01}_{-0.02}$	$19.1^{+1.6}_{-1.6}$	155^{+24}_{-24}	379	150/100
Suzaku 2005: 1	1.01	$6.38^{+0.02}_{-0.02}$	$15.7^{+3.0}_{-3.0}$	139^{+27}_{-27}	73	94/99
Suzaku 2005: 2	0.88	$6.40^{+0.02}_{-0.02}$	$24.1^{+3.2}_{-3.2}$	235^{+31}_{-31}	159	82/99
Suzaku 2005: 3	0.82	$6.42^{+0.02}_{-0.02}$	$18.0^{+3.2}_{-3.2}$	165^{+30}_{-30}	84	115/99
Suzaku 2005: 4	0.78	$6.38^{+0.02}_{-0.03}$	$19.4^{+3.6}_{-3.7}$	183^{+34}_{-35}	76	102/99
Suzaku 2008a	2.42	$6.40^{+0.02}_{-0.01}$	$22.3^{+1.7}_{-1.7}$	91^{+7}_{-7}	160	182/100
Suzaku 2008a: 1	2.61	$6.38^{+0.02}_{-0.03}$	$24.7^{+4.0}_{-4.0}$	95^{+15}_{-15}	100	119/99
Suzaku 2008a: 2	2.90	$6.40^{+0.02}_{-0.02}$	$24.4^{+5.5}_{-5.2}$	85^{+19}_{-18}	84	112/99
Suzaku 2008a: 3	2.66	$6.43^{+0.03}_{-0.04}$	$24.3^{+4.3}_{-4.3}$	91^{+16}_{-16}	86	84/99
Suzaku 2008a: 4	2.29	$6.39^{+0.05}_{-0.03}$	$21.0^{+4.0}_{-4.0}$	90^{+17}_{-17}	73	117/99
Suzaku 2008a: 5	1.96	$6.40^{+0.04}_{-0.06}$	$16.5^{+4.0}_{-4.0}$	83^{+20}_{-20}	46	85/99
Suzaku 2008a: 6	2.10	$6.40^{+0.02}_{-0.02}$	$23.7^{+4.1}_{-4.1}$	117^{+20}_{-20}	91	114/99
Suzaku 2008b	1.79	$6.41^{+0.02}_{-0.02}$	$20.0^{+3.0}_{-3.2}$	107^{+14}_{-14}	142	120/100
Suzaku 2008b: 1	1.83	$6.42^{+0.03}_{-0.03}$	$19.0^{+3.9}_{-3.9}$	99^{+20}_{-20}	64	109/99
Suzaku 2008b: 2	1.73	$6.40^{+0.03}_{-0.02}$	$22.0^{+3.9}_{-3.9}$	124^{+22}_{-22}	87	111/99

Table 5.6: The best-fitting parameters of the near-neutral Fe Kα emission line at $\sim$6.4 keV in time-sliced NGC 4051 data. The 2005, 2008a and 2008b spectra are split into 55 ks, 80 ks and 80 ks segments respectively and all spectral fitting took place in the 3–10 keV energy band. Errors are quoted at the 1σ level. [a]Flux from 2–10 keV in units $\times 10^{-11}$ erg cm^{-2} s^1; [b]Line energy in units keV; [c]Line flux in units $\times 10^{-6}$ photons cm^{-2} s^{-1}; [d]Equivalent width in units eV.

data. When represented by a Gaussian with a fixed width of $\sigma = 50$ eV[1], the line has a flux of $F_{\rm line} = (5.03^{+2.02}_{-2.01}) \times 10^{-6}$ photons cm^{-2} s^{-1} and corresponds to an improvement of the fit statistic of $\Delta\chi^2 = 32$ and an equivalent width of EW 46 ± 16 eV against the observed continuum. A second residual of excess counts was also observed at higher energies and could be accounted for with a second Gaussian (again with $\sigma = 50$ eV) with a centroid energy of $E_{\rm c} = 5.95 \pm 0.05$ keV and a line-flux of $F_{\rm line} = (5.05^{+2.05}_{-1.95}) \times 10^{-6}$ photons cm^{-2} s^{-1}. This line corresponds to an improvement in the fit statistic of $\Delta\chi^2 = 34$ and an equivalent width of EW $= 44^{+17}_{-16}$ eV against the observed continuum.

[1]Since it was not possible to constrain the intrinsic width of the line, it was fixed at $\sigma = 50$ eV, consistent with the value found for the neutral Fe Kα line. This was justified on the basis of the PCA of Miller et al. (2010b) suggesting a common origin for the two lines.

Observation	F_{2-10} [a]	$E_{6.40}$ [b]	$F_{6.40}$ [c]	$\mathrm{EW}_{6.40}$ [d]	$\Delta\chi^2$	$\chi^2/d.o.f.$
XMM 2001	2.31	$6.40^{+0.02}_{-0.02}$	$23.8^{+3.3}_{-3.3}$	95^{+15}_{-15}	143	117/109
XMM 2002	0.56	$6.41^{+0.02}_{-0.02}$	$18.1^{+2.6}_{-2.2}$	205^{+16}_{-16}	158	146/108
Suzaku 2005	0.87	$6.40^{+0.01}_{-0.02}$	$19.1^{+1.6}_{-1.6}$	155^{+24}_{-24}	379	150/100
Suzaku 2005 Low	0.70	$6.40^{+0.01}_{-0.01}$	$18.3^{+1.9}_{-1.9}$	201^{+20}_{-21}	261	107/100
Suzaku 2005 High	1.26	$6.39^{+0.02}_{-0.02}$	$21.0^{+3.01}_{-3.01}$	149^{+22}_{-22}	127	136/100
Suzaku 2008a	2.42	$6.40^{+0.02}_{-0.01}$	$22.3^{+1.7}_{-1.7}$	91^{+7}_{-7}	160	182/100
Suzaku 2008a Low	1.76	$6.39^{+0.01}_{-0.01}$	$22.0^{+2.0}_{-2.0}$	120^{+11}_{-11}	269	135/100
Suzaku 2008a Med.	2.75	$6.40^{+0.02}_{-0.02}$	$20.5^{+3.0}_{-3.0}$	74^{+11}_{-11}	131	117/100
Suzaku 2008a High	3.89	$6.40^{+0.02}_{-0.02}$	$27.8^{+5.2}_{-5.2}$	75^{+14}_{-14}	79	114/100
Suzaku 2008b	1.79	$6.41^{+0.02}_{-0.02}$	$20.0^{+3.0}_{-3.2}$	107^{+14}_{-14}	142	120/100

Table 5.7: The best-fitting parameters of the near-neutral Fe Kα emission line at $\sim$6.4 keV in flux-selected NGC 4051 data. All spectral fitting took place over the 3–10 keV energy band. Errors are quoted at the 1σ level. [a]Flux from 2–10 keV in units $\times10^{-11}$ erg cm^{-2} s^1; [b]Line energy in units keV; [c]Line flux in units $\times10^{-6}$ photons cm^{-2} s^{-1}; [d]Equivalent width in units eV.

To investigate the robustness of these detections to the form of the continuum model assumed, the lines were also included in the joint-fit of all three broad-band *Suzaku* observations, as described in Section 5.2.3.2. Adding in a line of fixed width ($\sigma = 50$ eV) constrained to lie in the 3–8 keV energy range yielded an improvement in the fit statistic of $\Delta\chi^2 = 20$ with a best-fitting centroid energy of $E_\mathrm{c} = 5.44 \pm 0.03$ keV and the addition of a second line under the same constraints resulted in an improvement in the fit statistic of $\Delta\chi^2 = 9$ with a best-fitting centroid energy of $E_\mathrm{c} = 5.98 \pm 0.05$ keV. This suggests that the detection of the 5.44 keV line is robust to the continuum-model used whereas the significance of the line at $\sim$5.9 keV is more sensitive to the form of the continuum assumed. No other emission lines are statistically required in the 3–8 keV energy range.

Since the two emission lines are found at somewhat 'unusual' rest-frame energies, it was important to check that they are attributable to the AGN and not, for example, a product of poor background subtraction. From analysing the *Suzaku* background spectrum, it was found that the background comprises just 2.5% of the source-flux from 5–7 keV when the source was at its dimmest (i.e. 2005) and this is reduced to 1.3% when the source was at its brightest (i.e. 2008). No significant emission line features were observed in the background spectrum

and, indeed, fixing a Gaussian at an energy of 5.44 keV yields an upper limit on the line flux of $F_{\rm line} < 4.14 \times 10^{-8}$ photons cm^{-2} s^{-1}, which is <1% of the detected line flux. The lack of a significant detection of any feature of comparable energy or equivalent width therefore also rules out its origin as a detector feature. The *Suzaku* XIS detector spectra were also analysed individually and the 5.44 keV emission line was found to be significantly detected by each XIS detector, as shown in Figure 5.12. The detection of the line at 5.95 keV, however, was a little more tentative and it was important to note that each *Suzaku* XIS chip contains a Mn calibration source which emits at ∼5.9 keV. Although the calibration sources are found at the edges of the chips and background- and source-extraction takes place well away from these regions, a weak Mn Kα emission line was detected in the background spectra. However, this feature has a flux <10% of that of the detected emission line in the source spectra and since the source spectra are extracted from regions further away from the edges of the chip than the background spectra, one should expect the contamination level to be even lower. Nevertheless, it is difficult to rule out any contribution from the slightly broad component of the Fe Kα line at ∼6.4 keV.

The robustness of the line detections is fully explored in Turner et al. (2010) where they also confirm the significance of the line at 5.44 keV by performing Monte Carlo simulations, following the method described in Porquet et al. (2004a) and Markowitz, Reeves & Braito (2006). Taking the null hypothesis that the spectrum is simply comprised of an absorbed power-law continuum with best-fitting parameters from the broad-band fit in Section 5.2.3.1 (and including the narrow Fe Kα emission at ∼6.4 keV) but with the statistical uncertainty from the broad-band fit, 3 000 fake *Suzaku* spectra were created, assuming that the same instruments were operational as for the 2005 exposure and using photon statistics expected from the 2005 observation. After grouping the simulated data in the same way as the observational data (i.e. at the HWHM of the energy resolution of the detectors), each spectrum was fitted and the presence of an emission line was tested for by stepping through the 3–10 keV energy range in 100 eV increments and fitting an emission line at each step (whose centroid energy was allowed to vary) and then measuring the resultant change in the χ^2 statistic. The most extreme statistical fluctuation in the 3–10 keV energy band was found to be $\Delta\chi^2 = 19.3$, compared to the measured value of $\Delta\chi^2 = 32$ in the 2005 observed mean

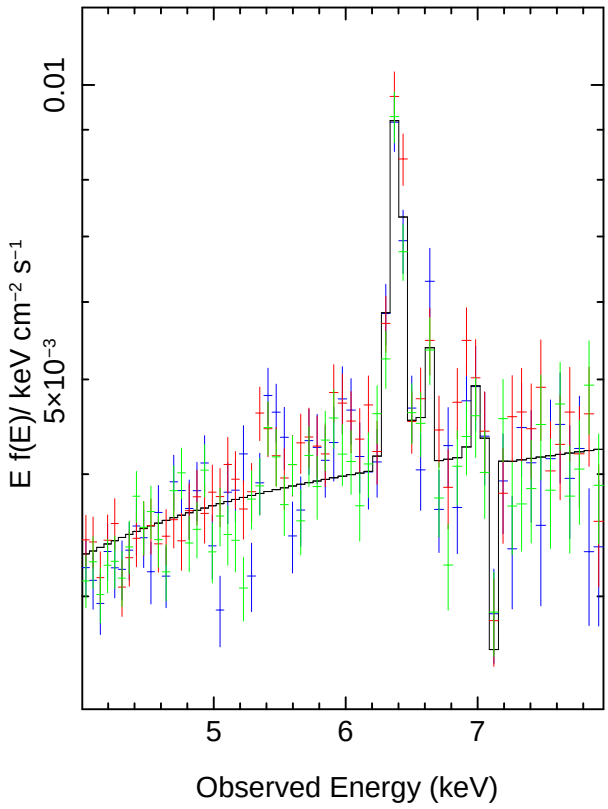

Figure 5.12: The three individual FI-XIS spectra from the 2005 *Suzaku* observation of NGC 4051 from 4–8 keV. The data are modelled with a simple absorbed power law. Note the data-to-model residuals at ∼5.4 keV apparent in the spectra of all three individual detectors.

spectrum. So, since no false line-detection was found at the same significance (or greater) than the observed detection in 3 000 simulated spectra, the probability of the emission line at 5.44 keV arising from a statistical fluctuation is found to be $p < 3.3 \times 10^{-4}$.

Finally, tests were performed to examine the nature of the variability of the two lines. The fits to mean spectra suggest that the line fluxes have remained constant over a three-year period with a variable equivalent width dependent upon the flux of the observed continuum. Indeed, fixing the flux of the two lines at the best-fitting values from the 2005 *Suzaku* data and re-fitting in the subsequent 2008 spectra results in a change in the fit statistic of $\Delta\chi^2 = 0$. To test this in a more robust fashion, the spectra were time-sliced and intensity-selected based

on count rate using the same criteria as described in Section 5.2.4. The results of fitting each spectrum are shown in Tables 5.8 and 5.9. As with the near-neutral Fe Kα emission line, the flux of the lines are observed to remain constant in time and independent of the source flux. The line at 5.44 keV also exists at the same energy throughout all three *Suzaku* observations. Furthermore, as the significance of the feature corresponds to $\Delta\chi^2 = 32$, $\Delta\chi^2 = 19$ and $\Delta\chi^2 = 19$ in the three respective mean *Suzaku* fits, the probability of all three detections being false is $p < 3 \times 10^{-11}$.

The variability test was also extended by including the *XMM-Newton* EPIC-pn data from 2001 and 2002 where the presence of the 5.44 keV line was found to be consistent with having the same flux as in the three *Suzaku* observations. An analysis of the *XMM-Newton* data was performed by de Marco et al. (2009) who also reported an excess of counts between 5.4–6.2 keV with a further hint of the weaker feature at $\sim$5.9 keV. NGC 4051 was also observed when the flux was very low with *BeppoSAX* (Guainazzi et al. 1998). Examining these data did not yield a significant detection with an upper limit on the flux of the line of $F_{\rm line} \lesssim 4 \times 10^{-5}$ photons cm^{-2} s^{-1}. Since the data did not allow for good constraints on the feature to be made (possibly owing to poor signal-to-noise), these data were not considered any further. Finally, combining the measured fluxes of the 5.44 keV line measured by *XMM-Newton* and *Suzaku* and sampled in flux (see Table 5.9) and comparing these data to a constant model yields $\chi^2/d.o.f. = 4.7/7$. The same test, but using the time-sliced data (see Table 5.8) yields an equally good fit. So, overall, there is strong evidence to suggest that the line is consistent with having a constant flux over the 7-year time-period considered and does not respond to changes in the continuum flux.

The possible origins of the two emission lines along with their relation to a perceived publication bias for such features in the literature are fully discussed in Section 5.3.3.

Observation	F_{2-10} [a]	$E_{5.4}$ [b]	$F_{5.4}$ [c]	$\mathrm{EW}_{5.4}$ [d]	$\Delta\chi^2$	$E_{5.9}$ [b]	$F_{5.9}$ [c]	$\mathrm{EW}_{5.9}$ [d]	$\Delta\chi^2$	$\chi^2/d.o.f.$
XMM 2001	2.31	$5.42^{+0.04}_{-0.04}$	< 4.1	< 110	0	$5.91^{+0.06}_{-0.06}$	< 5.2	< 96	0	108/99
XMM 2002	0.56	$5.39^{+0.04}_{-0.04}$	$2.5^{+1.9}_{-2.1}$	37^{+30}_{-30}	3	$5.90^{+0.06}_{-0.06}$	$4.1^{+1.4}_{-2.1}$	46^{+21}_{-20}	3	102/99
Suzaku 2005	0.87	$5.44^{+0.03}_{-0.03}$	$5.0^{+2.0}_{-2.0}$	46^{+16}_{-16}	32	$5.95^{+0.05}_{-0.05}$	$5.1^{+2.1}_{-2.0}$	44^{+17}_{-16}	22	100/99
Suzaku 2005: 1	1.01	$5.41^{+0.09}_{-0.08}$	$3.4^{+2.8}_{-2.8}$	23^{+19}_{-19}	4	$5.97^{+0.06}_{-0.06}$	$5.0^{+2.8}_{-2.8}$	40^{+22}_{-22}	9	94/99
Suzaku 2005: 2	0.88	$5.44^{+0.04}_{-0.04}$	$5.4^{+2.7}_{-2.7}$	41^{+21}_{-21}	10	$5.95^{+0.05}_{-0.05}$	$6.8^{+2.7}_{-2.7}$	62^{+25}_{-25}	16	82/99
Suzaku 2005: 3	0.82	$5.46^{+0.06}_{-0.05}$	$6.1^{+3.0}_{-3.1}$	44^{+22}_{-22}	11	$6.05^{+0.07}_{-0.07}$	$4.6^{+2.8}_{-2.9}$	39^{+24}_{-24}	7	115/99
Suzaku 2005: 4	0.78	$5.46^{+0.06}_{-0.06}$	$5.4^{+3.2}_{-3.2}$	41^{+24}_{-24}	8	$5.77^{+0.19}_{-0.08}$	< 6.1	< 54	2	102/99
Suzaku 2008a	2.42	$5.42^{+0.02}_{-0.01}$	$4.2^{+1.6}_{-1.6}$	13^{+5}_{-5}	19	$6.00^{+0.05}_{-0.05}$	$5.2^{+3.1}_{-3.0}$	20^{+10}_{-10}	8	112/99
Suzaku 2008a: 1	2.61	$5.38^{+0.07}_{-0.06}$	$6.3^{+3.9}_{-3.9}$	18^{+11}_{-11}	7	$5.89^{+0.10}_{-0.07}$	$4.4^{+3.7}_{-3.7}$	15^{+13}_{-13}	4	119/99
Suzaku 2008a: 2	2.90	$5.40^{+0.05}_{-0.05}$	< 5.8	< 14	0	$6.06^{+0.06}_{-0.06}$	$7.5^{+4.1}_{-4.0}$	24^{+13}_{-13}	9	112/99
Suzaku 2008a: 3	2.66	$5.46^{+0.08}_{-0.09}$	$7.2^{+4.2}_{-4.2}$	20^{+12}_{-12}	8	$6.11^{+0.08}_{-0.09}$	$5.5^{+4.0}_{-4.0}$	19^{+13}_{-13}	5	84/99
Suzaku 2008a: 4	2.29	$5.43^{+0.07}_{-0.05}$	< 6.9	< 23	2	$6.02^{+0.28}_{-0.11}$	< 7.4	< 29	3	117/99
Suzaku 2008a: 5	1.96	$5.44^{+0.04}_{-0.06}$	< 3.7	< 24	1	$5.89^{+0.08}_{-0.09}$	$4.6^{+3.6}_{-3.6}$	21^{+16}_{-16}	4	85/99
Suzaku 2008a: 6	2.10	$5.48^{+0.07}_{-0.07}$	$6.0^{+3.9}_{-3.9}$	22^{+14}_{-14}	7	$6.10^{+0.05}_{-0.05}$	$6.3^{+3.7}_{-3.7}$	27^{+16}_{-16}	8	114/99
Suzaku 2008b	1.79	$5.42^{+0.07}_{-0.06}$	$4.3^{+2.7}_{-3.0}$	17^{+12}_{-12}	19	$6.11^{+0.10}_{-0.08}$	$3.2^{+2.5}_{-2.7}$	16^{+12}_{-13}	4	115/99
Suzaku 2008b: 1	1.83	$5.58^{+0.12}_{-0.11}$	< 7.3	< 29	2	$6.12^{+0.06}_{-0.06}$	$4.0^{+3.6}_{-3.6}$	19^{+17}_{-17}	3	109/99
Suzaku 2008b: 2	1.73	$5.38^{+0.07}_{-0.11}$	$4.5^{+3.6}_{-3.6}$	20^{+16}_{-16}	4	$5.78^{+0.06}_{-0.06}$	< 6.23	< 32	2	111/99

Table 5.8: The best-fitting parameters of the two emission lines at ∼5.4 and ∼5.9 keV in time-sliced NGC 4051 data. The 2005, 2008a and 2008b spectra are split into 55 ks, 80 ks and 80 ks segments respectively and all spectral fitting took place in the 3–10 keV energy band. Errors are quoted at the 1σ level. [a]Flux from 2–10 keV in units $\times 10^{-11}\,\mathrm{erg\,cm^{-2}\,s^{1}}$; [b]Line energy in units keV; [c]Line flux in units $\times 10^{-6}\,\mathrm{photons\,cm^{-2}\,s^{-1}}$; [d]Equivalent width in units eV.

Observation	F_{2-10} [a]	$E_{5.4}$ [b]	$F_{5.4}$ [c]	$\mathrm{EW}_{5.4}$ [d]	$\Delta\chi^2$	$E_{5.9}$ [b]	$F_{5.9}$ [c]	$\mathrm{EW}_{5.9}$ [d]	$\Delta\chi^2$	$\chi^2/d.o.f.$
XMM 2001	2.31	$5.42^{+0.04}_{-0.04}$	< 4.1	< 110	0	$5.91^{+0.06}_{-0.06}$	< 5.2	< 96	0	108/99
XMM 2002	0.56	$5.39^{+0.04}_{-0.04}$	$2.5^{+1.9}_{-2.1}$	37^{+30}_{-30}	3	$5.90^{+0.06}_{-0.06}$	$4.1^{+1.4}_{-2.1}$	46^{+21}_{-20}	3	102/99
Suzaku 2005	0.87	$5.44^{+0.03}_{-0.03}$	$5.0^{+2.0}_{-2.0}$	46^{+16}_{-16}	32	$5.95^{+0.05}_{-0.05}$	$5.1^{+2.1}_{-2.0}$	44^{+17}_{-16}	22	100/99
Suzaku 2005 Low	0.70	$5.46^{+0.04}_{-0.04}$	$5.2^{+1.6}_{-1.6}$	46^{+14}_{-14}	27	$5.97^{+0.08}_{-0.07}$	$3.7^{+1.6}_{-1.6}$	39^{+16}_{-17}	15	92/99
Suzaku 2005 High	1.26	$5.44^{+0.05}_{-0.04}$	$4.8^{+2.9}_{-2.9}$	26^{+15}_{-15}	8	$5.96^{+0.04}_{-0.05}$	$7.8^{+2.8}_{-2.8}$	50^{+18}_{-18}	21	115/99
Suzaku 2008a	2.42	$5.42^{+0.02}_{-0.01}$	$4.2^{+1.6}_{-1.6}$	13^{+5}_{-5}	19	$6.00^{+0.05}_{-0.05}$	$5.2^{+3.1}_{-3.0}$	20^{+10}_{-10}	8	112/99
Suzaku 2008a Low	1.76	$5.30^{+0.36}_{-0.09}$	$2.4^{+2.0}_{-2.0}$	10^{+8}_{-8}	4	$5.92^{+0.06}_{-0.05}$	$5.3^{+2.0}_{-2.0}$	26^{+10}_{-10}	19	116/99
Suzaku 2008a Med.	2.75	$5.48^{+0.06}_{-0.06}$	$5.8^{+2.9}_{-2.9}$	16^{+8}_{-8}	11	$6.06^{+0.06}_{-0.06}$	$5.2^{+2.8}_{-2.8}$	17^{+9}_{-9}	10	107/99
Suzaku 2008a High	3.89	$5.40^{+0.08}_{-0.10}$	$6.8^{+5.1}_{-5.1}$	14^{+10}_{-10}	5	$6.07^{+0.15}_{-0.10}$	$7.8^{+4.9}_{-4.9}$	19^{+12}_{-12}	7	107/99
Suzaku 2008b	1.79	$5.42^{+0.07}_{-0.06}$	$4.3^{+2.7}_{-3.0}$	17^{+12}_{-12}	19	$6.11^{+0.10}_{-0.08}$	$3.2^{+2.5}_{-2.7}$	16^{+12}_{-13}	4	115/99

Table 5.9: The best-fitting parameters of the two emission lines at ∼5.4 and ∼5.9 keV in flux-selected NGC 4051 data. The 2005 data were intensity-selected based on a count rate of $0.47\,\mathrm{cts\,s^{-1}}$ and the 2008a data were intensity-selected based on count rates of $<2.0\,\mathrm{cts\,s^{-1}}$, 2.0–$3.0\,\mathrm{cts\,s^{-1}}$ and $>3.0\,\mathrm{cts\,s^{-1}}$. All spectral fitting took place in the 3–10 keV energy band. Errors are quoted at the 1σ level. [a]Flux from 2–10 keV in units $\times10^{-11}\,\mathrm{erg\,cm^{-2}\,s^{1}}$; [b]Line energy in units keV; [c]Line flux in units $\times10^{-6}\,\mathrm{photons\,cm^{-2}\,s^{-1}}$; [d]Equivalent width in units eV.

5.3 Discussion

5.3.1 Spectral Variability and Reverberation Time Delays

Despite the observations being made years apart and having used different observatories and methods, the results of the timing analysis of Miller et al. (2010b) with *Suzaku* are remarkably similar to those of McHardy et al. (2004) with *XMM-Newton* and *RXTE*. Both studies found NGC 4051 to be more variable at low energies than high energies and that the PSD is dependent upon photon energy with the high-energy PSD appearing much flatter. The enhanced variability at low energies was also spectroscopically demonstrated in Figure 5.8 where the flux at energies $\lesssim 5\,\mathrm{keV}$ can be seen to vary more than the harder X-ray flux $> 10\,\mathrm{keV}$. Furthermore, both studies revealed that the power spectrum shows a sharp break at $\sim 10^{-4}\,\mathrm{Hz}$ and they also detected the presence of frequency-dependent time lags where the hard band lags the soft band with the lag increasing with the difference in energy between the two bands and the period. The studies differ in the sense that McHardy et al. (2004) find that the lags continue to increase with period whereas Miller et al. (2010b) find that the longest period point is consistent with zero lag (albeit with large uncertainties). However, this may be due to the long baseline afforded by the 6-year *RXTE* monitoring campaign included by McHardy et al. (2004). Also, Miller et al. (2010b) find that the PSDs significantly differ between the 2005 and 2008 *Suzaku* observations at the 3σ level.

As mentioned in Section 5.2.1.2, a model has been proposed whereby frequency-dependent time lags in AGN are caused by perturbations propagating inwards on an accretion disc with the harder X-ray emission originating from smaller radii (Arévalo & Uttley 2006). This was then modified with a more complex relationship between time-lag and period being interpreted as arising from multiple zones of propagating fluctuations (McHardy et al. 2007). Miller et al. (2010b) instead state that although a model of propagating fluctuations cannot be ruled out in NGC 4051, a reverberation model (Peterson 1993) may instead explain the observed variations. At optical wavelengths, reverberation has become a powerful technique for estimating the size of the BLR by combining time delays between the response of an emission line to changes in the continuum with the observed line velocity widths. However,

at X-ray wavelengths, it is not possible to construct a time series based solely on emission line fluxes since the count rates are insufficiently small to probe the rapid variability without the line flux values becoming dominated by uncertainties in the Poisson distribution (i.e. shot noise). Instead, if nearby circumnuclear material is present then this will Compton-scatter the incident flux and, if the material is moderately ionised, the strong energy dependence of the absorption opacity means that higher energy photons will be scattered more efficiently than lower energy photons, which will mostly be absorbed.

Therefore, the effects of reverberation can be searched for by cross-correlating hard and soft energy bands with an expected time delay between the hard and soft bands. If the circumnuclear material only partially covers the central source, one can consider the case where direct light is observed in one time series and scattered light is observed in another. Such a model has been tested on NLS1s such as Mrk 766 (Miller et al. 2007) and 1H 0707-495 (Miller et al. 2010a). In the case of NGC 4051, Miller et al. (2010b) investigated a reverberation model to explain the observed time lags since they can be directly related to the PCA results. Indeed, if the hard constant offset component observed in the PCA of NGC 4051 has a significant contribution from reflection, this may result in the observed time delays. Miller et al. (2010b) show that in the reverberation model, the fact that the observed time lags increase with the difference between the two energy bands implies that the fraction of reflected light increases with increasing energy where the fall-off to low energy is a consequence of scattering in a medium in which the opacity increases with decreasing energy (e.g. Ross & Fabian 2005). The reverberation model is consistent with the spectroscopic evidence for high columns of absorbing and reflecting material presented in Sections 4.4.1 and 5.2.3.1.

Miller et al. (2010b) suggest that the large difference between the 2005 and 2008 *Suzaku* spectra may be explained by obscuring material blocking our line-of-sight so that the 2005 spectrum is dominated by distant reflection; an idea proposed for this source by Pounds et al. (2004a). This is supported by the *Suzaku* model presented in Section 5.2.3.2 where the flux of the intrinsic power law is found to be much lower in 2005 relative to the reflection component, in agreement with a reflection-dominated scenario (also see Table 5.4). An invariant reflection component was also proposed for this source by Guainazzi et al. (1998) and Terashima et al.

(2009) where they suggested that its constant nature could arise from light travel-time effects. However, this requirement may be relaxed if material obscuring the central source is instead responsible. Miller et al. (2010b) suggest that this may explain the difference between the two PSDs (Figure 5.3) since any rapid variations may be erased by reflection travel-time delays in the case where our view of the central source is blocked, thus resulting in the steeper cut-off to high frequencies in the 2005 PSD. So it may be the case that in more extreme cases (e.g. 2005), almost entirely scattered light is observed and so the high-frequency power may get averaged out. However, in a less extreme case, where the direct light is still seen, but absorbed, the PSD may not necessarily be expected to vary.

In Section 5.2.3.2 it was noted that, despite being less variable than at lower energies, the hard X-ray flux did increase in 2008 when the source brightened overall. This is maybe due to the variable component of ionised reflection required in the broad-band *Suzaku* model as shown in Table 5.4 and is consistent with eigenvector one of the PCA (see Figure 5.1). Miller et al. (2010b) suggest that this could be explained in one of two ways. Firstly, if the variable component of the hard excess arises from reflection and, if the 2005 low-flux spectrum was indeed due to obscuration, then the variable reflection component may have been obscured along our line-of-sight too, consistent with the partial-covering model of Terashima et al. (2009). Since there is evidence for a moderately broad component of Fe Kα emission (as required from modelling the *Chandra* HETG spectrum; see Section 4.4.2) that varies with the variable continuum, these components would need to originate closer in than the relatively invariant narrow component of Fe Kα emission from more distant material (also required by the *Chandra* HETG and *Suzaku* spectra; see Sections 4.4.2 and 5.2.4 respectively) and so could conceivably be obscured in this way. Alternatively, changes in the column density of some partially-covering absorber could be responsible since it may have allowed transmission at higher energies to produce the observed spectrum in 2008 (e.g. similar to the case of PDS 456; Reeves et al. 2009). Both possibilities require reflecting and absorbing material to exist over a wide range of radii and for the hard excess to be partially obscured in 2005 and possibly in 2008 too. In either case, Miller et al. (2010b) find no requirement for any inner-disc reflection since the large time lags suggest that the reflecting material must be more distant (e.g. $\sim 10^2\, r_{\rm g}$).

Regarding the variable, moderately broadened Fe Kα emission component observed with the *Chandra* HETG (as shown in Section 4.4.2) and in eigenvector one of the PCA of NGC 4051, it has a measured equivalent width of $\sim$60 eV against the observed continuum, which may correspond to $\sim$150 eV against the reflected continuum in the reverberation model (Miller et al. 2010b). This is much smaller than what would be expected for reflection from neutral material where equivalent widths on the order of 1 keV are predicted (George & Fabian 1991). However, Miller et al. (2010b) state that in the environment close to the primary X-ray continuum, the material is expected to be more highly ionised and, as such, this equivalent width appears reasonable if produced via reflection in ionised material where $\xi \gtrsim 100\,\mathrm{erg\,cm\,s^{-1}}$ (Ross & Fabian 2005)[2].

Finally, Miller et al. (2010b) state that, since the frequency- and energy-dependence of the observed time lags suggest reverberation from reflecting material, the required high fraction of reflected light ($\sim$80% at energies >6 keV) indicates a high global covering factor. They calculated the reverberating zone to be within a few light-hours of the central source and that, while obscuring and reflecting material may exist at larger radii, longer timescales would need to be probed for such signatures to appear in the time lags. They conclude that the time delays are well described by reverberation from material up to a few light-hours away from the central source and with a high global covering factor of $\gtrsim$ 40%.

The spectroscopic evidence presented in Chapters 4 and 5 help to confirm that the reverberation model of Miller et al. (2010b) provides a viable interpretation of the variability displayed by NGC 4051. In Sections 4.3 and 4.4.1, evidence was presented for discrete absorption features indicative of significant columns of absorbing gas. Furthermore, the broad-band *Suzaku* spectra analysed in Sections 5.2.3.1 and 5.2.3.2 show that significant reflectors also exist in this source. The spectral requirement for an additional zone of partially-covering gas and the ability of this model to account for the spectral shape in both 2005 and 2008 strongly supports the idea that NGC 4051 is surrounded by substantial amounts of circumnuclear material. This compliments the analysis of Miller et al. (2010b) providing

[2]It should be noted that in order to accurately model this scenario, the effects of Compton scattering and resonant absorption / line destruction in a hot medium would need to be taken into account (e.g. Matt, Fabian & Reynolds 1997).

robust evidence for the existence of high columns of optically-thick material with high covering factors lying within a few light-hours from the central source with the reverberating material extending up to a few hundred r_g from the central engine. However, the short-term variations (i.e. perhaps on timescales of less than a few ks) are most likely caused by a more compact intrinsic mechanism.

5.3.2 The Nature of the Long-Term Spectral Variability

NGC 4051 is found to be highly variable on both short- (ks) and long-term (months-to-years) timescales with the spectral trend being that the X-ray spectrum flattens above a few keV as the source flux drops. Occasionally NGC 4051 is found to fall into an extended period of low flux (e.g. Uttley et al. 1999) revealing a very hard X-ray spectrum. The general consensus is that the primary power law disappears from view as the flux drops leaving the remaining emission dominated by a hard reflection component (e.g. Guainazzi et al. 1998; Pounds et al. 2004a). Such a period of low flux was observed in 2005 by Terashima et al. (2009) when a very strong hard excess was observed at energies >10 keV which, if modelled with neutral reflection (i.e. a PEXRAV component), returns a value of $R \sim 7$ (where $R = 1$ corresponds to reflection from a semi-infinite slab). This is also apparent in Table 5.4 where it can be seen that the 0.5–100 keV flux of the reflector is significantly higher than that of the intrinsic power law in the 2005 *Suzaku* data. However, the excess could not be accounted for by reflection alone due to the relatively weak Fe Kα emission component (EW $\sim$ 140 eV). Instead, Terashima et al. (2009) were able to model the broad-band spectra by introducing a partially-covered power-law component which gives rise to the hard spectral shape. This allows for a variable soft power-law component superimposed on an almost constant hard component, dominated by reflection; a hypothesis supported spectroscopically by the presence of an absorbed reflector in the *Suzaku* spectra, by the PCA of Miller et al. (2010b) and, to some extent, by the flux-flux analysis in Section 5.2.2.

In Section 5.2.3.1, the broad-band 2008 *Suzaku* data were successfully modelled with a model consisting of an intrinsic power-law component, a partial-coverer, near-neutral and ionised reflection, ionised (outflowing) absorption from a variety of ionisation states and

several soft X-ray photo-ionised emission lines. This model accounts for the spectral curvature well with the partial-coverer having a low covering fraction of ∼30%. An attempt was then made to simultaneously fit all three broad-band *Suzaku* spectra from 2005 and 2008 using the same model (see Section 5.2.3.2). It was found that the long-term spectral variability can be accounted for primarily by changes in the normalisation of the intrinsic (unabsorbed) power law. This indicates that the covering fraction has changed between observations (where $f_{\rm cov}$ is given by the ratio between the absorbed and total power-law components). However, since the absorbed power law remains constant, the spectral variability cannot be accounted for by simple changes in the covering fraction of this Compton-thin ($N_{\rm H} \sim 10^{23}\,{\rm cm}^{-2}$) partial-coverer alone. If this were the case, then the total flux (intrinsic + absorbed) would not vary. However, since direct changes in the covering fraction are observed between observations, the spectral variability cannot be accounted for by intrinsic changes in the luminosity of the source alone either. Therefore, either the covering fraction of the Compton-thin partial-coverer and the luminosity of the source are inversely correlated or the long-timescale changes in L are not intrinsic.

If the covering fraction and luminosity are inversely correlated, one possible cause of this could be that the hot corona above the disc may be varying in area. This could have the effect of concentrating the continuum emission from a smaller region, therefore increasing the proportion which is absorbed by the partial-coverer and lowering the luminosity, such as is observed in the 2005 data.

Alternatively, if the observed changes in L are not intrinsic, then another possible reason for the observed changes in the flux of the intrinsic power law could be due to the intrinsic continuum emission disappearing from view as the covering fraction of a further Compton-thick, variable partial-coverer increases therefore resulting in an apparent drop in continuum flux. Thus, this leaves behind a constant, hard, reflection component which then dominates the spectrum at low fluxes leading to the spectral trend observed by Guainazzi et al. (1998) and Pounds et al. (2004a). If the proposed Compton-thick clouds form part of the same system as the more distant Compton-thin clouds, this could explain the correlation with the line-of-sight covering fraction of the Compton-thin partial-coverer (i.e. as $f_{\rm cov-thick}$ increases, $f_{\rm cov-thin}$ increases too). Such an interpretation of accounting for spectral variability

by allowing for changes in the covering fraction of an absorbing layer of gas has also been used as a solution to several other well-studied AGN (e.g. 1H 0419-577, Pounds et al. (2004b); NGC 1365, Risaliti et al. (2007); MCG–6-30-15, Miller, Turner & Reeves (2008); NGC 3516, Turner et al. (2008)).

The flux of the narrow, unresolved Fe Kα component is observed to remain constant between the 2005 and 2008 *Suzaku* observations (see Table 5.4) with the equivalent width of the line decreasing against the observed continuum as the flux level of the continuum increases (see Table 5.5). Furthermore, the flux of the narrow component has remained steady to within a factor of 2 since 1998 (spanning a baseline greater than a decade; Terashima et al. 2009; also see Table 5.6) and it is also observed to be invariant in the PCA of Miller et al. (2010b); see Figure 5.1, despite large apparent changes in the continuum flux. The constancy of the flux of this component over long-term timescales may then imply that the near-neutral Fe Kα emission does not respond to apparent changes in the continuum level and so perhaps originates in very distant material. However, this would require a radius $\gtrsim$ 10 light-years from the central source which well exceeds the $\sim$15–20 light-day dust sublimation radius of NGC 4051 (and the NLR radius; Krongold et al. 2007). So it does not appear possible to explain this away as a light-travel-time effect in such a compact system since a response to the continuum would be expected to be observed on timescales $>$ week. A more likely scenario is that the distribution of the absorbing clouds ($\ll$ pc-scale) is clumpy. In this case, the observed continuum level $\lesssim 10\,\mathrm{keV}$ falls as the line-of-sight covering fraction of the gas increases (and vice-versa) whereas the distant neutral reflection component and associated narrow Fe Kα line remain constant in flux since, at that radial location (e.g. the torus), and assuming that the global covering fraction (across all sight-lines) of the clumpy absorber is unchanged, the mean continuum flux remains invariant when integrated over all solid angles. The variations caused by the short-term flickering of the source (e.g. ks timescales) are then smeared out at this distant location. The highly-ionised outflow detected in the Fe K band may then be the high-velocity signature of such a clumpy accretion-disc wind.

In addition to the near-neutral Fe Kα emission from distant material, evidence is also found for a weak, broader component to the Kα emission in the HETG spectrum, as described in Section 4.4.2. Taking the FWHM of $16\,000^{+7\,000}_{-4\,000}\,\mathrm{km\,s^{-1}}$ (i.e. $\sigma \sim 8\,000\,\mathrm{km\,s^{-1}}$) of this

broad Fe Kα component from the HETG data allows an estimate of the radius from the central engine of the emitting material to be calculated assuming simple Keplerian motion. This yields an estimate of the radius of $R \sim 1 - 2 \times 10^3\, r_{\rm g}$ where $r_{\rm g} = GM/c^2$. Taking the value of $1.73 \times 10^6\, {\rm M}_{\odot}$ for the mass of the black hole calculated by Denney et al. (2009), this corresponds to a value of $R \sim 0.1$ light-days from the central source. This is largely consistent with the findings of Miller et al. (2010b) who find evidence of a weak variable hard excess at energies >20 keV with an associated weak, moderately broadened Fe Kα component which could respond to changes in the continuum on a 20 ks timescale. This may be related to the ionised reflector which is seen to vary somewhat in the *Suzaku* data (see Table 5.4) and may be associated with reflection occurring off the outer disc or off a disc wind similar to those calculated by Sim et al. (2010). The time lags found by Miller et al. (2010b) between the hard and soft bands, which are well described by reverberation from material a few light-hours away from the illuminating source, help to confirm the idea that NGC 4051 has a substantial amount of optically-thick material within a few $100\, r_{\rm g}$ from the central source and is again supportive of a partial-covering solution to account for the long-term spectral variability.

5.3.3 The Origin of the Line-Emission in the 5–6 keV Band

In Section 5.2.4.1, the significant detection of a narrow emission line at 5.44 keV was reported along with a more tentative detection of an additional line at ∼5.9 keV. The lines are largely constant in flux over a seven-year period strongly suggesting that they do not respond to the continuum (see Tables 5.8 and 5.9).

There have been numerous claims in the literature of the detection of various transient emission lines at unexpected energies. Such examples include NGC 7314 with a detection at 5.84 keV (Yaqoob et al. 2003), Mrk 335 with a line at 5.92 keV (Longinotti et al. 2007) and NGC 3516 (Turner et al. 2002) where narrow lines were discovered at 5.57 keV and 6.22 keV. In the latter case, the lines were concluded to be the signature of highly redshifted Fe perhaps originating in the accretion disc or an outflow such as an accretion-disc wind where material is viewed on the far side of the black hole (Turner, Kraemer & Reeves 2004). However, the significance of these features has been questioned by some. With a selection criteria of

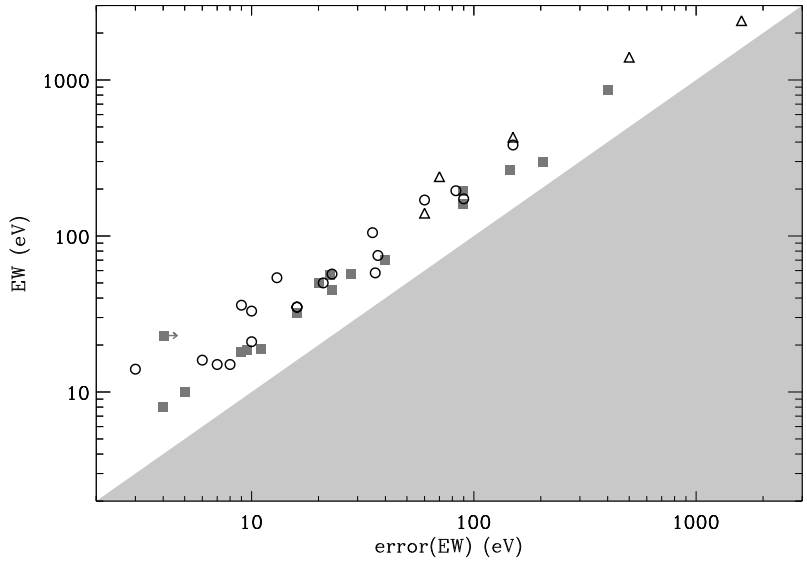

Figure 5.13: Plot taken from Vaughan & Uttley (2008) showing the relationship between the measured equivalent widths and associated errors of narrow, redshifted iron lines claimed in the literature. The shaded region indicates the zone in which a feature would not be reported as being detected; i.e. the measured value is less than its error. The open circles represent absorption lines, the filled squares represent emission lines and the open triangles represent absorption systems from lensed broad absorption-line quasars.

selecting lines with reported energy shifts of $v \geq 0.05c$ in the 1.5–20 keV band of Seyfert and quasar spectra, Vaughan & Uttley (2008) reviewed 38 claims of such narrow features in the literature. They found that the strength of the feature (i.e. its equivalent width) scales linearly with its uncertainty (see Figure 5.13, taken from Vaughan & Uttley 2008). The tight relationship in the EW/uncertainty plane demonstrates that weaker features are found to show up in better quality data whereas if the features are real, the stronger lines should be expected to show up in a well-constrained way with improved signal-to-noise. They state that there may be a high number of false detections (i.e. statistical fluctuations) in the literature and suggest that a publication bias may exist whereby only the strongest fluctuations are reported.

However, the issue has been addressed since such features have been observed multiple times in the same sources, e.g. NGC 3516 (Turner et al. 2002, Bianchi et al. 2004, Iwasawa, Miniutti & Fabian 2004) and NGC 4051 where the line at 5.44 keV was found to be consistent in flux in various *Suzaku* and *XMM-Newton* observations as shown in Section 5.2.4.1. Furthermore, the probability of the line arising from a statistical fluctuation was assessed through Monte Carlo simulations in NGC 4051 (also see Yaqoob & Serlemitsos 2005) and found to be very low ($p < 3.3 \times 10^{-4}$). Tombesi et al. (2010) performed a systematic analysis of a large sample of AGN, investigating the reality of energy-shifted absorption lines. They find a deviation from the relationship between the strength of a feature and its uncertainty reported by Vaughan & Uttley (2008) since they discovered more highly significant detections in their sample. They state that the absence of well-constrained features in the literature may, to some extent, arise from the ability of current X-ray missions to detect such features. A systematic study was also undertaken by de Marco et al. (2009) of a sample of 72 bright, type-1 Seyferts with *XMM-Newton* in the 4–9 keV energy range, increasing the number of detections of narrow, variable emission lines and confirming the reality of many previous claims in the literature.

5.3.3.1 An Origin in a Disc Hotspot

One interpretation is that the redshifted lines are actually the signature of a "hotspot" of Fe on the accretion disc surface where emission is enhanced perhaps due to events such as magnetic reconnection and forms an annulus due to a long exposure (i.e. sampled over many disc orbits). The profile of the line is then modified by Doppler and gravitational effects depending on the observer's line-of-sight and the radial location of the emitting material. In the non-relativistic case, each radius of the disc produces double-peaked emission lines as radiation approaching the observer is blueshifted whereas radiation moving away from the observer becomes redshifted. However, this requires a significant velocity component along the line-of-sight and so it is important that the emitting gas is viewed not too close to the polar axis. In the inner regions of the disc (e.g. at a radial location of, say, within $20\,r_{\rm g}$), both general and special relativistic effects become important. The observed centroid energy

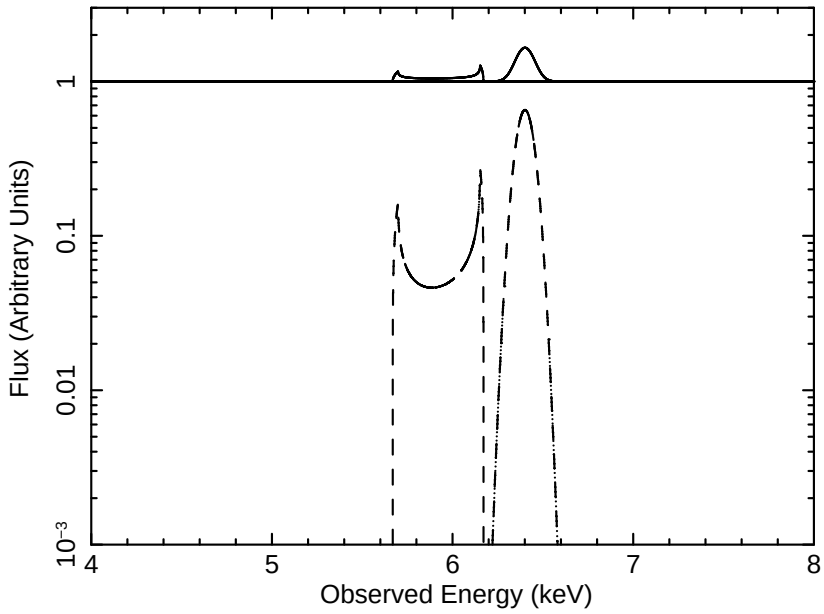

Figure 5.14: The DISKLINE model of Fabian et al. (1989). The line is assumed to originate from near-neutral Fe Kα at 6.4 keV and the double-horned profile at a redshifted energy arises from a combination of transverse Doppler effects and gravitational redshift. The model was simulated from an annulus $20\,r_{\rm g}$ from the black hole with a width of $\Delta r = 1\,r_{\rm g}$ and an observed inclination angle of 10°. For comparison, a standard symmetric Gaussian is also shown at 6.4 keV with an intrinsic width of $\sigma = 50$ eV.

of the peaks can be shifted red-ward as the photons give up energy to escape the strong potential well of the black hole and special relativistic beaming (i.e. Doppler boosting) can enhance the blue peak, thus giving rise to the broad, skewed profile shown in Figure 5.14. Confirmation of such an origin in the disc for such features would be useful since it would then allow parameters such as the emitting radius and the inclination angle of the system to be derived.

A test was performed to see if a disc hotspot model could explain the peak at 5.44 keV observed in NGC 4051. The Gaussians modelling the lines at ∼5.4 and ∼5.9 keV were removed from the model and replaced with a single DISKLINE component from a narrow annulus (Fabian et al. 1989). The DISKLINE component and its parameters are described in Section 2.5.1. The assumptions made were that the black hole is non-rotating, the emission

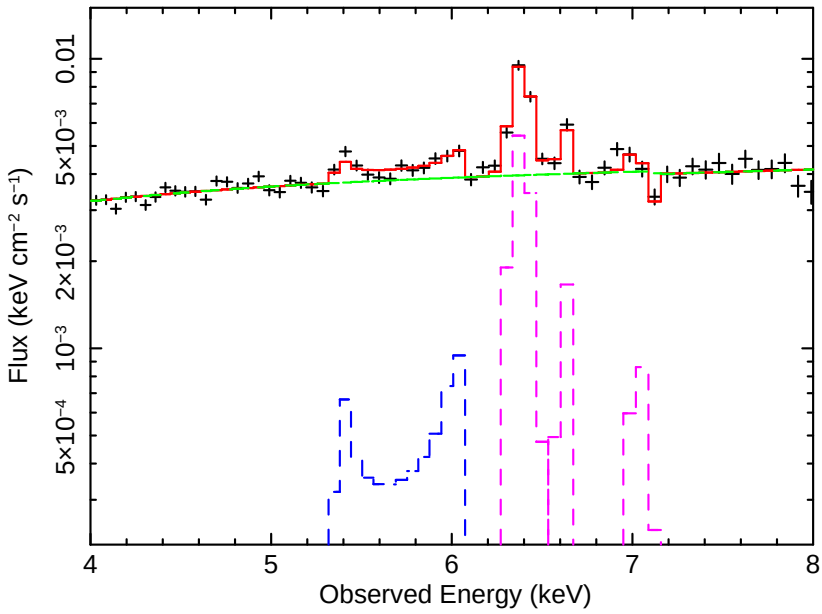

Figure 5.15: The DISKLINE component (Fabian et al. 1989) used to model the emission at ∼5.4 and ∼5.9 keV in the 2005 *Suzaku* data for NGC 4051 over the 4–8 keV energy range. The DISKLINE component has a best-fitting radius of $14 \pm 1\,r_{\rm g}$ and an inclination angle of $12 \pm 2\,^{\circ}$ for an annulus width of $\Delta r = 1\,r_{\rm g}$. The DISKLINE component is shown in navy blue and additional emission from Fe K is parameterised by Gaussians and shown in magenta.

is from near-neutral Fe Kα (by fixing the rest-energy of the line at 6.4 keV) and that the hotspot exists with a narrow annulus ($\Delta r = 1\,r_{\rm g}$). The free parameters were then the inner radius of the annulus (with the outer radius of the annulus fixed to be equal to $r_{\rm in} + 1$), the inclination angle and the normalisation. Note that the emissivity pattern across the disc was left fixed at the default value of $q = 2$ (where the pattern can be described by r^{-q}) since the influence of this parameter is negligible when considering a narrow annulus. A plot of this model is shown in Figure 5.15.

To account for the peaks at both ∼5.4 and ∼5.9 keV requires that the disc annulus exists at a radius of $14 \pm 1\,r_{\rm g}$ from the black hole and, since the blue extent of the line is a strong function of disc-inclination, it requires that the system is viewed at an angle of $12 \pm 2\,^{\circ}$ to the plane of the disc. Interestingly, this could perhaps go some way as to explaining the

observed narrow Fe and optical Hβ lines in this source. This model corresponds to a fit statistic of $\chi^2/d.o.f. = 119/95$ over the 3–8 keV energy range. At such a radial location, the orbital timescale is $t_{\rm orb} \sim 2$ ks (for a given black hole mass) and so would suggest that the emitting region is stable over many orbits. Note that allowing the emission to originate from a wider annulus does not significantly improve the fit statistic ($\Delta\chi^2 < 1$) with the best-fitting values for the radius and inclination angle consistent within the errors (i.e. $r_{\rm in} = 14^{+1}_{-2}\, r_{\rm g}$; $r_{\rm out} = 15^{+3}_{-2}\, r_{\rm g}$; inclination $= 11 \pm 1\,^\circ$).

The line at 5.44 keV can also be accounted for by allowing the DISKLINE component to model the blue peak at 6.62 keV (instead of emission from Fe XXV), as shown in Figure 5.16. This instead requires an emitting radius of $21 \pm 3\, r_{\rm g}$ and an inclination angle for the system of $21^{+1}_{-3}\,^\circ$. The fit, however, is slightly worse with $\chi^2/d.o.f. = 128/97$. As above, allowing the annulus width to vary does not significantly improve the fit ($\Delta\chi^2 < 1$) with the best-fitting values unchanged within the errors ($r_{\rm in} = 20^{+3}_{-2}\, r_{\rm g}$; $r_{\rm out} = 22^{+4}_{-2}\, r_{\rm g}$; inclination $= 20 \pm 2\,^\circ$). Furthermore, while there is evidence for line emission from 6.5–7 keV, this is normally due to ionised species of Fe and so some ambiguity remains over the nature of this particular solution.

The effects of a rotating black hole were also investigated by replacing the DISKLINE component with the LAOR model which describes the emission effects in a Kerr geometry (Laor 1991). This is shown in Figure 5.17. The parameters of the model are the same as those for the DISKLINE model except that the inner radius can be set as low as $1.24\, r_{\rm g}$ (the smallest radius of the ISCO around a Kerr black hole). In the case of a fixed narrow annulus ($\Delta r = 1\, r_{\rm g}$), the best-fitting parameters are similar to those found with the DISKLINE component: $r_{\rm in} = 13^{+3}_{-1}\, r_{\rm g}$ and inclination $= 14 \pm 2\,^\circ$ for the case where the blue peak models emission at $\sim$5.9 keV and $r_{\rm in} = 21^{+4}_{-2}\, r_{\rm g}$ and inclination $= 25^{+3}_{-4}\,^\circ$ for the case where the blue peak models emission at $\sim$6.6 keV (having removed the line modelling emission from Fe XXV). However, the two fits are slightly worse than when modelled with a DISKLINE component yielding $\chi^2/d.o.f. = 123/95$ and $\chi^2/d.o.f. = 134/97$ for the two fits respectively. Once again, allowing the emission to originate from a wider annulus does not improve the fit.

In the disc-hotspot model, if the hotspot co-rotates with the disc and is observed away from the polar axis (i.e. non-face-on), the line profile should show periodic patterns in

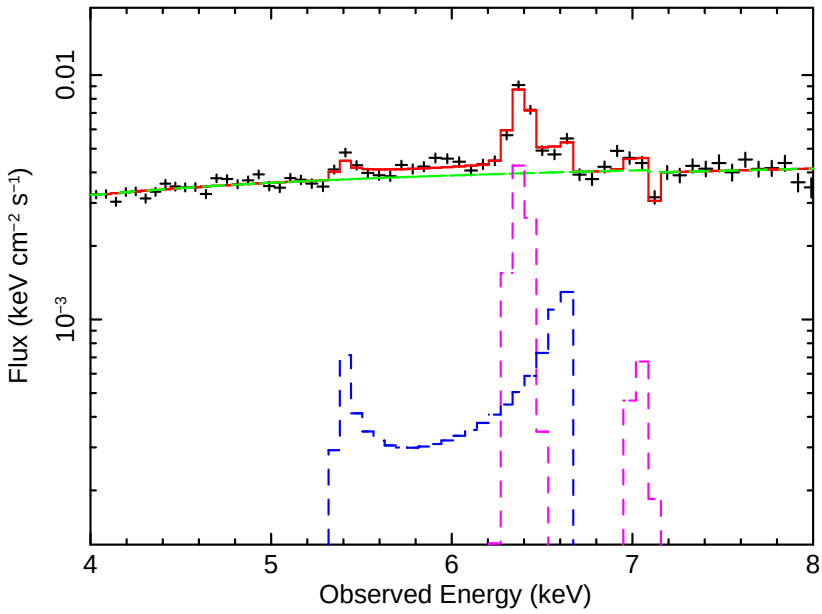

Figure 5.16: The DISKLINE component (Fabian et al. 1989) used to model the emission at ∼5.4 and ∼6.6 keV in the 2005 *Suzaku* data for NGC 4051 over the 4–8 keV energy range. The DISKLINE component has a best-fitting radius of $21^{+1}_{-3}\,r_{\rm g}$ and an inclination angle of $21^{+1}_{-3}\,^{\circ}$. An annulus width of $\Delta r = 1\,r_{\rm g}$ is assumed. The DISKLINE component is shown in navy blue and additional emission from Fe K is parameterised by Gaussians and shown in magenta.

energy and strength as a function of time. The profile should evolve distinctly and be phase-dependent with the azimuthal angle around the disc. Also, if the hotspot originates within $\sim 20\,r_{\rm g}$ from the black hole (where general relativistic effects are predicted to be measurable with current X-ray instruments), then the energy of the line peak should gradually show a shift to lower energies as the material spirals inwards[3] (Dovčiak et al. 2004; although with further complications due to the aberration and bending of light arising from the close proximity to the black hole). Such a profile could be confirmed, in principle, using time-resolved spectroscopy. However, in order to measure line evolution in azimuthally-selected time-slices without integrating for too long so that the variations become averaged out requires high

[3]The radial drift timescale is estimated to be on the order of weeks to months for NGC 4051 (Frank, King & Raine 2002).

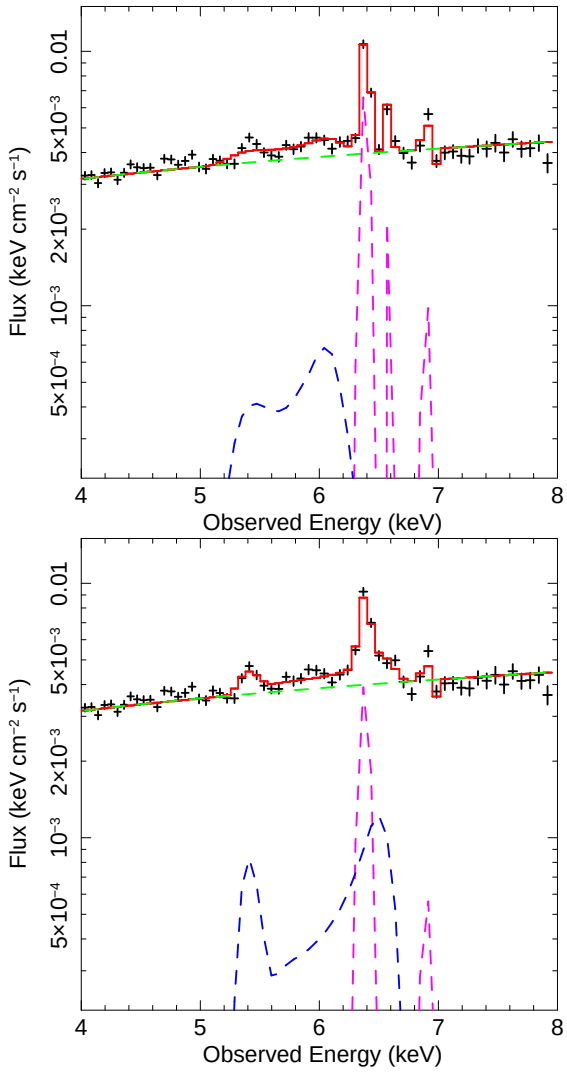

Figure 5.17: Upper panel: the LAOR component (Laor 1991) used to model the emission at ∼5.4 and ∼5.9 keV in the 2005 *Suzaku* data for NGC 4051 over the 4–8 keV energy range. The LAOR component has a best-fitting radius of $13^{+3}_{-1}\,r_{\rm g}$ and an inclination angle of $14 \pm 2\,^{\circ}$. An annulus width of $\Delta r = 1\,r_{\rm g}$ is assumed. The LAOR component is shown in navy blue and additional emission from Fe K is parameterised by Gaussians and shown in magenta. Lower panel: the LAOR component (Laor 1991) used to model the emission at ∼5.4 and ∼6.6 keV with a best-fitting radius of $21^{+4}_{-2}\,r_{\rm g}$ and an inclination angle of $25^{+3}_{-4}\,^{\circ}$.

signal-to-noise, yet few observations to date have sufficient duration, source brightness and the significant detection of such a variable feature to enable such a confident test to be performed (Turner & Miller 2010). Periodic flux variability for a line was claimed by Iwasawa, Miniutti & Fabian (2004) in the case of NGC 3516 but the evidence is tentative since it was only observed over three cycles of repetition.

At small radii, hotspots are not expected to survive for much longer than a few times the orbital timescale (Karas, Martocchia & Subr 2001). The solution shown above for NGC 4051 indicates that the emitting radius is approximately 13–24 $r_{\rm g}$ which would correspond to an orbital timescale of approximately 2–6 ks for a black hole mass of $M_{\rm BH} = 1.7 \times 10^6\,{\rm M}_\odot$ (Denney et al. 2009). Since the line at 5.44 keV is observed with a steady line flux over at least a three-year baseline from the *Suzaku* observations in 2005 and 2008, this would be equivalent to approximately 20 000 orbits around the black hole. In fact, the persistence of the flux would suggest up to ∼60 orbits in the 2005 observation alone. This is greater than the theoretical survival time for a hotspot from the modelling of Karas, Martocchia & Subr (2001).

Furthermore, since the disc hotspot and the X-ray continuum have a common origin in this model, the relativistic line should vary with continuum fluctuations and flares (Dovčiak et al. 2004). However, in the case of NGC 4051, the line shows up in the offset component of the PCA (Figure 5.18) of Miller et al. (2010b) suggesting that the line not only has a common origin with the narrow, near-neutral Fe Kα emission but that it also does not respond to changes in the continuum. Therefore, the persistence of the line with a radial location apparently close to the event horizon may disfavour the disc-hotspot interpretation.

5.3.3.2 A Special Accretion-Disc Radius?

In Section 5.3.3.1 it was suggested that the emission from 5–6 keV could have an origin in the disc. However, the persistency of the line at 5.44 keV and its constancy in flux over long timescales casts some doubt over this particular solution. Alternatively, the persistent steady nature of the line could be explained if one assumes that it arises from a special radius in the disc where the expectations of measurable changes in flux- and profile-variability are no

longer an issue.

One such interpretation of a special radius could be that the inner accretion disc is truncated at some radius. This could occur if the disc becomes unable to cool efficiently and then the majority of the thermal emission is carried into the black hole as opposed to being radiated. Such a model is known as an advection-dominated accretion flow (Narayan & Yi 1995; also see Section 3.4.3.1). In such a scenario, at the transition / truncation radius, the disc may become inflated due to radiation pressure and emit more strongly than the rest of the structure.

In the case of NGC 4051, the redshift of the line at 5.44 keV places the inner edge of the disc at $\sim 20\, r_{\rm g}$ from the event horizon. Taking the bolometric luminosity of Ogle et al. (2004) of $L_{\rm bol} \sim 2 \times 10^{43}\,{\rm erg\,s^{-1}}$ and correcting for the distance of 15.2 Mpc obtained from the Tully-Fisher relationship for nearby galaxies (Russell 2004) gives $L_{\rm bol} \sim 7 \times 10^{43}\,{\rm erg\,s^{-1}}$. When compared with the Eddington luminosity ($L_{\rm Edd} \sim 2 \times 10^{44}\,{\rm erg\,s^{-1}}$) for this source, this yields an estimate of the mass-accretion rate of $\sim 30\%\, \dot{M}_{\rm Edd}$. However, an advective accretion flow may not be expected to form when $\dot{m}/\dot{M}_{\rm Edd} > 0.1$ (Narayan, Mahadevan & Quataert 1998). Nevertheless, the bolometric luminosity for NGC 4051 was calculated to be lower by Vasudevan & Fabian (2009) by building up an SED using optical, UV and X-ray data from *XMM-Newton*. This results in a value of $L_{\rm bol} \sim 10^{43}\,{\rm erg\,s^{-1}}$ (when corrected for the distance assumed here). This differs from the bolometric luminosity calculated by Ogle et al. (2004) since the data used to create the SED were contemporaneous. However, Ogle et al. (2004) did use additional radio and infrared data to build up a larger SED. The value provided by Vasudevan & Fabian (2009) provides an estimate of the mass-accretion rate of $\sim 5\%\, \dot{M}_{\rm Edd}$. For such an accretion rate, the critical transition radius from a thin disc to an advection-dominated accretion flow could occur anywhere up to a radius of $\sim 2\,000\, r_{\rm g}$ from the event horizon (Narayan, Mahadevan & Quataert 1998). So it seems that the radius for the emitting line could be consistent with this scenario although it remains somewhat sensitive to the value of the bolometric luminosity.

It should be noted that if this scenario is correct, then such features at the truncation radius of the accretion disc should also be detected in the X-ray spectra of Galactic binaries when in the low-flux state. The absence of such features would cast doubt over the truncated

disc solution for the lines. Although similar features are yet to be reported in the spectra of Galactic binaries (Done, Gierliński & Kubota 2007), constraints on such features are yet to be fully explored in these objects.

5.3.3.3 Spallation of Fe Nuclei

A third possible alternative for the origin of the lines arose from the fact that the observed energies of ∼5.4 and ∼5.9 keV coincide with the expected rest energies from the Kα transitions of Cr and Mn at 5.41 and 5.89 keV respectively. However, the line strengths far exceed those expected from the simple illumination of material with cosmic abundance ratios. Considering Cr and taking the abundances of Anders & Grevesse (1989), the Fe:Cr abundance ratio is 100:1. Tying in the K-shell fluorescence yields for neutral atoms (i.e. the probability that a vacancy in a shell leads to a radiative transition as opposed to the ejection of an Auger electron; $Y_{\rm Fe} = 0.347$, $Y_{\rm Cr} = 0.282$; Bambynek et al. 1972) and taking into account the relative K-shell photo-ionisation cross-sections (i.e. the probability of an electron being emitted from its quantum electronic state) modifies the expected line-strength ratio to approximately 113:1 for Fe:Cr. Therefore, Cr emission lines should be too weak to be detected with current X-ray instruments. However, if, for example, the line at ∼5.4 keV is indeed due to Cr, then the observed equivalent width ratio in the 2005 *Suzaku* is Fe/Cr $= 4.24 \pm 1.57$. This would imply that the relative emission strength of Cr has been enhanced by a factor of ∼30 with respect to cosmic abundance ratios.

One possible mechanism for enhancing the abundances of such elements is spallation (Skibo 1997). Spallation can occur as a result of the impact of high-energy cosmic rays (e.g. protons with kinetic energy $\gtrsim 30$ MeV) on matter whereby heavy nuclei (such as Fe) become fragmented into lighter nuclei, thus enhancing the abundance of lower Z atoms such as Cr, Mn, Ti and V. Since the cross-section for spallation increases with atomic mass number approximately as $A^{0.7}$ (Letaw, Silberberg & Tsao 1983), and coupled with the high cosmic abundance of Fe, it is conceivable to expect the effects of spallation to be more readily detected in X-ray spectra where various Fe species are prominent. At low energies, the required protons need only be mildly relativistic. Therefore, it is plausible to expect spallation to occur in

a range of astrophysical environments. Our own Galaxy is one example where spallation significantly alters the observed abundance ratios (Reeves 1974). Here, abundant nuclei such as C, N, O and Fe seem to be most significantly affected; however, due to the low cross-sections ($\sigma < 10^{-24}\,\mathrm{cm}^{-2}$; Letaw, Silberberg & Tsao 1983), high proton fluxes and/or long timescales are required for the abundances to considerably vary through this process (Turner & Miller 2010). If spallation is to also occur in AGN, a mechanism for the production of cosmic rays is also required. Since the primary process for the production of X-rays in AGN is thought to be inverse-Compton scattering of UV photons from the accretion disc in a nearby corona of hot electrons (e.g. Haardt & Maraschi 1991), it is conceivable that a large flux of protons and/or heavier nuclei may also be present. A population of mildly relativistic protons (i.e. $E \lesssim 200\,\mathrm{MeV}$) could, in principle, be produced by shock acceleration or perhaps through a mechanism whereby magnetic fields tied to the rotating accretion disc accelerate the plasma (Blandford & Payne 1982). Spallation was considered by Turner et al. (2002) for the case of NGC 3516 to explain line emission at 5.6 and 6.1 keV. However, the observed line ratios were inconsistent with the predicted ratios of Skibo (1997).

Turner & Miller (2010) used NGC 4051 as a case study to re-visit spallation as interpretation for 'redshifted' emission lines. By taking into account the cross-sections for the primary products of the spallation of Fe and adjusting them for the decay of unstable isotopes, the most notable abundance enhancements would indeed occur for Cr and Mn. However, the authors largely focus just on Cr and the emission line at 5.44 keV[4]. Although the observed line ratios initially failed to match up with the theoretically predicted ratios, Turner & Miller (2010) show that the simulations by Skibo (1997) are conservative in the sense that they consider the enhancement of abundances in the entire mass of material surrounding the black hole; a solution which would require a very high efficiency of proton creation in order to produce large enhancements of the abundances of Cr and Mn. They argue that since many recent observations have provided a wealth of evidence for large columns of gas in the inner regions of Seyfert galaxies (from a wide range of ionisation states and often outflowing),

[4]The line at ∼5.9 keV was found to be less-well constrained because: (i) it was difficult to rule out any contamination from the nearby Fe Kα emission line at 6.4 keV, and (ii) the line shows some degree of sensitivity to the form of the continuum assumed.

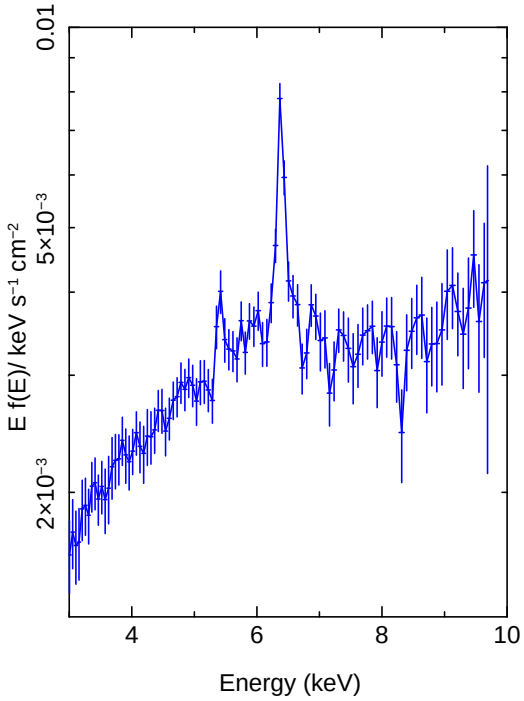

Figure 5.18: Plot taken from Turner et al. (2010) showing the offset component from the PCA decomposition of all the 2005 and 2008 *Suzaku* XIS 0 and 3 and HXD-PIN data. A strong narrow Fe Kα line is evident at 6.4 keV, along with emission at $\sim$5.4 keV and, more weakly, at $\sim$6 keV.

the predictions and consequences could differ dramatically from those of Skibo (1997) if the spallation instead takes place in the putative disc-wind away from the plane of the accretion disc. Turner & Miller (2010) show that if spallation does indeed take place in such circum-nuclear material, the required timescales could be as short as a few years provided that the cosmic-ray luminosity is comparable to the bolometric output of the AGN. If the cosmic-ray luminosity is lower, the spallation timescale would be proportionally longer but could still be orders of magnitude shorter than the accretion timescale onto the black hole. The spallation interpretation is also supported by the PCA of Miller et al. (2010b) which suggests a common origin for the emission line at 5.4 keV and the Fe Kα emission line at 6.4 keV (see Figure 5.18).

Finally, during the modelling of the *Suzaku* observations of NGC 4051, it was noted

that whether parameterising the broad-band data with a PEXRAV or REFLIONX model (see Sections 4.5.2 and 5.2.3.1 respectively), the data seem to prefer a sub-solar abundance of iron with a best-fitting value of $A_{\rm Fe} \sim 0.3$ times solar (see Table 5.5). Aside from an intrinsically sub-solar abundance of iron in NGC 4051, one other possible interpretation could be that this is perhaps indicative of the spallation interpretation described here since the fragmentation of Fe nuclei by high-energy cosmic-rays may have the effect of significantly lowering the abundance of Fe depending on the timescales and cosmic-ray fluxes involved.

5.4 Conclusions

NGC 4051 is found to be a highly variable source both on short (ks) and long (days to years) timescales. From the principal components and timing analyses of Miller et al. (2010b), a two-component model for the longer-term variations is suggested whereby a soft, varying power-law-like component of invariant photon index changes in amplitude superimposed on a hard, constant component. Miller et al. (2010b) interpret this as arising from variable partial-covering in our line of sight which could explain the steady, narrow component of the Fe Kα emission and may also explain the different shapes of the PSDs between observations if, in the case of the 2005 observation, the source was absorbed to such an extent that very little direct light was seen. From considering a reverberation model, Miller et al. (2010b) also find time lags whereby hard-band photons lag behind soft-band photons. This has previously been interpreted as arising from propagations moving inwards in the accretion flow although Miller et al. (2010b) conclude that they could arise from reverberation from material a few light-hours away from the source. The rapid X-ray variability, along with an associated moderately broadened component of Fe Kα emission, however, is hypothesised to arise from a mechanism that is more intrinsic to the source.

The long-term spectral variability is largely consistent with this picture as it can be modelled simply by variations in the covering fraction of an absorber (anti-correlated with the observed source luminosity) and a variable 'unabsorbed' power-law continuum superimposed on a quasi-constant distant reflection component. This can be interpreted as being

due to changes in the covering fraction of a Compton-thick absorber obscuring the intrinsic continuum emission and is consistent with the findings of Miller et al. (2010b) who, through studying the effects of reverberation in the hard band, find that a global covering factor of $\gtrsim 40\%$ of reflecting material is required in this source. The constancy of the flux of the near-neutral Fe Kα component across epochs then implies that it does not respond to significant changes in the continuum emission. Since NGC 4051 is a very compact source with a dust sublimation radius on the order of tens of light-days, it does not appear possible to explain this invariance away as arising from a delayed response from very distant ($\gtrsim 10$ light-years) material. Instead, this suggests that the absorbing clouds may have a clumpy distribution (i.e. a clumpy accretion-disc wind). In this scenario, the observed spectral changes arise from variations in the line-of-sight covering fraction of the absorber whereas, from the point of view of the torus, if the the global covering fraction of the clouds remains unchanged, the distant reflecting material will receive an invariant mean continuum flux when integrated over all solid angles.

Finally, strong evidence is seen for an emission line at $\sim$5.4 keV which is also detected in the constant offset component of the PCA, suggesting that it may have a common origin with the narrow Fe Kα emission line. The probability of this line arising from a statistical fluctuation is found to be $p < 3.3 \times 10^{-4}$. The origin of this feature remains debatable. One possible origin could be that it arises in a disc hotspot and so is the signature of gravitationally redshifted Fe. However, the long timescales over which the line is observed and constancy of its flux cast doubt over this interpretation. Spallation of Fe nuclei was also suggested which could produce an enhanced abundance of Cr, which has a laboratory rest-frame Kα transition at 5.44 keV. Alternatively, the line could originate at a special radius in the accretion disc; perhaps a truncation radius where the disc becomes inflated due to radiation pressure and produces enhanced emission.

6 Discussion & Conclusions

In Chapters 3–5, broad-band analyses of NGC 7213 and NGC 4051 were described in detail. The nature of the long-term spectral variability exhibited by many type-1 Seyfert galaxies is the primary focus of the discussion and this was investigated in both cases. Interestingly, NGC 7213 and NGC 4051 comprise two AGN covering a wide range in parameter-space. They significantly differ in many key aspects, such as their black hole masses and respective accretion rates, and this is further evidenced by the nature of the variability that they display.

NGC 7213 was found to display no significant spectral variability within any individual observations but was observed to have changed in luminosity by a factor of $\sim$2 between 2006 and 2009 with the observed 2–10 keV flux falling from $F_{2-10} = 2.46 \times 10^{-11}\,\mathrm{erg\,cm^{-2}\,s^{-1}}$ when observed with *Suzaku* to $F_{2-10} = 1.20 \times 10^{-11}\,\mathrm{erg\,cm^{-2}\,s^{-1}}$ when observed with *XMM-Newton*. The X-ray spectrum takes largely the same form between observations with little change in the observed spectral shape. Some debate can be held over the nature of the narrow Fe XXV emission line which is observed to be more consistent with the rest-frame energy of the corresponding forbidden transition in 2006 yet more consistent with the resonance transition of the same ion in the 2009 data. However, a common origin for the line in the two datasets cannot be ruled out.

NGC 7213 is an example of an AGN where very few parameters are statistically required to vary in between observations and so the long-term variability can accounted for by simply allowing for changes in the flux of the intrinsic power-law component (see Chapter 3) while the line emission remains relatively constant in flux. Like sources such as NGC 5548, NGC 7213 is a very low-accretion-rate source ($L \sim 0.07\%\,L_{\mathrm{Edd}}$); the result of which appears to be that no standard, optically-thick, geometrically-thin accretion disc is present in the inner regions.

In contrast, NGC 4051 was found to display much more significant X-ray spectral variability with dramatic changes in the observed 0.5–50 keV flux between 2005 and 2008. Upon modelling the broad-band *Suzaku* data with a four-zone, fully-covering, soft X-ray warm absorber (as required by the contemporaneous 2008 high-resolution *Chandra* HETG

data) plus an additional higher-velocity component in the Fe K band, a partial-coverer and two reflectors (one highly ionised; one from distant, near-neutral material), it was found that the bulk of the spectral variations could be accounted for by significant changes in the line-of-sight covering fraction of the partial-coverer. This could be interpreted as arising from Compton-thick clouds of gas passing into our sightline, explaining the variations in the observed flux $<$10 keV.

The constancy of the flux of the narrow Fe Kα emission line (most likely from distant material) then suggests that the absorber may take the form of a clumpy disc wind. This is because the line flux is constant to within a factor of $\sim$2 in all X-ray observations stretching back to *BeppoSAX* data acquired in 1998 thus spanning a baseline greater than a decade. If the Fe Kα emission line responds to long-term changes in the intrinsic continuum source (as expected), it is not possible to explain the invariant flux away as a delayed light travel-time effect in which the distant Fe Kα line is too distant to have responded yet. This arises from the fact that the low black hole mass of this source ($M_{\rm BH} \sim 1.7 \times 10^6\,{\rm M}_{\odot}$; Denney et al. 2009) places the location of the torus to within $\sim$15–20 light-days of the black hole (from dust sublimation radius arguments; Krongold et al. 2007) and so a response in the emission-line flux to long-term changes in the intrinsic continuum should be observed in such a compact system on timescales $>$week. This suggests that the intrinsic luminosity may be relatively constant but that the observed flux varies depending on the Compton-thick cloud coverage in our line-of-sight. The integrated continuum flux from the point of view of the torus seen over all solid angles would then remain constant if the global covering fraction of the clumpy disc wind remains unchanged, providing a natural explanation for the constancy of the narrow Fe Kα emission-line flux. Note that the short timescale variations (e.g. on ks timescales from the PCA of Miller et al. 2010b), however, are likely to be intrinsic to the source but would be averaged out on the scale of the torus (e.g. light-weeks).

In Section 1.4, two distinct forms of X-ray variability were introduced and discussed: intrinsic continuum changes and reprocessing of the intrinsic continuum emission by circum-nuclear material. In the reprocessing scenario, variability models are further sub-divided into those dominated by reflection and those dominated by absorption. The work in this thesis has largely favoured an absorption-dominated scenario to explain the most significant

X-ray variability. Two recent developments in the context of X-ray absorption are briefly summarised below.

6.1 Recent Developments in the Context of X-Ray Absorption

Some potentially important progress has very recently been made regarding the significance of line-of-sight absorption in the case of type-1 Seyfert galaxies. In this section, two significant observational and theoretical developments are briefly summarised.

6.1.1 Evidence for Compton-Thick Gas in a Large Fraction of Type-1 AGN

Evidence for substantial columns of absorbing material in the inner regions of type-1 AGN has emerged in recent years. Broad-band studies of sources such as PDS 456 (Reeves et al. 2009) and 1H 0419-577 (Turner et al. 2009) with *Suzaku* have revealed significant excesses of counts in the hard X-ray band (i.e. $E > 10\,\mathrm{keV}$). Since these spectra are difficult to model with blurred reflection, one implication has been that the source is viewed through a layer of Compton-thick gas covering the primary continuum emission by some significant fraction. Such an explanation was favoured in Chapter 5 to explain the broad-band spectral variability of NGC 4051 and may also account for the sharp / deep dips occasionally observed in the X-ray lightcurves of objects such as MCG–6-30-15 (McKernan & Yaqoob 1998) and NGC 3516 (Turner et al. 2011) (see Section 1.4.2.3).

A follow-up study (see Turner, Miller & Tatum 2012 and Tatum et al. 2013) has been prompted by these findings in which *Swift*-BAT data have been cross-correlated with *Suzaku* data (providing simultaneous data in the medium 2–10 keV and hard 15–50 keV X-ray bands) yielding a sample of 50 type-1 AGN (across 65 observations). Hardness ratios were calculated between the energy fluxes in the 2–10 and 15–50 keV energy bands and compared to those expected for pure reflection (where the illuminating continuum is hidden from view), the sum of a power-law ($\Gamma = 2.1$) plus reflection (using the PEXRAV model of Magdziarz & Zdziarski 1995, assuming a thin disc subtending 2π sr to the illuminating continuum, solar abundances,

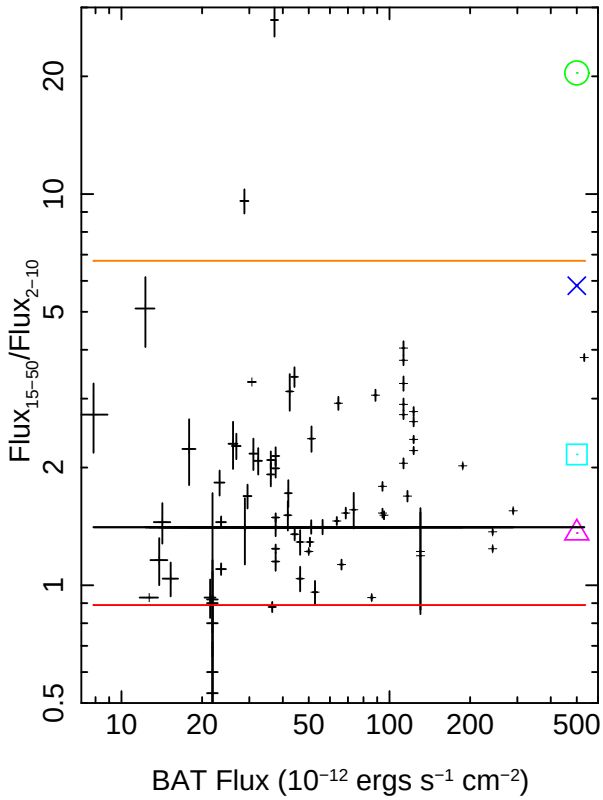

Figure 6.1: *Suzaku* hardness ratios plotted against the observed *Swift*-BAT flux. The black line represents the weighted mean hardness ratio for the sample and the hardness ratios expected from pure, neutral reflection and a power law reflected from a standard thin disc are represented by the orange and red lines respectively. The green, dark blue, light blue and magenta markers represent the hardness ratios expected from partially-covered power laws with neutral gas and covering fractions of 98%, 90%, 70% and 50% respectively. Figure taken from Turner, Miller & Tatum (2012). Also see Tatum et al. (2013).

no cut-off of the continuum and an inclination angle of 60°) and near-neutral columns of Compton-thick gas of varying covering factors. These are shown in Figure 6.1. Interestingly, the measured ratios are generally much harder than those expected for the power-law-plus-reflection model but are largely consistent with a pure reflection model. However, while such a pure reflection scenario may be consistent with the morphology of type-2 AGN, it is unlikely to be the case in type-1 AGN where direct continuum emission is seen. Furthermore, this is

also at odds with the relatively weak Fe Kα emission lines observed in many of these sources. Alternatively, however, 70% of the sample are consistent with having Compton-thick gas in the line-of-sight to the nucleus. This adds further weight to the notion that absorption may dramatically modify the observed X-ray spectra even in type-1 AGN. It may therefore be a natural consequence to anticipate variations in these absorbers significantly influencing the observed spectra, potentially producing the significant observed variations and perhaps prompting a reconsideration of the inner regions of AGN.

6.1.2 Accretion-Disc Wind Models

Combining the evidence for Compton-thick gas in the line-of-sight of type-1 AGN with the fact that the gas is almost certainly outflowing (e.g. through detections of highly-ionised absorption lines; Tombesi et al. 2010; Tombesi et al. 2011; Turner, Miller & Tatum 2012; Tombesi et al. 2012; Gofford et al. 2012; Tatum et al. 2013) has led to detailed calculations of the expected X-ray signatures from such a Compton-thick outflow (Sim et al. 2008; Sim et al. 2010). Interestingly, high wind densities predict strong emission from Fe K with typical line-widths of FHWM $\sim$ 1 keV. The line is significantly broadened by the velocity-shear across the flow and Compton down-scattering of Fe Kα line photons but since the launch radius of the wind is assumed to be no smaller than $\sim$30 $r_{\rm g}$ from the black hole, relativistic blurring does not contribute. Sim et al. (2008) and Sim et al. (2010) performed case studies of Mrk 766 and PG 1211+143 respectively (e.g. Figure 6.2) and found that a single Compton-thick flow could describe the broad Fe Kα emission component along with the absorption lines from Fe XXV and Fe XXVI.

As a further follow-up study, a sample of six 'bare' Seyfert galaxies harbouring moderately broad Fe Kα emission lines (Patrick et al. 2011b) has been taken by Tatum et al. (2012) and the *Suzaku* XIS data have been fitted over the 0.6–50 keV band with a model consisting of an intrinsic power-law component modified by a disc wind plus Galactic absorption. By convolving the continuum emission with the absorption and scattering effects of a wind, good fits can be found to the data with a narrow component of Fe Kα emission remaining in the residuals; most likely the signature of reprocessing from distant material. Since the current

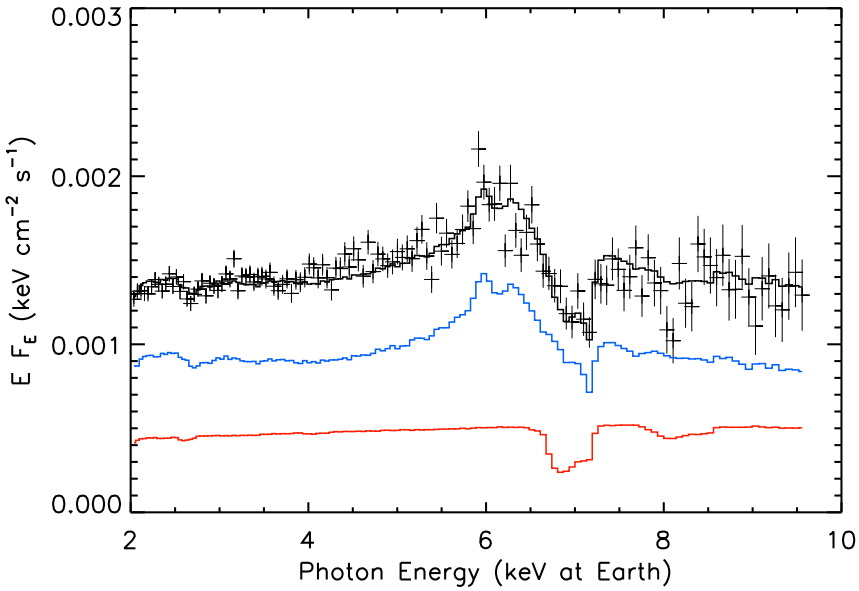

Figure 6.2: The wind model of Sim et al. (2010) applied to the PG 1211+143 data of Pounds & Reeves (2009). The model assumes a launch radius for the wind $\geq 50\,r_{\rm g}$ and a mass outflow rate of $\dot{M} = 0.53\,{\rm M}_{\odot}\,{\rm yr}^{-1}$. The data and model are shown in black. The red and blue lines show the contribution from the direct and scattered / reprocessed emission respectively. Figure taken from Sim et al. (2010).

results suggest that the wind model can equally provide a good account of all the observed broad lines tested so far, it could be conceivable that outflowing winds may be responsible for both the dominant absorption and emission characteristics of Seyfert galaxies (also see Turner, Miller & Tatum 2012).

6.2 Towards a Complete Picture of X-Ray Spectral Variability and the Importance of Absorption

One particular pattern that many AGN display is that the variability in sources with lower accretion rates is weaker and simpler. A good example of such a source is NGC 5548 where

neither absorption nor reflection are required to explain the variability. Instead, the variability may be due to simple spectral pivoting of the intrinsic power law ($\Delta\Gamma \sim 0.2$; Nicastro et al. 2000) and/or thermal instabilities in the accretion disc (Uttley et al. 2003). In Chapter 3, another low-accretion-rate source, NGC 7213 ($L \sim 0.07\% \, L_{\rm Edd}$), was analysed and the variability was also found to be subtle in that the long-term changes can be accounted for by simple changes in the flux of the intrinsic power-law component while the bulk of the (weak) reprocessed emission from distant material (e.g. Fe Kα emission) remains constant. So it could be the case that significant outflowing winds are not launched in sources such as NGC 7213 due to their low accretion rate and so there is less reprocessing material in the inner regions than in higher-accretion-rate sources. This may offer a clearer view of the intrinsic continuum processes and perhaps explain why the observed variability is much weaker than the strong-amplitude variations often observed in higher-accretion-rate sources.

In contrast, higher-accretion-rate sources are often observed to display much stronger variability. Sources such as MCG–6-30-15 (Fabian & Vaughan 2003), Mrk 766 (Miller et al. 2007) and NGC 3516 (Turner et al. 2011) are X-ray bright with high accretion rates, often displaying strong amplitude variability on both short and long timescales plus characteristic 'softer-when-brigher' behaviour (see Section 1.4.2 and Figures 1.7 and 1.13). In such sources, the existence of strong spectral curvature from 2–8 keV (e.g. Nandra et al. 2007; Miller et al. 2008) has led to the development of models based on reprocessing of the continuum emission by circumnuclear material close to the black hole (Section 1.4.2).

Regardless of the direct cause of the observed X-ray spectral variability exhibited by these type-1 Seyfert galaxies, an undeniable result obtained from recent grating data is the presence of absorption in these systems covering wide ranges in ionisation, column density and radial location with respect to the central source. The wealth of unambiguous evidence for substantial columns of line-of-sight gas (e.g. Crenshaw, Kraemer & George 2003; Turner & Miller 2009) suggests that obscuration may play a significant role in the modification of X-ray spectra. AGN accreting at close to the Eddington limit should be expected to generate significant outflows (e.g. via line and continuum radiation pressure); early models developed for AGN accreting at super-Eddington rates suggested that winds would typically be optically-thick in the central regions, obscuring the continuum source from being directly

observed (Camenzind & Courvoisier 1983) and later models, such as those by King & Pounds (2003) estimate that sources with accretion rates at a high fraction of the Eddington rate would be expected to generate high-velocity, Compton-thick, outflowing winds. However, it seems that X-ray spectra can even be modified in a significant way by absorbing gas without extreme column densities and, interestingly, outflowing winds now also appear to be a ubiquitous property of X-ray binaries observed in the high/soft-state (Ponti et al. 2012).

When considering absorption-dominated models to explain the large spectral and flux variations in type-1 AGN, the best-fitting parameters imply that the absorbing material consists of clumps of high-column-density gas each with relatively low global covering fractions (or volume-filling factors). The most natural geometry to explain this would be a clumpy, equatorial disc wind since considering simple individual clouds may be a plain oversimplification. One very interesting result was obtained from a *Swift*-BAT hard X-ray survey of the brightest nearby AGN whereby Beckmann et al. (2007) found that the most variable AGN tend to be those which are more absorbed. This implies that opacity variations could play a significant role in the variability of AGN. In some cases, absorption-dominated models have required an anti-correlation between the luminosity of the source and the covering fraction of the absorbing gas (e.g. MCG–6-30-15, Miller et al. 2008; NGC 4051, see Chapter 5). Although not a unique solution, if such a dependence between the two variables were to be confirmed, it could suggest a picture whereby the size of the continuum source varies, either becoming more visible or more obscured by an absorbing structure; e.g. an outflowing clumpy disc wind.

In Chapters 4 and 5, the high-accretion-rate, highly-variable NLS1 NGC 4051 was studied, which displays strong evidence for high columns of reprocessing material. It was found that an absorption-dominated scenario can explain the observed X-ray spectra well with the significant long-term spectral variability accounted for by changes in the covering fraction of a Compton-thick partially-covering absorber. The evidence for Compton-thick gas supports the findings of Turner, Miller & Tatum (2012) and Tatum et al. (2013) (see Section 6.1.1). Combining this with the spectral evidence for significant columns of outflowing gas (see Chapter 4) suggests that the variability may be linked to a high-velocity accretion-disc wind, supportive of the models developed by King & Pounds (2003) and Sim et al.

(2010). These results are also consistent with the reverberation model proposed by Miller et al. (2010b) to explain the X-ray timing properties of sources such as NGC 4051 and Mrk 766 (Miller et al. 2007) in the context of large columns of line-of-sight obscuring material.

In Section 1.4.2.1, it was noted that reflection-dominated models are also commonly used to account for the spectral variability whereby the dominant spectral features arise from an optically-thick reflecting surface, such as an accretion disc (Ross & Fabian 2005). Importantly, it should be noted that it is likely that both absorption and reflection occur naturally in AGN environs and so models should not completely neglect one process or the other. Interestingly, both processes may actually arise simultaneously in a clumpy accretion-disc wind. Models by Schurch & Done (2007) and Schurch, Done & Proga (2009) calculated the impact that accretion disc winds could have on X-ray spectra of AGN with relatively high Eddington ratios. By combining shells of absorption with XSTAR with the hydrodynamic disc-wind simulations of Proga & Kallman (2004), Schurch, Done & Proga (2009) showed that even a simple approach such as this could yield highly complex X-ray spectra containing many commonly observed features in AGN such as the highly-ionised, blueshifted Fe K absorption lines. The Monte Carlo simulations of Sim et al. (2008) and Sim et al. (2010) used to calculate disc-wind spectra including the effects of scattering and reflection through a detailed 3-D radiative transfer treatment also predict that significant Fe Kα emission with strong red wings may be observed, produced not through relativistic effects but instead via electron scattering and velocity effects (Section 6.1.2). Although the ambiguity between relativistic and outflow-based processes for some of these observed features is difficult to break, equatorial disc winds could provide self-consistent explanations for the majority of the X-ray spectral features and variations observed in type-1 Seyfert galaxies.

Interestingly, NGC 4051 was found to also require strong reflection components (both from neutral and ionised material; e.g. Section 5.2.3.1). However, a reflection-dominated model cannot account for the 2005 low-flux *Suzaku* spectrum primarily due to the weak emission from Fe and strong hard excess > 10 keV (e.g. Section 5.2.3.2). Consequently, the absorption model is favoured to explain the variability. The reflection features in the spectrum may then arise from a combination of distant material (i.e. the torus) and the surface of the accretion-disc wind, consistent with the recent predictions of Sim et al. (2008)

and Sim et al. (2010). Like in NGC 4051, absorption-dominated models often relax the requirement for broad emission lines. Prompting the question then of why relativistically broadened lines may be absent / not required in the X-ray spectra of many type-1 Seyfert galaxies, one possible solution could be that the inner accretion disc is not directly observed or we are viewing through an inner Compton-thick wind or screen. Another possibility could be that the inner disc is truncated. Alternatively, however, it could be the case that due to strong photoionisation of the inner accretion disc, the majority of Fe atoms at the disc's surface are fully ionised. Consequently, the line would then be too weak to be detected. In the magnetic flare model of Nayakshin (2000), the X-ray flux is concentrated in small, intense regions above the disc. This can have the effect of strongly ionising the surface layers of the disc producing a very weak Fe line and Compton reflection component, particularly so for harder photon indices.

A more contentious issue for absorption models, however, would be whether variable absorption can explain the complete range of X-ray spectral variations exhibited by AGN. Since AGN are often found to vary on both short and long timescales (e.g. NGC 4051; Figure 5.2), it is not really known whether the two types of variations are caused by the same physical process. Since no established model for the production of the continuum emission is currently agreed upon, the extent to which intrinsic processes can imprint variable spectral features in the data is unknown. A coupling between disc photons and the hot corona was supposed by Haardt & Maraschi (1991) to act as a cooling mechanism along with a coupling between the Comptonised photons and the disc to act as a heating source. In this corona-plus-disc model, the illuminating spectrum is therefore not entirely separate from the reprocessing material arising from cooler areas of the disc and should not be considered as being independent. However, one possibility could be that the longer-term variations (i.e. on timescales of tens of ks or more) could be accounted for by changing covering fractions of absorbing gas whereas the more rapid variations could be due to a more intrinsic mechanism perhaps related to the generation of the continuum emission itself. Potential explanations for the short-term variations include inwardly-propagating accretion fluctuations (Lyubarskii 1997) and magnetic flaring and reconnection.

So to summarise, the results presented in this thesis are consistent with a picture

whereby the most significant X-ray variability exhibited by higher-accretion-rate sources is dominated by reprocessing of the primary continuum by circumnuclear material (e.g. NGC 4051, MCG–6-30-15, Mrk 766, NGC 3516, etc). Absorption-dominated models are favoured on the basis of strong evidence for high columns of outflowing gas in the line-of-sight (e.g. Sections 4.4.1 and 4.5.2) and the ability to account for large spectral variations primarily with changes in the covering fraction (Section 5.2.3.2). In particular, this scenario is consistent with the disc-wind predictions of King & Pounds (2003), Proga & Kallman (2004), Schurch, Done & Proga (2009) and Sim et al. (2010). In contrast, lower-accretion-rate sources such as NGC 7213 then do not display such significant variability due to the lack of reprocessing material close to the black hole (i.e. Section 3.3.2) where perhaps the accretion rate is too low to launch an accretion-disc wind. Consequently, a more direct view of the central regions is afforded and so the weaker observed variability most likely originates from intrinsic processes.

Ultimately, if absorption is the key to understanding the spectral variability exhibited by Seyfert galaxies then its precise role in modifying the observed X-ray spectra is not yet fully understood. Changes in ionisation or opacity could play equally as important roles as the line-of-sight covering fraction of the gas in some sources while another plausible scenario could be that the changes arise from a combination of these various factors. Undeniably, though, a decade of grating data from *Chandra* and *XMM-Newton* plus broad-band coverage with *Suzaku* has yielded a wealth of information and greatly enhanced our understanding of the circumnuclear environments within AGN, revealing the presence of substantial columns of absorbing material in our line-of-sight. As a result, it is natural to expect absorption to play a significant role in shaping the observed X-ray spectra of Seyfert galaxies and, if outflowing accretion-disc winds are as prominent as current models may suggest, this may perhaps motivate a reconsideration of AGN unification schemes in order to incorporate outflowing winds as they may be a ubiquitous feature of high-accretion-rate sources.

6.3 Future Prospects

The limitations of current X-ray data make it difficult to distinguish between absorption and reflection models for the strong spectral curvature around 6 keV observed in many AGN. The limitations arise because, in the crucial Fe K band, current instruments either offer high throughput but with modest spectral resolution (e.g. the CCDs on-board *Suzaku* and *XMM-Newton* with energy resolution of FWHM $\simeq$ 130 eV at 6 keV) or higher resolution (e.g. the *Chandra* HEG with an energy resolution of FWHM $\simeq$ 40 eV at 6 keV) but with a low effective area. However, X-ray calorimeters have been designed to combine high throughput with unprecedented spectral resolution and should be able to resolve such issues.

A calorimeter (X-Ray Calorimeter Spectrometer; XCS) will be flown on-board the upcoming *Astro–H* mission, due for launch in 2014 with a projected energy resolution of FWHM $\simeq$ 4 eV at 6 keV. Along with *NuSTAR* (see below), the satellite will also carry the first imaging hard X-ray detector (Hard X-Ray Imager; HXI) extending the bandpass to $\sim$100 keV (0.3–100 keV overall). Looking further to the future, a calorimeter may also be flown on-board the *Advanced Satellite for High-Energy Astrophysics* (*ATHENA*; formerly the *International X-Ray Observatory*; *IXO*) mission, with a possible launch in 2028. With a projected energy resolution of FWHM $\simeq$ 2.5 eV at 6 keV, *ATHENA* will be able to measure key diagnostic features in bright Seyfert galaxies with unprecedented accuracy. Calorimeter observations will allow weak, narrow absorption features in the Fe K band to be resolved for the first time in Seyfert galaxies, enabling their widths to be measured. This should then allow the definitive origin of the spectral curvature around 6 keV to be established allowing the true extent of absorption in these systems to be revealed explicitly through line detections as opposed to inferring it through the spectral curvature. The high throughput (especially with *ATHENA*) will also permit line variations to be tracked on short timescales enabling variability studies to be undertaken in unprecedented detail allowing a much clearer picture of the inner regions of AGN to be built up. Indeed, for brighter sources, column densities and ionisation parameters will be able to be measured to within 10% and 1% respectively on timescales as short as 25 ks. Such a combination of high throughput and spectral resolution will also be vital for understanding the true nature of transient, rapidly-variable narrow

emission lines (see Section 5.2.4.1) since the lines will be able to be tracked on sub-orbital timescales, thus evaluating the true nature of these possible disc hotspots.

These observatories should complement well other future missions such as the *Nuclear Spectroscopic Telescope Array* Mission (*NuSTAR*; successfully launched in June 2012), the *Large Observatory For X-ray Timing* (*LOFT*; due for launch in 2022) and *Astrosat* (due for launch in 2013). *NuSTAR* is the first focusing high-energy X-ray mission enabling the sky to be imaged in the 5–80 keV energy range whereas *LOFT* will perform high-resolution timing analysis ($\sim$10 μs) while simultaneously achieving an effective area of $\sim$12 m^2 in the 2–30 keV range (over an order of magnitude higher than current spaceborne X-ray detectors) although its spectral resolution will be similar to that of *RXTE*. Overall, future missions combined with the development of new models should allow vital progress to be made towards a complete picture of spectral reprocessing and, should a wind origin be confirmed for the observed spectral features and variations observed in Seyfert galaxies, enable key parameters of these systems to be measured such as the acceleration / deceleration mechanism(s), the launch radius, the mass loss rate and ultimately allow us to understand the role that they play in galactic evolution.

6.4 Conclusions

This thesis has primarily explored the nature of X-ray spectral variability in type-1 Seyfert galaxies. The full range of variability has been probed with some sources displaying extreme variability on both short and long timescales but with other sources only showing very weak, gradual changes. Interestingly, no two AGN are observed to be exactly the same and processes ranging from intrinsic mechanisms to reprocessing by material close to the black hole have been invoked to explain the wide range of observed variations.

In Chapter 3, a *Suzaku* observation of NGC 7213 was explored in detail which showed no evidence for any significant variability within the observation itself. The spectrum was characterised with an intrinsic, hard power-law continuum ($\Gamma \sim 1.7$), a weak soft excess and narrow Fe K emission from near-neutral Fe plus highly-ionised Fe XXV and Fe XXVI.

Interestingly, the observed centroid energy of the Fe XXV emission was found to be more consistent with the forbidden transition, suggesting an origin in a low-density plasma. The source was found to exhibit no evidence for any significant reflection component (consistent with previous observations) which, combined with the very low accretion rate of the source ($\sim$0.07% $L_{\rm Edd}$), suggests that an inner, optically-thick accretion disc is absent in this source. Comparing the 2006 *Suzaku* data with *XMM-Newton* data from 2009 showed that NGC 7213 had changed in luminosity by a factor of $\sim$2 with the observed 2–10 keV flux falling from $F_{2-10} = 2.46 \times 10^{-11}$ erg cm^{-2} s^{-1} to $F_{2-10} = 1.20 \times 10^{-11}$ erg cm^{-2} s^{-1}. The X-ray spectrum takes largely the same form between observations with little change in the observed spectral shape and so overall it seems that the long-term variability in NGC 7213 can be accounted for simply by changes in the flux of the intrinsic power-law continuum with the line emission remaining relatively constant in flux.

The lack of a warm absorber in NGC 7213 could arise from the fact that the source has a low accretion rate with respect to Eddington. Therefore, there may not be sufficient radiation pressure to drive an outflow off the disc. Furthermore, given the additional lack of any broad Fe line or significant Compton reflection component, an optically-thick accretion disc may not even be present in the inner regions of this source. This may then explain why the observed spectral variations are relatively weak since there is no significant amount of reprocessing material available to modify the primary continuum emission. Instead, the lack of intervening material may allow us a clearer view of the central source, with the observed variations then arising from fundamental continuum processes (i.e. simple changes in the normalisation of the intrinsic power law). NGC 7213 could be similar to NGC 5548 which is also a low-accretion-rate source in which no significant outflow is observed. Again, the spectral variations are observed to largely arise from simple changes in the power-law normalisation, this time on weekly timescales.

In contrast, however, NGC 4051 was studied in Chapters 4 and 5 through contemporaneous *Chandra* HETG and *Suzaku* observations. A significant five-zone warm absorber was detected in the source including one high-velocity, highly-ionised zone observed in the Fe K band outflowing at $v_{\rm out} \sim 6\,000$ km s^{-1} plus one partially-covering zone to account for the additional spectral curvature $\lesssim 6$ keV. The estimated kinetic output of the outflow suggests

that NGC 4051 could be a low-mass analogue of QSOs such as PG 1211+143 and PDS 456 by depositing an amount of energy comparable to the binding energy of the galactic bulge should the wind persist for the lifetime of the AGN. By comparing the broad-band *Suzaku* data from 2008 with archival *Suzaku* data from 2005, dramatic changes in the observed 0.5–50 keV flux were observed with the spectral shape appearing much harder when the source flux was low. This is consistent with the typical variations observed in many other Seyfert galaxies such as Mrk 766 and MCG–6-30-15. The bulk of the long-term variations were accounted for in NGC 4051 by significant changes in the line-of-sight covering fraction of the partial-coverer which could be interpreted as arising from Compton-thick clouds of gas passing into our sightline, explaining the variations in the observed flux <10 keV. The constancy of the flux of the narrow Fe Kα emission line (most likely from distant material) then suggests that the absorber may take the form of a clumpy disc wind. The results are consistent with additional PCA / timing analysis which suggests that the variations can be accounted for by a simple two-component model (a soft, variable component superimposed on a pseudo-constant, hard offset component) and also suggests the presence of a significant amount of reverberating material within 100 $r_{\rm g}$ of the black hole. The observed short timescale variations on ks timescales are, however, likely to have an intrinsic origin.

Unlike sources such as NGC 7213 and NGC 5548, NGC 4051 forms part of a class of type-1 AGN whose X-ray spectral variations have been attributed to reprocessing of the intrinsic continuum emission by material close to the central black hole. Reprocessing models have largely taken the form of reflection-dominated and absorption-dominated models with light-bending models often invoked to explain the strong spectral variability in the reflection-dominated case. However, the weak Fe Kα emission in NGC 4051 combined with the very strong hard excess may rule out such a model. Instead, through high-resolution grating observations with *XMM-Newton* and *Chandra* and broad-band observations with *Suzaku*, it has become well established that significant amounts of line-of-sight absorption are present in higher-accretion-rate Seyfert galaxies and the observed spectral variations may arise from changes in the line-of-sight absorbing material. The exact role that absorption plays is not yet fully understood although changes in line-of-sight covering fractions, opacity and ionisation have been invoked to explain many sources such as NGC 3516 and Mrk 766. Such hypotheses

have been supported by recent hard X-ray evidence for significant amounts of Compton-thick gas in the sightline towards type-1 AGN. In reality, both absorption and reflection are likely to play significant roles and the rapidity of many of the observed variations indeed suggests that the reprocessing material is close to the central black hole. However, recent detections of high-velocity outflowing material suggests that clumpy accretion-disc winds could provide a natural explanation for the X-ray variability of many sources and may make direct views of 'naked' accretion discs improbable. Instead, the disc-winds themselves may be responsible for much of the *observed* absorption and reflection in X-ray spectra. If this is the case, then this may prompt a reconsideration of AGN unified schemes so as to include the presence of such outflowing winds in orientation-based and accretion-rate-based unification models and it is hoped that the advent of new spectral models and the future generation of X-ray data over the next decade may be the key to understanding the true nature of X-ray spectral variability enabling the fundamental accretion process and the role that the central engine plays in galactic feedback to be finally understood.

Glossary of Acronyms and Abbreviations

ACIS: Advanced CCD Imaging Spectrometer

ADAF: Advection-Dominated Accretion Flow

ADIOs: Advection-Dominated Inflows-Outflows

AGN: Active Galactic Nuclei

APEC: An emission-spectrum model from collisionally-ionised hot diffuse gas

ARF: Ancillary Response File

Ark: Arakelian

ASCA: Advanced Satellite for Cosmology and Astrophysics

AU: Astronomical Unit

BBB: Big Blue Bump

BELR: Broad-Emission-Line Region

BI: Back-Illuminated

BL Lac: BL Lacertae

BLR: Broad-Line Region

BLRG: Broad-Line Radio Galaxy

BAT: Burst Alert Telescope

CALDB: Calibration Database

CCD: Charge-Coupled Device

CCF: Current Calibration File

CDAF: Convection-Dominated Accretion Flow

CFHQS: Canada-France High-z Quasar Survey

CIAO: Chandra Interactive Analysis of Observations

CLEANSIS: Tool for cleaning event files

COR: Cut-Off Rigidity

COS: Cosmic Origins Spectrograph

CXB: Cosmic X-ray Background

CZT: Cadmium Zinc Telluride

DEC.: Declination

DISKLINE: Additive emission-line component arising from a relativistic accretion disc around a Schwarzschild black hole

DYE_ELV: Earth day-time elevation angle

ELV: Earth elevation angle

EPIC: European Photon Imaging Camera

ESO: European Southern Observatory

EUV: Extreme Ultraviolet

EW: Equivalent Width

EXOSAT: European X-Ray Observatory Satellite

FI: Front-Illuminated

FITS: Flexible Image Transport System

FOV: Field Of View

FR: Fanaroff-Riley

FTOOLS: Software package to manipulate FITS files

FWHM: Full-Width at Half-Maximum

GBHC: Galactic Black Hole Candidate

GRO: (Compton) Gamma Ray Observatory

GSFC: Goddard Space Flight Center

GSO: Gadolinium Silicate

GTI: Good Time Interval

HEAO: High Energy Astronomy Observatory

HEASARC: High Energy Astrophysics and Science Archive Research Center

HEAsoft: High Energy Astrophysics software package

HEG: High Energy Grating

HETG(S): High Energy Transmission Grating (Spectrometer)

HEXTE: High-Energy X-Ray Timing Experiment

HPGSPC: High Pressure Gas Scintillation Proportional Counter

HRC: High Resolution Camera

HST: Hubble Space Telescope

HWHM: Half-Width at Half-Maximum

HXD: Hard X-Ray Detector

HXDDTCOR: Script to correct for the HXD deadtime

HXI: Hard X-Ray Imager

INTEGRAL: International Gamma-Ray Astrophysics Laboratory

ISAS: Institute of Space and Astronautical Science

ISCO: Innermost Stable Circular Orbit

IXO: International X-Ray Observatory

LAT: Large Area Telescope

LBA: Long Baseline Array

LECS: Low Energy Concentrator Spectrometer

LETG(S): Low Energy Transmission Grating (Spectrometer)

LINER: Low-Ionisation Nuclear-Emission-Line Region

LOFT: Large Observatory For X-Ray Timing

MCG: Morphological Catalogue of Galaxies

MCMC: Markov Chain Monte Carlo

MECS: Medium Energy Concentrator Spectrometer

MEKAL: An emission-spectrum model from hot diffuse gas

MEG: Medium Energy Grating

MHD: Magnetohydrodynamic

MKGRMF: Tool for creating response files for the *Chandra* gratings

MOS: Metal-Oxide Semiconductor

Mrk: Markarian

NASA: The National Aeronautics and Space Administration

NGC: New General Catalogue

NLR: Narrow-Line Region

NLRG: Narrow-Line Radio Galaxy

NLS1: Narrow-Line Seyfert 1

NTT: New Technology Telescope

NuSTAR: Nuclear Spectroscopic Telescope Array

NXB: Non-X-Ray Background

OM: Optical Monitor

OVV: Optically-Violent Variable

PCA: Principal Components Analysis

PDS (instrument): Phoswich Detector System

PDS (catalogue): Planetary Data System

PEXRAV: Additive component for modelling reflection from neutral material

PG: Principal Galaxies (Catalogue)

PHA: Pulse-Height Amplitude

PI: PHA Invariant

PIN: Positive Intrinsic Negative

PMN: Parkes-MIT-NRAO

PSD: Power Spectral Density

PSF: Point-Spread Function

QDE: Quantum Detection Efficiency

QSO: Quasi-Stellar Object

R.A.: Right Ascension

REFLIONX: Ionised-reflection model

RGS: Reflection Grating Spectrometer

RIAF: Radiatively-Inefficient Accretion Flow

RMF: Response Matrix File

RQQ: Radio-Quiet Quasar

RRC: Radiative Recombination Continuum

RXTE: Rossi X-Ray Timing Explorer

SAA: South-Atlantic Anomaly

SAS: Scientific Analysis System

SED: Spectral Energy Distribution

SDSS: Sloan Digital Sky Survey

S/N: Signal-to noise

SSC: Synchrotron Self-Compton

SMBH: Supermassive Black Hole

UTA: Unresolved Transition Array

UV: Ultraviolet

WABS: Absorption model from cold, neutral material

WFC: Wide Field Camera

XIS: X-Ray Imaging Spectrometer

XISRMFGEN: Tool for creating XIS response files

XISSIMARFGEN: Tool for creating XIS ancillary response files

XCS: X-Ray Calorimeter Spectrometer

XMM: X-Ray Multi-Mirror Mission

XRS: X-Ray Spectrometer

XRT: X-Ray Telescope

XSELECT: Tool for filtering event files and generating images, spectra and lightcurves

XSPEC: X-ray spectral-fitting package

XSTAR: X-ray photo-ionisation code

Publications

- Turner T. J., Miller L., Reeves J. N., Lobban A. P., Braito V., Kraemer S. B., Crenshaw D. M., 2010, ApJ, 713, 209
  "Significant X-ray Line Emission in the 5–6 keV Band of NGC 4051"

- Miller L., Turner T. J., Reeves J. N., Lobban A. P., Kraemer S. B., Crenshaw D. M., 2010, MNRAS, 403, 196
  "Spectral Variability and Reverberation Time Delays in the Suzaku X-ray Spectrum of NGC 4051"

- Lobban A. P., Reeves J. N., Porquet D., Braito V. B., Markowitz A. G., Miller L., Turner T. J., 2010, MNRAS, 408, 551
  "Evidence for a Truncated Accretion Disc in the Low-Luminosity Seyfert Galaxy, NGC 7213?"

- Patrick A. R., Reeves J. N., Porquet D., Markowitz A. G., Lobban A. P., Terashima Y., 2011, MNRAS, 411, 2353
  "Iron Line Profiles in Suzaku Spectra of Bare Seyfert Galaxies"

- Lobban A. P., Reeves J. N., Miller L., Turner T. J., Braito V., Kraemer S. B., Crenshaw D. M., 2011, MNRAS, 414, 1965
  "Contemporaneous Chandra HETG and Suzaku X-ray Observations of NGC 4051"

- Patrick A. R., Reeves J. N., Lobban A. P., Porquet D., Markowitz A. G., 2011, MNRAS, 416, 2725
  "Assessing Black Hole Spin in Deep Suzaku Observations of Seyfert 1 AGN"

- Kraemer S. B., Crenshaw D. M., Dunn J. P., Turner T. J., Lobban A. P., Miller L., Reeves J. N., Fischer T. C., 2012, ApJ, 751, 84
  "Observations of Outflowing UV Absorbers in NGC 4051 with the Cosmic Origins Spectrograph"

- Patrick A. R., Reeves J. N., Porquet D., Markowitz A. G., Braito V., Lobban A P., 2012, MNRAS, 426, 2522

  "A Suzaku survey of Fe K lines in Seyfert 1 active galactic nuclei"

Bibliography

Abdo A., Ackermann M., Ajello M., et al., 2009a, ApJ, 699, 976

Abdo A., Ackermann M., Ajello M., et al., 2009b, ApJ, 707, 1310

Abdo A., Ackermann M., Ajello M., et al., 2010a, ApJ, 710, 1271

Abdo A., Ackermann M., Ajello M., et al., 2010b, ApJ, 715, 429

Aharonian F., Akhperjanian A., Barrio J., et al., 1997, A&A, 327, L5

Anders E., Ebihara M., 1982, Geochimica et Cosmochimica Acta, 46, 2363

Anders E., Grevesse N., 1989, Geochimica et Cosmochimica Acta, 53, 197

Antonucci R. R. J., Miller J. S., 1985, ApJ, 297, 621

Antonucci R., 1993, Annu. Rev. Astron. Astrophys., 31, 473

Arévalo P., Uttley P., 2006, MNRAS, 367, 801

Arnaud K., 1996, in Jacoby G. H., Jeannette Barnes e., eds, Astronomical Data Analysis Software and Systems V, ASP Conference Series, Vol. 101, 1996, p. 17

Avni Y., 1976, ApJ, 210, 642

Balbus S. A., Hawley J. F., 1991, ApJ, 376, 214

Ballantyne D. R., Vaughan S., Fabian A. C., 2003, MNRAS, 342, 239

Bambynek W., Crasemann B., Fink R., Freund H.-U., Mark H., Swift C., R.E. P., Venugopala Rao P., 1972, Rev. Mod. Phys., 44, 716

Barthelmy S., Barbier L., Cummings J., et al., 2005, Sp. Sci. Rev., 120, 143

Barvainis R., 1987, ApJ, 320, 537

Barvainis R., 1990, ApJ, 353, 419

Baumgartner W., Tueller J., Markwardt C., et al., 2010, ApJS, submitted

Bautista M., Kallman T., 2000, ApJ, 544, 581

Beckmann V., Shrader C. R., 2012, Active Galactic Nuclei

Beckmann V., Barthelmy S. D., Courvoisier T. J.-L., Gehrels N., Soldi S., Tueller J., Wendt G., 2007, A&A, 475, 827

Bell M., Tzioumis T., Uttley P., et al., 2011, MNRAS, 411, 402

Bertoldi F., Carilli C. L., Cox P., Fan X., Strauss M. A., Beelen A., Omont A., Zylka R., 2003, A&A, 406, L55

Bianchi S., Matt G., 2002, A&A, 387, 76

Bianchi S., Matt G., Balestra I., Perola G., 2003, A&A, 407, 21

Bianchi S., Matt G., Balestra, I. Guainazzi M., Perola G., 2004, A&A, 422, 65

Bianchi S., Matt G., Nicastro, F. Porquet D., Dubau J., 2005, MNRAS, 357, 599

Bianchi S., La Franca F., Matt G., Guainazzi M., Jiménez-Bailón E., Longinotti A., Nicastro F., Pentericci L., 2008, MNRAS, 389, 52

Bianchi S., Guainazzi M., Chiaberge M., 2006, A&A, 448, 499

Blandford R. D., Begelman M. C., 1999, MNRAS, 303, L1

Blandford R. D., Payne D. G., 1982, MNRAS, 199, 883

Blandford R. D., Znajek R. L., 1977, MNRAS, 179, 433

Blandford R. D., McKee C. F., Rees M. J., 1977, Nature, 267, 211

Blank D., Harnett J., Jones P., 2005, MNRAS, 356, 734

Blustin A. J., Page M. J., Fuerst S. V., Branduardi-Raymont G., Ashton C. E., 2005, A&A, 431, 111

Boella G., Butler R. C., Perola G. C., Piro L., Scarsi L., Bleeker J. A. M., 1997, A&AS, 122, 299

Boella G., Chiappetti L., Conti G., et al., 1997, A&AS, 122, 327

Boldt E., 1987, Phys.Rep., 146, 215

Boller T., Brandt W. N., Fink H., 1996, A&A, 305, 53

Brenneman L. W., Reynolds C. S., 2006, ApJ, 652, 1028

Brenneman L., Reynolds C., Nowak M., et al., 2011, ApJ, 736, 103

Brenneman L. W., Elvis M., Krongold Y., Liu Y., Mathur S., 2012, ApJ, 744, 13

Brinkman B., Gunsing T., Kaastra J., et al., 2000, in J. E. Truemper & B. Aschenbach, ed., Society of Photo-Optical Instrumentation Engineers (SPIE) Conference Series, p. p. 81

Brinkman A., Kaastra J., van der Meer R., Kinkhabwala A., Behar E., Kahn S., Paerels F., Sako M., 2002, A&A, 396, 761

Burrows D., Hill J., Nousek J., et al., 2000, in K. A. Flanagan & O. H. Siegmund, ed., Society of Photo-Optical Instrumentation Engineers (SPIE) Conference Series, p. p. 64

Camenzind M., Courvoisier T. J.-L., 1983, ApJL, 266, L83

Canizares C., Davis J., Dewey D., et al., 2005, PASP, 117, 1144

Cash W., 1979, ApJ, 228, 939

Chen X., Abramowicz M. A., Lasota J.-P., Narayan R., Yi I., 1995, ApJL, 443, L61

Churazov E., Sunyaev R., Revnivtsev M., 2007, A&A, 467, 529

Collinge M., Brandt W., Kaspi S., et al., 2001, ApJ, 557, 2

Crenshaw D. M., Kraemer S. B., 2007, ApJ, 659, 250

Crenshaw D. M., Kraemer S. B., George I. M., 2003, Annu. Rev. Astron. Astrophys., 41, 117

Crummy J., Fabian A. C., Gallo L., Ross R. R., 2006, MNRAS, 365, 1067

Czerny B., Hryniewicz K., 2011, A&A, 525, L8

Czerny B., Nikołajuk M., Różańska A., Dumont A.-M., Loska Z., Zycki P. T., 2003, A&A, 412, 317

Dadina M., 2008, A&A, 485, 417

Dai B., Li X., Liu Z., et al., 2009, MNRAS, 392, 1181

Dauser T., Wilms J., Reynolds C. S., Brenneman L. W., 2010, MNRAS, 409, 1534

Davis J. E., 2001, ApJ, 562, 575

de Marco B., Iwasawa K., Cappi M., Dadina M., Tombesi F., Ponti G., Celotti A., Miniutti G., 2009, A&A, 507, 159

den Herder J., Brinkman A., Kahn S., et al., 2001, A&A, 365, L7

Denney K., Watson L., Peterson B., et al., 2009, ApJ, 702, 1353

Dewangan G., Griffiths R., Di Matteo R., Schurch N., 2004, ApJ, 607, 788

Dickey J., Lockman F., 1990, Annu. Rev. Astron. Astrophys., 28, 215

Done C., Davis S., Jin C., Blaes O., Ward M., 2012, MNRAS, , 2196

Done C., Gierliński M., Kubota A., 2007, A&ARv, 15, 1

Dopita M. A., Sutherland R. S., 1995, ApJ, 455, 468

Dovčiak M., Bianchi S., Guainazzi M., Karas V., Matt G., 2004, MNRAS, 350, 745

Elitzur M., Ho L. C., 2009, ApJL, 701, L91

Elvis M., 2000, ApJ, 545, 63

Emmanoulopoulos D., Papadakis I. E., McHardy I. M., Arévalo P., Calvelo D. E., Uttley P., 2012, MNRAS, 424, 1327

Emmanoulopoulos D., Papadakis I. E., Nicastro F., McHardy I. M., 2013, MNRAS, 429, 3439

Fabian A. C., Vaughan S., 2003, MNRAS, 340, L28

Fabian A. C., 1994, ApJS, 92, 555

Fabian A., Rees M., Stella L., White N., 1989, MNRAS, 238, 729

Fabian A. C., Iwasawa K., Reynolds C. S., Young A. J., 2000, PASP, 112, 1145

Falcke H., Patnaik A., Sherwood W., 1996, ApJ, 473, 13

Fan X., Narayanan V., Lupton R., et al., 2001, AJ, 122, 2833

Fanaroff B. L., Riley J. M., 1974, MNRAS, 167, 31P

Fano U., 1947, Phys. Rev., 72, 26

Ferland G. J., Netzer H., 1983, ApJ, 264, 105

Ferrarese L., Merritt D., 2000, ApJL, 539, L9

Filippenko A., Halpern J., 1984, MNRAS, 285, 458

Filippenko A., Richmond M., Branch D., et al., 1992, AJ, 104, 1543

Ford H., Harms R., Tsvetanov Z., et al., 1994, ApJL, 435, L27

Foschini L., 2011, p. Narrow-Line Seyfert 1 Galaxies and their Place in the Universe

Foschini L., Ghisellini G., Kovalev Y. Y., et al., 2011, MNRAS, 413, 1671

Frank J., King A., Raine D. J., 2002, Accretion Power in Astrophysics: Third Edition

Frontera F., Costa E., dal Fiume D., Feroci M., Nicastro L., Orlandini M., Palazzi E., Zavattini G., 1997, A&AS, 122, 357

Fruscione A., McDowell J., Allen G., et al., 2006, p. Society of Photo-Optical Instrumentation Engineers (SPIE) Conference Series

Fukazawa Y., Mizuno T., Watanabe S., et al., 2009, PASJ, 61, 17

Garmire G. P., Bautz M. W., Ford P. G., Nousek J. A., Ricker, Jr. G. R., 2003, in J. E. Truemper & H. D. Tananbaum, ed., Society of Photo-Optical Instrumentation Engineers (SPIE) Conference Series, p. p. 28

Gaskell C. M., 1982, ApJ, 263, 79

Gebhardt K., Bender R., Bower G., et al., 2000, ApJL, 539, L13

George I., Fabian A., 1991, MNRAS, 249, 352

Gierliński M., Done C., 2004, MNRAS, 349, L7

Gillessen S., Eisenhauer F., Trippe S., Alexander T., Genzel R., Martins F., Ott T., 2009, ApJ, 692, 1075

Gofford J., Reeves J. N., Tombesi F., Braito V., Turner T. J., Miller L., Cappi M., 2012, ArXiv e-prints

Goodrich R. W., 1989, ApJ, 342, 224

Grevesse N., Noels A., Sauval A., 1996, ASPC, 99, 117

Gruber D., Matteson J., Peterson L., Jung G., 1999, ApJ, 520, 124

Guainazzi M., Bianchi S., 2007, MNRAS, 374, 1290

Guainazzi M., Mihara T., Otani C., Matsuoka M., 1996, PASJ, 48, 781

Guainazzi M., Nicastro F., Fiore F., et al., 1998, MNRAS, 301, L1

Haardt F., Maraschi L., 1991, ApJL, 380, L51

Haardt F., Maraschi L., 1993, ApJ, 413, 507

Halpern J., Filippenko A., 1984, ApJ, 285, 475

Hameed S., Blank D., Young L., Devereux N., 2001, ApJ, 546, 97

Häring N., Rix H.-W., 2004, ApJL, 604, L89

Heckman T. M., 1980, A&A, 87, 152

Heckman T. M., Armus L., Miley G. K., 1987, AJ, 93, 276

Ho L., 1999, ApJ, 516, 672

Hopkins P. F., Elvis M., 2010, MNRAS, 401, 7

Ishida M., Suzuki K., Someya K., 2007, JX-ISAS-SUZAKU-MEMO-2007-11

Ishisaki Y., Maeda Y., Fujimoto R., et al., 2007, PASJ, 59, 113

Iwasawa K., Miniutti G., Fabian A. C., 2004, MNRAS, 355, 1073

Jaffe W., Meisenheimer K., Röttgering H., et al., 2004, Nature, 429, 47

Jager R., Mels W., Brinkman A., et al., 1997, A&AS, 125, 557

Jansen F., Lumb D., Alteri B., et al., 2001, A&A, 365, L1

Kaastra J., Mewe R., 1993, A&AS, 97, 443

Kaastra J., 1992, An X-ray Spectral Code for Optically Thin Plasmas (Internal SRON-Leiden Report, updated version 2.0)

Kalberla P., Burton W., Hartmann D., Arnal E., Bajaja E., Morras R., Pöppel W., 2005, A&A, 440, 775

Kallman T., Bautista M., 2001, ApJS, 133, 221

Kallman T., McCray R., 1982, ApJ, 50, 263

Kallman T. R., Palmeri P., Bautista M. A., Mendoza C., Krolik J. H., 2004, ApJS, 155, 675

Karas V., Martocchia A., Subr L., 2001, PASJ, 53, 189

Kaspi S., Brandt W., Netzer H., et al., 2001, ApJ, 554, 216

Kaspi S., Brandt W., George I., et al., 2002, ApJ, 574, 643

Kataoka J., Reeves J., Iwasawa K., et al., 2007, PASJ, 59, 279

Kelley R., Mitsuda K., Allen C., et al., 2007, PASJ, 59, 77

King A. R., Pounds K. A., 2003, MNRAS, 345, 657

King A., 2003, ApJL, 596, L27

King A. R., 2010, MNRAS, 402, 1516

Kinkhabwala A., Sako M., Behar E., et al., 2002, ApJ, 575, 732

Kokubun M., Makishima K., Takahashi T., et al., 2007, PASJ, 59, 63

Korista K., Alloin D., Barr P., et al., 1995, ApJS, 97, 285

Kotov O., Churazov E., Gilfanov M., 2001, MNRAS, 327, 799

Koyama K., Tsunemi H., Dotani T., et al., 2007, PASJ, 59, 23

Kraemer S., George I., Crenshaw D., et al., 2005, ApJ, 633, 693

Kraemer S. B., Crenshaw D. M., Dunn J. P., Turner T. J., Lobban A. P., Miller L., Reeves J. N., Fischer T. C., Braito V., 2012, ApJ, 751, 84

Krolik J. H., Begelman M. C., 1988, ApJ, 329, 702

Krongold Y., Nicastro F., Brickhouse N. S., Elvis M., Mathur S., 2005, ApJ, 622, 842

Krongold Y., Nicastro F., Elvis M., Brickhouse N., Binette L., Mathur S., Jiménez-Bailón E., 2007, ApJ, 659, 1022

Krongold Y., Jiménez-Bailón E., Santos-Lleo M., et al.

Lamer G., McHardy I. M., Uttley P., Jahoda K., 2003, MNRAS, 338, 323

Lamer G., Uttley P., McHardy I. M., 2000, MNRAS, 319, 949

Laor A., 1991, ApJ, 376, 90

Laor A., Fiore F., Elvis M., Wilkes B. J., McDowell J. C., 1994, ApJ, 435, 611

Larsson J., Miniutti G., Fabian A. C., Miller J. M., Reynolds C. S., Ponti G., 2008, MNRAS, 384, 1316

Lawrence A., Watson M. G., Pounds K. A., Elvis M., 1985, MNRAS, 217, 685

Letaw J. R., Silberberg R., Tsao C. H., 1983, ApJS, 51, 271

Liedahl D., Osterheld A., Goldstein W., 1995, ApJL, 438, 115

Lightman A. P., White T. R., 1988, ApJ, 335, 57

Liu B. F., Yuan W., Meyer F., Meyer-Hofmeister E., Xie G. Z., 1999, ApJL, 527, L17

Longinotti A. L., Sim S. A., Nandra K., Cappi M., 2007, MNRAS, 374, 237

Lyubarskii Y. E., 1997, MNRAS, 292, 679

Maccarone T., 2003, A&A, 409, 697

Magdziarz P., Zdziarski A., 1995, MNRAS, 273, 837

Magorrian J., Tremaine S., Richstone D., et al., 1998, AJ, 115, 2285

Malizia A., Bassani L., Stephen J., Di Cocco G., Fiore F., Dean A., 2003, ApJL, 589

Manzo G., Giarrusso S., Santangelo A., Ciralli F., Fazio G., Piraino S., Segreto A., 1997, A&AS, 122, 341

Marconi A., Hunt L. K., 2003, ApJL, 589, L21

Markert T. H., Canizares C. R., Dewey D., McGuirk M., Pak C. S., Schattenburg M. L., 1994, in O. H. Siegmund & J. V. Vallerga, ed., Society of Photo-Optical Instrumentation Engineers (SPIE) Conference Series, p. p. 168

Markowitz A., Edelson R., 2004, ApJ, 617, 939

Markowitz A., 2005, ApJ, 635, 180

Markowitz A., Papadakis I., Arévalo P., Turner T. J., Miller L., Reeves J. N., 2007, ApJ, 656, 116

Markowitz A., Reeves J. N., Miniutti G., et al., 2008, PASJ, 60, 277

Markowitz A., Reeves J. N., Braito V., 2006, ApJ, 646, 783

Marscher A. P., 2009, ArXiv e-prints

Mason K., Breeveld A., Much R., et al., 2001, A&A, 365, L36

Matsuoka M., Piro L., Yamauchi M., Murakami T., 1990, ApJ, 361, 440

Matt G., Fabian A. C., Reynolds C. S., 1997, MNRAS, 289, 175

Matt G., Perola G., Pirlo L., 1991, A&A, 247, 25

Matt G., Pompilio F., La Franca F., 1999, New Astronomy, 4, 191

McHardy I., Czerny B., 1987, Nature, 325, 696

McHardy I. M., Papadakis I. E., Uttley P., Page M. J., Mason K. O., 2004, MNRAS, 348, 783

McHardy I., Koerding E., Knigge C., Uttley P., Fender R., 2006, Nature, 444, 730

McHardy I. M., Arévalo P., Uttley P., Papadakis I. E., Summons D. P., Brinkmann W., Page M. J., 2007, MNRAS, 382, 985

McKernan B., Yaqoob T., 1998, ApJL, 501, L29

McKernan B., Yaqoob T., Reynolds C. S., 2007, MNRAS, 379, 1359

McKinney J. C., 2006, MNRAS, 368, 1561

McQuillin R. C., McLaughlin D. E., 2012, MNRAS, 423, 2162

Meier D. L., Koide S., Uchida Y., 2001, Science, 291, 84

Mewe R., Gronenschild E., van den Oord G., 1985, A&AS, 62, 197

Mewe R., Lemen J., van den Oord G., 1986, A&AS, 65, 511

Middleton M., Done C., Gierliński M., 2007, MNRAS, 381, 1426

Miller L., Turner T. J., 2011, p. Narrow-Line Seyfert 1 Galaxies and their Place in the Universe

Miller L., Turner T. J., Reeves J. N., George I. M., Kraemer S. B., Wingert B., 2007, A&A, 463, 131

Miller J. M., Raymond J., Reynolds C. S., Fabian A. C., Kallman T. R., Homan J., 2008, ApJ, 680, 1359

Miller L., Turner T. J., Reeves J. N., Braito V., 2010, MNRAS, 408, 1928

Miller L., Turner T. J., Reeves J. N., Lobban A., Kraemer S. B., Crenshaw D. M., 2010, MNRAS, 403, 196

Miller L., Turner T. J., Reeves J. N., 2008, A&A, 483, 437

Miller L., Turner T. J., Reeves J. N., 2009, MNRAS, 399, L69

Miniutti G., Fabian A. C., 2004, MNRAS, 349, 1435

Miniutti G., Fabian A. C., Goyder R., Lasenby A. N., 2003, MNRAS, 344, L22

Miniutti G., Fabian A., Anabuki N., et al., 2007, PASJ, 59, 315

Mitsuda K., Bautz M., Inoue H., et al., 2007, PASJ, 59, 1

Morrison R., McCammon D., 1983, ApJ, 270, 119

Mortlock D., Warren S., Venemans B., et al., 2011, Nature, 474, 616

Mould J., Huchra J., Freedman W., et al., 2000, ApJ, 529, 786

Murphy K., Yaqoob T., 2009, MNRAS, 397, 1549

Murray N., Chiang J., 1998, ApJ, 494, 125

Murray S., Austin G., Chappell J., et al., 2000, in J. E. Truemper & B. Aschenbach, ed., Society of Photo-Optical Instrumentation Engineers (SPIE) Conference Series, p. p. 68

Nandra K., Pounds K., 1994, MNRAS, 268, 405

Nandra K., O'Neill P. M., George I. M., Reeves J. N., 2007, MNRAS, 382, 194

Narayan R., Yi I., 1995, ApJ, 452, 710

Narayan R., Igumenshchev I. V., Abramowicz M. A., 2000, ApJ, 539, 798

Narayan R., Mahadevan R., Quataert E., 1998, in M. A. Abramowicz, G. Bjornsson, & J. E. Pringle, ed., Theory of Black Hole Accretion Disks, p. p. 148

Nayakshin S., 2000, ApJL, 540, L37

Nayakshin S., Kazanas D., Kallman T. R., 2000, ApJ, 537, 833

Nelson C., Whittle M., 1995, ApJS, 99, 67

Netzer H., Laor A., 1993, ApJ, 404, 51

Netzer H., 1990, in R. D. Blandford, H. Netzer, L. Woltjer, T. J.-L. Courvoisier, & M. Mayor, ed., Active Galactic Nuclei, p. p. 57

Nicastro F., Piro L., De Rosa A., et al., 2000, ApJ, 536, 718

Nucita A. A., Guainazzi M., Longinotti A. L., Santos-Lleo M., Maruccia Y., Bianchi S., 2010, A&A, 515, A47+

Ogle P. M., Mason K. O., Page M. J., Salvi N. J., Cordova F. A., McHardy I. M., Priedhorsky W. C., 2004, ApJ, 606, 151

Osterbrock D. E., Pogge R. W., 1985, ApJ, 297, 166

Osterbrock D. E., Pogge R. W., 1987, ApJ, 323, 108

Osterbrock D. E., 1981, ApJ, 249, 462

Osterbrock D. E., 1989, Astrophysics of gaseous nebulae and active galactic nuclei

Paczyński B., Wiita P. J., 1980, A&A, 88, 23

Padovani P., Rafanelli P., 1988, A&A, 205, 53

Page M., 2001, MNRAS, 328, 925

Page M., Breeveld A., Soria R., Wu K., Branduardi-Raymont G., Mason K., Starling R., Zane S., 2003, A&A, 400, 145

Palmeri P., Mendoza C., Kallman T. R., Bautista M. A., Meléndez M., 2003, A&A, 410, 359

Panessa F., Barcons X., Bassani L., Cappi M., Carrera F., Ho L., Pellegrini S., 2007, A&A, 467, 519

Papadakis I. E., Petrucci P. O., Maraschi L., McHardy I. M., Uttley P., Haardt F., 2002, ApJ, 573, 92

Papadakis I., Sobolewska M., Arevalo P., Markowitz A., McHardy I., Miller L., Reeves J., Turner T., 2009, A&A, 494, 905

Papadakis I. E., Nandra K., Kazanas D., 2001, ApJL, 554, L133

Parmar A., Martin D., Bavdaz M., et al., 1997, A&AS, 122, 309

Patrick A. R., Reeves J. N., Lobban A. P., Porquet D., Markowitz A. G., 2011, MNRAS, 416, 2725

Patrick A. R., Reeves J. N., Porquet D., Markowitz A. G., Lobban A. P., Terashima Y., 2011, MNRAS, 411, 2353

Pearson K., 1900, Philosophical Magazine, 5th Series, 50, 157

Pearson T. J., Unwin S. C., Cohen M. H., Linfield R. P., Readhead A. C. S., Seielstad G. A., Simon R. S., Walker R. C., 1981, Nature, 290, 365

Penston M. V., Perez E., 1984, MNRAS, 211, 33P

Perola G., Matt G., Cappi M., Fiore F., Guainazzi M., Maraschi L., Petrucci P., Piro L., 2002, A&A, 389, 802

Peterson B. M., 1993, PASP, 105, 247

Peterson B. M., 1997, An Introduction to Active Galactic Nuclei

Peterson B., Ferrarese L., Gilbert K., et al., 2004, ApJ, 613, 682

Pogge R. W., 1989, ApJ, 345, 730

Ponti G., Miniutti G., Cappi M., Maraschi L., Fabian A. C., Iwasawa K., 2006, MNRAS, 368, 903

Ponti G., Fender R. P., Begelman M. C., Dunn R. J. H., Neilsen J., Coriat M., 2012, MNRAS, 422, L11

Porquet D., Dubau J., 2000, A&AS, 143, 495

Porquet D., Reeves J. N., Uttley P., Turner T. J., 2004, A&A, 427, 101

Porquet D., Reeves J., O'Brien P., Brinkmann W., 2004b, A&A, 422, 85

Pounds K., Page K., 2005, MNRAS, 360, 1123

Pounds K. A., Reeves J. N., 2009, MNRAS, 397, 249

Pounds K. A., Vaughan S., 2011, MNRAS, 413, 1251

Pounds K. A., Vaughan S., 2012, MNRAS, 423, 165

Pounds K. A., Reeves J. N., King A. R., Page K. L., O'Brien P. T., Turner M. J. L., 2003, MNRAS, 345, 705

Pounds K. A., Reeves J. N., Page K. L., Wynn G. A., O'Brien P. T., 2003, MNRAS, 342, 1147

Pounds K. A., Reeves J. N., King A. R., Page K. L., 2004, MNRAS, 350, 10

Pounds K. A., Reeves J. N., Page K. L., O'Brien P. T., 2004, ApJ, 616, 696

Pounds K. A., Page K. L., Reeves J. N., 2007, in V. Karas & G. Matt, ed., IAU Symposium, p. p. 105

Pozdnyakov L. A., Sobol I. M., Syunyaev R. A., 1983, Astrophysics and Space Physics Reviews, 2, 189

Proga D., Kallman T. R., 2004, ApJ, 616, 688

Proga D., Ostriker J. P., Kurosawa R., 2008, ApJ, 676, 101

Proga D., Stone J. M., Kallman T. R., 2000, ApJ, 543, 686

Rana V. R., Cook, III W. R., Harrison F. A., Mao P. H., Miyasaka H., 2009, p. Society of Photo-Optical Instrumentation Engineers (SPIE) Conference Series

Rees M. J., 1977, QJRAS, 18, 429

Rees M. J., 1984, Annu. Rev. Astron. Astrophys., 22, 471

Reeves J., Turner M., 2000, MNRAS, 316, 234

Reeves R., 1974, Annu. Rev. Astron. Astrophys., 12, 437

Reeves J. N., Wynn G., O'Brien P. T., Pounds K. A., 2002, MNRAS, 336, L56

Reeves J. N., Nandra K., George I. M., Pounds K. A., Turner T. J., Yaqoob T., 2004, ApJ, 602, 648

Reeves J. N., O'Brien P. T., Braito V., Behar E., Miller L., Turner T. J., Fabian A. C., Kaspi S., Mushotzky R., Ward M., 2009, ApJ, 701, 493

Reeves J. N., O'Brien P. T., Ward M. J., 2003, ApJL, 593, L65

Reyes R., Zakamska N., Strauss M., et al., 2008, AJ, 136, 2373

Reynolds C., Fabian A., 1995, MNRAS, 273, 1167

Reynolds C. S., Wilms J., 2000, ApJ, 533, 821

Reynolds C. S., Wilms J., Begelman M. C., Staubert R., Kendziorra E., 2004, MNRAS, 349, 1153

Risaliti G., Bianchi S., Matt G., Baldi A., Elvis M., Fabbiano G., Zezas A., 2005, ApJL, 630, L129

Risaliti G., Elvis M., Fabbiano G., Baldi A., Zezas A., Salvati M., 2007, ApJL, 659, L111

Risaliti G., Miniutti G., Elvis M., et al., 2009, ApJ, 696, 160

Risaliti G., Maiolino R., Salvati M., 1999, ApJ, 522, 157

Ross R., Fabian A., 2005, MNRAS, 358, 211

Ross R. R., Fabian A. C., Young A. J., 1999, MNRAS, 306, 461

Rothschild R., Blanco P., Gruber D., et al., 1998, ApJ, 496, 538

Różańska A., Czerny B., 2000, A&A, 360, 1170

Russell D. G., 2004, ApJ, 607, 241

Rybicki G. B., Lightman A. P., 1979, Radiative processes in astrophysics

Sadler E., 1984, AJ, 89, 53

Sahayanathan S., Godambe S., 2012, MNRAS, 419, 1660

Sambruna R., Reeves J., Braito V., et al., 2009, ApJ, 700, 1473

Schmitt H. R., Antonucci R. R. J., Ulvestad J. S., Kinney A. L., Clarke C. J., Pringle J. E., 2001, ApJ, 555, 663

Schurch N. J., Done C., 2006, MNRAS, 371, 81

Schurch N. J., Done C., 2007, MNRAS, 381, 1413

Schurch N., Warwick R., 2002, MNRAS, 334, 811

Schurch N. J., Done C., Proga D., 2009, ApJ, 694, 1

Seyfert C. K., 1943, ApJ, 97, 28

Shakura N., Sunyaev R., 1973, A&A, 24, 337

Shemmer O., Brandt W., Netzer H., Maiolino R., Kaspi S., 2006, ApJ, 646, 29

Shlosman I., Begelman M. C., Frank J., 1990, Nature, 345, 679

Shu X. W., Yaqoob T., Wang J. X., 2010, ApJS, 187, 581

Sim S. A., Long K. S., Miller L., Turner T. J., 2008, MNRAS, 388, 611

Sim S. A., Miller L., Long K. S., Turner T. J., Reeves J. N., 2010, MNRAS, 404, 1369

Singh K. P., 1999, MNRAS, 309, 991

Singh V., Shastri P., Risaliti G., 2011, A&A, 532, A84

Sitko M. L., Sitko A. K., Siemiginowska A., Szczerba R., 1993, ApJ, 409, 139

Skibo J. G., 1997, ApJ, 478, 522

Smith R., Brickhouse N., Liedahl D., Raymond J., 2001, ApJ, 556, 91

Starling R., Page M., Branduardi-Raymont G., Breeveld A., Soria R., Wu K., 2005, MNRAS, 356, 727

Steenbrugge K. C., Fenovčík M., Kaastra J. S., Costantini E., Verbunt F., 2009, A&A, 496, 107

Strüder L., Briel U., Dennerl K., et al., 2001, A&A, 365, L18

Takahashi T., Abe K., Endo M., et al., 2007, PASJ, 59, 35

Tanaka Y., Inoue H., Holt S. S., 1994, PASJ, 46, L37

Tatum M. M., Turner T. J., Sim S. A., Miller L., Reeves J. N., Patrick A. R., Long K. S., 2012, ApJ, 752, 94

Tatum M. M., Turner T. J., Miller L., Reeves J. N., 2013, ApJ, 762, 80

Taylor R. D., Uttley P., McHardy I. M., 2003, MNRAS, 342, L31

Terashima Y., Gallo L., Inoue H., et al., 2009, PASJ, 61, 299

Terlevich R., Tenorio-Tagle G., Franco J., Melnick J., 1992, MNRAS, 255, 713

Thorne K. S., 1974, ApJ, 191, 507

Titarchuk L., 1994, ApJ, 434, 570

Tombesi F., Cappi M., Reeves J. N., Palumbo G. G. C., Yaqoob T., Braito V., Dadina M., 2010, A&A, 521, A57+

Tombesi F., Cappi M., Reeves J. N., Palumbo G. G. C., Braito V., Dadina M., 2011, ApJ, 742, 44

Tombesi F., Cappi M., Reeves J. N., Braito V., 2012, MNRAS, 422, L1

Trump J., Impey C., Kelly B., et al., 2011, ApJ, 733, 60

Tully R. B., Fisher J. R., 1977, A&A, 54, 661

Turner T. J., Miller L., 2009, A&ARv, 17, 47

Turner T. J., Miller L., 2010, ApJ, 709, 1230

Turner T. J., Pounds K. A., 1989, MNRAS, 240, 833

Turner M., Abbey A., Arnaud M., et al., 2001, A&A, 365, L27

Turner T., Mushotzky R., Yaqoob T., et al., 2002, ApJL, 574, L123

Turner T. J., Kraemer S. B., George I. M., Reeves J. N., Bottorff M. C., 2005, ApJ, 618, 155

Turner T. J., Miller L., Reeves J. N., Kraemer S. B., 2007, A&A, 475, 121

Turner T. J., Reeves J. N., Kraemer S. B., Miller L., 2008, A&A, 483, 161

Turner T. J., Miller L., Kraemer S. B., Reeves J. N., Pounds K. A., 2009, ApJ, 698, 99

Turner T. J., Miller L., Reeves J. N., Lobban A., Braito V., Kraemer S. B., Crenshaw D. M., 2010, ApJ, 712, 209

Turner T. J., Miller L., Kraemer S. B., Reeves J. N., 2011, ApJ, 733, 48

Turner T. J., Kraemer S. B., Reeves J. N., 2004, ApJ, 603, 62

Turner T. J., Miller L., Tatum M., 2012, in Petre R., Mitsuda K., Angelini L., eds, American Institute of Physics Conference Series, p. p. 165

Urry C. M., Padovani P., 1995, PASP, 107, 803

Uttley P., McHardy I. M., 2001, MNRAS, 323, L26

Uttley P., McHardy I. M., Papadakis I. E., Guainazzi M., Fruscione A., 1999, MNRAS, 307, L6

Uttley P., Fruscione A., McHardy I., Lamer G., 2003, ApJ, 595, 656

Uttley P., Taylor R. D., McHardy I. M., Page M. J., Mason K. O., Lamer G., Fruscione A., 2004, MNRAS, 347, 1345

Uttley P., McHardy I. M., Vaughan S., 2005, MNRAS, 359, 345

van Dyk D. A., Connors A., Kashyap V. L., Siemiginowska A., 2001, ApJ, 548, 224

Vasudevan R. V., Fabian A. C., 2009, MNRAS, 392, 1124

Vaughan S., Edelson R., 2001, ApJ, 548, 694

Vaughan S., Fabian A. C., 2004, MNRAS, 348, 1415

Vaughan S., Uttley P., 2008, MNRAS, 390, 421

Vaughan S., Reeves J., Warwick R., Edelson R., 1999, MNRAS, 309, 113

Vaughan S., Uttley P., Pounds K. A., Nandra K., Strohmayer T. E., 2011, MNRAS, 413, 2489

Vaughan S., Fabian A. C., Nandra K., 2003, MNRAS, 339, 1237

Verheijen M. A. W., Sancisi R., 2001, A&A, 370, 765

Verner D., Ferland G., Korista K., Yakovlev D., 1996, ApJ, 465, 487

Walter F., Bertoldi F., Carilli C., et al., 2003, Nature, 424, 406

Wandel A., 1999, ApJ, 527, 657

Weisskopf M. C., Tananbaum H. D., Van Speybroeck L. P., O'Dell S. L., 2000, in J. E. Truemper & B. Aschenbach, ed., Society of Photo-Optical Instrumentation Engineers (SPIE) Conference Series, p. p. 2

Wilkes B., Elvis M., 1986, BAAS, 18, 925

Wilkes B. J., Elvis M., 1987, ApJ, 323, 243

Wilks W. R., Richardson S., Spiegelhalter R. J., 1996, Markov Chain Monte Carlo in Practice

Willott C., Delorme P., Omont A., et al., 2007, AJ, 134, 2435

Wilms J., Reynolds C. S., Begelman M. C., Reeves J., Molendi S., Staubert R., Kendziorra E., 2001, MNRAS, 328, L27

Wilson A. S., Tsvetanov Z. I., 1994, AJ, 107, 1227

Wolter H., 1952a, Ann. Physik, 10, 286

Wolter H., 1952b, Ann. Physik, 10, 94

Woo J.-H., Urry C., 2002, ApJ, 579, 530

Wu C.-C., Boggess A., Gull T., 1983, ApJ, 266, 28

Yamaguchi H., Nakajima H., Koyama K., et al., 2006, p. Society of Photo-Optical Instrumentation Engineers (SPIE) Conference Series

Yaqoob T., Serlemitsos P., 2005, ApJ, 623, 112

Yaqoob T., George I. M., Kallman T. R., Padmanabhan U., Weaver K. A., Turner T. J., 2003, ApJ, 596, 85

Yaqoob T., Murphy K., Miller L., Turner T., 2010, MNRAS, 401, 411

Young A., Nowak M., Markoff S., Marshall H., Canizares C., 2007, ApJ, 669, 830

Zdziarski A. A., Poutanen J., Paciesas W. S., Wen L., 2002, ApJ, 578, 357

Zoghbi A., Fabian A. C., Uttley P., Miniutti G., Gallo L. C., Reynolds C. S., Miller J. M., Ponti G., 2010, MNRAS, 401, 2419